Techniques for
BOLD and blood volume weighted fMRI

Benedikt Poser

F.C. Donders Centre for Cognitive Neuroimaging
Erwin L. Hahn Institute for Magnetic Resonance Imaging

Techniques for BOLD and blood volume weighted fMRI

Een wetenschappelijke proeve op het gebied van de
Natuurwetenschappen, Wiskunde en Informatica

PROEFSCHRIFT

ter verkrijging van de graad van doctor
aan de Radboud Universiteit Nijmegen
op gezag van rector magnificus prof. mr. S.C.J.J. Kortmann,
volgens besluit van het college van decanen
in het openbaar te verdedigen op vrijdag 26 juni 2009
om 10.30 uur precies
door

Andreas Benedikt Poser

geboren op 4 oktober 1978
te Wolfenbüttel, Duitsland

Promotor:	Prof. dr. David G. Norris
Manuscriptcommissie:	Prof. dr. Arno Kentgens
	Prof. dr. Arend Heerschap
	Prof. dr. Penny Gowland, University of Nottingham, UK

The studies presented in this thesis were performed at the F.C. Donders Centre for Cognitive Neuroimaging at the Radboud University in Nijmegen, The Netherlands, and at the Erwin L. Hahn Institute for Magnetic Resonance Imaging in Essen, Germany.

ISBN: 978-90-9024115-9

Printed by: Print Partners Ipskamp, Enschede, The Netherlands

For my parents.

Table of Contents

Chapter 1 Introduction

Great efforts are continuously being made by researchers from a broad range of fields to further our understanding of the human brain. Clearly, this mission relies on the continued improvement of existing, and the development of new techniques to probe the brain's structure, physiology and cognitive processes, and even so the task will likely remain a challenge for decades to come. As a relatively recent addition to available methods, functional magnetic resonance imaging (fMRI) has established itself as one of the most important neuroscientific tools for investigating brain function. In contrast to for instance electro-physiological measures which are characterised by very high temporal but low spatial resolution, fMRI can provide answers as to where in the brain certain processes take place, on the millimetre scale. This is achieved trough the detection of small signal variations that result from the haemodynamic changes accompanying brain activation. Images of the brain are acquired every few seconds or faster while the subject performs a controlled task; brain regions involved in that task can then be revealed by a temporal correlation analysis of the detected signal timecourse.

Objective of this thesis

The work presented in this doctoral thesis is concerned with the improvement, development and evaluation of fMRI acquisition methodology.

A technique known as gradient-echo echo-planar imaging (GE-EPI) has been the workhorse of functional MRI for almost fifteen years, largely thanks to its very high acquisition speed and inherent sensitivity to even subtle blood oxygenation level dependent (BOLD) signal changes that occur during brain activation. Despite its merits, the method has disadvantages that are particularly problematic at high main magnetic field; this includes geometric image distortions and signal loss in regions of poor main magnetic field homogeneity. There is considerable scope not only for improving the EPI method, but also the development of alternative techniques that are less prone to artefact formation.

In the first part of the thesis, a multi-echo GE-EPI scheme is developed by which multiple images of different BOLD contrast are acquired in rapid succession using the relatively new technique of parallel imaging. These images are subsequently optimally combined so as to simultaneously achieve artefact reduction and sensitivity enhancement as compared to existing EPI methods. This method is evaluated by application to a cognitive activation study at 3 T and 7 T.

The second part is concerned with the development of a spin echo fMRI technique that is based on the RARE sequence (rapid acquisition with relaxation enhancement). The motivation is twofold. First, the acquired images are free of inhomogeneity artefacts, and second, they are only sensitive to a subset of the BOLD contrast mechanisms which in principle results in a better spatial localisation of brain activation. The technique is subsequently applied in a study of the post-stimulus BOLD undershoot. This is a feature in the BOLD response that is usually observed after the offset of sensory stimulation, but the underlying haemodynamic mechanism remains poorly understood. Deeper insights into the origins of the BOLD undershoot are widely believed to yield valuable information on the metabolic processes related to brain activation on the whole.

The third part is focused on the development of fMRI techniques that are based on measuring activation related changes in cerebral blood volume (CBV). Again derived from the RARE sequence, a CBV method is implemented that yields artefact free images, and is moreover considerably more sensitive than previous methods based on EPI. This is revealed by an evaluation study with a visual activation experiment. The limited applicability for cognitive neuroscientists however remains as only a single brain slice can be imaged. In the second chapter on this topic this limitation is addressed by the development of a CBV method with whole brain coverage. The underlying GRASE (gradient and spin echo) sequence is a fast imaging method that combines elements of both RARE and EPI. Evaluation is performed by means of a visual and motor activation task.

Structure of this thesis

The first four chapters serve as introduction and provide an overview of concepts that are important in the context of later chapters. Chapters 5 – 10 are the scientific chapters in the form of already published work, or work in the process of being published. The last chapter provides a brief summary and discussion.

Chapter 2 The Physics of Nuclear Magnetic Resonance

Nuclear magnetic resonance (NMR) is the consequence of a physical property of atomic nuclei called ‘spin’ which causes an interaction with an externally applied magnetic field. The NMR phenomenon was first observed by Edward Purcell (Purcell et al. 1946), and independently by Felix Bloch (Bloch 1946). Only a few years later both were awarded the 1952 Nobel Prize for Physics in recognition of their work.

A complete description of NMR would require quantum mechanical treatment. However, many aspects of NMR can be explained by semi-classical mechanics, which are valid in the situation of large samples of weakly coupled spin-1/2 systems such as the water proton ^{1}H. This Chapter describes how an NMR signal is generated by the interaction of spin magnetic moments with an external static and oscillating radio-frequency magnetic field. The second part of the Chapter addresses signal (‘echo’) formation in NMR experiments where multiple RF pulses are applied. For fuller and quantum-mechanical descriptions of NMR see the standard text books (e.g. Callaghan 1994; Hoult and Chen 1989; Slichter 1996).

2.1 The magnetic resonance phenomenon

Spin and Magnetic Moment

Fundamental particles possess a quantum mechanical property referred to as ‘spin’, which depending on the type of particle can take a value of either 1/2, 1 or 2. The unpaired constituents of protons and neutrons, which together make up atomic nuclei, each belong to the family of fermions and carry a spin $\boldsymbol{I}$ with the spin quantum number of 1/2. Magnetic resonance can be observed in any single or multi-particle system with a non-zero net spin quantum number. Due to its large abundance in biological systems, the water proton ^{1}H with spin-1/2 is hence an ideal candidate for imaging applications. No NMR can in contrast be observed in systems with an even number of protons and neutrons and hence zero net spin, such as the ^{12}C or ^{16}O nuclei.

In a given energy state a non-zero spin system has a total magnetic dipole moment $\boldsymbol{\mu}$ and spin angular momentum $\boldsymbol{I}$. Consider the magnetic moment of a simple loop current j, which is given by

$$\boldsymbol{\mu} = j \cdot \boldsymbol{A}, \qquad [2.1]$$

where $\boldsymbol{A}$ is the surface vector of the area enclosed by the current. This basic system is analogous to a rotating electrically charged object, and it can be shown that its angular momentum $\boldsymbol{I}$ is related to the magnetic moment by

$$\boldsymbol{\mu} = \gamma \cdot \boldsymbol{I}. \qquad [2.2]$$

γ is the so called gyromagnetic ratio and for a spherical object with uniform distribution of charge q and mass m is equal to $q/2m$. However, due to the non-uniform charge distribution that results from the spatial arrangement and behaviour of subatomic particles (quarks), the gyromagnetic ratio of the proton is given by

$$\gamma = g_p \cdot e \,/\, (2 \cdot m_p), \qquad [2.3]$$

where the dimensionless proportionality constant $g_p = 5.59$ is the so called g-factor, and e and m_p are the charge and mass of the proton, respectively. Analogously, for nuclei consisting of multiple protons and neutrons, their characteristic charge distribution results in a gyromagnetic ratio that is characteristic of the type of nucleus.

Interaction of free spins with a **B** field

If an external magnetic field $\boldsymbol{B}_0$, by convention along the z-direction, is applied to the spin system, an interaction results which causes the z-component I_z of the spins' magnetic moment to be aligned either parallel, or anti-parallel with $\boldsymbol{B}_0$. Following from the quantisation of energy levels in quantum mechanics the magnitude of I_z is quantised in steps given by the reduced Planck's constant $\hbar = h / 2\pi$, where Planck's constant h has a value of $6.63 \cdot 10^{-34}$ J·s (hence $\hbar = 1.05 \cdot 10^{-34}$ J·s). The possible values for I_z are given by

$$I_z = m \cdot \hbar. \qquad [2.4]$$

m are the $2I + 1$ eigenvalues of I_z and can take the values

$$m = -I, I+1, \ldots, I-1, I. \qquad [2.5]$$

The z-component of the magnetic moment μ_z, and hence spin orientation, are therefore also quantised according to

$$\mu_z = \gamma \cdot I_z, \qquad [2.6]$$

and hence each eigenstate corresponds to a precession of the magnetic moment around the z-axis at fixed angle.

For $\boldsymbol{B}_0$ purely along z, the energy eigenvalues are given by application of the time invariant Schrödinger equation as

$$E_m = -\hbar \cdot \gamma \cdot B_0 \cdot m, \tag{2.7}$$

and hence the energy difference between the two energy levels of an $I = 1/2$ system is

$$\Delta E = E_{m=-½} - E_{m=+½} = \hbar \cdot \gamma \cdot B_0. \tag{2.8}$$

This is illustrated in Fig. 2.1. The eigenstate with the magnetic moment that has a z-component anti-parallel to $\boldsymbol{B}_0$ has the higher energy. The energy difference between the two possible states is

$$\Delta E = \hbar \cdot \gamma \cdot B_0 = \hbar \cdot \omega_0. \tag{2.9}$$

A change in state occupancy can be induced by application of a transverse magnetic field $\boldsymbol{B}_1$ of angular frequency ω_0. Through the gyromagnetic ratio this frequency is characteristic of the kind of nucleus and is referred to as the Larmor frequency $\omega_0 = \gamma \cdot B_0$.

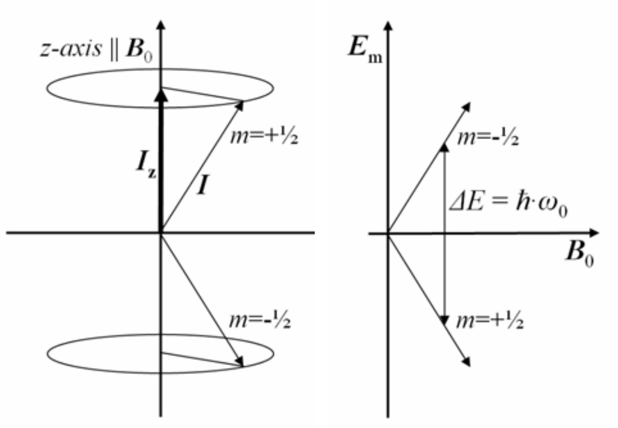

Figure 2.1: *Left: Precession of two spins with the z-component I_z of their angular momentum aligned parallel (m = +½) or anti-parallel (m = -½) with the B_0 field, which is along the z-axis. Right: The energy difference between the two states is $\Delta E = \hbar \cdot \omega_0$, where the eigenstate with a magnetic moment component anti-parallel to B_0 has the higher energy.*

nucleus	rel. abundance in human body	spin	Larmor frequ. [MHz/T]	Magnetic moment μ [μ_N]
^{1}H	1	1/2	42.58	2.793
^{23}Na	10^{-3}	3/2	11.27	2.216
^{31}P	$1.4 \cdot 10^{-3}$	1/2	17.25	1.131
^{13}C	$2.5 \cdot 10^{-4}$	1/2	10.71	0.702
^{19}F	$6.3 \cdot 10^{-5}$	1/2	40.08	2.627

Table 2.1: *Examples of atomic nuclei that are used in biomedical NMR. The table shows their natural abundance relative to ^{1}H, as well as their spin number, magnetic moment and Larmor frequency (Haacke et al. 1999; Hahn et al. 1992).*

Bulk Magnetisation

The above description was given for single particle systems. The NMR signal however is produced by a large sample consisting of many spins. If one considers the spins in the macroscopic sample to be uncoupled (or weakly coupled), then the state occupancy of the two energy levels follows the Boltzmann distribution. Taking the number of particles in the m = 1/2 and m = -1/2 states as N_+ and N_-, respectively, then the relative equilibrium distribution can be written as

$$N_- / N_+ = \exp(-\Delta E / k_B \cdot T) = \exp(-\hbar \cdot \omega_0 / k_B \cdot T) \qquad [2.10]$$

where $k_B = 1.3807 \cdot 10^{-23}$J/K is the Boltzmann constant and T the absolute temperature in Kelvin. In thermal equilibrium at non-zero temperature there is hence an occupancy difference between the two energy levels, and the states of high energy anti-parallel to $\boldsymbol{B}_0$ are less populated than the low energy states.

In typical biological tissue used for medical imaging at room temperature the ratio $(N_- - N_+) / (N_+ + N_-)$ is small, approximately 10^{-5} at 3 T, but the result is a small net magnetisation of the system along the direction of the externally applied field $\boldsymbol{B}_0$. This equilibrium magnetisation is called longitudinal magnetisation $\boldsymbol{M}_0$ and is the maximum magnetisation that is available for the formation of the NMR signal. It is given by the expression

$$\boldsymbol{M}_0 = \rho_0 \cdot \hbar^2 \cdot \gamma^2 \cdot \boldsymbol{B}_0 / (4 \cdot k_B \cdot T), \qquad [2.11]$$

where ρ_0 is the proton spin density.
The transverse component of the magnetisation in the equilibrium state is equal to zero since the orientation of individual spins within the transverse plane has no associated energy states and is hence equally probable.

When the transverse field $\boldsymbol{B}_1$ is applied, then individual spins in the system will undergo state transitions and the thermal equilibrium will be lost. This process of rotating (parts of) the magnetisation vector into the transverse plane is referred to as ‘spin excitation’.

Relaxation Mechanisms

The process of an arbitrary magnetisation $M \leq M_0$ returning back to its equilibrium magnetic moment M_0 is called spin relaxation. One can distinguish between two fundamentally different types of relaxation: First, ‘spin-lattice relaxation’ which describes the relaxation of the longitudinal ($\boldsymbol{M}_z$) component of the magnetisation, and second, ‘spin-spin relaxation’ which describes the evolution of the transverse component ($\boldsymbol{M}_T$).

Spin-Lattice Relaxation

Following from the conservation of energy and angular momentum, a change in longitudinal magnetisation $\boldsymbol{M}_z$ must be associated with an energy exchange of the spin system with its environment, the ‘lattice’ (hence the term spin-lattice relaxation). Phenomenologically, spin-lattice relaxation is described by the differential equation

$$dM_z / dt = (M_z - M_0) / T_1. \qquad [2.12]$$

Taking into account a possible initial longitudinal magnetisation $M_z(t=0)$ the solution to this is given by the exponential expression

$$M_z(t) = M_0(1 - \exp(-t/T_1)) + M_z(0)\cdot \exp(-t/T_1) \qquad [2.13]$$

The time constant T_1 is the so called longitudinal or spin-lattice relaxation time, sometimes also expressed as relaxation rate $R_1 = 1 / T_1$. For solid insulators the relaxation process can be very slow with a T_1 of the order of minutes, or even hours. In conductors, where free conduction electrons form a highly efficient energy sink, the relaxation process is typically much faster and T_1 can be as short as milliseconds. With increasing field strength the spin-lattice relaxation times also increase. This is related to the resonant protons available to transfer energy from the spin system to the lattice. Biological systems have T_1 values of the order of one second, depending in tissue type, and field strength. Some examples for important body tissues at 1.5 T and 3 T are given in Table 2.2.

Spin-spin relaxation

Spin-spin or transverse relaxation occurs due to a stochastic process called dephasing. If spin particles undergo Brownian motion there will be a rapidly and randomly varying interaction between them (hence the term spin-spin relaxation). The consequence of this interaction is a rapidly changing local magnetic field and therefore an effective broadening of the resonance frequency ω_0. Due to this spread of resonance frequencies the ‘phase coherence’ of the transverse magnetisation is lost over time, causing an attenuation of the net transverse magnetisation. Mathematically, the transverse relaxation process can be expressed as

$$dM_T / d_T = -M_T / T_2, \qquad [2.14]$$

which has an exponential solution given by

$$M_T(t) = M_T(0)\cdot\exp(-t/T_2) = M_T(0)\cdot\exp(-t\cdot R_2). \qquad [2.15]$$

Here, T_2 is called the spin-spin or transverse relaxation time (sometimes written as relaxation rate $R_2 = 1 / T_2$). $M_T(0)$ is the magnitude of the transverse magnetisation vector immediately after the application of the $\boldsymbol{B}_1$ field, i.e. spin excitation.

Spin-spin dephasing is mechanistically different from the exchange processes underlying T_1 decay, however since the transverse magnetisation vector will inevitably diminish to zero as the system reaches equilibrium, T_2 can never be longer than T_1 and therefore $T_2 \leq T_1$ always holds.

In addition to the purely stochastic process of T_2 relaxation, the signal will decay under the influence of small static field gradients that arise from imperfections of the magnet, and the local distribution of $\boldsymbol{B}_0$ within the sample. These static field offset effects are proportional to $\boldsymbol{B}_0$. The combined decay is generally assumed to be exponential in nature, and denoted by T_2*, or R_2*

$$R_2^* = 1 / T_2^* = 1 / T_2 + 1 / T_2', \qquad [2.16]$$

where $1 / T_2' = \gamma \cdot \Delta \boldsymbol{B}_0 / 2\pi$. From this follows that $T_2^* \leq T_2$. The time evolution of the transverse magnetisation including static dephasing is then given by

$$M_T(t) = M_T(0) \cdot \exp(-t/T_2^*) = M_T(0) \cdot \exp(-t \cdot R_2^*). \qquad [2.17]$$

The inhomogeneities giving rise to T_2* scale with $\boldsymbol{B}_0$ and are strongly influenced by differences in the magnetic susceptibility between different parts within the sample. *In vivo*, this could be differences in magnetic susceptibility of neighbouring tissue types. The greatest inhomogeneity effects are hence observed at tissue interfaces, but also, and in particular the air-tissue or air-bone interfaces. Some examples for important body tissues at 1.5 T and 3 T are given in Table 2.2.

Tissue	**T_1 [ms] at 1.5T**	**T_2 [ms] at 1.5T**	**T_1 [ms] at 3T**	**T_2 [ms] at 3T**
white matter	600	80	832	80
grey matter	950	100	1209	90
CSF	4500	2200	4300	1442
blood	1350	~120	1627	80

Table 2.2 *Different bodily tissues and their T_1 and T_2 relaxation times at 1.5 T and 3 T (Haacke et al. 1999; Lu et al. 2004; Lu et al. 2003; Wansapura et al. 1999).*

Interaction with an external *B* field

When a sample of spins with a net magnetisation $\boldsymbol{M}$ is placed in a $\boldsymbol{B}_0$ field, a torque $\boldsymbol{T}$ perpendicular to both $\boldsymbol{M}$ and $\boldsymbol{B}$ will act on the magnetisation and change the system's total angular momentum $\boldsymbol{I}$ according to Newton's second law

$$\boldsymbol{T} = d\boldsymbol{I} / dt = \boldsymbol{M} \times \boldsymbol{B}_0. \qquad [2.18]$$

Using $\boldsymbol{M} = \gamma \cdot \boldsymbol{I}$, and $\omega_0 = \gamma \cdot B_0$, the change in magnetic moment can be rewritten as

$$dM / dt = \boldsymbol{M} \times \gamma \cdot \boldsymbol{B}_0 = \boldsymbol{\omega_0} \times \boldsymbol{M}. \qquad [2.19]$$

Magnetic resonance can be observed when exposing the system to the $\boldsymbol{B}_1$ radiofrequency field. $\boldsymbol{B}_1$ is a magnetic field perpendicular to the main magnetic field $\boldsymbol{B}_0$ and oscillates at angular frequency ω_0, i.e. at a frequency equal to the Larmor frequency of the nucleus of interest. Including both the $\boldsymbol{B}_0$ and $\boldsymbol{B}_1$ fields in the previous equation yields

$$dM / dt = \boldsymbol{M} \times \gamma \cdot \boldsymbol{B} \text{ with } \boldsymbol{B}(t) = [B_1 \cos(\omega_0 \cdot t)\ B_1 \sin(\omega_0 \cdot t)\ B_0]^T. \qquad [2.20]$$

To simplify the formulation of the rather complicated magnetisation vector that results from the simultaneous precession around the two perpendicular fields in the stationary 'laboratory' frame of reference [x, y, z], a frame [$x', y', z' = z$] rotating about the z-axis at frequency ω_0 is generally used to describe the effects of the $\boldsymbol{B}_1$ field. In this rotating reference frame the precession about $\boldsymbol{B}_0$ is 'invisible' and $\boldsymbol{B}_1$

is parallel to the x'-axis, and hence only precession about the oscillating field $\boldsymbol{B}_1$ is observed.

The magnetisation $\boldsymbol{M'}$ in the rotating frame then follows

$$d\boldsymbol{M'}/dt = \boldsymbol{M'} \times \gamma\cdot\boldsymbol{B'} \text{ with } \boldsymbol{B'}(t) = [B_1\ 0\ 0]^T. \qquad [2.21]$$

The precession about a field $\boldsymbol{B}_1$ which is applied for duration Δt causes the magnetisation to be diverted from the z-axis by an angle α that is given by

$$\alpha(t,B_1) = \omega_1\cdot\Delta t = \gamma\cdot B_1\cdot\Delta t. \qquad [2.22]$$

This angle is called flip angle or tip angle, and can be arbitrarily chosen by adjusting amplitude and/or duration of the RF field.

Depending on the context in which such an RF pulse is applied, it may be an 'excitation pulse' which serves to tip the magnetisation by an arbitrary angle α from the z-axis into the transverse plane, or a 'refocusing' or 'inversion pulse' which as the names suggest rotates the magnetisation vector by 180°.

Bloch's equations

When including the effects of longitudinal and transverse relaxation in the description of the magnetisation vector $\boldsymbol{M}(t)$, three equations result for the x-, y- and z-components of $\boldsymbol{M}$. These equations are known as the Bloch equations (Bloch 1946).

$$dM_x/dt = (\boldsymbol{M} \times \gamma\cdot\boldsymbol{B})_x - M_x/T_2 = \gamma\,(M_y\cdot B_z - M_z\cdot B_y) - M_x/T_2$$

$$dM_y/dt = (\boldsymbol{M} \times \gamma\cdot\boldsymbol{B})_y - M_y/T_2 = \gamma\,(M_z\cdot B_x - M_x\cdot B_z) - M_y/T_2$$

$$dM_z/dt = (\boldsymbol{M} \times \gamma\cdot\boldsymbol{B})_z - (M_z - \mathrm{M}_0)/T_1 = \gamma\,(M_x\cdot B_y - M_y\cdot B_x) - (M_z - M_0)/T_1 \qquad [2.23]$$

Given that

$$M_T = M_x + iM_y = M_T \exp(-i\cdot\omega_0\cdot t), \qquad [2.24]$$

the differential equations for the transverse and longitudinal component of the magnetisation M_T and M_z including relaxation terms can then be expressed as

$$dM_T/dt = -\,i\cdot\omega_0\cdot M_T - M_T/T_2$$

$$dM_z/dt = -\,(M_z - M_0)/T_1. \qquad [2.25]$$

Detection of the NMR signal

The precession of the magnetisation vector is in principle analogous to a small dynamo and generates an *e.m.f.* oscillating at the Larmor frequency in one or more receiver coils that are placed above, or around the sample. The induced voltage is directly proportional to the magnitude of the transverse magnetisation, and typically of the order of microvolts. No signal results from the longitudinal component. Using the above expression for $M_T(t)$, the time dependent NMR signal $S(x,y,z, t)$ originating from position (x,y,z) in the sample can be written as

$$S(x,y,z, t) \sim M_T(x,y,z, t=0)\, dxdydz \cdot \exp(-t / T_2) \cdot \exp(-i \cdot \omega_0 \cdot t). \qquad [2.26]$$

In biological systems the received signal depends directly on the spin density, which varies spatially. While this is a basic prerequisite for MR imaging and for the formation of (clinically) useful tissue contrasts, the received signal $S(t)$ will always be a composite signal stemming from the entire portion of the sample that has a non-zero transverse magnetisation at time t :

$$S(t) \sim \exp(-t / T_2) \cdot \exp(-i \cdot \omega_0 \cdot t) \cdot \int_V M_T(x,y,z, t=0)\, dxdydz \qquad [2.27]$$

Here, $S(x,y,z, t)$ has been integrated over the entire sample volume V.

Safety considerations

B_1 fields and energy deposition (SAR)

When a sample, for instance the human body, is exposed to the RF field then part of the energy will be absorbed, with the consequence of heating up the sample. The effective energy deposition due to RF radiation is called specific absorption rate (SAR) and is measured in [W/kg]. It has been shown that the amount of power absorbed depends on the sample properties, and is quadratically dependent on both resonance frequency (therefore B_0) and B_1 field amplitude (Hoult and Chen 1989):

$$\text{SAR} \sim (\omega_0 \cdot B_1)^2. \qquad [2.28]$$

To avoid the risk of excessive RF heating during MRI measurements on living tissues it is therefore important to monitor power deposition and ensure that certain limits are adhered to. For measurements on humans, the current guidelines of the International Commission on Non-Ionizing Radiation Protection (ICNERP) make the recommendations for SAR exposure in the 'normal operating mode' as shown in Table 2.3 (Matthes and Internat Com Non-Ioniz Rad 2004). In any measurement, the spatially localised temperature limits should be 38° C for the head, 39° C for the trunk, and 40° C for the extremities, while the average body core temperature should not rise by more than 0.5° C (by 1° C in the 'controlled operating mode'). Stricter recommendations apply to pregnant patients and children. These limits are still relatively easy to meet for typical MRI protocols at 1.5 T; however practical restrictions already apply at 3 T for MR pulse sequences that employ a large number of RF pulses with large amplitude (flip angle). At higher field strengths, for instance at 7 T, the square dependence on ω_0 and B_1 increasingly results in practical limits that have to be addressed by careful RF pulse and sequence design.

Site	Dose	SAR [W/kg] averaged over 6 min
entire body	body average	2
partial body	partial body	2 – 10
head	head average	3
head, torso	per each 10g of tissue	10
arms, legs	per each 10g of tissue	20

Table 2.3: *ICNERP recommendations for SAR safety limits in the human body, for the 'normal operating mode' at room temperature. Partial body SAR scales with the ratio r = (exposed patient mass / total patient mass) according to SAR = (10 – 8·r) W/kg. Values for whole and partial body SAR are less restricted the 'controlled' and 'experimental operating mode'. Short term exposure averaged over any 10s should not exceed three times to the corresponding average value (Matthes and Internat Com Non-Ioniz Rad 2004).*

Static and time varying B fields

Potential risks may also be associated with the static $\boldsymbol{B}_0$ field. The upper limit for clinical routine whole body exposure to static magnetic fields recommended by ICNERP is 4 T, largely due to the limited information concerning possible effects above this static field strength. Due to static field gradients magnetic fields above 2 T can produced vertigo and nausea, hence careful medical supervision is recommended. Examinations at fields exceeding 4 T should only be done after careful risk–benefit analysis and obtaining informed consent from the subject; moreover, online physiological monitoring during the measurement should be done. The issue of static field safety is also and especially important for medical personnel that by necessity frequently move around in the static fringe field during subject or patient preparation.

In addition to the static $\boldsymbol{B}_0$ field, MRI uses rapidly switched field gradients for signal localisation. These time varying fields may cause peripheral nerve stimulation and muscle twitching if the *dB/dt* is above a certain threshold. Empirically, the median perception threshold was found to be $dB/dt = 20\cdot(1 + 0.36/\tau)$ T/s. The ICNERP recommendation is that the maximum exposure level for time varying magnetic fields be set equal to a *dB/dt* of 80% of the median perception threshold for normal operation, and 100% of the median for controlled operation.

2.2 Echo formation and coherence pathways

Most pulse sequences that are used for MRI consist of (many) more than just one RF pulse. During a train of RF pulses, the magnetisation will evolve in a complex manner. The following section describes the formation of the 'free induction decay', the 'spin echo' and the 'stimulated echo', and the concept of coherence pathways is introduced.

Single pulse experiment: The free induction decay

The most straightforward pulse sequence uses only a single RF pulse which tips the magnetisation away from its equilibrium orientation along the longitudinal direction. The NMR signal that results from a single RF pulse is called the free induction decay (FID).

If a $\boldsymbol{B}_1$ field is applied along the y'-axis in the rotating frame so as to tip the magnetisation by an angle α from the longitudinal axis, then the solution of the Bloch equation for the transverse magnetisation $\boldsymbol{M}_\mathrm{T}(t)$ yields

$$\boldsymbol{M}_\mathrm{T}(t) = \boldsymbol{M}_0 \cdot \sin(\alpha) \cdot \exp(\mathrm{i}\cdot\omega\cdot t - t\,/T_2{}^*). \qquad [2.29]$$

The transverse magnetisation $\boldsymbol{M}_0 \cdot \sin(\alpha)$ immediately after application of the RF pulse is maximal for a flip angle $\alpha = 90°$. Simultaneous recording of the x- and y-components of $\boldsymbol{M}_\mathrm{T}$ by quadrature detection yields the complex signal $S(t)$. The line shape of the decaying signal $S(\mathrm{t})$ reveals the frequency spectrum $S(\omega)$, i.e. the spread of resonance frequencies that are present in the decaying signal. The frequency spectrum is obtained by applying a Fourier transformation to $S(t)$:

$$S(\omega) = \int S(t) \cdot \exp(-i\cdot\omega\cdot t)\mathrm{d}t \qquad [2.30]$$

which gives the expression

$$S(\Delta\omega) = \boldsymbol{M}_0 \cdot \sin(\alpha) \cdot (1/T_2{}^* - i\cdot\Delta\omega) \,/\, ((1/T_2{}^*)^2 + (\Delta\omega)^2) \qquad [2.31]$$

for the complex frequency spectrum of $S(t)$. The frequency offset $\Delta\omega = \omega - \omega_0$ is here measured relative to the main resonance frequency ω. Clearly, in the absence of transverse relaxation and $\boldsymbol{B}_0$ inhomogeneity the spectrum would simply be a delta function at ω_0. In practice, however, the line shape of the absorptive (real) component follows a Lorentzian which has a FWHM given by

$$\Delta\nu = (\pi \cdot T_2{}^*)^{-1}. \qquad [2.32]$$

Two pulse experiment: The spin echo

If two RF pulses are applied in succession with a time τ between them, then three NMR signals will be seen. Each of the pulses is immediately followed by an FID as described above, but in addition a third signal will form at time 2τ from the first RF pulse (τ from the second). For the two RF pulses being applied in the x'- and y'-direction, respectively, the short hand notation for this type of sequence is $\alpha_{x'} - \tau - \beta_{y'} - \tau$. The signal at 2τ is called the spin echo (SE), or Hahn Spin Echo, named after the physicist Erwin L. Hahn who first described it in 1950 (Hahn 1950). Again, the maximum transverse magnetisation is achieved for $\alpha = 90°$, and a full rotation by β = 180° optimally keeps the magnetisation in the transverse plane for the formation of the spin echo.

The formation of the spin echo can be described by a simple vector model (see Fig. 2.2), if we assume that there is no T_2 decay due to spin-spin dephasing, but spin dephasing does take place due to static field inhomogeneity (T_2') effects. Consider two sets of spins, so called 'isochromats', that experience equal and opposite off-resonance effects. They hence resonate at the two frequencies ($\omega_0+\Delta\omega$) and ($\omega_0-\Delta\omega$) centred around the Larmor frequency ω_0. Immediately after the first pulse the isochromats will have the same phase, but during time τ this phase coherence is lost as the isochromats move away from the ω_0 vector, with the same speed but in opposite directions. If the second RF pulse is a perfect 180° refocusing pulse, the magnetisation vectors of the two isochromats are phase-conjugated and effectively rotated by 180°. Since they continue moving at the same speed, they will 'meet up' again after another period τ. The magnetisation is then said to be 'rephased' and forms an echo at time 2τ from the first pulse, which is hence also called echo time *TE*. The maximum echo signal is produced by application of a 90° followed by a 180° pulse. After the spin echo at *TE*, the isochromats continue dephasing again and the signal is eventually lost unless another RF pulse is applied.

It is evident from the above description that the most useful property of the spin echo is that all signal dephasing due to static $\boldsymbol{B}_0$ inhomogeneities is recovered at the point of echo formation (hence the term 'refocusing pulse'). The value of this will become more apparent in the discussion of pulse sequences and image artefacts in Chapter 3.

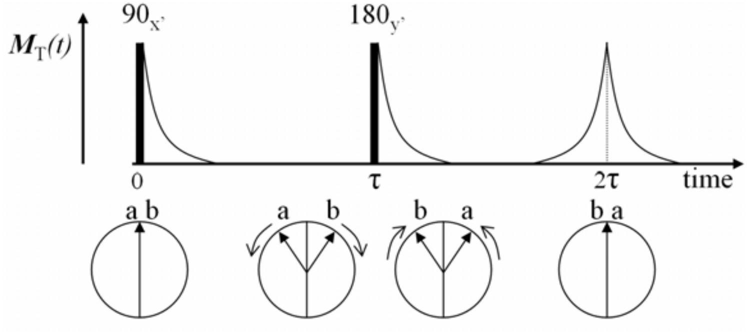

Figure 2.2: *The formation of the spin echo. 'a' and 'b' in the lower part of the figure represent to spin isochromats that experience equal and opposite static off-resonance effects. Immediately after the first 90° pulse, the two isochromats are still aligned, but due to their difference in resonance frequency they move in into opposite direction away from the on-resonance magnetisation during time τ. The 180° refocusing pulse reverses the phase while the spins keep precessing at the same constant frequency, so that a and b realign to form the echo at time 2τ, which is called the echo time TE.*

In practice there will always be T_2 decay between excitation and echo formation, so that the signal amplitude at echo time *TE* = 2τ from the first pulse is given by

$$S(TE) = S(0) \cdot \exp(-TE/T_2). \qquad [2.33]$$

If the sample is a liquid, an additional time dependent attenuation factor due to diffusive spin motion comes into play in presence of a field gradient. As the process of T_2 decay itself, diffusive motion is a stochastic process which is not reversible by the application of any type of RF pulse. However, if multiple RF pulses are applied in succession the effect of diffusion decreases with decreasing RF interval. The full description if the spin echo intensity at *TE* is then

$$S(TE) = S(0) \cdot \exp(-TE/T_2) \cdot \exp(-\kappa \cdot \tau^3), \qquad [2.34]$$

where κ is a constant containing several different terms describing the diffusive behaviour of the spins.

Three pulse experiment: The stimulated echo

Adding only one additional RF pulse to the previous spin echo experiment will drastically increase the number of generated signals: when three pulses are applied, then eight MR signals are generated. In addition to the FIDs that follow each pulse, there will be four spin echoes, and a special signal that forms after the third pulse that is referred to as a 'stimulated echo'. A timing diagram of the pulses and resulting signals is shown in Fig. 2.3. The short hand notation for this sequence is $\alpha_{x'} - \tau_1 - \beta_{y'} - (\tau_2\text{-}\tau_1) - \delta_{y'}$, where $\alpha_{x'}$, $\beta_{y'}$ and $\delta_{y'}$ are RF pulses of arbitrary flip angle.

Since the vector model that was used in the above description of the spin echo becomes increasingly more complicated for larger number of RF pulses, the extended phase graph (EPG) method was introduced by Hennig (Hennig 1988), based on earlier work of spin echo formation (Kaiser et al. 1974; Woessner 1961). The clear advantage of the EPG is that the echo pathways and their corresponding signal amplitudes can easily be depicted even for a very long train of RF pulses. The EPG takes into account the three possible effects that an RF pulse can have on the transverse magnetisation, the ratio of which depends on its flip angle:

(a) part of the magnetisation continues to dephase as thought it has not 'seen' the pulse

(b) part of the magnetisation experiences a phase conjugation about the axis along which the RF pulse was applied

(c) part of the magnetisation is flipped (back) along the longitudinal axis where it remains in the same state it was in before the application of the pulse.

Each RF pulse will thus split the magnetisation into three fractions, which are called coherence pathways. For an increasing number of RF pulses the number of possible echo path ways clearly increases very rapidly.

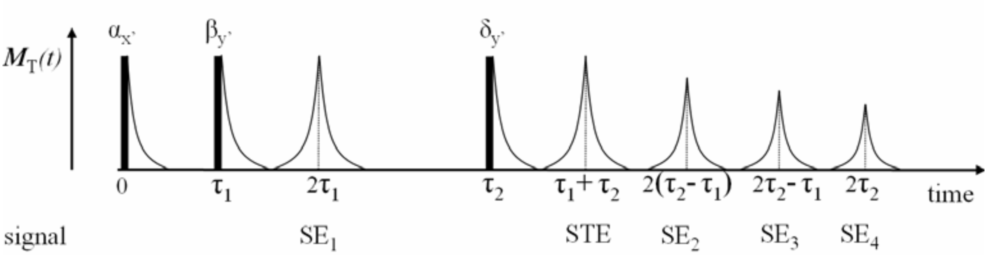

Figure 2.3: *MR signals that result from the application of three RF pulses. In addition to the three FIDs, there are four spin echoes, and a stimulated echo (STE) which forms after the third pulse.*

The EPG for the three pulse experiment of Fig. 2.3 is shown in Fig. 2.4. RF pulses are represented by the thick vertical lines. Time evolves along the horizontal axis, and the signal phase φ of a spin isochromat that experiences the same constant off-resonance effect throughout the experiment is plotted on the vertical axis. Relaxation and diffusion effects are neglected. The coherence pathways are represented by the lines that run between pulses. At each pulse, each already existing coherence pathway splits into a component that continues dephasing (a), is rephased (b) or is stored along the longitudinal axis (c, dotted horizontal lines); a new coherence pathway with zero initial phase is also created.

An echo forms each time magnetisation is effectively refocused, that is, a coherence pathway crosses the horizontal axis and $\varphi = 0$. The first spin echo (SE_1) is thus created at time $2\tau_1$ from the magnetisation that is refocused by the second RF pulse $\beta_{y'}$. The second spin echo (SE_2) results from the (re-)refocusing of SE_1 by the third RF pulse $\delta_{y'}$ and forms at time $2(\tau_2-\tau_1)$. The remaining two spin echoes SE_3 and SE_4 are 'simple' spin echoes again in that they directly originate from the pulse pairs $\beta_{y'} - \tau_2 - \delta_{y'}$ (echo forms at time $2\tau_2 - \tau_1$), and $\alpha_{x'} - \tau_1 - \tau_2 - \delta_{y'}$ (echo forms at time $2\tau_2$), respectively.

The stimulated echo (STE) is formed at time $\tau_2+\tau_1$, and results from magnetisation that was stored along the longitudinal axis between pulse $\beta_{y'}$ and $\delta_{y'}$, and was then flipped back into the transverse plane by the third pulse.

True multi-pulse experiments: The CPMG sequence

As the EPG for the three echo experiment illustrates, a very large number of coherence pathways is present after only a few RF pulses. In the typical imaging situation one aims at maximising the available signal, and so following a 90° excitation, a train of pure 180° refocusing pulses would ideally be used to repeatedly refocus the signal half-way between them. This is the Carr-Purcell (CP) sequence (Carr and Purcell 1954). However, perfect refocusing cannot be achieved in practice due to hardware imperfections and electrodynamic effects in the sample: First, there may be spatial coil-dependent variations in the transmit ($\boldsymbol{B}_1$)

field which result in parts of the sample experiencing an effective flip angle slightly smaller or greater than 180°. In addition, there are ‘field focussing effects’ caused by the interaction of the $\boldsymbol{B}_1$ field with the sample, an effect that increases with field strength where the RF wavelength is similar to the sample dimensions (in MR images this is often seen as ‘central brightening’).

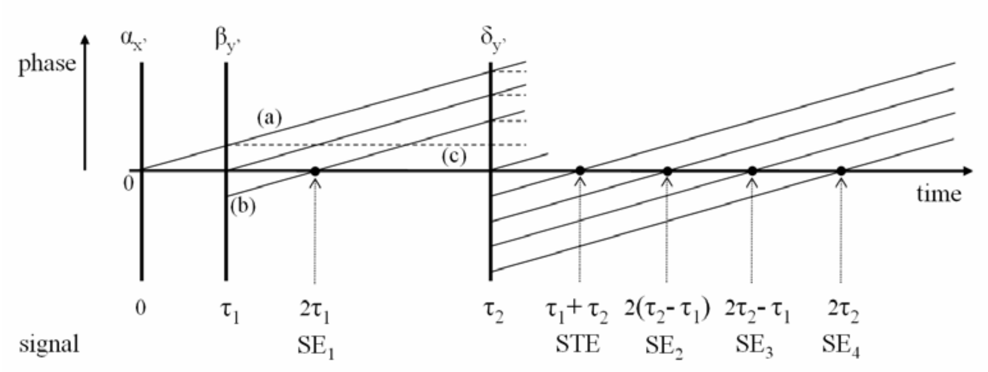

Figure 2.4: *Extended phase graph showing the possible coherence pathways that result from three RF pulses of arbitrary flip angle. The single coherence pathway generated by the first pulse is split up into three components by the second pulse: (a) a component that remains unaffected and continues dephasing, (b) a component that is rotated by 180°, and (c) a component that is flipped onto (and thus stored along) the longitudinal axis. Furthermore, an additional pathway is created by the second pulse. After the third RF pulse, this is repeated for each coherence pathway that exists at the moment the pulse is applied. The four spin echoes and the stimulated echo are indicated by the black dots where coherence pathways cross the horizontal ($\varphi = 0$) axis.*

An effective technique that intrinsically compensates these static $\boldsymbol{B}_1$ imperfections is the Carr-Purcell Meiboom-Gill (CPMG) sequence which does not rely on 180° pulses (Meiboom and Gill 1958). The CPMG condition imposes the requirement that the phase of all refocusing pulses be the same, and orthogonal to the phase of the excitation pulse. The short hand notation for this multi-pulse sequence is thus $\alpha_{x'} - TE/2 - \beta_{y'} - TE - \beta_{y'} - TE - \beta_{y'} - TE - \ldots$, where TE is the echo time as before, and also the duration of inter-RF and inter-echo intervals. The coherence pathways from spin and stimulated echoes will now superimpose coherently at integer multiples of TE. Only the first echo will be a pure spin echo. Note that again each RF pulse will also result in an FID and thereby create a new coherence pathway; however due to the constant RF interval these pathways are refocused a period $2TE$ later during the application of the second-next RF pulse, and hence they do not contribute a measurable signal. In MR imaging sequences however, the FID of the refocusing pulses is usually destroyed by surrounding the pulse with so called spoiler gradients.

References

Bloch F. (1946) NUCLEAR INDUCTION. *Physical Review* 70:460-474

Callaghan PT. (1994) *Principles of Nuclear Magnetic Resonance Microscopy*. London: Oxford University Press 1994

Carr HY, Purcell EM. (1954) EFFECTS OF DIFFUSION ON FREE PRECESSION IN NUCLEAR MAGNETIC RESONANCE EXPERIMENTS. *Physical Review* 94:630-638

Haacke EM, Brown RW, Thomson MR, Venkatesan R. (1999) *Magnetic Resonance Imaging. Physical Principles and Sequence Design*. New York: Wiley-Liss (John Wiley & Sons),

Hahn EL. (1950) SPIN ECHOES. *Physical Review* 80:580-594

Hahn EL, Bagguley DMS, Abragam A. (1992) *Pulsed Magnetic Resonance: NMR, ESR, and Optics : a Recognition of E.L. Hahn*. Oxford: Published by Oxford University Press

Hennig J. (1988) MULTIECHO IMAGING SEQUENCES WITH LOW REFOCUSING FLIP ANGLES. *Journal of Magnetic Resonance* 78:397-407

Hoult DI, Chen CN. (1989) *Biomedical Magnetic Resonance Technology*: Taylor & Francis

Kaiser R, Barthold.E, Ernst RR. (1974) DIFFUSION AND FIELD-GRADIENT EFFECTS IN NMR FOURIER SPECTROSCOPY. *Journal of Chemical Physics* 60:2966-2979

Lu H, Clingman C, Golay X, van Zijl PC. (2004) Determining the longitudinal relaxation time (T1) of blood at 3.0 Tesla. *Magn Reson Med* 52:679-682

Lu H, Golay X, Pekar JJ, van Zijl PCM. (2003) Functional magnetic resonance Imaging based on changes in vascular space occupancy. *Magn Reson Med* 50:263-274

Matthes R, Internat Com Non-Ioniz Rad P. (2004) Medical magnetic resonance (MR) procedures: Protection of patients. *Health Physics* 87:197-216

Meiboom S, Gill D. (1958) MODIFIED SPIN-ECHO METHOD FOR MEASURING NUCLEAR RELAXATION TIMES. *Review of Scientific Instruments* 29:688-691

Purcell EM, Torrey HC, Pound RV. (1946) RESONANCE ABSORPTION BY NUCLEAR MAGNETIC MOMENTS IN A SOLID. *Physical Review* 69:37-38

Slichter CP. (1996) *Principles of Magnetic Resonance*: Springer

Wansapura JP, Holland SK, Dunn RS, Ball WS, Jr. (1999) NMR relaxation times in the human brain at 3.0 tesla. *J Magn Reson Imaging* 9:531-538

Woessner DE. (1961) EFFECTS OF DIFFUSION IN NUCLEAR MAGNETIC RESONANCE SPIN-ECHO EXPERIMENTS. *Journal of Chemical Physics* 34:2057-&

Chapter 3 Magnetic Resonance Imaging (MRI)

The NNR phenomenon described in the previous Chapter forms the basis of Magnetic Resonance Imaging (MRI). The important addition is the ability to spatially localise the MR signal by a spatial encoding process which results in images that are useful for instance in clinical diagnostics or neuroscientific research. A multitude of possibilities exists to 'manipulate' the way relaxation occurs, so that a rich variety of useful image contrasts can be achieved. Not only due to this great flexibility, but also the fact that MRI works without harmful ionising radiation (in contrast to x-rays and computed tomography) it has long established itself as a routine application in the clinic, and for research on healthy volunteers.

It is the aim of this Chapter to describe how NMR can be used for image formation when combined with methods for signal localisation and image reconstruction. The two 'basic' MR pulse sequences, the gradient echo (GE) and spin echo (SE) sequence are introduced. Based on these, other sequence variants are discussed that aid the understanding of later Chapters, including echo planar imaging (EPI), rapid acquisition with relaxation enhancement (RARE), as well as the gradient and spin echo (GRASE) sequence. A number of common imaging artefacts are then discussed in the context of these sequences. Furthermore, the principles of simultaneous signal reception with multiple receive coils, and how this can be used to accelerate the spatial encoding process, are described. For further details on the topics treated in this chapter the reader is referred to the standard text books (Bernstein et al. 2004; Callaghan 1994; Haacke et al. 1999) and the recent MR literature.

3.1 The principles of spatial encoding in MRI

The Larmor frequency at which a spin system resonates is directly proportional to the external magnetic field B_0 acting upon it, and this basic fact is exploited in MRI: If by the introduction of field gradients B_0 can be made a function of space, then the spins will resonate at different frequencies depending on their spatial location. Therefore direct mapping from object to image can be achieved by recording and analysing frequencies contained in the MR signal. Furthermore, the relative intensity of a given frequency component is proportional to the number of spins at the corresponding location which contribute to the MR signal, and an image in form of a 'spin-density map' can be constructed. The following sections explain in more detail how multi-dimensional signal encoding is performed by means of ‘slice selection’, ‘frequency encoding’ and ‘phase encoding’. The effects of longitudinal relaxation will be neglected in this description.

Slice selection

The process of selectively exciting only the spins within a certain slice of the sample is referred to as slice selection. Historically, the z-axis is used as slice direction, but the following description equally applies to any arbitrary axis. Strictly speaking, slice selection does not serve to spatially ‘localise’ the origin of the MR signal that is coming from within the entire resonating sample. In contrast, it offers a way of making only a defined portion of the sample along one dimension contribute to the MR signal in the first place.

Slice selective spin excitation is achieved by applying a linear imaging gradient G_z, the ‘slice select gradient’, during the time the RF excitation pulse is played out. The gradient, typically with strength of the order of mT / m, causes the spins to precess at a Larmor frequency that depends on the position z along the direction of the gradient, and is given by

$$\omega(z) = \gamma\cdot(B_0 + z\cdot G_z) = \omega_0 + \gamma\cdot z\cdot G_z. \qquad [3.1]$$

At the same time, the RF pulse is chosen to have a particular bandwidth $\Delta\omega$ such that only spins in a well defined range of Larmor frequencies enter resonance, namely where the frequencies in the RF pulse meet the resonance condition. This range defines the slice thickness

$$\Delta z = \Delta\omega / (\gamma\cdot G_z). \qquad [3.2]$$

The pulse bandwidth $\Delta\omega$ is determined by the pulse duration and pulse shape. The centre frequency of the RF pulse determines the slice position along the direction in which the gradient is applied. Thus by using the appropriate combination of RF pulse bandwidth, and gradient orientation and strength, an imaging slice of arbitrary thickness at an arbitrary position and with an arbitrary orientation can easily be excited. This process is illustrated in Fig 3.1.

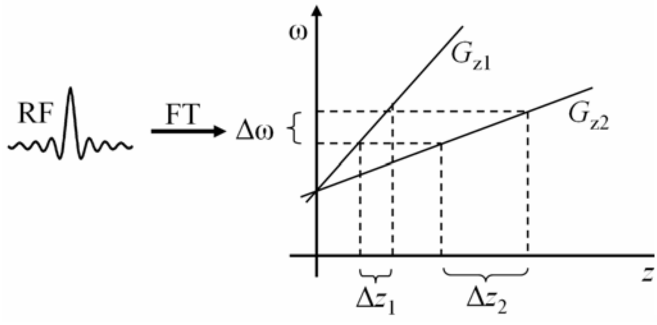

Figure 3.1: *Principle of slice selection. An RF pulse of a given bandwidth $\Delta\omega$ is applied in the presence of a gradient G_z. Only spins within $z + \Delta z$ meet the resonance condition and are excited. Application of a weaker gradient yields a thicker slice. The slice profile is defined by the Fourier transform of the RF pulse.*

Slice profile

For flip angles smaller than approximately 60° the slice profile is obtained by taking the Fourier transform (FT) of the pulse shape, and vice versa. The typical desired slice profile is that of a sharp rectangular (top hat, boxcar) function. That an absolutely rectangular profile however cannot be achieved in practice is best understood by considering that the RF pulse bandwidth would then have to contain *all* frequencies, i.e. the pulse would need to be of infinite duration and have the shape of a true *sinc* function. The practical limitations which require a compromise are threefold: First, there are technological and physiological limits to the maximum gradient amplitude that can be used. Second, the RF pulse amplitude and hence power deposition rapidly increase for a higher bandwidth to be achieved in a finite time and under a finite gradient. And third, while increasing the time during which gradient and RF pulse are played out obviously helps alleviate the former problems, there are additional time constraints in most pulse sequences, and limits to what is sensible or worth the additional time investment: Many applications do not require a 'perfect' slice profile. Gaussian pulse shapes (yielding a Gaussian slice profile) or truncated *sinc* pulse shapes (yielding a boxcar function with a degree of 'ringing' at the edges) are often an acceptable compromise. Optimised RF pulse shapes for better slice profiles at relatively acceptable RF power deposition can be calculated using advanced analytical and numerical methods (Hargreaves et al. 2004; Pauly et al. 1991; Shinnar et al. 1989; Silver et al. 1984a; Silver et al. 1984b).

If very thin and sharply defined slices are required, a 3D imaging scheme is often used as alternative. A thick slice, or slab, is then excited and subdivided into arbitrarily thin sections by means of phase encoding (see below), and the problems of imperfect slice profile are circumvented entirely (apart from edge effects at the borders of the thick slice).

Slice rephasing

The presence of the slice select gradient during the RF pulse causes spins within the slice to experience a different magnetic field. While this is the pre-requisite for slice selective excitation, this introduces a linear phase across the slice, so that the magnetisation is effectively dephased after the end of the RF pulse. In order to obtain a signal it is therefore necessary to undo the effect of the G_z gradient and to realign all spins in the slice to a phase of zero. This is achieved by applying the 'slice rephase' gradient, which for a symmetric RF pulse has a gradient moment equal to half the moment of the slice select gradient. It is worth pointing out that slice selective 180° refocusing and selective inversion pulses do not require a rephasing gradient: all phase accumulation during the first half of the RF pulse will automatically cancel out during the second, provided that both RF pulse and gradient are symmetric about the pulse centre.

Frequency encoding

The first dimension of Fourier spatial encoding is the ‘frequency encoding direction’, or ‘readout direction’, which by convention is described for the x-axis. Again, a linear field gradient G_x (the ‘frequency encoding gradient’) is applied, but while the signal is acquired. Hence the alternative name ‘readout gradient’. As in the case of slice selection, the presence of G_x introduces a position dependence of the frequency along the x-direction. The resulting signal will have a readout bandwidth which is defined as the difference of the lowest and highest frequency, and is proportional to the strength of the applied gradient G_x.

Ignoring relaxation, the signal $S(t_{RO})$ which is received at time t_{RO} during acquisition while G_x is switched on will thus be a composite signal over a spread of frequencies, whereby each frequency uniquely defines a certain position along the x-axis:

$$S(t_{RO}) = \int_x \rho(x) \cdot \exp(-i \cdot \gamma \cdot G_x \cdot t_{RO}) dx. \qquad [3.3]$$

Here, $\rho(x)$ is the proton spin density distribution along the frequency encoding direction.

If slice selective excitation was performed, then $S(t)$ is the signal coming from the spins within that slice, and signal localisation along two dimensions has now been achieved.

Phase encoding

Localisation along the remaining dimension is done by a process called phase encoding. As the name implies, the MR signal is localised by introducing a phase to the signal which depends on the position along the y-axis. This is achieved by playing a short gradient pulse G_y of length t_{PE} before the signal is acquired. This ‘phase encode gradient’ causes the magnetisation along y to only momentarily precess at different frequencies. During this time however, the spins accumulate a space dependent phase difference $\Delta\varphi(y)$, which they keep as a ‘tag’ once they have returned to their original frequency. This phase difference $\Delta\varphi(y)$ is given by

$$\Delta\varphi(y) = \gamma \cdot G_y \cdot t_{PE} \cdot y. \qquad [3.4]$$

Since there is now no frequency dependence along the y-axis, a single phase encode gradient is not sufficient to localise the origin of the signal. Therefore the process is repeated as many times as sample points along y are required, but each time a different gradient moment $G_y \cdot t_{PE}$ is played out before the signal is acquired in presence of a the readout gradient. For practical reasons, t_{PE} is usually kept constant while only the amplitude G_y is varied.

Mathematically, frequency and phase encoding are identical processes along two different dimensions. For $S(t_{RO},G_y)$ this results in a simple extension of the previous expression for the frequency encoded signal:

$$S(t_{RO}, G_y) = \int_y\int_x \rho(x,y) \cdot \exp(-i\cdot\gamma\cdot G_x\cdot t_{RO}+ G_y\cdot t_{PE})dxdy. \qquad [3.5]$$

where $\rho(x,y)$ is again the spin distribution in the sample.

Phase encoding along two dimensions (3D imaging)

To achieve spatial resolution in the z-direction one can replace the series of slice selective experiments by a scheme in which always the same thick 'slab' of tissue is excited. Analogous to the primary phase encoding, signal localisation in z is then performed by a secondary phase encoding loop with a step-wise incremented phase encoding gradient $G_{z,PE2}$ of duration t_{PE2} that is played out on the z-axis. The three-dimensional signal is then

$$S(t_{RO}, G_y, G_{z,PE2}) = \int_z\int_y\int_x \rho(x,y,z) \cdot \exp(-i\cdot\gamma\cdot(G_x\cdot t_{RO}+G_y\cdot t_{PE}+ G_{z,PE2}\cdot t_{PE2}))dxdydz. \qquad [3.6]$$

The advantages of this so called 3D imaging are at least threefold. First, no compromise has to be made on the slice profile. Only at the edge of the thick slab the intensity will be imperfect; however this can be overcome by either exciting a slab slightly thicker than required, or by performing a small number of additional phase encoding steps that are later discarded during the image reconstruction. Second, the slice thickness is not limited. In practice there is typically a minimum allowed slice thickness for selective excitation which for a given pulse duration and bandwidth is determined by the maximum available (or allowed) gradient strength. This restriction does not apply in 3D acquisitions as the amplitude of the select gradient for a thick slice is very low. Third, the SNR of the received signal is potentially a factor of $\sqrt{N_z}$ higher, where N_z is the number of phase encoding steps in the z-direction (equal to the number of slices into which the thick slab is subdivided). Unlike for slice selective excitation where the signal per definition only comes from the excited slice, the 3D MRI signal received at each phase encoding point originates from the entire thick slab, and therefore a factor N_z larger sample of excited spins. In practice however, the resulting theoretical factor of $\sqrt{N_z}$ SNR benefit is reduced due to the smaller available longitudinal magnetisation which results from the factor N_z shorter excitation interval.

k-space

Before the discussion of MRI pulse sequences, it is helpful to introduce *k*-space, which is a powerful concept that originates from solid state physics and is now commonly used in MRI (Ljunggren 1983; Twieg 1983). *k*-space allows the

description of the phase and frequency encoding processes in Fourier space, which considerably aids the (graphical) representation and understanding of MR imaging sequences even with very complex encoding schemes.
If the spatial encoding terms $\gamma \cdot G_x \cdot t_{RO}$ and $\gamma \cdot G_y \cdot t_{PE}$ are treated equivalent to wave numbers of a Fourier transformation such that they can be expressed as $\boldsymbol{k}(t)$ with

$$k_x(t) = (\gamma / 2\pi) \cdot G_x \cdot t_{RO}$$

$$k_y(t) = (\gamma / 2\pi) \cdot G_y \cdot t_{PE}, \qquad [3.7]$$

then at each point in time during the application of a linear gradient, the k-space vector (i.e. the position in k-space) is given by the time integral of the gradients

$$\boldsymbol{k}(t) = \int_t \boldsymbol{G}(t)dt. \qquad [3.8]$$

This makes k-space very convenient in that pulse sequence diagrams of the RF pulse and gradient switching can directly be translated into how k-space is traversed. For a sequence diagram drawn to scale this means that the area under the gradient timecourse accumulated at time t is directly proportional to the position in k-space at that point in time. This benefit will become clear in the discussion of pulse sequences.
Using this formalism and neglecting the relaxation term, the sampled (two-dimensional) signal can be rewritten as

$$S(k_x, k_y) = \int_y\int_x \rho(x,y) \cdot \exp(-i \cdot 2\pi\, (x \cdot k_x + y \cdot k_y))\, dxdy. \qquad [3.9]$$

Essentially, signal encoding is treated as the process of sampling the wave numbers k_x and k_y. In MRI, this has led to the term ‘sampling k-space’. The image is obtained by performing a Fourier transformation on the k-space data.

Discrete sampling of k-space, the Nyquist criterion and sampling PSF

The k-space formalism described above assumes the phase of the magnetisation to only depend on the variable $\boldsymbol{k}$(t). Until now, the sampling of the signal was treated as a process by which k-space is sampled continuously and to infinity. Clearly, both these conditions cannot be fulfilled in practice. The finite and discrete sampling of k-space has a number of implications for how MRI is performed.
The discrete sampling intervals Δt_{RO} in the readout direction depend on the analogue-to-digital converter (ADC) and are given by the effective sampling rate, or bandwidth. In the phase encoding direction the sampling is defined by the number of phase encoding steps and the increment ΔG_y between them. This leads to the following expressions for the increment Δk_x between points on the k_x-axis and Δk_y for the distance between points in k_y:

$$\Delta k_x = (\gamma / 2\pi)\, G_x \cdot \Delta t_{RO}$$

$$\Delta k_y = (\gamma / 2\pi) \cdot \Delta G_y \cdot t_{PE}, \tag{3.10}$$

The discrete sampling process is mathematically equivalent to a multiplication of the continuous MR signal with a comb of equidistant delta functions so that the digitally sampled signal can be expressed as

$$S(k_x, k_y)_{\text{sampled}} = S(k_x, k_y) \cdot \Delta k \cdot \Sigma_i\, \delta(k - i \cdot \Delta k) \tag{3.11}$$

In reconstructing the image, a Fourier transform is applied so the FT of the train of delta functions must be considered. This again is a comb of equidistant deltas, with a spacing of $n / \Delta k$:

$$\Delta k \cdot \Sigma_i\, \delta(k - i \cdot \Delta k) \;\leftrightarrow\; \Sigma_n\, \delta(x - n / \Delta k) \tag{3.12}$$

From this follows that the FT of $S(k_x, k_y)_{\text{sampled}}$ yields an image that is the object spin distribution $\rho(x, y)$, convolved with the FT of the sampling comb function:

$$\rho(x, y)_{\text{sampled}} = \rho(x, y) * \Sigma_n\, \delta(x - n / \Delta k) \tag{3.13}$$

This essentially means that each point in the sampled image ‘reappears’ with a periodicity of $1 / \Delta k$. For a desired ‘field of view’ (FoV) of dimensions FoV_x and FoV_y the important requirement is thus that the image does not fold onto itself within this region. This requirement defines the sampling increments:

$$\begin{aligned} \Delta k_x &= 1 / \text{FoV}_x \\ \Delta k_y &= 1 / \text{FoV}_y. \end{aligned} \tag{3.14}$$

From these expressions follows directly the sampling criterion for the non-overlapping signal if an image of matrix size N_x and N_y data points, and a spatial resolution of Δx and Δy is desired. After making the substitutions $\text{FoV}_x = N_x \cdot \Delta x$ and $\text{FoV}_y = N_y \cdot \Delta y$ and inserting into the discrete wave number equations this yields

$$\begin{aligned} \Delta t_{RO} &= 2\pi / (\gamma \cdot G_x \cdot N_x \cdot \Delta x) \\ \Delta G_y &= 2\pi / (\gamma \cdot t_y \cdot N_y \cdot \Delta y). \end{aligned} \tag{3.15}$$

This condition is the direct equivalent of the so called Nyquist theorem which states that for discrete sampling of a continuous signal the sampling rate has to be more than twice the maximum frequency that is to be resolved. Frequencies higher than half the sampling rate will aliase back into the spectrum at the point corresponding to half their frequency.

The practical implications are as follows: To prevent folding-in in the read direction, it is sufficient to simply apply a band-pass filter to the acquired signal, such that all frequencies that correspond to positions outside the required FoV are suppressed. For the phase encoding direction this is not an option since position is not encoded by frequency but phase, and hence it must be ensured that FoV_y is greater than the size of the object along that direction; portions of the object that protrude beyond FoV_y will ‘wrap around’ and appear in the image on the opposite side.

Finite k-space coverage

The sampling of *k*-space is not only discrete, but also only spans over a finite range of *k*-values. To account for this, the infinitely long train of equally spaced deltas considered in the above derivation thus needs to be multiplied with a rectangular box car function which takes a value of unity within the sampled range of *k*-space (between k_{min} and k_{max}), and zero elsewhere.

The by now familiar result of Fourier transforming the finite-range boxcar is again a *sinc* function:

$$\sin(\pi \cdot k_{\text{x,max}} \cdot x) / (\pi \cdot x) \;=\; \sin(\pi \cdot x / \Delta x) / (\pi \cdot x)$$

$$\sin(\pi \cdot k_{\text{y,max}} \cdot \text{y}) / (\pi \cdot y) \;=\; \sin(\pi \cdot y / \Delta y) / (\pi \cdot y). \qquad [3.16]$$

After FT to the image domain, the train of deltas is thus convolved with this *sinc* function, yielding a train of equally spaced *sincs*.

The complete description of discrete and finite *k*-space sampling is hence that each point of the sampling volume is imaged as its convolution with a *sinc* function. This is called the sampling PSF.

Again however this is an approximation of the ideal world, and is strictly speaking only valid if there is no appreciable T_2 decay during the signal acquisition. As mentioned previously this is often not the case in practice. The line shape of the signal decay during acquisition will change the point spread function and may distort the mapping from object to image by blurring and even displacement of image points. Spatial resolution is hence compromised if the PSF of T_2 blurring is broader than the sampling PSF. This is avoided if the sampling window T_{acq} is sufficiently short; the condition for this is given by

$$T_{\text{acq}} \leq \pi \cdot T_2 \qquad [3.17]$$

from the previously stated expression $\Delta \nu = (\pi \cdot T_2)^{-1}$ for the linewidth.

In pulse sequences where following a single excitation multiple k_{y} steps are acquired in a string of differently phase encoded readouts, the lower effective sampling rate is clearly along the PE direction. If for instance the entire k_{y} dimension is sampled in a linear fashion the condition becomes $N_{\text{y}} \cdot \Delta TE \leq \pi \cdot T_2$. Considerably more complex PSFs will result when the sampling scheme causes discontinuities in *k*-space, a situation which should generally be avoided. If B_0 inhomogeneities act on the decay, the above considerations equally apply to T_2*.

Two important properties of *k*-space

Conjugate symmetry is a property of *k*-space that results from the fact that complex data are sampled from a strictly real distribution of the magnetisation in the sample. Under conjugate symmetry, opposite points in *k*-space are related such that $S(-k_{\text{x}}, -\text{k}_{\text{y}}) = S(k_{\text{x}}, k_{\text{y}})^*$, where * denotes complex conjugation. There is hence a redundancy in the *k*-space information which can be exploited in MRI by so called ‘half Fourier’ or ‘partial Fourier’ acquisitions to reduce sampling time. Ideally, only one half of *k*-space needs to be acquired and the missing half synthesised for the formation of a full image. In practice however, phase errors due to signal decay and inhomogeneity make it necessary to acquire slightly more than half of *k*-space and to perform a phase correction on the basis of the fully sampled central portion.

Image contrast and resolution: In MRI one typically considers the SNR and image contrast to be determined by the centre of *k*-space. Information on finer structures in the object is encoded in the higher spatial frequencies, and hence outer regions of *k*-space. This is sometimes exploited in fast imaging methods that rely on data sharing strategies, for example key-hole imaging where only the central portion of *k*-space is sampled frequently and the outer regions are updated at much larger intervals.

3.2 MRI pulse sequences

A very large number of different pulse sequences have been developed. Essentially all of them are in some way variants of two basic sequences, the gradient (GE) and the spin echo (SE) sequence. These will be introduced in the following section. Three additional sequences that find application in later chapters are also described.

The gradient echo sequence

A pulse sequence to produce a ‘gradient-recalled echo’ was first proposed by the Aberdeen group in 1978 (Hutchison et al. 1978). Following excitation, the so called gradient-, or gradient-recalled echo is formed by first dephasing, and then rephasing the transverse magnetisation with the readout gradient.

This generates a time symmetrical echo which allows an image to be formed by taking the magnitude of the complex signal after Fourier transformation. The first sequence still Fourier-encoded the signal only along the read direction, but two years later a 2D-FT sequence with phase encoding was presented under the name ‘spin-warp imaging’ (Edelstein et al. 1980). Today, this is more commonly known as the gradient echo (GE) sequence, which is shown in Fig 3.2. This figure is also a good illustration of the intuitive and direct relationship between the pulse sequence diagram and *k*-space trajectory, shown on the right.

The read dephasing gradient is chosen so as to bring the *k*-space vector to $k_{x,\min}$, and is typically played out together with the slice rephase and phase encode gradients to save time. Then a continuous read gradient is applied while the ADC is opened. The echo will form at the time where the phase accumulated during the dephase gradient is effectively rewound by the readout gradient, that is the time integral of the two gradients is zero. In case of symmetric *k*-space sampling the read gradient is left on and sampling continued until the $k_{x,\max}$ position is reached. This is repeated as many times as there are phase encoding steps, and the required range $k_{y,\min}$ to $k_{y,\max}$ has been covered. Each time the *y*-component of the *k*-space vector is incremented by Δk_y, by appropriately incrementing the amplitude of the phase encode gradient.

The time that elapses between excitation and echo formation is called echo time *TE*, and the time interval between consecutive excitations is the repetition time *TR*.

A short *TR* leads to two considerations. First, the magnetisation will continue to dephase after signal acquisition in an ‘uncontrolled’ fashion, and signal from previously excited spins may leak into the following acquisitions. To avoid this, the phase encode gradient is either rewound after the ADC by applying a phase gradient with opposite moment, or a pseudo-random ‘spoiler’ gradient is applied after the readout, typically along *x*, to destroy the residual transverse magnetisation.

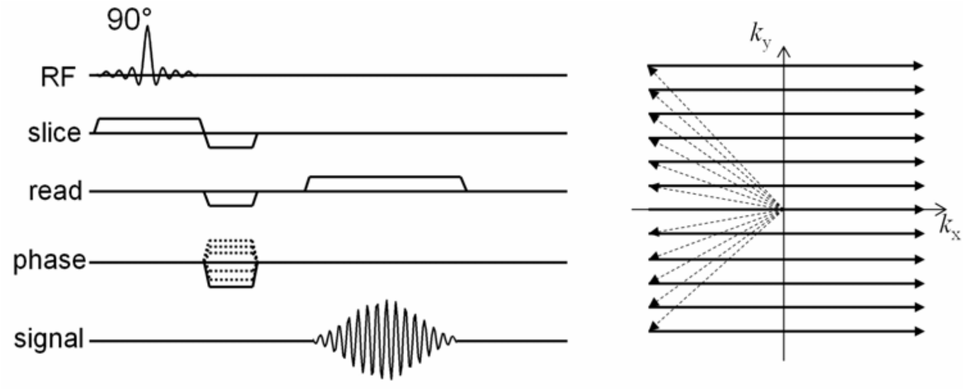

Figure 3.2: *Sequence diagram of the gradient echo sequence and corresponding k-space trajectory*

The second consideration for short TR sequences is that $TR \ll T_1$ and hence the longitudinal magnetisation will not fully recover (return to equilibrium) before the next excitation. Instead, after a number of TR intervals a steady state magnetisation M_z is reached that depends on T_1, TR and flip angle α:

$$M_z = M_0\,(1 - \exp(-TR\,/\,T_1)\,)\,/\,(1 - \cos(\alpha)\cdot\exp(-TR\,/\,T_1)\,)\,. \qquad [3.18]$$

Differentiation of this expression with respect α yields the angle for which the maximum possible steady state signal is obtained for a given TR and T_1. This optimal flip angle is known as the Ernst angle and follows

$$\alpha_{\mathrm{Ernst}} = \arccos\,(\exp(-TR\,/\,T_1)\,). \qquad [3.19]$$

The gradient echo sequence with $TR \ll T_1$, and hence a flip angle much smaller than 90° is the so called fast low angle shot (FLASH) sequence.

The echo planar imaging sequence

Echo planar imaging (EPI) is an extreme multi-echo variant of the GE sequence. It was first proposed thirty years ago by Mansfield (Mansfield 1977), who shared the Nobel Prize with Lauterbur in 2003. Even today EPI is one of the fastest imaging methods available and routinely finds application in functional MRI, particularly in the neurosciences: An entire 2D image can be obtained in less than about 50 ms, with very high sensitivity to the physiological changes upon brain activation. The EPI sequence works as follows: Longitudinal magnetisation (typically near equilibrium) is flipped into the transverse plane by an α pulse to produce an FID, followed by a train of rapidly oscillating read gradients each of which effectively recalls an echo. Phase encoding is achieved by incrementing the G_y gradient by small gradient ‘blips’ between the acquisitions of successive gradient echoes. The effective echo time TE is the time between excitation and acquisition of the central line of k-space ($k_y = 0$). The pulse sequence diagram of the EPI sequence is shown in Fig. 3.3. Between excitation and the start of the readout train, the read dephase gradient and phase encode gradient are switched so that the *k*-space vector points to ($k_{x,\mathrm{min}}$, $k_{y,\mathrm{min}}$), i.e. one ‘corner’ of *k*-space. The oscillating read gradient then describes a back-and-forth trajectory along k_x, while the phase encode blip between echoes increments k_y by Δk_y and thereby effects a jump to the next line in *k*-space. After acquisition, every other line must be time-reversed (flipped) to account for the alternating acquisition order. In this way the complete *k*-space is typically sampled per slice selective excitation, and then the following slice is acquired. To optimise timing efficiency, the signal is often acquired during the ramping up and ramping down of the read gradient (‘ramp sampling’). This causes non-equidistant sampling of *k*-space under ramps, and re-gridding onto the Cartesian *k*-space grid has to be performed before image reconstruction.

The demands of this type of sequence on the hardware are extremely high. The system must support the fast switching and high slew rates, and cope with the resulting eddy currents and the heat they produce in various parts of the system. Especially eddy current effects that feed back into the gradients must be well compensated by adjusting the gradient pre-emphasis, to prevent gradient delays that would result in a zigzag pattern in *k*-space after time-reversing alternate lines. However even EPI data acquired on a well tuned system require phase correction during reconstruction.

The readout train samples the T_2* decay of the FID which is essentially mapped into the phase encoding direction of *k*-space: It is clear from the sequence timing diagram that the effective sampling rate in the read direction is very much higher than along the phase encode dimension. Hence any (unwanted) phase accumulation due to contributions from static field inhomogeneity will dominate in the PE direction. Moreover, the condition $T_{\mathrm{acq}} \leq \pi \cdot T_2^*$ is not generally fulfilled. The consequence is that the $\mathrm{PSF}_{\mathrm{PE}}$ can have a width and/or shift of up to a few pixels, resulting in blurring and geometric distortions. This issue is addressed again in the section on image artefacts.

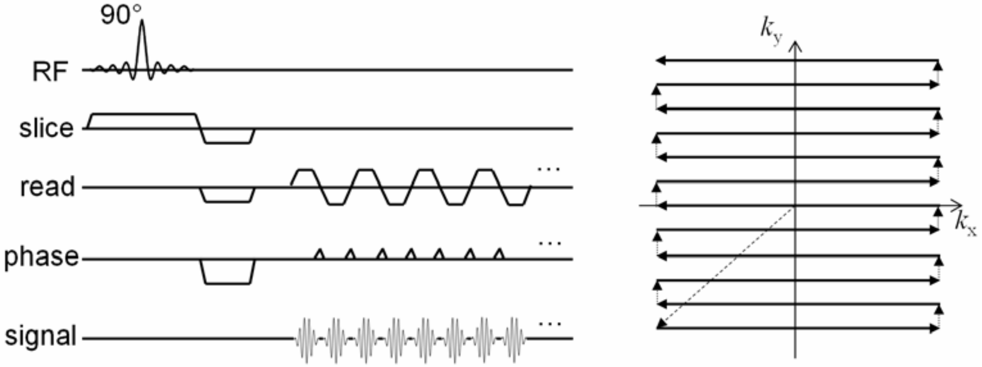

Figure 3.3: *EPI sequence diagram and corresponding k-space trajectory.*

The spin echo sequence

The spin echo (SE) sequence essentially consists of the same elements as the GE sequence, however with the important difference that the echo is sampled at the point where the magnetisation is refocused by a 180° pulse. The formation of the spin echo was illustrated in Fig. 2.2. Figure 3.4 shows the spin echo sequence. For each pair of excitation and refocusing pulses, one k_y-line is acquired under the readout gradient. As in the case of the GE sequence, this read gradient is first prephased by a gradient with half the gradient moment. Again, this gradient is typically applied together with the slice rephase and phase encode gradient immediately after excitation for optimal time efficiency of the sequence. If it is placed before the refocusing pulse, the read-dephase gradient must be applied with opposite polarity since the subsequent 180° pulse will conjugate the phase of the magnetisation.

In the sequence shown here, the 180° pulse is played without accompanying slice select gradient, but it is equally possible, and more common, to use slice selective refocusing. Furthermore, so called spoiler gradients are usually placed around the refocusing pulse in order to destroy any FID signal that might be produced by the RF pulse and could interfere with the spin echo signals.

It is worth mentioning that the single readout gradient can in principle be replaced by an EPI readout module so as to acquire a large number of gradient recalled echoes around the spin echo. The resulting sequence is known as spin echo echo planar imaging (SE-EPI) and for instance commonly applied in diffusion imaging.

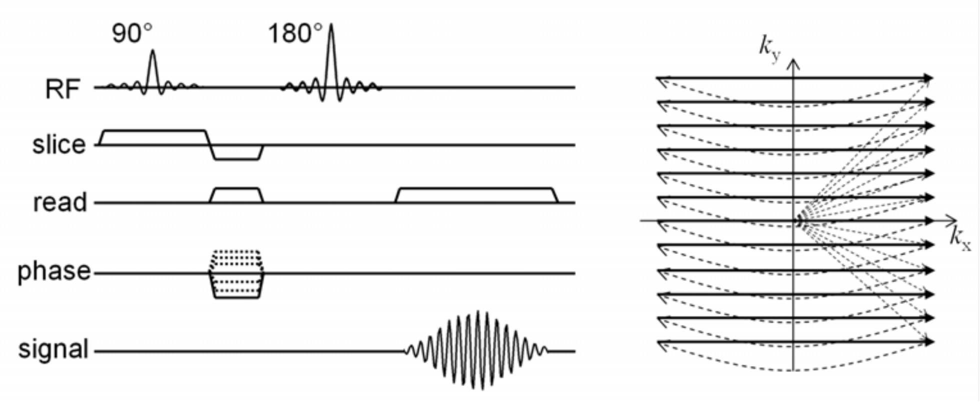

Figure 3.4: *Schematic pulse diagram of a spin echo sequence and the corresponding k-space trajectory. The sequence is repeated for each phase encoding step. The different strengths of the phase encoding gradient for each phase encoding step are indicated by the dashed lines.*

The rapid acquisition with relaxation enhancement (RARE) sequence

First proposed by Hennig and colleagues (Hennig et al. 1986), the RARE sequence is today more commonly known as turbo spin echo (TSE), or fast spin echo (FSE) sequence. The sequence is shown in Fig. 3.5. As already described in the context of multi-pulse experiments, a train of spin echoes can be formed by repeatedly refocusing a spin echo by a string of 180° pulses. In this sense, RARE is similar to EPI, where the echo is repeatedly formed by gradients instead of RF pulses. With a sufficiently long RF pulse train, RARE can also be used to capture the entire *k*-space following only a single excitation, although a segmentation over a number of excitations is typically used in practice. In contrast to EPI however, there is in principle complete freedom to choose the order in which k_y lines are acquired, or to omit portions of *k*-space, so as to influence the time after excitation at which the central (non-phase encoded) line of *k*-space is acquired. This time is referred to as the effective echo time TE_{eff} and is largely responsible the resulting contrast between tissue types in the image. Phase encoding is performed separately for each RF interval: the phase gradient is switched before the readout of a given echo as in the SE sequence, but the phase is then rewound again by a gradient of equal and opposite moment before the next RF pulse; this is to ensure that the coherences remain unaltered between RF intervals.

As for SE techniques in general, the obvious advantage of the RARE sequence is that it is insensitive to static B_0 inhomogeneity effects since these are perfectly refocused by the 180° pulses. From this results a further advantage compared to e.g. the GE-EPI sequence, namely that the signal attenuation is ruled by T_2 rather than T_2* decay. Since $T_2 > T_2$*, longer readout trains can be used without compromising the PSF. A clear disadvantage of the RARE sequences is the power deposition. Due to the large number of refocusing pulses SAR is considerable and depending on RF train length may impose a lower limit on the possible repetition time *TR*, and especially so at high B_0. A vital requirement for RARE imaging is furthermore the fulfilment of the CPMG condition between the 90° and 180°, and all later pulses; if violated, different coherences interfere uncontrollably during echo formation. *In vivo*, the CPMG condition may be violated for instance by gross subject movement but also by local pulsatile tissue motion during the acquisition. This results in image artefacts, predominantly in form of a smearing artefact along the phase encoding direction.

RARE type sequences have long been the workhorse of clinical MRI. Often preceded by some kind of magnetisation preparation experiment, they are the most commonly used sequence for the diagnosis of a wide variety of pathologies.

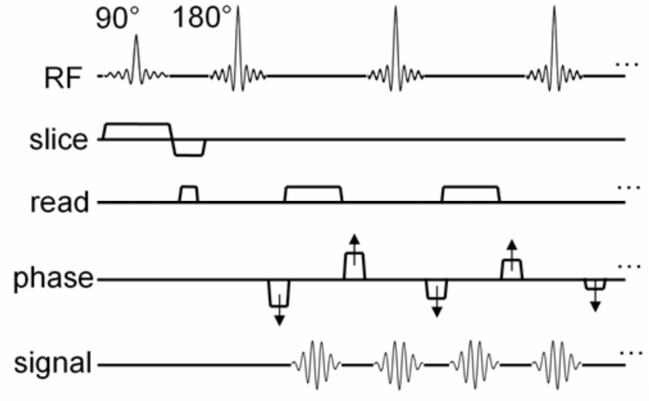

Figure 3.5: *Sequence diagram of the RARE sequence. One line of k-space is acquired per RF interval. The acquisition order can be chosen arbitrarily by application the corresponding pre-phase / rephase gradients before / after each readout.*

The gradient and spin echo (GRASE) sequence

As suggested by its name, the GRASE sequence combines elements of both spin- and gradient echo sequences (Feinberg and Oshio 1991; Oshio and Feinberg 1991). Following excitation, an RF pulse train forms a string of spin echoes as in the RARE sequence. In addition, an oscillating read gradient as in the EPI sequence is used to produce a train of gradient echoes around them. Like EPI and RARE, the GRASE sequence is often applied as single-shot method. An example of the GRASE sequence with acquisition of three echoes per spin echo is shown in Fig. 3.6.

There are many possible ways in which the phase encoding can be performed, and this is critically important for the resulting PSF. One typical scheme would be to acquire the gradient echoes in a given RF interval such that are separated by large blip increments $n\cdot\Delta k_y$. From pulse to pulse, these *k*-space 'segments' are shifted by Δk_y with respect to one another other, so that the complete *k*-space is covered by *n* RF intervals (Johnson et al. 1996a; Oshio and Feinberg 1991). Also the number of gradient echoes per spin echo is flexible, but usually between three and nine are used in a 'true' GRASE sequence. Hence the ratio between spin and gradient echoes can be varied, and fewer RF pulses are be required if more gradient echoes are sampled in each RF interval. In this respect, the above mentioned SE-EPI sequence may be viewed as the most extreme case of GRASE where all of *k*-space is acquired around one spin-echo. The opposite extreme is the RARE sequence itself, with only one line per RF pulse.

The signal decay in GRASE is determined by a mixture of T_2 and T_2* effects: The overall decay along the RF train is ruled by T_2, and so is the signal seen in the pure spin echoes at the centre of each RF interval. The decay along the gradient echoes that flank the spin echoes is ruled by T_2*. As a result of this, phase errors due to off-resonance build up linearly along the gradient echo train with increasing distance from the spin echo. It is therefore clear that the resulting *k*-space is inevitably both amplitude and phase modulated along the phase encoding direction. The optimal phase encoding order is hence the one that gives the most 'benign'

PSF, and numerous studies have focused on this topic (Feinberg et al. 1995; Johnson et al. 1996a; Johnson et al. 1996b; Jovicich and Norris 1998; Mugler 1999). A compromise between desired image contrast and artefact level often needs to be made.

GRASE combines the advantages and disadvantage of EPI and RARE. From the perspective of RARE, GRASE has the advantage that more echoes are sampled per RF pulse, resulting in a shorter total readout duration and lower energy deposition due to the smaller number or required RF pulses. A disadvantage compared to RARE is the phase modulation introduced by the EPI-like readout and the amplitude modulation due to the mix of T_2 and T_2* decay. From the perspective of EPI, GRASE has the advantage of spin echo sequences that the sensitivity to inhomogeneity effects is reduced, and the overall T_2 dominated decay allows longer acquisition trains.

The described GRASE scheme can be modified by introducing a secondary phase encode direction such that a three dimensional *k*-space is sampled. This provides an additional degree of freedom for how the phase and amplitude modulated signals are distributed in *k*-space (Mugler 1999). An extreme variant of 3D GRASE is one by which an entire k_x-k_y plane is acquired at a given k_z during one RF interval; during the following RF interval another k_x-k_y plane is acquired with the next k_z-phase encoding step and so on (Song et al. 1994). This scheme thus yields a 3D *k*-space in which the T_2* decay and phase modulation are completely along the primary phase encode direction, and the T_2 decay (at constant phase) is completely along the secondary phase encode direction. This variant of GRASE is used for the work presented in Chapter 10.

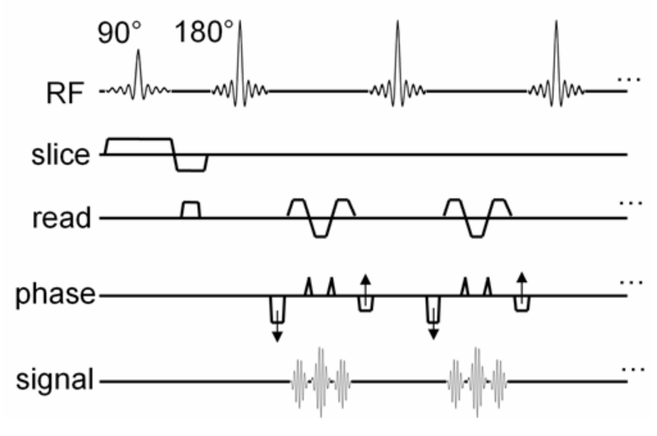

Figure 3.6: *Sequence diagram of the GRASE sequence. Slice selective excitation is followed by a string of RF pulses, between each of which a number of gradient echoes are acquired (in this case three).*

3.3 MRI artefacts

The following section describes a few selected artefacts that are sometimes encountered in the sequences discussed above. The description is by no means complete and a large number of other artefacts exist.

Chemical shift artefact

The effective magnetic field experienced by a nucleus depends on its chemical environment through a mechanism known as electronic shielding, and there is hence a corresponding dependence of its Larmor frequency (Proctor and Yu 1950). The amount of shielding is characterised by the electronic shielding factor σ, so that the field at the nucleus is given by

$$\boldsymbol{B}_{\mathrm{eff}} = \boldsymbol{B}_0 \cdot (1 - \sigma) \qquad [3.20]$$

The relative difference to the main Larmor frequency ω_0 is denoted by δ and expressed in parts per million (ppm). While the chemical shift effect is very useful in that it enables chemical analysis by means of NMR spectroscopy, it is generally considered a nuisance in MRI. The most important source of chemical shift artefact in human MRI is fat which has $\delta = 3.5$ppm. The protons in a fatty environment precess at a different frequency than water protons (440 Hz at 3 T), causing the fat signal in the image to be displaced. The amount and direction of displacement depend on the effective acquisition bandwidth in readout and phase encoding directions. The shift is largest in EPI and other single-shot sequences which have a low bandwidth in the phase encoding direction. In typical EPI at 3 T, 2.5 kHz bandwidth over 64 pixels would cause the fat signal to be displaced by about six pixels along the phase encode direction and give rise to the well-known fat rim artefact from the fat layer around the skull.

The fat signal can be suppressed by applying a narrow-band saturation pulse before the imaging sequence. This way the magnetisation from the fat protons can be selectively saturated, and only the (water) spins of interest experience the subsequent excitation and contribute to the signal. An alternative approach is to selectively excite only the water spins by what is effectively a narrow-band pulse; this however requires a low degree of B_0 variation.

Inhomogeneity artefacts

B_0 inhomogeneity on the microscopic level plays an important role in imaging with T_2* contrast, and through this also in the ability to detect the small signal changes during brain activation (see following Chapter).

On the macroscopic scale, on the other hand, main field inhomogeneity is a major cause of image artefacts. Considering that the imaging experiment relies on deliberately applied field gradients for spatial localisation, any additional unwanted and usually unknown field variations inevitably lead to mis-localisation of the signal and/or broadening of the PSF. The reconstructed image will hence be geometrically distorted in the presence of off-resonances that are sufficiently strong in relation to the imaging gradients. The inhomogeneity gradients are proportional to field strength, and hence the severity of distortion scales with B_0. As with chemical shift, the effect is proportional to, and largest in the direction of the lowest effective sampling bandwidth. In conventional GE and SE sequences there is no artefact in the PE direction as all k-space lines are acquired at the same TE and therefore have the same phase; the same is true for the RARE sequence. In the readout direction there will be some distortion that depends on the sampling window, but typically much less than one pixel. The strongest distortions are observed in sequences with an EPI like readout where the magnetisation is allowed to accumulate phase errors over long periods. Examples for distortions in echo planar images are shown in Fig. 3.7.

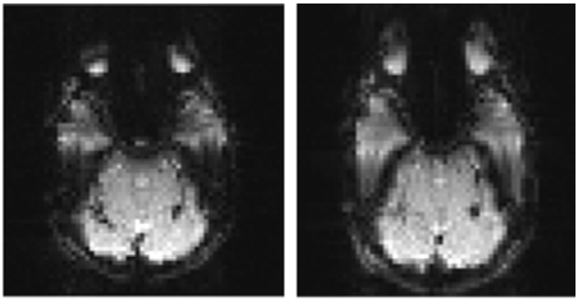

Figure 3.7: *Distortions in echo planar images at 1.5 T acquired with a readout BW of 2000 Hz per pixel (left), and 1000 Hz per pixel (right). This approximately translates into a phase encoding bandwidth of 30 and 15 Hz per pixel, respectively. The difference in distortion and signal displacement is clearly visible. As B_0 effects scale linearly with field strength, the artefacts on the right are similar to what would have been observed at 3 T with otherwise unchanged acquisition parameters.*

There are only two practicable ways in which distortion can be reduced during acquisition. First, field variations must be minimised which in the presence of the object is achieved by fine tuning the magnetic field with so called high order shim fields. Second, acquisition schemes must be optimised so as to avoid long gradient echo trains where possible; here, the recently developed methods for parallel imaging are of great help (see following Section). Methods of passive shimming (e.g. paramagnetic mouth and ear inserts) have also been suggested (Constable and Spencer 1999; Cusack et al. 2005; Wilson et al. 2002). Furthermore, three classes of retrospective distortion correction schemes have been proposed (Chang and Fitzpatrick 1992; Jezzard and Balaban 1995; Zeng and Constable 2002) which in some way rely on B_0, phase or PSF mapping and the subsequent generation of pixel-shift maps which are used for image correction. While these approaches greatly improve the perceived image quality, their benefit in case of long image time series as required for fMRI has not been fully established (Hutton et al. 2002).

A second type of inhomogeneity artefact that occurs only in gradient echo sequences is through-plane dephasing. If there are unwanted field gradients perpendicular to the imaging slice, the signal will dephase through the slice, causing signal voids. Unlike for distortion which depends on the length of the sampling window, the effect of the perpendicular gradient increases with echo time: In a long *TE* acquisition the unwanted gradient has more time to dephase the spins. This effect is illustrated in Fig. 3.8 which shows GE-EPI images of the corresponding brain slices acquired at five different echo times.

The problem of signal loss can be addressed in various ways. First, by choosing a shorter *TE*. Second, choosing thinner slices; if a thinner slice is excited, then in the presence of a given through-plane gradient the spread of off-resonance frequencies in absolute terms will be less and the undesired signal modulation reduced. Third, the insertion of passive shim plates as mentioned above. Fourth, multiple acquisitions with different amounts of ‘z-shimming’, a method that uses gradients on the slice axis in an attempt to compensate the inhomogeneity-induced gradients (Constable and Spencer 1999).

Spin echo sequences, including SE-EPI do not suffer from signal voids. Here the undesired phase accumulation through the slice is perfectly refocused by the 180° pulse.

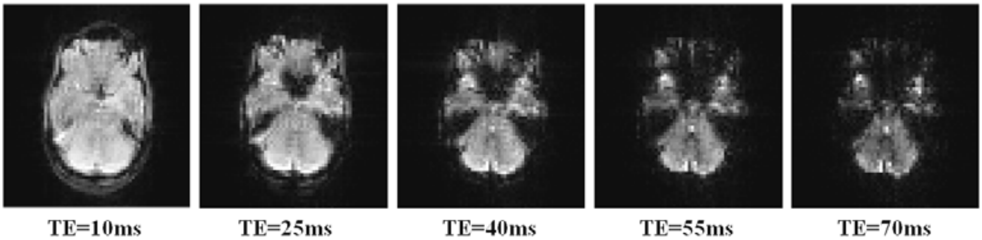

Figure 3.8: *GE-EPI acquisition at five different echo times, illustrating the effect of through-plane dephasing. The signal loss is most pronounced in regions of strong susceptibility gradients, in this case the auditory canal and near the mouth and sinuses. Spin echo sequences in contrast are insensitive to through-plane dephasing as phase errors are refocused by the 180° pulse.*

Nyquist ghosting

The ghosting artefact is typical for EPI sequences where a readout gradient of alternating polarity is used. The fast switching, high slew rates and large gradient amplitude induce eddy currents in the system that may feed back into the gradients. Despite great efforts in gradient design and fine-tuning of the so called gradient pre-emphasis to avoid gradient delays, a certain degree of imperfection remains. This is not a problem in most pulse sequences for two reasons. First, maximum possible switching and slew rates are not typically used, and second, *k*-space lines are usually acquired under readouts of the same polarity, so any error would be constant for all lines and hence not noticeable in the final image. In EPI however, alternate lines need to be time-reversed to compensate their opposite acquisition order under the oscillating gradient, and so any residual time delay will result in a zigzag phase pattern in *k*-space (Schmitt et al. 1998). This gives a small phase error of periodicity $2 \cdot \Delta k_y$ and the Nyquist condition is not fully satisfied. Upon Fourier transformation, this causes part of the signal to be shifted by half the FoV. The phase error can largely be eliminated by performing a first order phase correction, usually based on two non-phase encoded scans obtained under opposite gradient polarity just before the actual EPI readout. An example of a standard EPI acquisition with and without phase correction is shown in Fig. 3.9. Under most circumstances, a ghost signal exceeding 5% of the main signal is not acceptable.

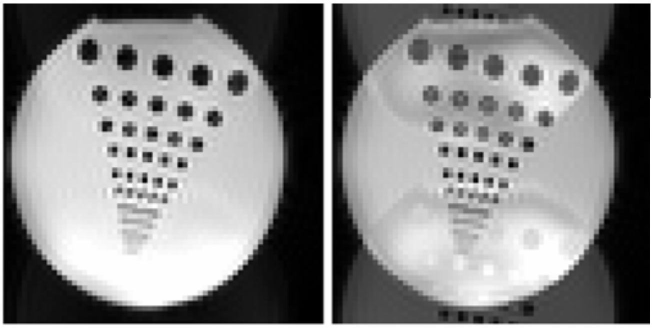

Figure 3.9: *EPI image reconstructed with (left) and without (right) phase correction for removing the ghosting artefact (3 T, matrix 64x64, FoV 250x250 mm^2, BW 2000 Hz / pixel).*

Gibbs Ringing

Ringing artefacts appear in MR images as a striping pattern that is sometimes seen parallel to sharp intensity discontinuities in the object. Adequate sampling of sharp edges in the object would require the sampling of high spatial frequencies. However due to the finite range of *k*-space which acts as a low-pass filter, the higher spatial frequencies are effectively cut out, which upon Fourier transformation to the image domain results in a series of over- and undershoots (hence ‘ringing’) near the discontinuity. This is the Gibbs phenomenon which in signal processing is also known as truncation or apodisation artefact. To avoid ringing in the images, *k*-space is almost always multiplied by a Hanning window or similar filter, which gives a smooth transition to zero at the border of *k*-space.

Artefacts due to concomitant gradient fields

Following from Maxwell’s equations, a magnetic field gradient purely along one direction cannot be produced, and hence the application of a linear gradient along one Cartesian axis will unavoidably result in the presence of concomitant gradients along the orthogonal axes (Norris and Hutchison 1990). For a typical cylindrical gradient coil, the concomitant field B_c at position (x, y, z) in the physical laboratory frame during application of the gradients G_x, G_y and G_z is given by

$$B_c = [\,(G_x \cdot z - G_z \cdot x / 2)^2 + (G_y \cdot z - G_z \cdot y / 2)^2\,] / 2B_0 \;\geq\; 0 \qquad [3.21]$$

Since $B_0 > 0$, B_c is a non-negative quantity that is independent of the polarity of the imaging gradients. Hence gradient G_x on the x-axis (or G_y on the y-axis) produces an unwanted concomitant gradient along the z-axis that is given by

$$B_c(z) \approx z^2 \cdot G_x^{\,2} / 2B_0, \qquad [3.22]$$

while a gradient G_z along the z will result in a concomitant field

$$B_c(x, y) \approx (x^2 + y^2) \cdot G_z^{\,2} / 8B_0. \qquad [3.23]$$

Importantly, x, y and z are in the magnet coordinate system, so depending on the slice orientation, the effect of the Maxwell gradients it not necessarily restricted to one imaging dimension. At high field ($B_0 > 1.5$ T) both terms are often negligible, however this is not true for sequences which are sensitive to phase effects, so the two examples of EPI and CPMG sequences are considered.

For EPI with an *axial* slice orientation where the strong read gradient is along the physical x- or y-axis, the concomitant gradient causes a frequency offset that predominantly results in a uniform shift of the image along the phase encoding direction. Due to the z^2 dependence however, each slice in a stack of slices will be shifted by a different amount, even at 3 T by up to several pixels. With knowledge of the slice tilt and imaging parameters, this shift is easily corrected during image reconstruction. A second consideration is that the phase difference acquired by spins across a slice must be << 2π, which either imposes a limit on slice thickness at a given off-centre position, or defines a maximum z for a certain thickness. A third and more complex effect must be taken into account in the (usual) case that the signal is partly acquired during the gradient ramps: during the readout, the frequency offset varies due to the G^2 dependence of the concomitant field, which can give rise to image blurring if not corrected for during the regridding process. For *sagittal* or *coronal* slice orientation the unwanted frequency offset with the z^2 dependence is within the imaging plane. For phase encoding along z, this causes a pixel stretching or compression that increases with off centre position. For frequency encoding along z, B_c depends on $x^2 + y^2$; one of the terms causes a stretching and compressing, while the other effects a shift along the phase encoding direction (depending on whether sagittal and coronal encoding is used).

Each of the above named effects on EPI acquisitions can in principle be corrected during reconstruction, provided that the slice position and angulations are known. For further details on Maxwell effect in EPI see (Du et al. 2002; Meier et al. 2008; Schmitt et al. 1998; Zhou et al. 1998a; Zhou et al. 1998b).

More severe effects can occur in CPMG sequences. The CPMG condition requires that the phase of all refocusing pulses must be the same, and orthogonal to the phase of the excitation pulse: $\alpha_{x'} - TE/2 - \beta_{y'} - TE - \beta_{y'} - \ldots$ Imbalanced gradient time integrals between RF pulses usually occur for the $\alpha_{x'} - \beta_{y'}$ interval vs. the $\beta_{y'}$ –

$\beta_{y'}$ intervals, since for instance the read gradient is only applied after the first refocusing pulse. The resulting mismatch in phase accumulation may result in uncontrolled interference of different echo pathways and cause a smearing artefact along the phase encoding direction that is not correctable during reconstruction. For RARE sequences at clinical field strengths ($B_0 \geq 1.5$ T) this is not typically a problem as the readout gradients are usually not very strong. In the case of the GRASE sequence however, the use of a rapidly switched EPI like readout in the $\beta_{y'} - \beta_{y'}$ intervals, but importantly not after excitation, can result in artefacts even at 3 T as demonstrated in Chapter 10. One commonly used remedy is the application of typically bipolar 'dummy' gradients with zero net moment between the $\alpha_{x'}$ and $\beta_{y'}$ pulses in order to cancel out the unwanted phase contribution.

3.4 (Partial) parallel imaging

Parallel imaging refers to a set of relatively recent developments in signal reception and image reconstruction. The basic principle is that the MR signal is received with (many) more than just one receiver coil in parallel. Conventionally, MRI is performed by placing a single volume coil around the body part of interest; this has the advantage of a very homogeneous sensitivity profile throughout the enclosed volume. Modern multi-channel receive coils in contrast are essentially arrays of individual surface coils. Each of these coils has a characteristic sensitivity profile depending on its position and orientation within the array. This offers two possibilities:

First, the MR pulse sequence is applied in the usual manner and the resulting individual images simply combined (Carlson 1987; Hutchinson and Raff 1988). This is done for instance by taking the sum-of-squares, or more preferably if the sensitivity profile is known and the phase information to be preserved, by conjugate sensitivity summation; the latter will moreover yield the optimal SNR. A well designed array of surface coils typically has a much higher average SNR than a corresponding single channel volume coil. The strong spatial sensitivity dependence (highest SNR near the coil elements and decreasing towards the centre) might however be considered a drawback for some applications.

Second, the variation between the individual coils' sensitivity profile and the thereby implicitly encoded spatial information can be exploited in such a way, that part of the gradient spatial encoding in the pulse sequence is replaced by coil spatial encoding during the image reconstruction. Satisfying the Nyquist criterion during acquisition is then no longer required. First advances in this direction where made by Ra in 1993, followed only much later by a variety of clinically useful and now commercially implemented techniques, including SMASH, SENSE and GRAPPA (Griswold et al. 2002; Pruessmann et al. 1999; Ra and Rim 1993; Sodickson and Manning 1997). Several other techniques have been proposed, but only the basic SENSE and GRAPPA variants are discussed here. All these approaches are sometimes called 'partial parallel imaging', or more commonly just 'parallel imaging'.

The fraction of phase encoding steps (k_y-lines) that are skipped during acquisition is denoted by the acceleration factor a (also called reduction or undersampling factor). Depending on the type of acquisition sequence up to a factor a time saving is achieved, and herein lies the main benefit of parallel imaging which has revolutionised fast MRI. For (single-shot) sequences such as RARE, EPI or GRASE this means that the duration of the readout train is effectively shortened, resulting in a great reduction of blurring and distortion artefacts while the full spatial resolution is maintained or even improved.

Parallel imaging techniques must be divided into two classes: First, those that operate in image space and belong to the SENSE family, and second, those that first synthesise the non-sampled *k*-space lines prior to Fourier reconstruction and belong to the SMASH family.

For the following illustrations consider a factor two accelerated acquisition with two receiver coils; alternate phase encoding steps are skipped. There are hence two sets of *k*-space in which every other line is missing.

Reconstruction in image space: Sensitivity encoding (SENSE)

In SENSE, each coil's undersampled *k*-space is first Fourier transformed to the image domain. The Nyquist criterion is clearly violated, so this yields two aliased images with a factor two reduced FoV, according to FoV = 1 / Δk_y. To reconstruct a single full FoV from the two aliased images, the coil sensitivity profiles are required. These are usually obtained at the start of the scan session by performing a low resolution full FoV scan of the object with the surface coils on the one hand, and a scan with a homogenous volume coil (e.g. scanner body coil) on the other. These images are then reconstructed and spatially smoothed, and the sensitivity maps generated by dividing the surface coil images by the body coil image to remove object related intensity variation. To ensure smoothness and to avoid edge effects in the SENSE reconstruction, polynomial fitting is performed and the sensitivity profiles extrapolated beyond the object boundaries.

The actual SENSE reconstruction is then performed by solving the linear equations that relate the two aliased images, the two coil sensitivity profiles and the full FoV image to be reconstructed. This is illustrated for the example shown in Fig. 3.10. For each of the two coils, full FoV scans are acquired from which the corresponding sensitivity profiles s_1 and s_2 are derived (top). Now consider two points y_1 and y_2 in the object which are separated by exactly half the FoV and have spin densities of ρ_1 and ρ_2, respectively. In the factor two accelerated acquisition and subsequent reconstruction, the signal from y_1 and y_2 will aliase into the same pixel in accordance with the Nyquist theorem (bottom). The image intensity in the two aliased images at the position where the signals from y_1 and y_2 coincide is then given by the sum of the signals originating from the two points, weighted by the coil sensitivity at the corresponding position. It can hence be written as

$$S_{\text{coil 1}} = s_1(y_1) \cdot \rho_1 + s_1(y_2) \cdot \rho_2$$
$$S_{\text{coil 2}} = s_2(y_1) \cdot \rho_1 + s_2(y_2) \cdot \rho_2 \qquad [3.24]$$

The problem is now expressed as a set of two linear equations with the two unknowns ρ_1 and ρ_2, and can thus be solved. More generally, this can be expressed in matrix form as $\boldsymbol{S} = \boldsymbol{s} \cdot \boldsymbol{\rho}$. The example problem is exactly solvable by simple matrix inversion $\boldsymbol{\rho} = \boldsymbol{s}^{-1} \cdot \boldsymbol{S}$. In the more favourable case where $N_{\text{coils}} > a$, the pseudo inverse is calculated (e.g. in the least squares sense) and the image intensities in the reconstructed full FoV image are then given by

$$\rho = (\boldsymbol{s}^{\mathrm{H}} \cdot \boldsymbol{s})^{-1} \cdot \boldsymbol{s}^{\mathrm{H}} \cdot \boldsymbol{S}. \qquad [3.25]$$

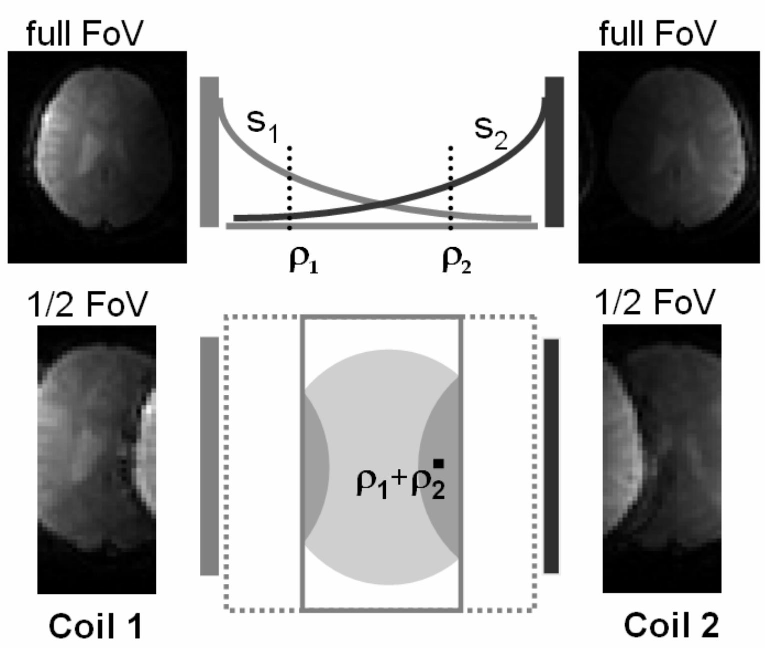

Figure 3.10: *Principle of the sensitivity encoding (SENSE) reconstruction, illustrated here for the example of factor two undersampling with two receive coils.* s_1 *and* s_2 *are the two coil sensitivity profiles which are generated from a smoothed version the full FoV coil images (top left end right). The accelerated acquisition results in half the effective FoV, and the signal from two points in the object with spin density* ρ_1 *and* ρ_2 *separated by 1/2·FoV will aliase into the same position in the undersampled image (bottom). For each coil, the image intensity at this position is simply the sum of the two MR signal intensities from* ρ_1 *and* ρ_2*, weighted by the coil sensitivity at the corresponding positions in the object.*

One feature of SENSE is that only the final full FoV image can be reconstructed, and only the magnitude information is available. There is also no way of reconstructing full FoV images of the individual coils. In addition to the factor $\sqrt{a}$ sensitivity reduction that results from the acquisition of a factor a smaller data sample, there is a spatially varying noise contribution. The structure of this noise map depends on the noise correlation between individual coil elements through the geometric properties of the array, and the way the image aliases under the reduced FoV condition. This noise contribution is described by the geometry factor g. For details on the g-factor calculation see Ref (Pruessmann et al. 1999). The effective SNR of a SENSE acquisition with respect to a fully sampled one is given by

$$SNR_{\text{factor-a}} = SNR_{\text{full}} / (g \cdot \sqrt{a}). \quad [3.26]$$

Reconstruction in k-space: Generalised autocalibrating partially parallel acquisitions (GRAPPA)

GRAPPA solves the undersampling problem in *k*-space. Moreover, each of the undersampled *k*-space sets from the different coils is first 'completed' by synthesising the missing *k*-space lines. Full FoV images of each coil are then reconstructed by Fourier transformation in the usual way, and subsequently combined using the SOS method. The crucial step is hence the synthesis of the missing data lines.

In addition to the undersampled *k*-space, the sequence acquires a small number of additional k_y lines near the centre of *k*-space so as to cover a small contiguous region, the so called reference lines (This corresponds to the low resolution full FoV scan in SENSE but is acquired as part of the undersampled scan; no body coil image for intensity normalisation is required in this autocalibrating approach.).

The reconstruction process for the above example is illustrated in Fig. 3.11. Acquired data from each coil are fit to a reference line of one coil. This linear fit yields the weights which can subsequently be used to generate all missing k_y-lines of that coil. This is done in a blockwise sliding manner, where each block contains *a* lines of which one was originally acquired. The whole process is repeated for all coils until a complete *k*-space is obtained for each.

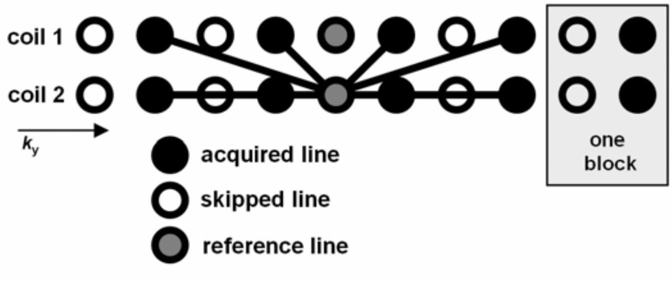

Figure 3.11: *Schematic illustration of the GRAPPA algorithm. Four acquired lines (full circles) of each coil are fit to a reference line (grey circles) of one coil, here in coil 2. The weights thus obtained are later used to calculate the missing lines in coil 2 as a linear combination of acquired k_y lines in all coils. Once the fitting process is completed for all acquired reference lines and coils, the missing k_y data are generated and a full k-space obtained for each coil. Figure after (Griswold et al. 2002).*

The marked difference to the SENSE algorithm is thus that full FoV images are reconstructed for each coil. Furthermore, since the fitting routine is performed in (complex) *k*-space, phase images are available for each coil separately. This is a useful property for some applications where the phase information is important, for instance susceptibility weighted imaging (SWI) (Haacke et al. 2004; Reichenbach et al. 2000).

Similar to SENSE there is a sensitivity loss greater than factor $\sqrt{a}$. The spatial characteristics of the noise map are different from *g*-maps since the reconstruction is performed in *k*-space. It is reasonable to assume that under comparable conditions the total noise enhancement is similar in both methods, but the spatial noise distribution is in general much smoother in GRAPPA. An analytical formulation for the GRAPPA *g*-factor was only developed recently and can be found in Ref (Breuer et al. 2008).

References

Bernstein MA, King KF, Zhou XJ. (2004) *Handbook of MRI Pulse Sequences*. London: Elsevier Academic Press

Breuer FA, Blaimer M, Seiberlich N, Jakob PM, Griswold MA. (2008) A general formulation for quantitative g-factor calculation in GRAPPA reconstructions. In: *Proceedings of the 16th Annual Meeting of ISMRM*, Toronto, p 10

Callaghan PT. (1994) *Principles of Nuclear Magnetic Resonance Microscopy*. London: Oxford University Press 1994

Carlson JW. (1987) AN ALGORITHM FOR NMR IMAGING RECONSTRUCTION BASED ON MULTIPLE RF RECEIVER COILS. *Journal of Magnetic Resonance* 74:376-380

Chang H, Fitzpatrick JM. (1992) A technique for accurate magnetic resonance imaging in the presence of field inhomogeneities. *IEEE Trans Med Imaging* 11:319-329

Constable RT, Spencer DD. (1999) Composite image formation in z-shimmed functional MR imaging. *Magnetic Resonance in Medicine* 42:110-117

Cusack R, Russell B, Cox SML, De Panfilis C, Schwarzbauer C, Ansorge R. (2005) An evaluation of the use of passive shimming to improve frontal sensitivity in fMRI. *Neuroimage* 24:82-91

Du YPP, Zhou XHJ, Bernstein MA. (2002) Correction of concomitant magnetic field-induced image artefacts in nonaxial echo-planar imaging. *Magnetic Resonance in Medicine* 48:509-515

Edelstein WA, Hutchison JMS, Johnson G, Redpath T. (1980) SPIN WARP NMR IMAGING AND APPLICATIONS TO HUMAN WHOLE-BODY IMAGING. *Physics in Medicine and Biology* 25:751-756

Feinberg DA, Johnson G, Kiefer B. (1995) INCREASED FLEXIBILITY IN GRASE IMAGING BY K-SPACE-BANDED PHASE-ENCODING. *Magnetic Resonance in Medicine* 34:149-155

Feinberg DA, Oshio K. (1991) GRASE (GRADIENT-ECHO AND SPIN-ECHO) MR IMAGING - A NEW FAST CLINICAL IMAGING TECHNIQUE. *Radiology* 181:597-602

Griswold MA, Jakob PM, Heidemann RM, Nittka M, Jellus V, Wang J, Kiefer B, Haase A. (2002) Generalized autocalibrating partially parallel acquisitions (GRAPPA). *Magn Reson Med* 47:1202-1210

Haacke EM, Brown RW, Thomson MR, Venkatesan R. (1999) *Magnetic Resonance Imaging. Physical Principles and Sequence Design*. New York: Wiley-Liss (John Wiley & Sons),

Haacke EM, Xu YB, Cheng YCN, Reichenbach JR. (2004) Susceptibility weighted imaging (SWI). *Magnetic Resonance in Medicine* 52:612-618

Hargreaves BA, Cunningham CH, Nishimura DG, Conolly SM. (2004) Variable-rate selective excitation for rapid MRI sequences. *Magnetic Resonance in Medicine* 52:590-597

Hennig J, Nauerth A, Friedburg H. (1986) RARE imaging: a fast imaging method for clinical MR. *Magn Reson Med* 3:823-833

Hutchinson M, Raff U. (1988) FAST MRI DATA ACQUISITION USING MULTIPLE DETECTORS. *Magnetic Resonance in Medicine* 6:87-91

Hutchison JMS, Sutherland RJ, Mallard JR. (1978) NMR IMAGING - IMAGE RECOVERY UNDER MAGNETIC-FIELDS WITH LARGE NONUNIFORMITIES. *Journal of Physics E-Scientific Instruments* 11:217-221

Hutton C, Bork A, Josephs O, Deichmann R, Ashburner J, Turner R. (2002) Image Distortion Correction in fMRI: A Quantitative Evaluation. *NeuroImage* 16:217-240

Jezzard P, Balaban RS. (1995) Correction for geometric distortion in echo planar images from B0 field variations. *Magn Reson Med* 34:65-73

Johnson G, Feinberg DA, Venkataraman V. (1996a) A comparison of phase encoding ordering schemes in T-2-weighted GRASE imaging. *Magnetic Resonance in Medicine* 36:427-435

Johnson G, Feinberg DA, Venkataraman V. (1996b) Single-shot GRASE imaging with short effective TEs. *Jmri-Journal of Magnetic Resonance Imaging* 6:944-947

Jovicich J, Norris DG. (1998) GRASE imaging at 3 Tesla with template interactive phase-encoding. *Magn Reson Med* 39:970-979

Ljunggren S. (1983) A SIMPLE GRAPHICAL REPRESENTATION OF FOURIER-BASED IMAGING METHODS. *Journal of Magnetic Resonance* 54:338-343

Mansfield P. (1977) Multi-Planar Image-Formation Using Nmr Spin Echoes. *Journal of Physics C-Solid State Physics* 10:L55-L58

Meier C, Zwanger M, Feiweier T, Porter D. (2008) Concomitant field terms for asymmetric gradient coils: Consequences for diffusion, flow, and echo-planar imaging. *Magnetic Resonance in Medicine* 60:128-134

Mugler JP, 3rd. (1999) Improved three-dimensional GRASE imaging with the SORT phase-encoding strategy. *J Magn Reson Imaging* 9:604-612

Norris DG, Hutchison JM. (1990) Concomitant magnetic field gradients and their effects on imaging at low magnetic field strengths. *Magn Reson Imaging* 8:33-37

Oshio K, Feinberg DA. (1991) GRASE (GRADIENT-ECHO AND SPIN-ECHO) IMAGING - A NOVEL FAST MRI TECHNIQUE. *Magnetic Resonance in Medicine* 20:344-349

Pauly J, Leroux P, Nishimura D, Macovski A. (1991) PARAMETER RELATIONS FOR THE SHINNAR-LEROUX SELECTIVE EXCITATION PULSE DESIGN ALGORITHM. *Ieee Transactions on Medical Imaging* 10:53-65

Proctor WG, Yu FC. (1950) THE DEPENDENCE OF A NUCLEAR MAGNETIC RESONANCE FREQUENCY UPON CHEMICAL COMPOUND. *Physical Review* 77:717-717

Pruessmann KP, Weiger M, Scheidegger MB, Boesiger P. (1999) SENSE: sensitivity encoding for fast MRI. *Magn Reson Med* 42:952-962

Ra JB, Rim CY. (1993) FAST IMAGING USING SUBENCODING DATA SETS FROM MULTIPLE DETECTORS. *Magnetic Resonance in Medicine* 30:142-145

Reichenbach JR, Barth M, Haacke EM, Klarhofer M, Kaiser WA, Moser E. (2000) High-resolution MR venography at 3.0 Tesla. *Journal of Computer Assisted Tomography* 24:949-957

Schmitt F, Stehling MK, Tuner R. (1998) *Echo-Planar Imaging*. Heidelberg: Springer

Shinnar M, Bolinger L, Leigh JS. (1989) THE USE OF FINITE IMPULSE-RESPONSE FILTERS IN PULSE DESIGN. *Magnetic Resonance in Medicine* 12:81-87

Silver MS, Joseph RI, Hoult DI. (1984a) HIGHLY SELECTIVE PI/2 AND PI-PULSE GENERATION. *Journal of Magnetic Resonance* 59:347-351

Silver MS, Joseph RI, Hoult DI. (1984b) SELECTIVE PULSE CREATION BY INVERSE SOLUTION OF THE BLOCH-RICCATI EQUATION. *Magnetic Resonance in Medicine* 1:294-294

Sodickson DK, Manning WJ. (1997) Simultaneous acquisition of spatial harmonics (SMASH): fast imaging with radiofrequency coil arrays. *Magn Reson Med* 38:591-603

Song AW, Wong EC, Hyde JS. (1994) ECHO-VOLUME IMAGING. *Magnetic Resonance in Medicine* 32:668-671

Twieg DB. (1983) THE K-TRAJECTORY FORMULATION OF THE NMR IMAGING PROCESS WITH APPLICATIONS IN ANALYSIS AND SYNTHESIS OF IMAGING METHODS. *Medical Physics* 10:610-621

Wilson JL, Jenkinson M, Jezzard P. (2002) Optimization of static field homogeneity in human brain using diamagnetic passive shims. *Magnetic Resonance in Medicine* 48:906-914

Zeng H, Constable RT. (2002) Image distortion correction in EPI: comparison of field mapping with point spread function mapping. *Magn Reson Med* 48:137-146

Zhou XHJ, Du YPP, Bernstein MA, Reynolds HG, Maier JK, Polzin JA. (1998a) Concomitant magnetic-field-induced artefacts in axial echo planar imaging. *Magnetic Resonance in Medicine* 39:596-605

Zhou XJ, Tan SG, Bernstein MA. (1998b) Artefacts induced by concomitant magnetic field in fast spin-echo imaging. *Magnetic Resonance in Medicine* 40:582-591

Chapter 4 The Basics of functional MRI

Functional MRI has become one of the major techniques for investigating brain function in animals and humans. This Chapter gives a brief overview on how MRI techniques can be used to measure the haemodynamic changes that accompany changes in the level of neuronal activity in the brain. For a recent review on the subject matter the reader is referred to Ref (Norris 2006).

Measures of brain activation

Brain 'activation' is a term that usually refers to the increase in the electro-physiological activity of a population of neurons when a certain process is taking place in the brain. These net changes in membrane potentials result in a number of directly related and measurable effects including electrical, magnetic and metabolic changes, and are furthermore accompanied by local changes in cerebral blood volume (CBV), blood flow (CBF) and blood oxygenation. That neural activity gives rise to these latter haemodynamic changes has been established beyond doubt, but the underlying mechanisms by which they are mediated are still not fully understood. A great diversity of methods exists today for the different effects to be measured externally. These include electro-encephalography (EEG), magneto-encephalography (MEG), single photon emission computed tomography (SPECT), positron emission tomography (PET) and a number of optical imaging techniques. EEG and MEG directly measure changes in electric or magnetic field distributions that result from the neuronal activity, and are hence characterised by an excellent temporal resolution. Especially EEG however has a very limited spatial resolution and the considerably better MEG is not widely available. SPECT and PET in contrast measure metabolic rate changes by detecting local changes in the decay activity of previously injected radioactive tracers that are coupled to glucose and which accumulate in regions of increased metabolic demand (Terpogossian et al. 1975). While providing a spatially well localised measure of activation that allows direct interpretation of the underlying metabolism, both methods are relatively expensive and rely on the administration of radioactive contrast media, making them less favourable for studies on healthy volunteers. Externally applied optical imaging techniques such as near-infrared spectroscopy offer temporally well resolved information on CBF, CBV and oxygenation state, but spatial resolution is relatively poor and the limited penetration depth restricts their application to near the cortical surfaces (Wolf et al. 2007).

fMRI refers to a set of relatively young techniques that allow the spatial and temporal mapping of haemodynamic changes upon neuronal activation. As the exact relation between the two is still unclear, measures of the haemodynamic response in terms of the most widely used blood oxygenation level dependent (BOLD) signal are to be regarded as phenomenological. Nevertheless, BOLD fMRI has become the favoured method for neuroscientific investigations on healthy volunteers for several reasons: First, BOLD fMRI is highly sensitive over the whole brain and offers temporal and spatial resolution power that matches well the temporal and spatial extent of the haemodynamic changes; second, it is relative 'inexpensive' compared to SPECT and PET; and third, it is entirely non-invasive as no contrast agents are required. While fMRI is established as a routine tool for mapping brain activity, great efforts are continuously made by physicists and other scientists to further improve fMRI methodology and to establish the mechanisms of the neurovascular coupling.

General requirement for fMRI pulse sequences

The ideal acquisition method for fMRI should meet a number of criteria as follows. First, high sensitivity to activation-related signal changes, that is large signal changes at low noise levels (high contrast to noise ratio). Second, the acquisition rate should be sufficiently high so as to adequately sample the stimulus response. This is especially important as many modern cognitive fMRI studies no longer use 'blocked' stimulus designs but instead sample the 'event related' signal response to single briefly presented stimuli. Third, spatial resolution should approximately match the point spread function of the signal response being measured. Fourth, volume coverage should be large, and preferably cover the entire brain. Fifth, as long image time series are acquired (often 30 minutes or more) the motion sensitivity of the method should be low. It is clear from the discussion of pulse sequences in Chapter 3 that a compromise would typically have to be made between requirements 1 – 4.

fMRI of haemodynamic changes

During neuronal activation there is increased metabolic demand and an increase in the local cerebral metabolic rate of oxygen consumption ($CMRO_2$); this is accompanied by an increase in the local blood supply through vasodilation (CBV increase) and hence an increase in CBF. Initial fMRI experiments measured blood volume changes by administering a bolus of paramagnetic compound into the vasculature and recording T_2*-weighted images as the bolus passes (Belliveau et al. 1991; Belliveau et al. 1990). The paramagnetic agent creates transient local field gradients which effect an attenuation of the MR signal that is taken to be proportional to the contrast agent concentration, and hence relative blood volume in the imaging voxels. The limitations of this approach are obvious. Modern fMRI techniques use the blood itself as an endogenous intravascular and freely diffusible 'contrast agent' which allows the assessment of CBV or CBF, or most commonly the BOLD signal which results from an interplay of the three parameters CBF, CBV and $CMRO_2$. Both BOLD and CBV methods play an important role in the later chapters of this thesis and are therefore introduced in the following. A range of CBF weighted fMRI methods has been proposed but will not be further discussed here.

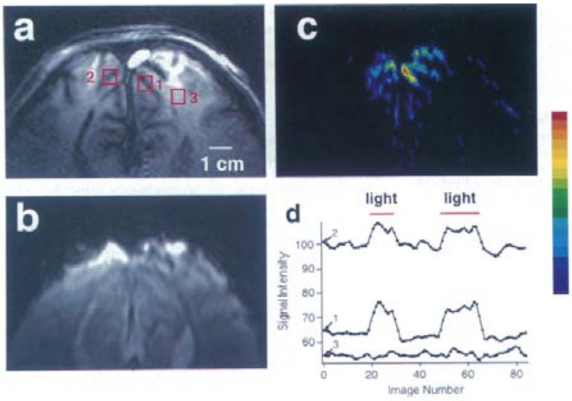

Figure 4.1 *(see Appendix for colour version): One of the first BOLD activation maps obtained in the human brain by Ogawa and colleagues in 1992. The signal in the ROIs 1 and 2 placed within the visual cortex clearly shows an increase during the periods where a visual stimulus was applied (panel d); no change is seen in the ROI outside the visual cortex. Panel c shows a signal change map (Figure adapted from Ogawa et al, PNAS 1992 89:5951-5955 'Intrinsic signal changes accompanying sensory stimulation: functional brain mapping with magnetic resonance imaging').*

BOLD fMRI and BOLD contrast mechanisms

The magnetic susceptibility of blood depends linearly on its oxygenation level. This property was already noticed in 1932 by Pauling and Coryell and could be ascribed to the fact that oxy-haemoglobin contains diamagnetic iron while deoxy-haemoglobin contains paramagnetic iron. Four decades later Ogawa and colleagues could exploit this fact to demonstrate in the rat brain how the T_2*-weighted MR signal near vessels decreased with decreasing oxygenation levels (Ogawa et al. 1990). The first human BOLD activation studies with sensory stimulation soon followed (Kwong et al. 1992; Ogawa et al. 1992) and the usefulness of the gradient echo EPI sequence as both sensitive and fast imaging method was convincingly demonstrated (Bandettini et al. 1992; Blamire et al. 1992). The vast majority of fMRI studies today still use EPI.

The initially counterintuitive observation of *increasing* MR signal with increasing activation and hence increasing production of paramagnetic deoxy-haemoglobin is explained by three changes taking place as follows, and gives rise to the typical BOLD response to a sensory stimulus as shown in Fig. 4.2: First, local $CMRO_2$ increases and with it oxygen consumption and hence the amount of deoxy-haemoglobin. This may or may not cause the elusive 'fast response' (Buxton 2001; Ernst and Hennig 1994; Rother et al. 2002), a brief initial period of signal attenuation due to deoxy-haemoglobin accumulation very near the site of neuronal activation. Second, after a small delay local CBV increases. This would by itself increase the blood volume and hence the absolute amount of deoxy-haemoglobin so as to reduce the signal; however linked with the vessel dilation there is third: a local CBF increase which is by far the dominant contribution and leads to a deoxy-haemoglobin washout much greater than in the resting state. The overall result is hence a *decrease* in absolute deoxy-haemoglobin upon activation and therefore a *signal increase* in the imaging voxels near the site of activation. The maximum signal is typically reached after about 6 to 8 seconds. After stimulus offset, this main response is followed by the post-stimulus undershoot (Bandettini et al. 1992; Frahm et al. 1996; Jones et al. 1998). The mechanisms underlying the undershoot are unclear, although the phenomenon has attracted considerable interest over the years. For a long time the consensus was that it is caused by a temporal decoupling of CBF and CBV after the stimulus, whereby CBV of venous vessels returns to baseline slower than CBF and hence causes a temporary increase of the deoxy-haemoglobin (Buxton et al. 1998; Mandeville et al. 1999). More recent results from optical imaging and CBV studies however provide converging evidence not only that CBV returns to baseline rapidly, but also that the changes occur primarily in the arteriolar vasculature (Devor et al. 2007a; Devor et al. 2007b; Donahue et al. 2008; Hillman et al. 2007; Kim et al. 2007; Tuunanen et al. 2006; Zhao et al. 2007). This suggests a mechanism by which the undershoot is caused due sustained elevation in $CMRO_2$ even after the baseline return of the vascular response. Evidence for this later hypothesis is also provided by work presented in Chapter 8 of this thesis.

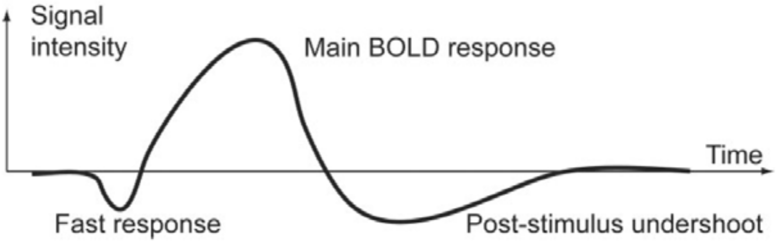

Figure 4.2: *BOLD signal response to a brief stimulus.*

The changes in the oxygenation state of blood result in the observed signal changes through four different BOLD contrast mechanisms. Their sources are differently localised, and they contribute differently to the signal changes depending on the imaging sequence used.

Two of the effects are due to extravascular dephasing (Ogawa et al. 1993). When the blood oxygenation changes, the associated local field change extends way beyond the vessel boundaries, giving rise to a significant extravascular effect as illustrated in Fig. 4.3. At a distance r and azimuthal angle φ, the frequency offset due to the dipole field that is produced by a vessel of diameter a oriented at an angle θ to $\boldsymbol{B}_0$ is given by

$$\Delta\omega = 2\pi\cdot\omega_0\cdot\Delta\chi\cdot(1-Y)\cdot\sin^2\theta\cdot(a/r)^2\cdot\cos(2\varphi), \qquad [4.1]$$

where Y is the relative blood oxygenation, and $\Delta\chi$ the susceptibility difference between fully oxygen-saturated blood and the neighbouring tissue. Panels (a) to (c) t in Figure 4.3 show simulated dipole fields at three different oxygenation levels.

Two important features are that there is no net field change, and no field distortion if the vessel is oriented parallel to $\boldsymbol{B}_0$.

Water spins move around in the inhomogeneous field surrounding a vessel, and so during the time between excitation and acquisition (at time *TE*) they will loose phase coherence. If the path length of their diffusive motion is relatively small with respect to the extent of the field distortion, this process is referred to as *extravascular static dephasing*, and results directly in the classical T_2*-weighted signal decay described in Chapter 2. Since the phase accumulation occurs in a static sense, it will be refocused in spin echo sequences. This mechanism applies to vessel diameters of approximately 10 μm and larger. The signal changes due to static extravascular dephasing scale roughly linearly with $\boldsymbol{B}_0$. Around smaller capillary and post capillary vessels, moving spins will experience a large field variation and their loss of phase coherence becomes stochastic and can no longer be refocused by a spin echo. This contrast mechanism is called *extravascular dynamic dephasing*, and its signal contribution is well localised to the capillaries close to the site of neuronal activation. It increases approximately quadratically with B_0.

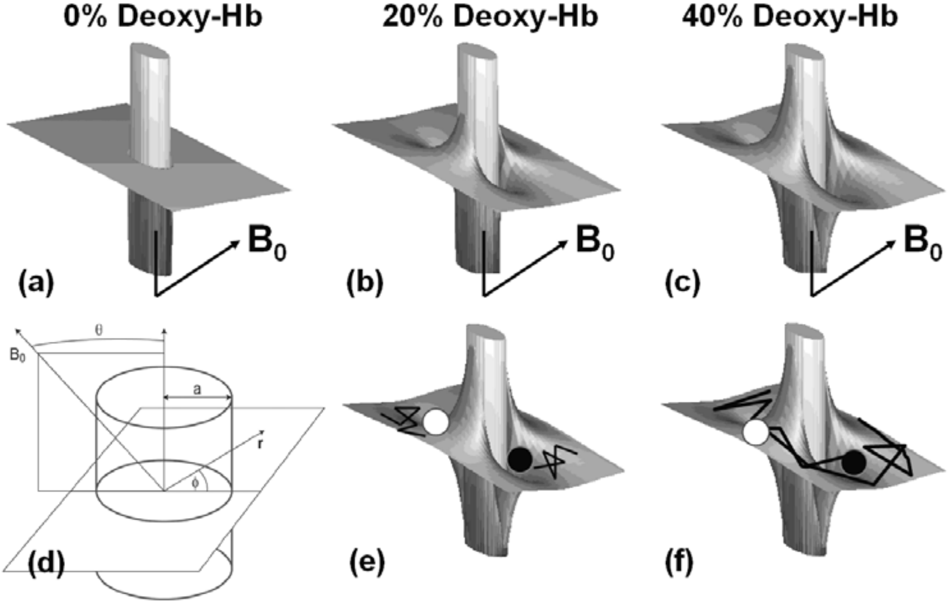

Figure 4.3: *Magnetic dipole field around a vessel orientated at an angle to B_0. The degree of field perturbation depends on the deoxy-haemoglobin concentration and gives rise to extravascular static dephasing (vessel diameter > 10μm) and extravascular dynamic dephasing (vessel diameter < 10μm). The two mechanisms are illustrated in panel (e) and (f), respectively.*

The third BOLD contrast mechanism is of intravascular origin and due to *changes in T_2 of blood*. These result from the interaction between deoxy-haemoglobin in the red blood cells with nearby water spins, both within the erythrocytes themselves and the surrounding plasma (Gardener et al. 2004; Stefanovic and Pike 2004). In this sense the interaction is equivalent to dynamic dephasing. The alternative hypothesis is a two-site exchange whereby the water spins diffuse in an out of the erythrocytes. In any case, the loss of phase coherence is a random process, and will contribute in a spin echo experiment. Again, stronger interaction occurs in the presence of more deoxy-haemoglobin, yielding a shorter T_2. The blood T_2 contribution to the BOLD signal stems from the entire vasculature downstream from the site of activation.

The fourth mechanism is another intravascular effect and is called *vascular dephasing*, or *intravascular frequency offset effect* (Ogawa et al. 1993). Spins in a vessel at an angle to $\boldsymbol{B}_0$ will experience a frequency shift. In case of a single large vessel, the interference between intra- and extravascular signals results in an oscillatory modulation (‘beating’) that depends on *TE* (Yablonskiy and Haacke 1994). In the more realistic case of many randomly oriented vessels the signal attenuation in a voxel will behave like a static dephasing effect (Haacke et al. 1995; Yablonskiy and Haacke 1994). It can hence be refocused and will not contribute to a spin echo. The frequency offset in the vessel is independent of the vessel size and given by

$$\Delta\omega = 2\pi \cdot \omega_0 \cdot \Delta\chi \cdot (1 - Y)\cdot(3\cos^2\theta - 1) / 3. \qquad [4.2]$$

The fact that dynamic averaging is better localised with respect to the site of neuronal activation, and that the four BOLD contrast mechanisms differentially contribute to gradient and spin echo measurements is an important feature. Moreover, the ratio of the different contributions depends strongly on B_0. For instance, spin echo measurements at 1.5 T will effectively only be sensitive to intravascular T_2 changes (Jones et al. 1998; Oja et al. 1999); at 3 T there is about 50% contribution from both intravascular T_2 and dynamic dephasing about the capillaries (Norris et al. 2002). At 7 T and above, this latter mechanism is by far the dominant. The consequence is hence that with increasing B_0 the BOLD signal is more and more weighted towards the microvasculature and hence the site of neuronal activation. The differences between the different mechanisms may also be viewed as a useful property and is exploited in the study on the origin of the post-stimulus BOLD undershoot presented in Chapter 8.

Relevance of the echo time

The most important parameter for functional imaging sequences is the echo time *TE*. To distinguish brain regions involved in a certain task, images of the brain are continuously acquired over the duration of the experiment, and the timecourse of each pixel subsequently compared with the stimulation protocol by means of correlation analysis or linear regression. The imaging parameters should thus be chosen so as to maximise the difference in signal intensity between the ‘activated’ and ‘resting’ state of the brain which results from the corresponding small changes in T_2*. For exponential signal decay, it follows from differentiation of $S(TE) = S_0 \cdot \exp(-TE / T_2^*)$ that this is achieved by setting the echo time equal to the T_2* of grey matter, since this is where the activation takes place. As T_2* is strongly influenced by the presence of local inhomogeneity gradients for instance near tissue-air interfaces, the optimal *TE* typically varies across the brain. This is not a concern in case of T_2-weighted (spin-echo) imaging sequences, where *TE* should be equal to the grey matter T_2.

fMRI based on CBV contrast

Following the above mentioned initial experiments with CBV fMRI that used a passing bolus of contrast agent (Belliveau et al. 1990), BOLD fMRI is now used on humans almost exclusively. In animals the super-paramagnetic but toxic compound MION found (and finds) frequent application as intravascular signal booster, but this provides no alternative to BOLD fMRI in humans. Most studies that have attempted to measure BOLD, CBV and CBF in isolation for the formulation of haemodynamic response models have therefore primarily been conducted on rodents (Buxton et al. 1998; Mandeville et al. 1999).

Only very recently Lu and colleagues developed a technique for CBV weighted fMRI that again uses the blood itself as intravascular contrast medium (Lu et al. 2003). The vascular space occupancy (VASO) method exploits the small difference between the T_1 of blood and the surrounding grey matter and is based on the inversion recovery experiment: A 180° inversion pulse is applied to invert the entire longitudinal magnetisation; after an inversion time *TI* when the blood magnetisation is zero, but the grey matter magnetisation is not, the excitation pulse is applied. This results in an effective ‘nulling’ of the intravascular blood pool, which will hence not contribute to the subsequently recorded image. For an illustration see Fig 4.4. *TI* for which this is achieved under steady conditions depends on the T_1 of blood and the repetition time *TR*, and is given by

$$TI = -T_1 \cdot \ln(\tfrac{1}{2} + \tfrac{1}{2} \cdot \exp(-TR / T_1)). \qquad [4.3]$$

In VASO, the increased blood volume during brain activation results in a larger fraction of the magnetisation being nulled, and hence a signal decrease is observed. Several considerations are important for successful VASO imaging. First, T_1 of blood is similar to grey matter T_1 and must therefore be known precisely. Moreover, T_1 of arterial and venous blood differ (albeit marginally) and so an average value is used (Lu et al. 2004a; Lu et al. 2003); this is a potential confound as it is not even established where precisely in the vasculature the CBV changes take place. Second, the inversion volume must be as large as possible to avoid the inflow of ‘fresh’ spins into the imaging slice; this is a risk given the typically long *TR* (Donahue et al. 2006; Lu et al. 2003). Third, ideally a *TE* of zero would be used to avoid contamination by (opposite going) BOLD signal changes; with the typically used GE-EPI readout this requirement is hard to meet, and hence SE-EPI (Donahue et al. 2006) or RARE (Poser and Norris 2007) have been used to alleviate this problem.

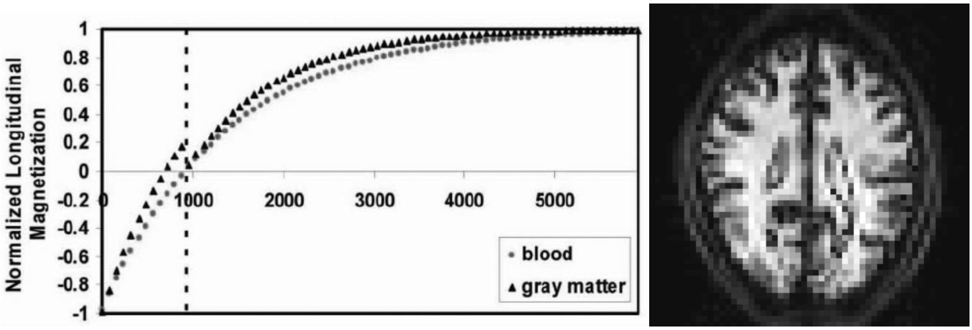

Figure 4.4: *Left: Principle of the VASO experiment. Following a global inversion, the excitation pulse is applied when the blood magnetisation is zero. The blood compartment will hence not contribute to the subsequently recorded signal (Figure adapted from Lu et al, MRM 2003 50:263-274 'Functional magnetic resonance imaging based on changes in vascular space occupancy') Right: Typical VASO image; strongly perfused tissues (grey matter) has a dark appearance due to the absence of the blood signal.*

This is one of the issues addressed in Chapter 9. Fourth, the previous requirement allows the acquisition of only a single slice in the original VASO method. While the method is attractive in that it permits CBV response curves to be measured for e.g. input for haemodynamic modelling, the extremely limited volume coverage renders it effectively useless for 'real' fMRI studies. This led to the proposal of multi-slice methods including several variants of MAGIC (multiple acquisitions with global inversion cycling) VASO (Lu et al. 2004b; Scouten and Constable 2007) and 3D GRASE based VASO (Poser and Norris submitted). The latter forms the essence of Chapter 10.

References

Bandettini PA, Wong EC, Hinks RS, Tikofsky RS, Hyde JS. (1992) TIME COURSE EPI OF HUMAN BRAIN-FUNCTION DURING TASK ACTIVATION. *Magnetic Resonance in Medicine* 25:390-397

Belliveau JW, Kennedy DN, McKinstry RC, Buchbinder BR, Weisskoff RM, Cohen MS, Vevea JM, Brady TJ, Rosen BR. (1991) FUNCTIONAL MAPPING OF THE HUMAN VISUAL-CORTEX BY MAGNETIC-RESONANCE-IMAGING. *Science* 254:716-719

Belliveau JW, Rosen BR, Kantor HL, Rzedzian RR, Kennedy DN, McKinstry RC, Vevea JM, Cohen MS, Pykett IL, Brady TJ. (1990) FUNCTIONAL CEREBRAL IMAGING BY SUSCEPTIBILITY-CONTRAST NMR. *Magnetic Resonance in Medicine* 14:538-546

Blamire AM, Ogawa S, Ugurbil K, Rothman D, McCarthy G, Ellermann JM, Hyder F, Rattner Z, Shulman RG. (1992) DYNAMIC MAPPING OF THE HUMAN VISUAL-CORTEX BY HIGH-SPEED MAGNETIC-RESONANCE-IMAGING. *Proceedings of the National Academy of Sciences of the United States of America* 89:11069-11073

Buxton RB. (2001) The elusive initial dip. *Neuroimage* 13:953-958

Buxton RB, Wong EC, Frank LR. (1998) Dynamics of blood flow and oxygenation changes during brain activation: the balloon model. *Magn Reson Med* 39:855-864

Devor A, Tian P, Nishimura N, Teng IC, Hillman EM, Narayanan SN, Ulbert I, Boas DA, Kleinfeld D, Dale AM. (2007a) Suppressed neuronal activity and concurrent arteriolar vasoconstriction may explain negative blood oxygenation level-dependent signal. *J Neurosci* 27:4452-4459

Devor A, Trevelyan A, Kleinfeld D. (2007b) Is there a common origin to surround-inhibition as seen through electrical activity versus hemodynamic changes? Focus on "Duration-dependent response in SI to vibrotactile stimulation in squirrel monkey". *J Neurophysiol* 97:1880-1882

Donahue M, Stevens R, de Boorder M, Pekar J, Hendrikse J, van Zijl P. (2008) Hemodynamic changes after visual stimulation and breath holding provide evidence for an uncoupling of cerebral blood flow and volume from oxygen metabolism. *J Cereb Blood Flow Metab*

Donahue MJ, Lu H, Jones CK, Edden RA, Pekar JJ, van Zijl PC. (2006) Theoretical and experimental investigation of the VASO contrast mechanism. *Magn Reson Med* 56:1261-1273

Ernst T, Hennig J. (1994) OBSERVATION OF A FAST-RESPONSE IN FUNCTIONAL MR. *Magnetic Resonance in Medicine* 32:146-149

Frahm J, Kruger G, Merboldt KD, Kleinschmidt A. (1996) Dynamic uncoupling and recoupling of perfusion and oxidative metabolism during focal brain activation in man. *Magn Reson Med* 35:143-148

Gardener AG, Gowland PA, Francis ST. (2004) Measuring blood oxygenation at 2.35 T using a multi-echo sequence. In: *Proceedings of the 12th Annual Meeting of ISMRM*, Kyoto, p 46

Haacke EM, Lai S, Yablonskiy DA, Lin WL. (1995) IN-VIVO VALIDATION OF THE BOLD MECHANISM - A REVIEW OF SIGNAL CHANGES IN GRADIENT-ECHO FUNCTIONAL MRI IN THE PRESENCE OF FLOW. *International Journal of Imaging Systems and Technology* 6:153-163

Hillman EM, Devor A, Bouchard MB, Dunn AK, Krauss GW, Skoch J, Bacskai BJ, Dale AM, Boas DA. (2007) Depth-resolved optical imaging and microscopy of vascular compartment dynamics during somatosensory stimulation. *Neuroimage* 35:89-104

Jones RA, Schirmer T, Lipinski B, Elbel GK, Auer DP. (1998) Signal undershoots following visual stimulation: A comparison of gradient and spin-echo BOLD sequences. *Magnetic Resonance in Medicine* 40:112-118

Kim T, Hendrich KS, Masamoto K, Kim SG. (2007) Arterial versus total blood volume changes during neural activity-induced cerebral blood flow change: implication for BOLD fMRI. *J Cereb Blood Flow Metab* 27:1235-1247

Kwong KK, Belliveau JW, Chesler DA, Goldberg IE, Weisskoff RM, Poncelet BP, Kennedy DN, Hoppel BE, Cohen MS, Turner R, et al. (1992) Dynamic magnetic resonance imaging of human brain activity during primary sensory stimulation. *Proc Natl Acad Sci U S A* 89:5675-5679

Lu H, Clingman C, Golay X, van Zijl PC. (2004a) Determining the longitudinal relaxation time (T1) of blood at 3.0 Tesla. *Magn Reson Med* 52:679-682

Lu H, Golay X, Pekar JJ, van Zijl PCM. (2003) Functional magnetic resonance Imaging based on changes in vascular space occupancy. *Magn Reson Med* 50:263-274

Lu H, van Zijl PC, Hendrikse J, Golay X. (2004b) Multiple acquisitions with global inversion cycling (MAGIC): a multislice technique for vascular-space-occupancy dependent fMRI. *Magn Reson Med* 51:9-15

Mandeville JB, Marota JJ, Ayata C, Zaharchuk G, Moskowitz MA, Rosen BR, Weisskoff RM. (1999) Evidence of a cerebrovascular postarteriole windkessel with delayed compliance. *J Cereb Blood Flow Metab* 19:679-689

Norris DG. (2006) Principles of magnetic resonance assessment of brain function. *Journal of Magnetic Resonance Imaging* 23:794-807

Norris DG, Zysset S, Mildner T, Wiggins CJ. (2002) An investigation of the value of spin-echo-based fMRI using a Stroop color-word matching task and EPI at 3 T. *Neuroimage* 15:719-726

Ogawa S, Lee TM, Kay AR, Tank DW. (1990) Brain magnetic resonance imaging with contrast dependent on blood oxygenation. *Proc Natl Acad Sci U S A* 87:9868-9872

Ogawa S, Menon RS, Tank DW, Kim SG, Merkle H, Ellermann JM, Ugurbil K. (1993) Functional brain mapping by blood oxygenation level-dependent contrast magnetic resonance imaging. A comparison of signal characteristics with a biophysical model. *Biophys J* 64:803-812

Ogawa S, Tank DW, Menon R, Ellermann JM, Kim SG, Merkle H, Ugurbil K. (1992) Intrinsic signal changes accompanying sensory stimulation: functional brain mapping with magnetic resonance imaging. *Proc Natl Acad Sci U S A* 89:5951-5955

Oja JM, Gillen J, Kauppinen RA, Kraut M, van Zijl PC. (1999) Venous blood effects in spin-echo fMRI of human brain. *Magn Reson Med* 42:617-626

Poser BA, Norris DG. (submitted) 3D single-shot VASO using a Maxwell-gradient compensated GRASE sequence

Poser BA, Norris DG. (2007) Measurement of activation-related changes in cerebral blood volume: VASO with single-shot HASTE acquisition. *Magn Reson Mater Phy*

Rother J, Knab R, Hamzei F, Fiehler J, Reichenbach JR, Buchel C, Weiller C. (2002) Negative dip in BOLD fMRI is caused by blood flow - Oxygen consumption uncoupling in humans. *Neuroimage* 15:98-102

Scouten A, Constable RT. (2007) Applications and limitations of whole-brain MAGIC VASO functional imaging. *Magn Reson Med* 58:306-315

Stefanovic B, Pike GB. (2004) Human whole-blood relaxometry at 1.5 T: Assessment of diffusion and exchange models. *Magn Reson Med* 52:716-723

Terpogossian MM, Phelps ME, Hoffman EJ, Mullani NA, Coleman RE, Grubb RL, Raichle ME. (1975) POSITRON EMISSION TRANSVERSE TOMOGRAPH FOR 3-DIMENSIONAL ASSESSMENT OF CEREBRAL HEMODYNAMICS AND METABOLISM. *Stroke* 6:231-231

Tuunanen PI, Vidyasagar R, Kauppinen RA. (2006) Effects of mild hypoxic hypoxia on poststimulus undershoot of blood-oxygenation-level-dependent fMRI signal in the human visual cortex. *Magn Reson Imaging* 24:993-999

Wolf M, Ferrari M, Quaresima V. (2007) Progress of near-infrared spectroscopy and topography for brain and muscle clinical applications. *Journal of Biomedical Optics* 12

Yablonskiy DA, Haacke EM. (1994) Theory of NMR signal behavior in magnetically inhomogeneous tissues: the static dephasing regime. *Magn Reson Med* 32:749-763

Zhao F, Jin T, Wang P, Kim SG. (2007) Improved spatial localization of post-stimulus BOLD undershoot relative to positive BOLD. *Neuroimage* 34:1084-1092

Chapter 5 BOLD contrast sensitivity enhancement and artefact reduction with multi-echo EPI: parallel-acquired inhomogeneity-desensitised fMRI

Abstract

Functional MRI (fMRI) generally employs gradient-echo EPI to measure BOLD signal changes that result from changes in tissue relaxation time T_2* between activation and rest. As T_2* strongly varies across the brain and BOLD contrast is maximal only where the echo time (TE) equals the local T_2*, imaging at a single TE is a compromise in terms of overall sensitivity. Furthermore, the long echo train makes EPI very sensitive to main field inhomogeneities, causing strong image distortion.

A method is presented that uses accelerated parallel imaging to reduce image artefacts and acquire images at multiple TEs following a single excitation, with no need to increase TR. Sensitivity gains from the broadened T_2* coverage are optimised by pixel-wise weighted echo summation based on measured local T_2*, or contrast-to-noise measurements. The method is evaluated both using an approach that allows differential BOLD CNR to be calculated without stimulation, and a Stroop experiment. Results at 3 T show that BOLD sensitivity improves by 11% or more in all brain regions, with larger gains in areas typically affected by strong susceptibility artefacts. Using parallel imaging markedly reduces image distortion. The method should hence find widespread application in functional brain imaging.

Poser BA, Versluis MJ, Hoogduin JM, Norris DG. Magn Reson Med 55(6): 1227-1235; 2006

Introduction

Over the past decade, functional MRI (fMRI) has come to play an important role in the study of brain function. The gradient-echo echo-planar imaging (GE-EPI) sequence (Mansfield 1977) is most commonly used. A 2D image is generally acquired following a single excitation pulse, thus allowing the entire brain to be imaged in about two seconds at sufficient resolution and with minimal energy deposition. Information about brain activation can be deduced from intensity changes along the image time series, caused by small regional changes in the tissue relaxation parameter T_2* that arise due to the blood oxygenation level dependent (BOLD) contrast mechanism (Ogawa et al. 1990). This BOLD contrast is maximal where echo time (TE) equals T_2*.

Despite being used widely and successfully, conventional GE-EPI has a number of shortcomings:

(a) In-plane signal dephasing during the readout period leads to strong image distortion and blurring along the phase encoding direction. This poses problems particularly in regions of strong magnetic field inhomogeneity, so that at 3 T imaging inferior brain regions such as the inferior prefrontal and inferior temporal lobes is often compromised.

(b) Through-plane signal dephasing leads to signal voids (dropout) that increase both with echo time and main magnetic field strength. To avoid this, many applications for imaging the inferior brain demand a very short echo time, at the cost of a loss in BOLD contrast sensitivity in other brain areas. Furthermore, dropout can prevent use of higher field strengths simply because the echo train length precludes the use of a suitably short TE.

(c) Conventional EPI records a single echo, which results in optimal sensitivity only for a narrow range of T_2* values. The latter vary strongly across the brain (see e.g. Ref (Hagberg et al. 2002) and references therein), and between subjects, so that single-TE imaging always implies a compromise if the whole brain is to be imaged.

Two technical developments can be utilised to reduce these problems:
First, multi-TE acquisitions have been suggested (Yang et al. 1997). In a practical fMRI setting such methods are most beneficial if multiple echoes (ME) can be acquired in a single shot, so as to not compromise temporal resolution and to avoid motion artefacts. This has been demonstrated with spectroscopic imaging sequences such as turbo-PEPSI (Posse et al. 1999), as well as multi-echo EPI sequences (Speck and Hennig 1998). As grey matter signal decay behaves mono-exponentially over a range of echo times, changes in both T_2* and initial signal intensity S_0 can be quantified and used in subsequent statistical analysis (Hagberg et al. 2002; Speck and Hennig 1998). Alternatively, separate statistical maps can be obtained from each TE image time series and combined afterwards (Posse et al. 1999). An approach that is more compatible with conventional processing procedures is to obtain a single image by combining the multiple TE images. For

this, a number of weighting strategies have been suggested, ranging from simple image summation to more sophisticated approaches that aim at BOLD contrast-to-noise maximisation (Posse et al. 1999; Weiskopf et al. 2005). In a recent study, Weiskopf et al. proposed a multi-echo scheme with alternating phase gradients for distortion correction, combined with a subsequent echo combination for BOLD contrast enhancement. To reduce the effects of susceptibility gradients, it has also been suggested to use a spiral in / out approach (Glover and Law 2001) or to combine ME acquisitions with *z*-gradient compensation schemes (Posse et al. 2003) for selected volumes of interest.

One focus of this paper is on the problem of optimising the echo weighting so as to maximise the BOLD contrast sensitivity.

Second, parallel imaging techniques have recently been developed that allow a significant reduction in the echo train length, by acquiring under-sampled *k*-space datasets with multi-coil arrays. Image reconstruction is then performed either in image space using e.g. SENSE (Pruessmann et al. 1999) or *k*-space based methods such as SMASH (Sodickson and Manning 1997) or GRAPPA (Griswold et al. 2002). Reduced image acquisition times result in distortion reductions by the same factor, and shorter echo times can be achieved. By repeatedly running the EPI readout in rapid succession, multiple images can be recorded at different TEs, without the need to increase the repetition time (TR). If the phase encoding gradient is rewound after each echo so that the *k*-space trajectory is identical for all images, distortions will be identical and the images can be combined.

The work presented here investigates the benefits of using parallel-acquired inhomogeneity desensitised fMRI, which combines parallel imaging with optimised multi-echo acquisitions. The expected gains are strongly reduced dropout and distortion artefacts, and near-optimal sensitivity for all brain regions. For two acquisition protocols using different acceleration factors, three echo combination strategies are evaluated against a conventional protocol: image summation with equal weights (‘simple summation’), echo weighting based on T_2* maps (‘T_2*-weighting’) and echo weighting according to actually measured differential contrast-to-noise (‘CNR-weighting’). Comparisons with conventional single-echo EPI are based on a method that calculates relative BOLD sensitivity from in vivo measures of differential contrast in the resting state, as well as functional experiments with a colour-word interference Stroop task paradigm.

Methods

Data acquisition and pre-processing

All experiments were performed at 3 T. Scans were obtained in three acquisition modes using no acceleration (a = 1) as well as twofold (a = 2) and threefold acceleration (a = 3). The pulse sequences are multi-echo versions of the product GE-EPI sequence. Phase encoding gradients are rewound between consecutive echoes to keep distortion the same, and permit echo combination. For conventional scans, a non-accelerated single echo was recorded at the commonly used echo time of 35 ms. For ME scans, the maximum possible number of echoes for an inter-slice TR of 100 ms was recorded in immediate succession, starting with the shortest possible TE.

Resting state measurements for the CNR analysis were performed during 12 sessions (5 different subjects) using a 3 T Philips Intera system equipped with the product 6-channel phased-array head coil (8 coils with 2 x 2 channels combined). The three acquisition protocols were (a) conventional single-echo EPI at TE = 35 ms, (b) ME-2 (a = 2) sampling at TE = 12, 34, 56 and 78 ms, and (c) ME-3 (a = 3) with TE = 8, 22, 36, 50, 64 and 78 ms. 100 volumes were acquired for each protocol and subject. SENSE image reconstruction (Pruessmann et al. 1999) was used for accelerated acquisitions.

Functional experiments on 6 subjects were performed on a 3 T Siemens Magnetom Trio system, using the same type of 8-channel head coil but with an 8-channel ADC. Here, the three acquisition protocols were (a) conventional single-echo EPI at TE = 35 ms, (b) ME-2 with TE = 15, 37 and 58 ms, and (c) ME-3 with TE = 11, 27, 44, 56 and 71 ms. Scan time was 14 min per run (340 volumes). GRAPPA image reconstruction (Griswold et al. 2002) was used for accelerated scans.

All resting state and fMRI acquisitions shared the following parameters: 25 axial slices with 3.5 mm isotropic voxels and 10% slice gap (224 mm FOV, 64 x 64 matrix), TR = 2.5 s, flip angle 90 degrees and a receiver bandwidth of 1816 Hz / pixel.

Echo combination was performed offline, after motion correction with SPM2 (www.fil.ion.ucl.ac.uk). Motion correction parameters were extracted from the shortest TE images, and applied to all echoes of a given excitation. T_2* maps were obtained by mono-exponential fitting to the average of the first ten resting state volumes. Values below 15 ms and above 50 ms were set to these values, respectively. All computer programs were implemented in Matlab (The MathWorks, Inc., USA).

Echo weighting strategies

While ME recordings improve BOLD CNR by covering a larger range of T_2*, the optimal contrast for different brain regions will be spread over the different echo time images. One approach is to perform separate statistical analyses at each TE. However, this is very time consuming, and poses the problem of finding a statistically sound method to subsequently combine multiple statistical maps. An unbiased approach is using an ‘OR’ filter, but this would yield suboptimal results as activation can generally be detected at more than one TE. A single image time series with near-optimal CNR for all T_2* values is hence favourable in that it requires only conventional statistical treatment in subsequent processing. This approach was chosen here.

The MR signal received from a given voxel at echo time TE depends on the signal S_0 available immediately after excitation, and the subsequent signal decay. The signal intensity as a function of TE can be written in a general form as

$$S = S_0 \cdot H(TE) \cdot \exp\left(-TE \cdot R^*_{2(BOLD)}\right), \tag{5.1}$$

where it is assumed that the susceptibility difference between oxy- and deoxygenated blood causes BOLD spin dephasing that can be described by the exponential $\exp(-TE \cdot R_2{}^*{}_{(BOLD)})$ (Yablonskiy and Haacke 1994). The echo time dependent term $H(TE)$ incorporates T_2 decay, and any other time dependent modulation of the signal decay curve caused by inhomogeneities in the main magnetic field that are unrelated to the BOLD effect, including for example any *sinc* modulation caused by a linear component of an inhomogeneity gradient acting through the slice (Fernandez-Seara and Wehrli 2000).

As BOLD contrast as a function of TE is proportional to the signal change per unit change in $R_2{}^*{}_{(BOLD)}$, it can be expressed as the differential

$$\frac{dS}{dR^*_{2(BOLD)}} = -TE \cdot S_0 \cdot H(TE) \cdot \exp\left(-TE \cdot R^*_{2(BOLD)}\right) = -S \cdot TE \cdot \tag{5.2}$$

This curve provides a measure of BOLD sensitivity, which if $H(TE)$ represents a purely exponential decay, is well known to be maximal at TE = T_2*.

For the purpose of sensitivity optimisation, it is useful to consider the relative BOLD *contrast-to-noise* of the different methods under investigation. An expression for the differential CNR (dCNR) follows from Eq. 5.2:

$$dCNR = \frac{S \cdot TE}{\sigma}, \tag{5.3}$$

where σ is the standard deviation of image noise, which for the sake of the following treatment is taken to be white and echo time independent, and the minus sign of Eq. 5.2 is neglected for simplicity. If multiple echoes are acquired, several strategies can be used to obtain a composite image. The computationally cheapest is simple echo summation, which results in a relative BOLD CNR given by

$$dCNR_{summation} = \frac{\sum_{n=1}^{N} TE_n \cdot S_n}{\sqrt{N} \cdot \sigma}, \tag{5.4}$$

where N is the total number of echoes acquired at the different echo times TE_n, and S_n is the intensity at the n^{th} echo.

The treatment by Posse et al. (Posse et al. 1999) has shown that for exponential decay the maximum CNR for simple summation is reached at a total sampling time of

$$T = 3.2 \cdot T_2{}^*, \tag{5.5}$$

after which CNR will decrease again. While simple echo summation may result in gains for all T_2*, Eq. 5.5 cannot generally be satisfied due to the range of T_2* values across the brain, and the overall sensitivity increase is hence not optimal.

Higher gains can be achieved by a weighted echo summation. One approach is to weight the echoes by their relative expected BOLD contrast contribution, which in principle is equivalent to weighting the ideal contrast curve by itself. This approach relies on the assumption of a mono-exponential signal decay for each voxel, as the pixel T_2* needs to be determined by exponential fitting to the multi-echo data (Posse et al. 2003). The normalised summation weights are then given by

$$w(T_2{}^*)_n = \frac{TE_n \cdot \exp(-TE_n / T^*_{2(fit)})}{\sum_n TE_n \cdot \exp(-TE_n / T^*_{2(fit)})} . \qquad [5.6]$$

The dCNR achievable by combining N echoes is thus

$$dCNR_{T_2^*-weighted} = \frac{\sum_{n=1}^{N} w(T_2^*)_n TE_n \cdot S_n}{\sigma \sqrt{\sum_{n=1}^{N} w(T_2^*)_n^2}} . \qquad [5.7]$$

Equations 5.4 and 5.7 are valid for the general case where each of the multiple echoes is acquired with the same echo train length as the single-echo measurement represented by Eq. 5.3. If the effective acquisition window in the ME acquisitions is different, e.g. as here due to the use of parallel imaging, the right hand side of Eqs. 5.4 and 5.7 must be corrected by division by $g \cdot \sqrt{a}$, where a is the acceleration factor, and g a factor that describes any additional coil-dependent losses arising from a (SENSE) parallel reconstruction (Pruessmann et al. 1999).

An alternative strategy is to weight the echoes by their *measured* relative temporal CNR. From Eq. 5.3 it follows that without loss of generality, this can simply be calculated from the temporal SNR measured at each TE:

$$dCNR_n = SNR_n \cdot TE_n . \qquad [5.8]$$

The relative weights are thus obtained by calculation of the SNR over a few resting state volumes (100 in this study) and multiplication of the result by the corresponding TE:

$$w(CNR)_n = \frac{SNR_n \cdot TE_n}{\sum_n SNR_n \cdot TE_n} . \qquad [5.9]$$

The attraction of this latter method is that it makes no intrinsic assumptions about the signal and the nature of the noise, as both are measured directly from the data. Note that this approach is equivalent to T_2*-weighting, if (a) noise is white and echo-time independent, (b) signal decay is purely mono-exponential and therefore (c) T_2* can be quantified accurately. None of these conditions are necessarily fulfilled: through-plane dephasing may contribute dominantly to the signal decay, and physiological contributions to noise have been shown to exhibit an echo time dependence (Kruger and Glover 2001). It is therefore reasonable to expect that CNR-weighting results in more optimal BOLD contrast enhancement than the other methods.

CNR analysis

Measured contrast-to-noise can be also be used as the basis for estimating the relative functional sensitivities of different protocols and weighting strategies. For a single-echo measurement, CNR is determined using Eq. 5.8: Mean contrast is the product of pixel-wise temporal SNR measured in the time series, and echo time. For multi-echo measurements, the mean contrast of the combined echoes is calculated by applying a weighted summation to the individual echo mean contrasts as desired; the noise is calculated as the standard deviation of the signal time series that results from applying exactly the same weights to the multi-echo series at each time point.

The results from different weighting schemes can thus be directly compared against each other, or a conventional single echo method, to obtain a measure of relative sensitivity. As SNR measures are ‘self-normalising’ the result does not depend on local or global differences in image intensity scaling. The approach does, however, require that physiological effects are comparable across different scans, which appears reasonable for the relatively long resting state scan time.

The main advantage is that a functional experiment is not required to quantify the relative performance of different acquisition schemes. Relatively robust and reproducible activation can be induced in some brain regions (e.g. motor, visual, auditory), but even here the inter-scan variation can be substantial. Furthermore, brain areas that are typically more difficult to image are often related to higher cognitive functions and subsequently even more prone to strong inter-subject and inter-session variability. Circumventing the difficulties with functional paradigms is particularly useful where inferior brain regions are of interest.

The method can also be used to compare acquisitions with different TEs or flip angles, different image reconstruction methods, different coil selections, different pulse sequences or any arbitrary combinations of the above. The only requirements are that the underlying contrast mechanism is the same (e.g. T_2* or T_2 decay), head position does not change significantly and that for the measurements to be comparable, the shim has to remain constant so as not to affect the decay behaviour.

For each subject, SNR along the pixel time course was calculated from the resting state data at each echo time and for all acquisition protocols. Thirteen corresponding regions of interest were manually selected in each subject and relative BOLD CNR with respect to the conventional scan was calculated for simple summation, T_2*-weighting and CNR-weighting. Figure 5.1 shows the ROIs overlaid on short-TE images acquired with $a = 3$. To minimise the effects of differing distortion, average values as a function of a relatively large ROI were compared. For each ROI, CNR and T_2* based weighting coefficients were plotted together against TE for comparison. This is illustrated in Fig. 5.5 (see Results section) for two pixel sets of different T_2*.

Functional Experiment

A Stroop colour-word interference experiment was used as previously described (Norris et al. 2002; Zysset et al. 2001). This paradigm was chosen because it invokes activations in regions across the whole brain, including inferior regions that are generally difficult to image.

Six subjects (age 23-29 years, all right-handed) gave written consent prior to the experiment which was conducted in compliance with the local regulations. The experiment consisted of three conditions presented in blocks of 30 s, separated by 10 s of baseline. This was repeated six times (total of 18 blocks) with pseudo-random permutation of block order. The order of the six repeats was permuted for different subjects, and the same stimulus set was used for all three acquisition protocols. 60 s of baseline were recorded at the beginning and end of each scan. The scan order of the three methods was balanced between subjects to minimise habituation effects. Further details of the functional design and the task can be found in Ref (Norris et al. 2002). Stimuli were shown using Presentation (Neurobehavioral Systems, Inc., USA).

T_2*-weighted and individual echo time series were subjected to standard pre-processing and statistical analysis in Brainvoyager 2000 (Brain Innovation, The Netherlands). All datasets were transformed to stereotactic (Talairach) space to allow multi-subject comparisons.

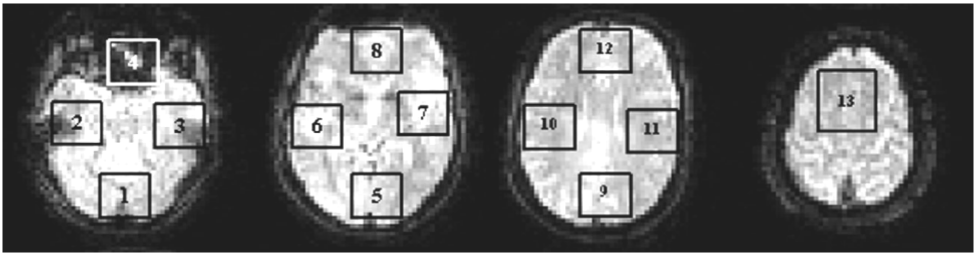

Figure 5.1: *ROIs used in the CNR analysis*

Results

Image quality

Visual inspection shows that the quality of parallel-acquired inhomogeneity desensitised images is markedly superior to conventional images (Fig. 5.2). This conforms to expectations that (a) the shorter echo train length reduces in-plane image distortion, which is proportional to the EPI readout time, and (b) the inclusion of short TE contributions reduces the dropout artefacts. Improvements are most apparent in the comparison of ME-2 and conventional images (readout time reduction by factor 2). The further distortion reduction of factor 1.5 by going from ME-2 to ME-3 is not as apparent (images not shown). These improvements are as expected and in agreement with previous observations for SENSE imaging, e.g. (Preibisch et al. 2003).

CNR analysis

Simulations of the relative BOLD sensitivities for the 6-echo ME-3 protocol and the conventional scan are shown in Fig. 5.2, using Eqs. 5.4 and 5.7 and assuming mono-exponential signal decay. Sensitivities are normalised to the peak sensitivity of the conventional protocol (at $T_2^* = \mathrm{TE}$). For accelerated scans, the theoretical image SNR of single echoes was corrected by factor $1 / \sqrt{a}$ to account for the reduced echo train length, and perfect coil geometry was assumed. The simulations show that the artefact reduction does not result in a sensitivity loss, but rather, that the benefit of multi-TE sampling outweighs the losses associated with accelerated sampling. The minimum expected gain for T_2^*-weighting is approximately 10%, with considerably larger gains expected in regions of shorter and longer T_2^*. Sensitivities predicted for 4-echo ME-2 are very similar and hence not shown.

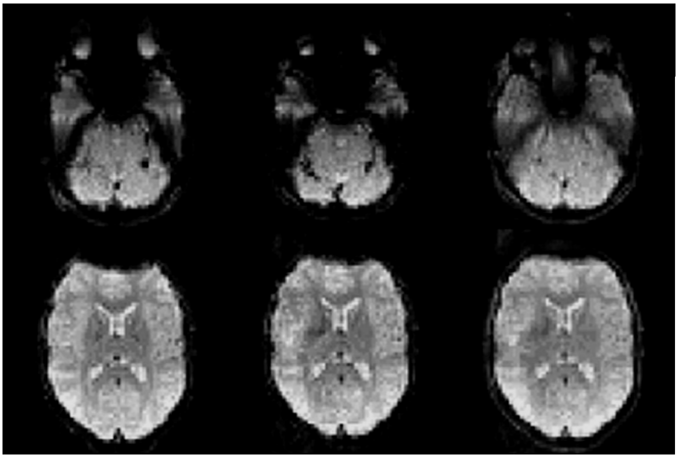

Figure 5.2: *Images acquired at TE=35 ms using the conventional protocol (left) and an acceleration factor of 2 (middle). The image on the right is a T_2^*-weighted ME-2 image. Here, artefacts are strongly reduced by the shortened echo train and inclusion of short-TE signal.*

The results of the differential CNR measurements are shown in Fig. 5.4 and Table 5.1. Values are the ROI averages over all twelve subjects, and are relative to the non-accelerated single-echo scans, for the same coil configuration. The measured relative BOLD sensitivity of parallel-acquired inhomogeneity desensitised acquisitions generally follows the simulations. However, it is slightly lower than simulated for regions of longer fitted T_2* (non-dropout regions), while significantly exceeding predictions in typical dropout regions (ROI 2, 3, 4 and 8, fitted $T_2* < 25$ ms).

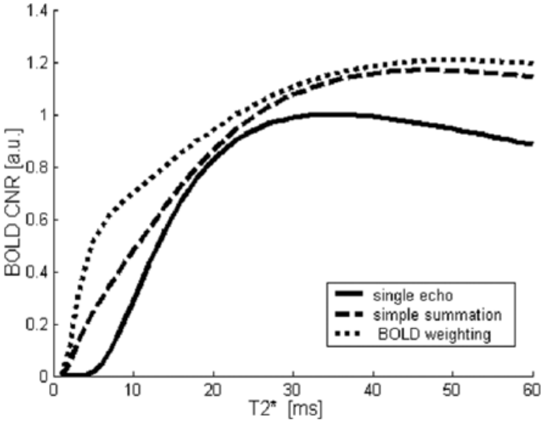

Figure 5.3: *Simulated sensitivity gains for the ME-3 protocol with the six echo times used in this study. The plot shows sensitivity as function of T_2* for the conventional protocol (solid line), simple echo summation (dashed line) and T_2* weighted summation (dotted line). Sensitivities were normalised to the peak sensitivity of the conventional protocol.*

The performance of the two ME protocols is comparable in all regions. For regions not affected by dropout, they result in an average gain of 16% ± 15% (ME-2) and 14% ± 10% (ME-3) even for simple summation. T_2*-weighting yields 20% ± 14% (ME-2) and 19% ± 10% (ME-3). CNR- weighted echo combination performs best with 25% ± 13% (ME-2) and 23% ± 10% (ME-3). In dropout regions, average gains are 67% or higher. Here, the results exceed expectations from the simulation. Overall, the findings meet the prediction of very similar performance of the two ME protocols. Both the T_2*- and CNR-weighting schemes at both acceleration factors show significant sensitivity gains over the conventional protocol in all ROIs ($p < 0.05$, one-sided t-test). CNR based weighting yields the greatest sensitivity. Simple echo summation shows slightly worse performance than T_2*-weighting but for both protocols still results in significant gains in all ROIs ($p < 0.05$, one-sided t-test). The variation between subjects which gives rise to the relatively large average standard deviation stated in Table 5.1 can largely be attributed to the manual selection of ROIs which were hence not exactly the same for all subjects. Furthermore, levels of physiological effects (such as motion) may have been different between runs, thus affecting the gains measured relative to the standard protocol. Also, shim settings might have differently affected transverse relaxation rates across subjects, adding to the error on the calculated relative CNR.

Relative gains are averaged separately over the four regions affected most strongly by distortion and dropout (ROI 2, 3, 4 and 8), and the remaining ROIs. The error shown is the average of the standard deviations on the individual ROIs.

Regions of Interest	weighting strategy	ME-3 protocol with 6 echoes		ME-2 protocol with 4 echoes		ME-3 protocol with 4 echoes	
		mean	± SD	mean	± SD	mean	± SD
Mean over *dropout* regions	summation	**1.83**	**± 0.20**	**1.67**	**± 0.19**	**1.79**	**± 0.28**
	T_2* based	**1.84**	**± 0.22**	**1.69**	**± 0.21**	**1.83**	**± 0.29**
ROI 2, 3, 4 and 8 (mean apparent T_2* = 23 ms)	CNR	**2.04**	**± 0.26**	**1.85**	**± 0.23**	**2.01**	**± 0.32**
Mean over *non-dropout* regions	summation	**1.14**	**± 0.10**	**1.16**	**± 0.15**	**1.03**	**± 0.15**
	T_2* based	**1.19**	**± 0.10**	**1.20**	**± 0.14**	**1.07**	**± 0.14**
Remaining ROIs (mean apparent T_2* = 43 ms)	CNR	**1.23**	**± 0.10**	**1.25**	**± 0.13**	**1.11**	**± 0.15**

Table 5.1: *Relative BOLD sensitivity gains of parallel-acquired inhomogeneity desensitised fMRI over conventional single-echo EPI*

To match the minimum possible TR of the conventional protocol for a fair comparison, calculations were repeated using only 4 of the 6 echoes (ME-3). In non-dropout regions, average gains were 3% ± 15%, 7% ± 14% and 11% ± 15% for simple summation, T_2*- and CNR-weighting, re-spectively. Excluding the later echoes only appreciably affected performance in the superior brain where longer T_2* values can be expected, but typical dropout regions remained unaffected, with gains of 79% ± 28%, 83% ± 29% and 101% ± 32%. TR matching for ME-2 only allowed inclusion of two echoes and was hence not further considered.

The approximate equivalence of CNR- and T_2*-weighting is illustrated in Fig. 5.5. The solid line shows the predicted relative BOLD contrast curve for T_2* = 25 ms and 45 ms; the dotted line represents the mean over measured dCNR in all pixels in one of the subjects for which T_2* values of 25 ms (394 pixels) and 45 ms (1318 pixels) were found by exponential fitting (rounded to nearest integer values). The values are normalised to the maximum of the predicted curve (at TE = T_2*). The small error bars (one standard deviation) suggest that the dCNR measures can be obtained consistently and reliably. However, in both plots the T_2* value as implied by the measured dCNR is slightly greater than the fitted T_2*.

Functional Results

In the evaluation of the functional results, three aspects were considered.
First, on a single-subject basis it was checked that at a given threshold, both simply summed and weighted time series show the same or larger activation areas than

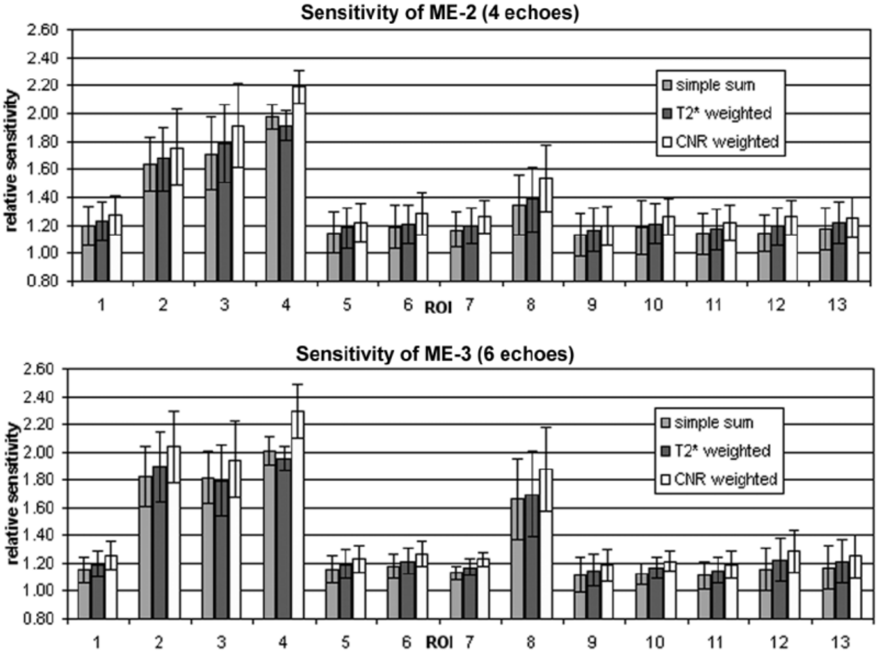

Figure 5.4: *Results of the CNR analysis (12 subjects). The plots show the average sensitivity of the ME protocols relative to the conventional scans, for each echo weighting scheme. Error bars indicate standard deviation.*

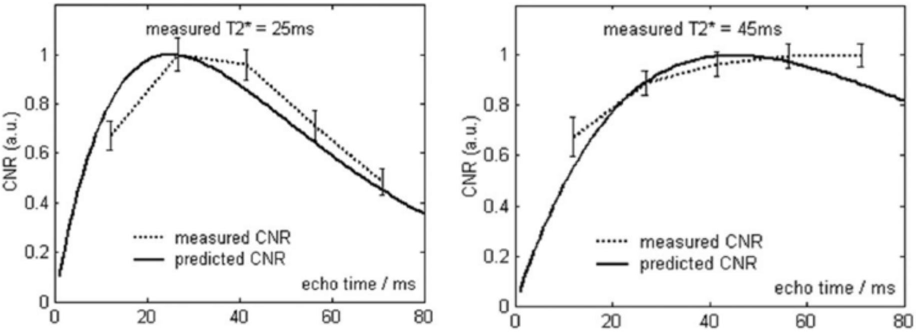

Figure 5.5: *Measured and predicted CNR as function of echo time. The dotted line shows average CNR calculated from all pixels with* $T_2^* = 25$ *ms (top, 394 pixels) and* $T_2^* = 45$ *ms (bottom, 1318 pixels) in one of the functional subjects. The solid line is the expected BOLD contrast curve for the measured* T_2^*.

any of the individual echoes. This also illustrated the expected regional differences in sensitivity at different echo times (not shown).

Second, activation levels were compared for the two weighting strategies in a group analysis. Figure 5.6 shows that in the ‘incongruent vs. neutral’ (most difficult vs. easy) task contrast at the same significance threshold (corrected p <

0.001), significance increased slightly, and as a result some additional clusters of activation became visible. This is particularly true for inferior regions, and can be attributed to the noise-suppressing nature of the weighting filter.

Third, the T_2*-weighted ME-2 and ME-3 time series were compared to the conventionally acquired data. To facilitate comparisons of the different experimental runs, group averages over the six subjects were taken to minimise habituation effects. Although scan order was counterbalanced across subjects, strong residual variation appeared to remain, making it impossible to draw quantitative conclusions from the functional data. However, in several inferior brain regions, activation for some task contrasts could be observed with both ME-2 and ME-3 that could not be observed with the conventional protocol (results not shown). This supports the expectations.

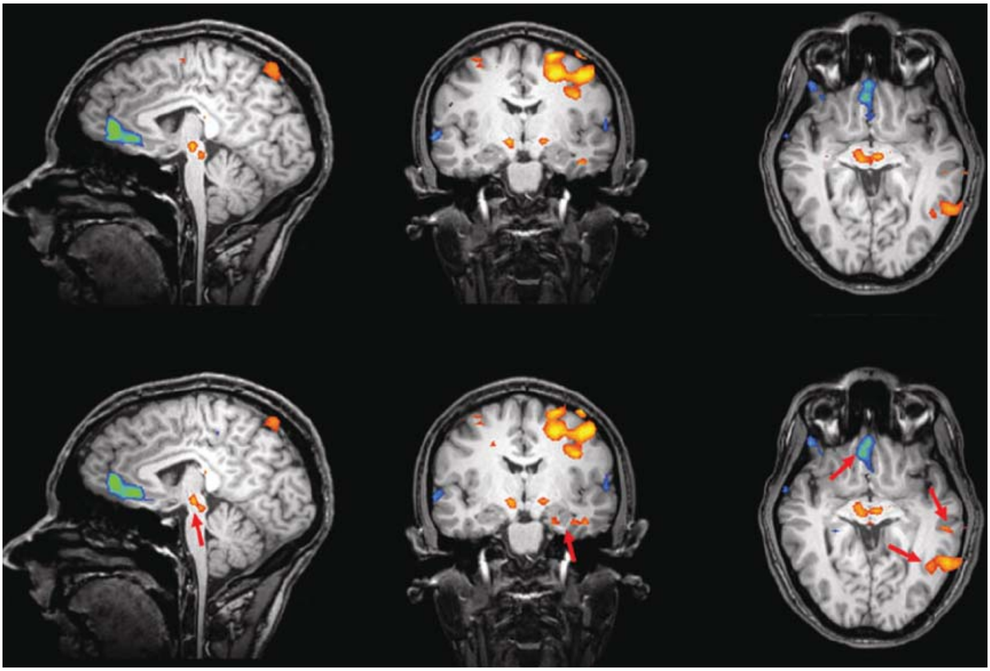

Figure 5.6 *(see Appendix for colour version): Activation maps for simple (top) and T_2* weighted (bottom) echo combination at acceleration factor 3 (5 echoes). 'Incongruent vs. neutral' task contrast over all subjects is shown at p(corr.) < 0.001 (Talairach coordinates -4, -7, -7). Arrows indicate larger and additional activation sites in the T_2* weighted data.*

Discussion

The results show that accelerated ME sampling with optimised echo weighting can be beneficial for functional experiments by reducing distortion and dropout artefacts while improving, or at least maintaining, BOLD contrast sensitivity.

The shortened EPI readout in parallel imaging has a further advantage. With a non-accelerated protocol, studies of inferior brain regions such as the hippocampus are often confined to 1.5 T. A sufficiently short TE necessary to avoid signal dropout would be precluded at higher fields due to the length of the non-accelerated EPI readout. While optimised ME sampling can be used at 1.5 T to acquire additional echoes at some cost in TR, the experiment could also be performed at 3 T, and without the increase in TR. This still reduces distortions compared to a conventional acquisition at the lower field strength, allows capitalizing on the higher CNR at 3 T, and improves the sensitivity in brain regions of longer T_2* which would typically be compromised by use of a single short TE. Preliminary data from an ongoing medial temporal lobe study at 3 T with parallel-acquired inhomogeneity desensitised fMRI suggest the method's suitability for such investigations (Piekema et al. 2005).

The reduced distortion is also expected to allow better co-registration of functional and anatomical data, resulting in greater overlap when multiple subjects are scanned (Cusack et al. 2003). This could significantly improve the outcome of group statistics, particularly in a conservative random effects analysis. In this study, motion was corrected for by extracting the movement parameters from the shortest TE image and applying the same transformations to all echoes of a given shot. Alternative approaches have been suggested that may yield better results (Jonsson et al. 1999; Speck and Hennig 2001), indicating that the full potential of the ME data might not have been exploited.

Using differential contrast, calculated from simple SNR measurements, as a metric for BOLD sensitivity has proven very useful as it alleviates the need for functional stimulation in the assessment of different acquisition schemes. In principle, the approach should make it possible to predict gains and losses in *t*-scores more accurately than model approaches that require quantification of the different noise sources (i.e. physiological, protocol and hardware dependent noise).

Regarding the dCNR calculations it should be noted that this treatment is valid, irrespective of the form of *H(TE)*, and should yield optimal results in all brain regions. This is to be contrasted with the T_2*- weighted approach, where exponential fitting to a *sinc*-modulated decay can give inaccurate results for T_2* in strongly affected ('dropout') brain regions (Chen et al. 2003; Fernandez-Seara and Wehrli 2000). The T_2*-weighting is then based on a hybrid between actual and theoretically expected signal behaviour, potentially resulting in suboptimal sensitivity enhancement. This probably explains the results for ROI 3 and 4 (see Fig. 5.4) where the theoretically better T_2*-weighting performs less well than simple summation.

BOLD contrast sensitivity of accelerated single-echo SENSE EPI (Pruessmann et al. 1999) has previously been studied (de Zwart et al. 2002; Preibisch et al. 2003). In (de Zwart et al. 2002), it is suggested that the relative contributions of intrinsic image and temporal noise determine the overall reduction in temporal stability and hence BOLD sensitivity. The expected relative sensitivity of an accelerated SENSE acquisition can be written as

$$\frac{\sigma_{\text{temp}}^{\text{parallel}}}{\sigma_{\text{temp}}^{\text{conv}}} = \sqrt{1 + \left(g^2 a - 1\right) \cdot \left(\frac{\sigma_{\text{image}}^{\text{conv}}}{\sigma_{\text{temp}}^{\text{conv}}} \right)^2} \quad , \qquad [5.10]$$

where the indices *temp* and *image* denote temporal and intrinsic (white) image noise, and *conv* and *parallel* denote conventional and factor-*a* accelerated acquisition respectively; *g* describes the spatially varying reconstruction noise related to coil geometry.

Equation 5.10 shows that in the presence of signal fluctuations that arise from physiological processes such as pulsation, the effective sensitivity reduction incurred by *a*-fold acceleration will be *smaller* than factor $\sqrt{a}$ as BOLD contrast to *total* temporal noise, here measured as dCNR, determines functional sensitivity. This has been demonstrated in previous functional and resting state studies (de Zwart et al. 2002; Preibisch et al. 2003). Analogously, the effective sensitivity gain from combining multiple echoes will be somewhat *lower* than predicted purely on the basis of image noise. The present results for the non-dropout regions confirm this with sensitivity gains smaller than simulated. In the limit of complete dominance of coherent and TE independent physiological noise, neither the use of parallel imaging nor a multi echo approach can be expected to have an appreciable effect on sensitivity as Eq. 5.10 converges to 1. For small contributions of physiological noise, σ_{temp} approaches σ_{image}. This limit is reached with increasing spatial resolution (smaller voxel volume) and / or decreasing field strength (see e.g. Fig. 5.3 in reference (Triantafyllou et al. 2005)). For a *single* echo measurement, the penalty for using parallel imaging is now largest as Eq. 5.10 converges to a loss factor of $g \cdot \sqrt{a}$. The benefits of acquiring *multiple* echoes, however, are maximised in this regime, resulting in an overall *increase* in sensitivity. An optimised ME measurement can combine this with the advantages of sampling at different TEs and reduced image artefacts.

With the acquisition parameters used, the TR for the conventional and a 4-echo version of the ME-3 protocol could have been shortened to 1.75 s. As a result of T_1 effects, the image SNR would then approximately be reduced by a factor 1.11 (assuming grey matter $T_1 = 1250$ ms and use of the respective Ernst angles), thereby reducing the relative contribution of physiological noise; thus, the relative sensitivity gain of a realistic 4-echo ME-3 scan would have been larger than calculated from the data that was acquired with the artificially long TR of 2.5 s.

The *g*-dependence of Eq. 5.10 implies that the relative sensitivity gain of accelerated ME sampling would exhibit a spatial variation that depends on the coil geometry and acceleration factor. We could not identify a strong spatial variation in the non-dropout regions; however, this might be attributable to the relatively strong inter-subject variation, or indeed suggest that for the imaging parameters used in this study physiological noise is still an important contributor. For coil

geometries different from a circularly symmetric one used as here, the *g*-dependence of the sensitivities is likely to be stronger, particularly if the acceleration factor is approaching the number of receive channels.
ME acquisitions as used in this study should allow the quantitative separation of the two noise sources, and the investigation of how the use of parallel imaging reconstruction affects the total noise level, for different relative noise contributions.

Both researchers and manufacturers are continuously striving to further improve the quality of parallel reconstruction algorithms and the design of coils with quickly growing numbers of channels (Wiggins et al. 2005). It can be expected that parallel imaging will play an increasingly important role in fMRI, particularly at high fields. The results presented here suggest that combining reduced sampling with multi-echo acquisition can lead not only to reduced image artefacts, but also to substantial gains in BOLD contrast sensitivity. As the method is straightforward to implement on the scanner software, suitable for-operator independent use, and the resulting image data requires no special treatment, parallel-acquired inhomogeneity desensitised fMRI as described in this paper may well become the method of choice for many routine applications in functional imaging.

Acknowledgements
The work presented in this paper has been supported by STW grant NGT.6154. The authors would like to thank Markus Barth for useful discussions and helpful comments during the preparation of the manuscript.

References

Chen NK, Egorova S, Guttmann CR, Panych LP. (2003) Functional MRI with variable echo time acquisition. *Neuroimage* 20:2062-2070

Cusack R, Brett M, Osswald K. (2003) An Evaluation of the Use of Magnetic Field Maps to Undistort Echo-Planar Images. *NeuroImage* 18:127-142

de Zwart JA, van Gelderen P, Kellman P, Duyn JH. (2002) Application of sensitivity-encoded echo-planar imaging for blood oxygen level-dependent functional brain imaging. *Magn Reson Med* 48:1011-1020

Fernandez-Seara MA, Wehrli FW. (2000) Postprocessing technique to correct for background gradients in image-based R*(2) measurements. *Magn Reson Med* 44:358-366

Glover GH, Law CS. (2001) Spiral-in/out BOLD fMRI for increased SNR and reduced susceptibility artefacts. *Magn Reson Med* 46:515-522

Griswold MA, Jakob PM, Heidemann RM, Nittka M, Jellus V, Wang J, Kiefer B, Haase A. (2002) Generalized autocalibrating partially parallel acquisitions (GRAPPA). *Magn Reson Med* 47:1202-1210

Hagberg GE, Indovina I, Sanes JN, Posse S. (2002) Real-time quantification of T(2)(*) changes using multiecho planar imaging and numerical methods. *Magn Reson Med* 48:877-882

Jonsson T, Wennerberg AB, Forssberg H, Glover GH, Li TQ. (1999) An image registration strategy for multi-echo fMRI. *J Magn Reson Imaging* 10:154-158

Kruger G, Glover GH. (2001) Physiological noise in oxygenation-sensitive magnetic resonance imaging. *Magn Reson Med* 46:631-637

Mansfield P. (1977) Multi-Planar Image-Formation Using Nmr Spin Echoes. *Journal of Physics C-Solid State Physics* 10:L55-L58

Norris DG, Zysset S, Mildner T, Wiggins CJ. (2002) An investigation of the value of spin-echo-based fMRI using a Stroop color-word matching task and EPI at 3 T. *Neuroimage* 15:719-726

Ogawa S, Lee TM, Kay AR, Tank DW. (1990) Brain magnetic resonance imaging with contrast dependent on blood oxygenation. *Proc Natl Acad Sci U S A* 87:9868-9872

Piekema C, Poser BA, Fernandez G, Norris DG. MTL study with Multi-Echo PAID fMRI at 3T, abstract #610, Proceedings to HBM Toronto 2005

Posse S, Shen Z, Kiselev V, Kemna LJ. (2003) Single-shot T(2)* mapping with 3D compensation of local susceptibility gradients in multiple regions. *Neuroimage* 18:390-400

Posse S, Wiese S, Gembris D, Mathiak K, Kessler C, Grosse-Ruyken ML, Elghahwagi B, Richards T, Dager SR, Kiselev VG. (1999) Enhancement of BOLD-contrast sensitivity by single-shot multi-echo functional MR imaging. *Magn Reson Med* 42:87-97

Preibisch C, Pilatus U, Bunke J, Hoogenraad F, Zanella F, Lanfermann H. (2003) Functional MRI using sensitivity-encoded echo planar imaging (SENSE-EPI). *Neuroimage* 19:412-421

Pruessmann KP, Weiger M, Scheidegger MB, Boesiger P. (1999) SENSE: sensitivity encoding for fast MRI. *Magn Reson Med* 42:952-962

Sodickson DK, Manning WJ. (1997) Simultaneous acquisition of spatial harmonics (SMASH): Fast imaging with radiofrequency coil arrays. *Magnetic Resonance in Medicine* 38:591-603

Speck O, Hennig J. (1998) Functional imaging by I0- and T2*-parameter mapping using multi-image EPI. *Magn Reson Med* 40:243-248

Speck O, Hennig J. (2001) Motion correction of parametric fMRI data from multi-slice single-shot multi-echo acquisitions. *Magn Reson Med* 46:1023-1027

Triantafyllou C, Hoge RD, Krueger G, Wiggins CJ, Potthast A, Wiggins GC, Wald LL. (2005) Comparison of physiological noise at 1.5 T, 3 T and 7 T and optimization of fMRI acquisition parameters. *Neuroimage* 26:243-250

Weiskopf N, Klose U, Birbaumer N, Mathiak K. (2005) Single-shot compensation of image distortions and BOLD contrast optimization using multi-echo EPI for real-time fMRI. *Neuroimage* 24:1068-1079

Wiggins G, Potthast A, Triantafyllou C, Lin F, Benner T, Wiggins C, Wald L. A 96-channel MRI-system with 23- and 90-channel phase array head coils at 1.5T, abstract #671, Proceedings to ISMRM Miami 2005

Yablonskiy DA, Haacke EM. (1994) Theory of NMR signal behavior in magnetically inhomogeneous tissues: the static dephasing regime. *Magn Reson Med* 32:749-763

Yang QX, Dardzinski BJ, Li S, Eslinger PJ, Smith MB. (1997) Multi-gradient echo with susceptibility inhomogeneity compensation (MGESIC): demonstration of fMRI in the olfactory cortex at 3.0 T. *Magn Reson Med* 37:331-335

Zysset S, Muller K, Lohmann G, von Cramon DY. (2001) Color-word matching stroop task: separating interference and response conflict. *Neuroimage* 13:29-36

Chapter 6 Investigating the benefits of multi-echo EPI at 7 T

Abstract

Functional MRI studies on humans with BOLD contrast are increasingly performed at high static magnetic field in order to exploit the increased sensitivity. The downside of high-field fMRI using the gradient-echo echo-planar imaging (GE-EPI) method is that images are typically very strongly affected by image distortion and signal loss. It has been demonstrated at 1.5 T and 3 T that image artefacts can be reduced and functional sensitivity simultaneously increased by the use of parallel-accelerated multi-echo EPI. Using sensitivity measurements and an activation study with a cognitive Stroop task experiment (N = 7) we here investigate the potential of this method at 7 T. The main findings are: (a) image quality compared to a conventional acquisition scheme is drastically improved; (b) according to CNR estimations the average BOLD sensitivity increases by 6.1 ± 4.3% and 13.9 ± 5.5% for unweighted and CNR-weighted echo summation, respectively; (c) both functional signal changes and sensitivity in the multi-echo data do not exhibit a pronounced dependence on TE. The consequence is that (d) in practice the performance of simple echo summation at very high field is comparable to that based on a CNR filter. Finally, (e) temporal noise observed in the different echo time courses is not strongly correlated, thus explaining why echo summation is advantageous.

The results at typical spatial resolution show that multi-echo EPI acquisition leads to considerable artefact reduction and sensitivity gains, making it superior to conventional GE-EPI for fMRI at 7 T.

Poser BA, Norris DG. Neuroimage 45(4):1162-72; 2009

Introduction

In recent years MRI systems with field strengths of 3 T and above have increased in popularity, and a growing number of human research systems with 7 T and higher has been installed. Despite the numerous technical challenges associated with high magnetic field (Ladd 2007) the attraction lies in the significantly increased signal-to-noise ratio (SNR) that can be obtained and translated into higher spatial resolution or reduced measurement time. In addition to the approximately linear increase of SNR with field strength, the blood oxygenation level dependent (BOLD) effect used in functional MRI (fMRI) shows a well-above linear increase (Yacoub et al. 2001).

In a typical fMRI protocol using echo planar imaging (EPI), a 2D image is acquired following a single slice selective excitation pulse, which allows the entire brain to be imaged in about 2.5 s at an isotropic resolution of 3 – 4 mm or better. It has been shown in studies at 1.5 T and 3 T that this sampling strategy can be modified such that following each RF excitation *multiple* images are acquired in rapid succession (Gowland and Bowtell 2007; Poser et al. 2006; Speck and Hennig 1998; Weiskopf et al. 2005). The rationale behind this approach is that the optimal echo time (TE) for maximum functional contrast is generally taken to be TE = T_2*, assuming a single compartment with a mono-exponential decay and a small change in T_2* resulting from activation. However, T_2* is known to vary considerably across the brain (Hagberg et al. 2002; Peters et al. 2007). At 1.5 T this has also led to the proposal of a (single echo) EPI sampling scheme by which slices in superior brain regions are acquired at longer TE than in inferior brain regions (Stocker et al. 2006), where the T_2* is typically shorter and the effect of susceptibility artefacts greater. Strong susceptibility gradients acting perpendicular to a slice with a square profile may cause a TE-dependent *sinc* modulation of the otherwise exponentially decaying signal, and thereby an even shorter ‘apparent’ T_2*. Signal decay that is always exponential (albeit faster) can be enforced by the use of an exponential slice profile (Preibisch et al. 2008). In the more ideal case where images of each slice are acquired at multiple TE they can be submitted to a (weighted) summation so as to optimise the functional contrast in each brain region, for instance by using a global estimate of T_2* (Posse et al. 1999; Weiskopf et al. 2005), a local estimate (T_2* maps), or a measure of voxelwise contrast-to-noise (Poser et al. 2006).

In previous work at 3 T we demonstrated that employment of parallel imaging to shorten the EPI readout and to acquire several GE echo planar images, with subsequent weighted echo summation results in an increase in functional sensitivity in all brain regions. The multi-TE acquisition and larger effective sampling window than in single echo EPI clearly outweighed the signal-to-noise (SNR) reduction incurred by the coil-geometry related loss factor inherent to parallel imaging reconstruction. Depending on the choice of TE and other imaging parameters, an accelerated readout in EPI almost always creates a ‘dead time’ after the excitation pulse, which can be utilised for the acquisition of additional images at different TE in a single-shot multi-echo fashion, and without necessarily having to increase TR.

The main drawback of the EPI method is its sensitivity to magnetic field inhomogeneities. This causes susceptibility artefacts in the form of signal voids and geometric distortions. Signal voids result from 'through-plane' spin dephasing due to inhomogeneity gradients across the imaging slice, leading to irreversible, TE- and slice thickness dependent, signal loss in GE (but not SE) EPI. Image distortions up to several pixels are often observed along the phase encoding direction. These distortions increase linearly with both field strength, and the duration of the EPI readout train and hence tend to become especially problematic at higher field. Even at 3 T they are often severe enough so as to compromise a faithful coregistration of functional and anatomical data sets (Cusack et al. 2003). Hence the additional major benefit of using a short (parallel-accelerated) EPI readout for individual echoes is the corresponding reduction of image distortion.
The continued drive towards higher field strengths has thus increased the need for accelerated acquisition schemes that result in a low degree of distortion, or additionally post-hoc distortion correction methods (Chang and Fitzpatrick 1992; Chen and Wyrwicz 1999; Jezzard and Balaban 1995; Zaitsev et al. 2004; Zeng and Constable 2002). While new variants of retrospective correction schemes are frequently proposed in the literature, the neuroscience community remains wary of using them as they all rely on some form of previously acquired reference data which may have been invalidated by subject motion during the timecourse of the experiment (Hutton et al. 2002). Parallel imaging on the other hand is already applied routinely in functional studies, in order to reduce sampling time, gradient acoustic noise (de Zwart et al. 2002b) or more importantly for fMRI, image distortions (de Zwart et al. 2002a; Preibisch et al. 2003). In addition to the effect of the reduced effective acquisition bandwidth, the reconstruction procedure of parallel undersampled data generally results in spatially varying '*g*' noise that is related to the geometry of the coil array and the acceleration factor, whereby the exact spatial distribution of the noise depends most strongly on the acceleration factor and the chosen reconstruction algorithm, e.g. image based SENSE (Pruessmann et al. 1999), or k-space based GRAPPA (Griswold et al. 2002). However, as temporal fluctuations of physiological origin typically dominate fMRI time series especially at high field, the effective loss in BOLD sensitivity when using moderate parallel acceleration is rather small (de Zwart et al. 2002a; Preibisch et al. 2003).

For BOLD signal changes that originate from T_2* changes in the grey matter compartment, the expected relative contrast-to-noise (CNR) gain of multi-echo acquisitions is greater, and more obvious, at lower field strengths. Here, the conventional single echo would be sampled at a later TE due to the longer grey matter T_2*, thereby leaving more time for the acquisition of additional earlier echoes. Furthermore, a longer T_2* implies a broader spread of T_2* values in absolute terms, and thus a broader sensitivity curve. This in turn results in a

functional CNR that is less dependent on the exact choice of TE, thereby making the sampling of additional echoes, particularly at longer TE, more beneficial.
Considering the short T_2 of blood at 7 T, approximately 7 ms (Yacoub et al. 2001), it is conceivable that intravascular BOLD contributions will be detectable at corresponding very short TE-values where the physiological noise in T_2* is small. In addition, a CSF contribution to functional signal changes has been reported both qualitatively (Metzler et al. 1998; Song et al. 1996) and quantitatively (Hoogenraad et al. 2001). This is attributed to extravascular static dephasing in the CSF, resulting in a BOLD signal contribution from the CSF compartment. Since the T_2 of CSF is very long this may lead to additional functional signal changes being detectable at longer TE. Both contributions would also effectively broaden the BOLD sensitivity range at 7 T, conceivably making multi-echo acquisitions more beneficial than would be predicted on the basis of a grey matter T_2* model alone.

The most appropriate choice of spatial resolution for fMRI would appear to be the one where the dimensions of the imaging voxels match the spatial point spread function (PSF) of the BOLD response. At 3 T the BOLD PSF for GE-EPI was measured to be 3.9 ± 0.7 mm in human visual cortex (Parkes et al. 2005), and more recently, values were reported for 7 T with 2.34 ± 0.20 mm (Shmuel et al. 2007). Only marginal additional information can be expected from an image resolution that is higher than the physiological limits set by the BOLD response. Moreover, a higher resolution requires more imaging slices (hence longer measurement time for each volume) and longer EPI readouts (resulting in greater distortion). Clearly, shorter readouts are more suited for multi-echo acquisition.
A contradictory argument for the use of smaller voxel sizes is based on the consideration of physiological contributions to total temporal noise. The ratio of physiological to ‘white’ and reconstruction-related image noise increases with voxel volume and field strength, and it has been suggested that for acquisition at a *single* echo time the voxel volume should be chosen such that the two contributions are approximately equal (Bodurka et al. 2007). At what resolution this conditions is achieved, and whether this is practicable at high field, depends on imaging parameters such as TR, readout bandwidth, use of parallel undersampling, but also on the choice of TE: the ‘non-BOLD like’ physiological noise contribution is proportional to S(TE), while ‘BOLD-like’ physiological noise has a TE dependence as it is induced by small changes in T_2* (Kruger and Glover 2001).
In the absence of bulk motion and spin-history effects which manifest themselves in S_0 signal fluctuations, the dominant source of physiological noise is temporal fluctuations in the T_2* of grey matter. Since this accounts for approximately 80% of the voxel volume in the parenchyma, the consequence at 3 T is an overall ‘BOLD-like’ and hence bell-shaped echo time dependence of physiological noise (Kruger and Glover 2001). Therefore, the BOLD functional sensitivity becomes less echo time dependent on TE especially at longer TE. This has been observed in previous studies at 3 T (Gorno-Tempini et al. 2002; Lehericy et al. 2006), and

recently been simulated and expressed more formally (Van de Moortele et al. 2008).

For multi-echo experiments the following important considerations apply to the three types of noise: First, 'white' image and reconstruction related noise are fully independent of TE (uncorrelated and of equal magnitude), thus echo summation will clearly reduce this source of variance, and maximal relative benefits be obtained in the domain where this noise dominates. Second, non-BOLD physiological fluctuations in S_0 scale with the exponential form of S(TE) and thus affect the signal at different TE in the same coherent way; hence any kind of echo combination will not serve to reduce this source of variance. Third: does the BOLD-like portion constitute the dominant contribution to physiological noise, and if so, to what degree does it correlate between the different echo times? These are the crucial questions with regard to the effectiveness of the combination of single-shot multi-echo data for BOLD contrast enhancement in the domain of dominant physiological noise. The lower the correlation, the more effective echo summation will be in reducing unwanted variance. Furthermore, this will also have implications for the ideal echo weighting strategy.

It is the purpose of this study to investigate the value of combining parallel-acceleration with multi-echo sampling at 7 T. From a user perspective, any protocol that offers substantial artefact reductions without loss in functional sensitivity will be very beneficial for routine application in neuroimaging, and even more so if sensitivity is increased at the same time.

The multi-echo approach is compared to a conventional acquisition scheme using a previously described method based on the differential functional CNR measured in the resting state (Poser et al. 2006), and an activation study with a colour-word interference Stroop task experiment. In the functional experiment, two echo combination schemes ('simple' and 'CNR-weighted summation') are investigated at the group level, as is the echo time dependence of functional sensitivity. A more detailed ROI based analysis of BOLD signal changes and noise levels is performed on three functional data sets.

Materials and Methods

MRI protocols

All experiments were performed on a Siemens Magnetom 7 T scanner (Siemens, Erlangen, Germany) using an 8-channel RX/TX head coil (all channels combined in transmit mode; RAPID Biomedical, Rimpar, Germany). Seven healthy volunteers (three female, mean age 26 ± 3 years, all right-handed) with normal or corrected-to-normal vision were scanned in compliance with the regulations of the local ethics committee.

For the functional experiments (see below) two acquisition protocols were used, with the following common parameters: matrix size 88 x 88 in-plane resolution 2.5 mm (224 mm FoV), 36 slices with 2 mm thickness and 0.3 mm gap, bandwidth

2470 Hz per pixel, repetition time TR 2.5 s. The in-plane spatial resolution was chosen to approximately match the BOLD PSF reported for 7 T (Shmuel et al. 2007); a slice thickness of 2 mm was used as an acceptable compromise between signal loss due to through-plane dephasing and the otherwise much longer TR for an increased number of slices. Transversal slices were positioned with a tilt angle of approximately 10 – 20 degrees, which has been shown to be relatively less sensitive to signal voids (Speck et al. 2008). The conventional scan was acquired at echo time TE = 25 ms which approximately corresponds to the predominant grey matter T_2* at 7 T; this required the use of 7/8 partial-Fourier acquisition. The multi-echo scan comprised acquisition of four echoes starting with the shortest possible TE: using GRAPPA parallel imaging (Griswold et al. 2002) with an acceleration factor 3 (61 reference lines for weight set calculation acquired at start of scan) this gives a TE-increment of 13 ms and hence the echo times 9, 22, 35 and 48 ms. In both protocols fat saturation was disabled due to SAR restrictions, with the positive consequence of reduced TR (13 ms less per slice) and slightly increased (BOLD) signal due to the absence of magnetisation transfer effects(Speck et al. 2008; Zhang et al. 1997). The excitation pulse angle was chosen as close to the Ernst angle as permitted by the SAR monitor ($54° < \alpha < 65°$, depending on subject weight and transmitter adjustment).

For anatomical reference, a T_1 weighted scan was performed using the MP-RAGE sequence (1 mm isotropic resolution, 176 slices, TI 1.1s, TR 2.5 s, TE 1.1ms, $\alpha = 5$ °, GRAPPA with acceleration factor 2 and 50 ‘inplace’ reference lines).

Prior to the experiments, simulations were performed to ensure that the ME protocol could be expected to yield at last equal sensitivity compared to the conventional EPI protocol for the entire range of typical T_2* values, assuming the typical TE dependence of signal changes $dS \sim TE \cdot \exp(-TE / T_2^*)$. For the predominant grey matter T_2* of 25 ms, simple summation should thus yield a sensitivity gain of 4.3%, while weighted summation according to the theoretical BOLD contribution of each echo with the weights $w_n \sim TE_n \cdot \exp(-TE_n / T_2^*)$ should yield a gain of 5.4%, relative to the single conventional echo and under the assumption of TE independent, uncorrelated Gaussian noise and pure T_2* based BOLD contrast. The effective differences in sampling time due to partial Fourier and parallel undersampling, respectively, were accounted for. For T_2*-values around 25 ms, the difference between simple and weighted summation is hence predicted to be rather small, but weighting is expected to become increasingly beneficial for very short and very long T_2*. The simulations thus indicate that in all brain regions an at least equal sensitivity should be obtained by the multi-echo protocol.

Echo weighting

Multi-echo fMRI data can be processed and analysed in a number of different ways. First, a standard statistical analysis can be performed on the individual echo time courses, with subsequent generation of a single activation map by use of an ‘OR filter’ to select the maximum statistical score for each voxel (Posse et al.

1999). However, this would not in general yield an overall CNR gain and thus suboptimal results, is more laborious and generates large amounts of image data.

CNR benefits are generally achieved by echo combination prior to statistical processing. Simple summation will result in CNR gains when combining echoes acquired up to an echo time TE = 3.2 · T_2* (Posse et al. 1999), but more optimal BOLD sensitivity can be obtained by a weighted combination. If for simplicity overall random Gaussian noise that equally affects all echo times is assumed, then the ideal weighting should follow the relative BOLD contrast curve expected from each voxel's T_2*. The normalised voxelwise weights would thus be

$$w(T_2^*)_n = \frac{TE_n \cdot \exp(-TE_n / T_2^*)}{\sum TE_n \cdot \exp(-TE_n / T_2^*)} . \qquad [6.1]$$

Note that this scheme assumes a mono-exponential decay, and a corresponding T_2* that can be obtained reliably for each voxel. In case of strong through-plane inhomogeneities, the signal decay is not necessarily exponential and depending on the slice profile may be modulated by e.g. a *sinc* function which can then result in under-estimation of T_2*.

A simplified version of this might assume a 'representative' T_2* for the entire brain (Weiskopf et al. 2005). A superior method that does not require T_2* maps and that takes into account temporal noise that is actually present in the data, is the previously described CNR weighting approach (Poser et al. 2006). Here, the images acquired at $\mathrm{TE_n}$ are weighted according to

$$w(CNR)_n = \frac{SNR_n \cdot TE_n}{\sum SNR_n \cdot TE_n} . \qquad [6.2]$$

The voxelwise temporal SNR_n is determined from a period of 'rest' at the beginning of the scan.

Note that the CNR weighting makes no assumption about the TE dependence of noise, as it simply works on the basis of fluctuations actually present in the data, but irrespective of their origin and correlation (e.g. white noise, S_0 noise, BOLD-like or non-BOLD like noise). This is in marked contrast to T_2* weighting which assumes a flat distribution of noise that equally affects all TEs, which is unlikely to be true in practice (Kruger and Glover 2001; Van de Moortele et al. 2008).

Estimation of BOLD CNR from resting state data

Based on arguments and assumptions from the previous section, the CNR of the different weighting schemes relative to a single echo measurement can be obtained directly from baseline ('resting state') data. Three different methods were used to look at the resting state data: 'simple summation' (by adding up the echo images with equal weights), 'T_2*-weighted summation' (according to Eq. 6.1), and 'CNR-weighted summation' (according to Eq. 6.2).For each of the seven subjects, the relative BOLD sensitivity of simple, T_2* weighted and CNR weighted summation was calculated for 13 manually drawn regions of interest (Fig. 6.1). For T_2* weighting, T_2* maps were estimated directly from the ME data, with ten time points averaged, using a mono-exponential fitting routine in Matlab (The MathWorks, Inc., Natick, MA, USA).

To assess the temporal noise introduced by the use of parallel acceleration, the average pixelwise percentage noise was calculated from the non-accelerated data and the second echo of the ME scan for each subject, considering all pixels within a brain mask (pixel intensity > 200; assuming a negligible effect due to the small TE difference). Furthermore, the 'within-image' SNR was obtained from the tenth volume of all datasets, using identical ROIs over four slices in occipital cortex (843 pixels) as signal ROIs, and ROIs in the corners of the corresponding slices as noise ROIs.

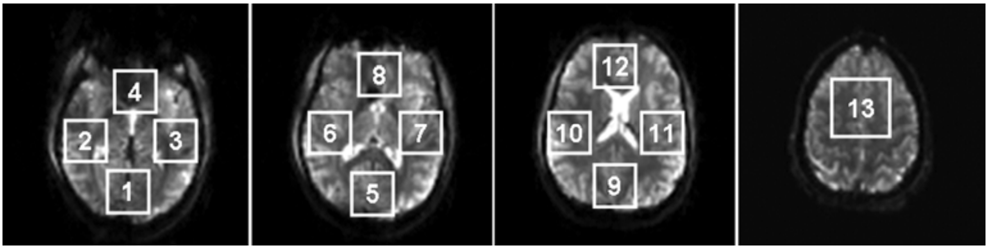

Figure 6.1: *Regions of interest considered in the calculation of the relative BOLD CNR of the multi-echo vs. single echo protocol.*

Activation study

A Stroop colour-word interference task was used for the activation study (Zysset et al. 2001). The Stroop paradigm was chosen because it is known to robustly invoke well-described activations in various regions across the entire brain, as well as 'deactivations' in parts of the default mode network. This makes the experiment very suitable for evaluation and comparison of different protocols, and as such the focus is here on sensitivity (*t*-score and cluster size). The experiment consisted of three different task conditions ('neutral', 'congruent', 'incongruent') which were intermixed in order to maintain the subjects' attention. Task conditions were presented in blocks of 30 s, separated by 10 s of baseline (30 s baseline after every third block). These were repeated six times (total of 18 blocks). 60 s of baseline were recorded at the beginning and the last baseline block was omitted, resulting in a total experiment time of 14' 30" per run (preceded by proximately 20 s for preparation scans and reference line acquisition. To avoid habituation effects, subjects were trained for approximately five minutes immediately before entering the scanner, and scan order of the conventional and ME measurement protocols was alternated between subjects. Further details of the functional design and the task can be found in (Zysset et al. 2001). Stimuli were shown using Presentation software (Neurobehavioral Systems, Inc., USA). Subjects responded by button presses which were recorded and used to verify that subjects were performing the task.

The functional multi-echo data were combined in two ways, by ‘simple summation’, and by ‘CNR-weighted summation’ (according to Eq. 6.2), which was previously found to be the optimal approach at 3 T. Both weighted and single TE series were subjected to standard preprocessing and statistical analysis in Brainvoyager QX (Brain Innovation, The Netherlands); this included motion correction, linear trend removal and high-pass filtering. All data sets were then coregistered with the corresponding T_1 weighted image, transformed to stereotactic Talairach space and spatially smoothed with a 6 mm isotropic Gaussian kernel for the group analysis. For statistical analysis a standard GLM was used.

To investigate in detail the TE dependence of functional signal changes and noise, and the effect of the different echo weighting methods, activation maps were computed at each TE from unsmoothed data of three subjects. Temporal noise and signal-to-noise measures where obtained, and the correlation coefficients calculated for the correlation between the different echo time courses.

Results

EPI images acquired with the two EPI protocols are shown in Fig. 6.2, using simple summation for the multi-echo data. Distortion is considerably reduced in the ME scan due to the shortened EPI readout, as expected. Furthermore, the signal dropout is much lower as a result of including the signal from the shorter-TE images. This is particularly apparent in the frontal brain regions in the two central slices shown which are strongly affected by both the in-plane and through-plane artefacts.

CNR estimation from resting state data

The CNR estimates obtained from the 60 s period of rest prior to the functional experiment are in good agreement with the simulations. This was confirmed by the CNR estimation from the resting state data, for all regions of interest (Fig. 6.1). Moderate gains are seen in ROIs 6 and 10 (for simple and T_2* weighted summation), however larger gains are evident in the remaining regions. The average gain over all ROIs for the three weighting methods: simple summation, T_2* weighted summation and CNR-weighted summation are 6.1 ± 4.3%, 6.4 ± 5.1% and 13.9 ± 5.5%, respectively (mean ± SD). Considering the ROIs not strongly affected by susceptibility artefacts (i.e. excluding ROI 2, 3, 4, and 8) still yields 4.4 ± 2.6%, 4.4 ± 3.2% and 11.2 ± 3.7%, respectively. Hence as expected, the CNR weighting filter outperforms the other two methods due to its ‘noise-suppressing’ nature, and by not relying on an explicit value for T_2* in each voxel.

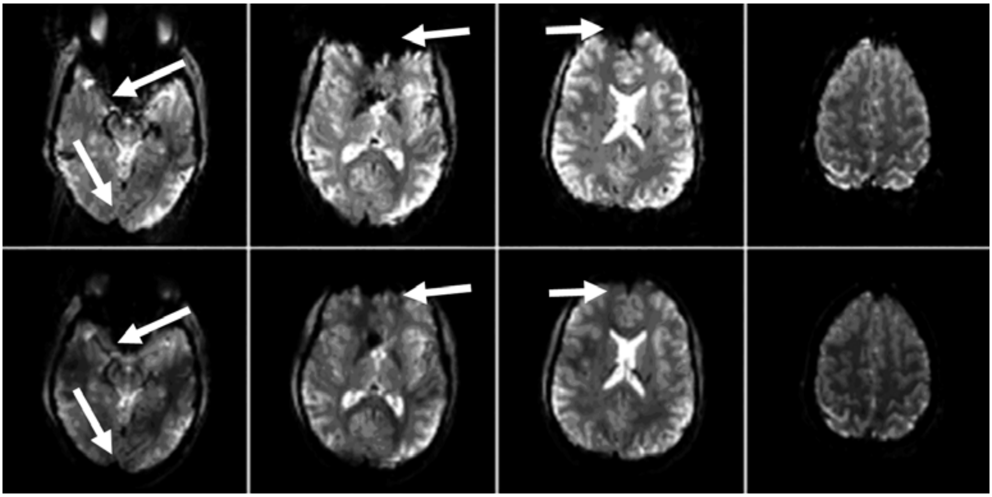

Figure 6.2: *Four brain slices of one subject, acquired with the conventional (top row) and multi-echo EPI protocol (simple summation, bottom row). The arrows indicate regions of the brain where distortion and dropout are strongly reduced by use of the accelerated multi-echo sampling. In the two middle slices a considerable portion of the frontal signal appears compressed / lost in the conventional image, but is 'recovered' in the ME scan.*

A diagram showing the results for all ROIs can be found in Fig. 6.3, where the ROIs with significant sensitivity increases are indicated (*t*-test, $p < 0.05$, $p < 0.01$). Displaying the relative CNR gains for each weighting scheme as a function of T_2* in a scatter plot results in a U-shaped curve, confirming that larger gains are obtained in regions of short T_2* and in those with longer T_2* (not shown).

The results for the different ROIs also reflect a slightly inhomogeneous distribution of (temporal) SNR in the brain: ROI 2 / 6 / 10 (left) benefit marginally less from ME sampling (with average relative gains = 6 / 5 / 13%) than do their contralateral counterparts (ROI 3 / 7 / 11, with average relative gains = 2 / 3 / 10%). This is in qualitative agreement with the tSNR images obtained during the CNR analysis (not shown). Hardware imperfections and B_1 inhomogeneity can be excluded as a cause, since they would have equally affected both multi- and single echo measurements, and we thus attribute the effect to the spatially varying noise introduced by the GRAPPA reconstruction. The percentage temporal noise calculated pixelwise and averaged over all brain pixels and all subjects was 2.44 ± 0.31 for the non-accelerated single-echo acquisition, and 3.22 ± 0.49 for the second echo of the multi-echo protocol. The relative average tSNR is thus 1.32, which is far less than the ratio of 1.62 that one would expect in the absence of physiological noise, based on consideration of the effective acquisition windows alone (in addition there will be a g-noise contribution). The average SNR over subjects within the multi-echo images at TE = [9 22 35 48] ms was found to be 124.69 ± 30.40, 89.91 ± 16.41, 52.67 ± 17.36 and 32.44 ± 9.46, respectively. With 96.98 ± 22.88 the image SNR of the non-accelerated scan is thus about 8% higher in this ROI than for the second echo acquired at comparable TE.

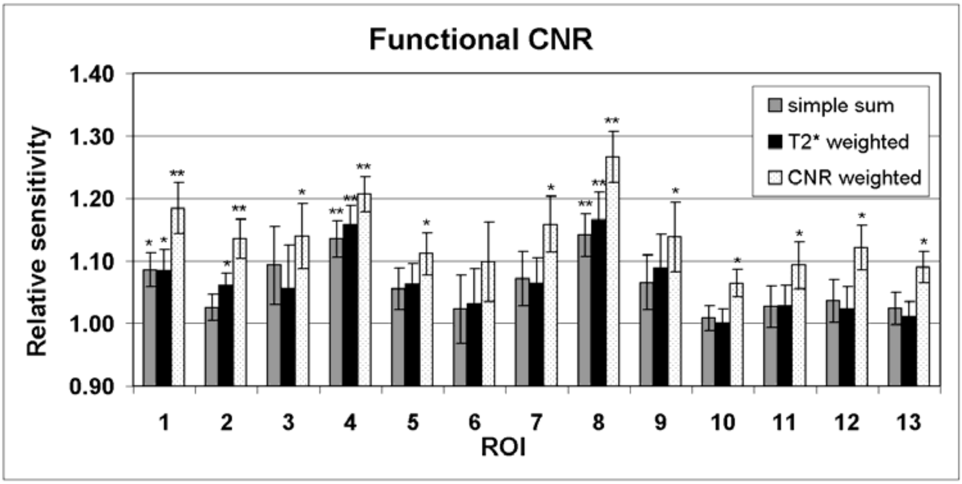

Figure 6.3. *Estimated relative functional sensitivity of the multi- versus single echo data, for the three echo weighting schemes described in the text. The calculations suggest CNR gains from approximately zero to 10%, with slightly larger values for regions more strongly affected by dropout. CNR weighting consistently outperforms the other methods. Significant CNR differences are indicated by * ($p < 0.05$) or ** ($p < 0.01$); error bars show SEM over subjects. The labels on the horizontal axis refer to the regions of interest defined in Fig. 6.1.*

Activation study

Group activation results for all task conditions vs. baseline were obtained using a *t*-threshold of ± 13, and a cluster threshold of 50 voxels. Overall, the pattern of activation agrees extremely well with previous reports for this type of Stroop task (Zysset et al. 2001).

The images in the left hand column of Fig. 6.4 show the group activation maps obtained by separately analyzing the time courses at the four different echo times. It is worth pointing out here that unequivocal comparisons can be made between the different TEs, and combined data, since the multi-echo data are acquired in ‘a single shot’ and as part of the same experimental runs.

Already at the very short TE of 9 ms the typical negative signal changes in anterior (ACC) and posterior cingulate cortex (PCC) are detected with high significance, and two clusters of positive activation are seen in left intraparietal sulcus and occipitotemporal gyrus. The positive activation clusters in the more superior brain regions are detected better at the later TE which more closely match the local grey matter T_2*. A surprisingly large amount of activation however is still found at the very late TE of 48 ms; this includes ACC and PCC. Thus on the whole, the echo time dependence of the functional activation is not very pronounced. Detailed group results for all detected activation clusters are summarised in Table 6.1.

The right hand side of Fig. 6.4 shows the activation maps for the group analysis of the conventional single echo (top), and the multi-echo data with simple (middle) and CNR-weighted summation (bottom) for comparison. At a first glance, the activation plots look rather comparable, reflecting similar brain activations in the separately acquired conventional and multi-echo experiments. Especially the transverse view however reveals an increased sensitivity of the multi-echo protocol for most brain regions. At the same significance and cluster thresholds, four activation clusters in left and right occipitotemporal gyrus, right intraparietal and right frontal sulcus go undetected in the single echo data while they are well visible in the multi-echo experiments. The clusters in right frontal sulcus and left occipitotemporal gyrus are detected at a lower threshold ($t > 10$, marked by '*' in Table 6.1). On the other hand, the single echo data shows a cluster of deactivation near the right post central gyrus, which in the multi-echo is only seen at the lower threshold and with smaller cluster size; *t*-scores in three of the commonly activated brain regions (right parietal, ACC and PCC) are marginally larger. In the multi-echo data the left hemispheric activation in intraparietal and frontal sulci has merged into one large activation cluster. Application of an extremely high significance threshold in fact divides the cluster into *three* separate regions, with the third representing activation in primary motor cortex (subjects responded by right hand button presses). Similarly, the corresponding left-lateral activation in the single echo data reveals a separate primary motor cluster at very high threshold. This primary motor activation is not considered in isolation.

In contrast to the CNR estimates obtained from the resting state data, the differences between simple and CNR-weighted summation are relatively small. Slightly larger maximum *t*-scores and cluster sizes are observed for the CNR-weighted summation in all but two brain regions, ACC and PCC (in the PCC the activation cluster is larger, but *t*-score marginally lower). The group results thus confirm that weighted echo summation results in greater functional sensitivity than simple echo combination with equal weights, but only by a small margin.

To further investigate the echo time dependence of activation and noise, activation maps were obtained from the unsmoothed individual and combined echo data timecourses of three subjects. Figure 6.5 shows two sections of a single-subject activation map, containing two arbitrarily chosen activation clusters in very different brain regions that were considered in more detail: anterior cingulate cortex (ACC), and supplementary motor area (pre-SMA), marked by red circles in Fig. 6.5. Here the aim is not a comparison of the multi-echo with the conventional EPI data, but rather a detailed investigation of the effects of echo combination.
First, trial-averaged absolute and percent signal change, maximum *t*-score and activated pixel count were noted for *separate* analysis of each data set of the three subjects, at a *t* -threshold of ± 6 and cluster threshold of two voxels (see left hand side of Table 6.2). For the ACC ROI, the largest voxel count was observed at the two shorter echo times; however the maximum *t*-score was nearly identical at the three shorter TE. For the ROI in pre-SMA, the largest voxel count was seen at 35 ms or 48 ms, with the maximum *t*-score showing at one of the three later TE. In

all cases echo summation increased the cluster size (maximum for CNR weighting), however in all but one case simple summation outperformed CNR weighted summation (the exception being pre-SMA in subject 3; for ACC in this subject echo summation also did not increase the maximum *t*-score).

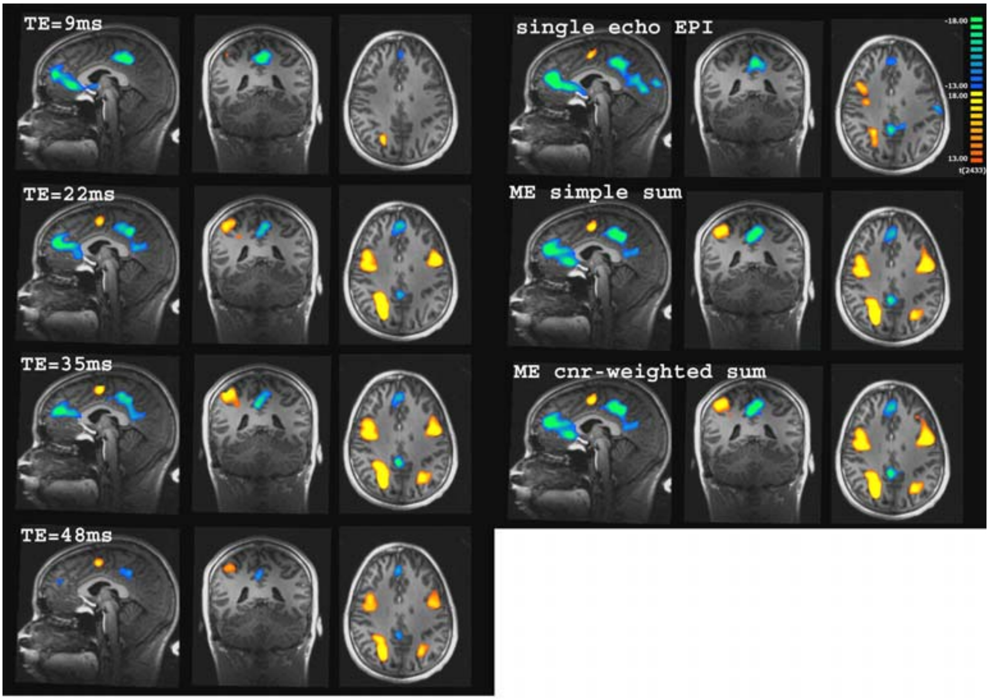

Figure 6.4 *(see Appendix for colour version): Group activation maps for all task conditions vs. baseline (Talairach coordinate [0 -41 33], t > 13). LEFT: activation maps obtained by separate analysis of the four echo time courses (TE as indicated). Especially the 'deactivation' in anterior and posterior cingulate cortex is well visible at the very short TE of 9 ms. At 22 ms the positive activations become apparent, and a considerable amount is still detected in the latest echo (TE 48 ms). The overall echo time dependence of activation does not appear to be very pronounced. RIGHT: comparison of activation in the single echo EPI data (top), with the multi-echo results for simple (middle) and CNR-weighted summation (bottom). Considerably larger activation clusters are detected with the ME protocol, especially in the more superior brain. Overall, CNR-weighted summation outperforms simple summation, albeit with only a small difference in activation volume and t-score. For detailed results see Table 6.1.*

Second, ROI analysis was performed for a direct comparison of *exactly the same voxels* in the different TE and combined datasets. Here, the trial-averaged absolute and percent signal changes, as well as average and maximum *t*-score were obtained from the ROIs defined by the activated regions in the CNR-weighted timecourse, which for all three subjects showed the largest super-threshold activation in both ROIs. Average *t*-score and BOLD signal change are now a more meaningful measure for comparison across data sets. In all cases, echo combination resulted in

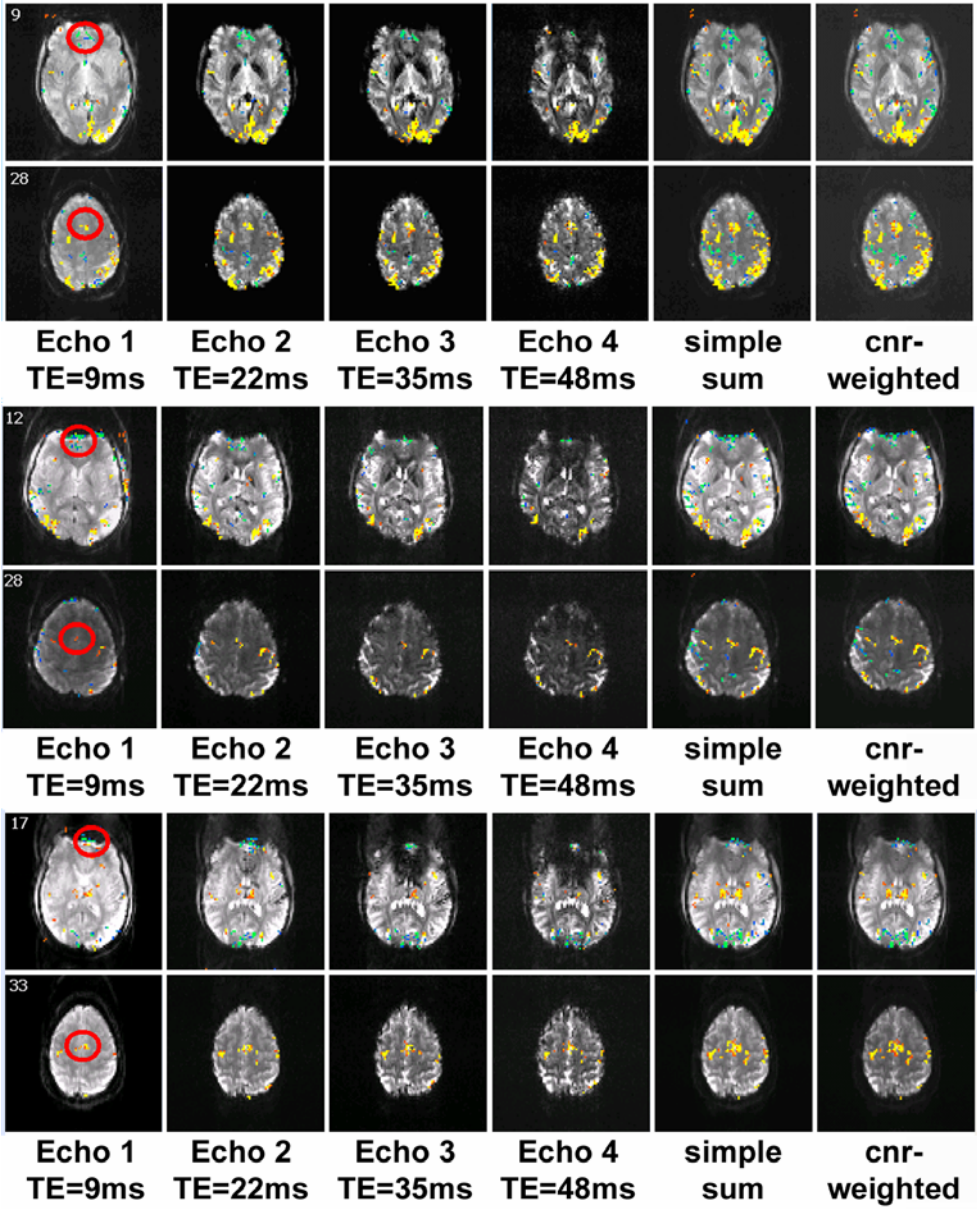

Figure 6.5 *(see Appendix for colour version): Echo time dependence of activation in the unsmoothed data of three subjects, shown separately for the individual echoes, simply summed and CNR-weighted data (from left to right). A larger than expected amount of activation is detected at the very early (9 ms) and very late (48 ms) echo times. The two ROIs which were investigated in detail are marked by the red circle in the 9 ms echo.which were investigated in detail are marked by the red circle in the 9 ms echo.*

a considerable increase of the average *t*-score. Again, simple summation outperformed CNR-weighted summation, with the exception of pre-SMA in subject 2 (equal performance) and ACC in subject 3 (CNR weighted > simple summation). Figure 6.6 shows the mean and maximum *t*-scores, as well as percent BOLD signal changes for the two ROIs in the three single subjects, for each individual echo time and the two combined datasets.

These results are in good agreement with the 'actual CNR' which was calculated as the average absolute BOLD signal change signal in the ROI, divided by the average pixelwise temporal SNR as determined from the first 25 resting state volumes: only in one dataset (subject 3, ACC) did CNR weighted summation prove more beneficial than simple summation; again, this is in contrast to the simulations. That simple summation can perform better on average than CNR-weighted summation can be understood by reference to Fig. 6.7 which shows results for the three single subjects . Four curves are shown to illustrate the TE dependence of the observed absolute BOLD signal changes (full circles), the 'actual' BOLD CNR as ratio of observed signal change and measured temporal noise (open circles), the theoretical BOLD contrast curve as proportional to TE · exp(-TE / T_2*) (solid line), and the theoretical CNR calculated as measured tSNR · TE (asterisk). Note that this latter curve corresponds to the summation weights that are applied in the CNR-weighting. Its departure from the 'actual' CNR results in underestimation of the sensitivity of the first echo in the ACC. Similarly, in pre-SMA the early echoes are underweighted while the fourth echo receives too much weight. This effectively leads to larger sensitivity gains for echo summation with equal weights, at least for the two ROIs considered here. In the pre-SMA region with the longer T_2* (28 ms) there is rather good agreement of both BOLD signal changes and BOLD CNR with the model BOLD curve. However, and in accordance with the *t*-scores shown in Fig. 6.6, the sensitivity in the ACC (fitted T_2* of 17 ms) is high and comparable at TE 9, 22, and 35 ms followed by a decrease at the TE of 48 ms.

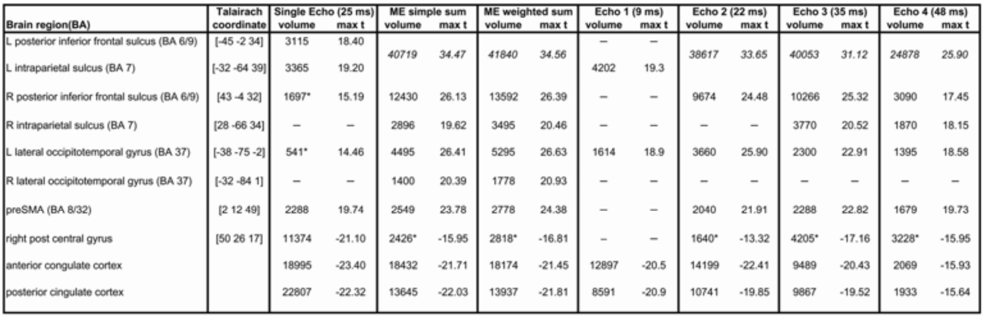

Brain region(BA)	Talairach coordinate	Single Echo (25 ms)		ME simple sum		ME weighted sum		Echo 1 (9 ms)		Echo 2 (22 ms)		Echo 3 (35 ms)		Echo 4 (48 ms)	
		volume	max t	volume	max t	volume	max t	volume	max t	volume	max t	volume	max t	volume	max t
L posterior inferior frontal sulcus (BA 6/9)	[-45 -2 34]	3115	18.40	*40719*	*34.47*	*41840*	*34.56*	–	–	*38617*	*33.65*	*40053*	*31.12*	*24878*	*25.90*
L intraparietal sulcus (BA 7)	[-32 -64 39]	3365	19.20					4202	19.3						
R posterior inferior frontal sulcus (BA 6/9)	[43 -4 32]	1697*	15.19	12430	26.13	13592	26.39	–	–	9674	24.48	10266	25.32	3090	17.45
R intraparietal sulcus (BA 7)	[28 -66 34]	–	–	2896	19.62	3495	20.46	–	–	–	–	3770	20.52	1870	18.15
L lateral occipitotemporal gyrus (BA 37)	[-38 -75 -2]	541*	14.46	4495	26.41	5295	26.63	1614	18.9	3660	25.90	2300	22.91	1395	18.58
R lateral occipitotemporal gyrus (BA 37)	[-32 -84 1]	–	–	1400	20.39	1778	20.93	–	–	–	–	–	–	–	–
preSMA (BA 8/32)	[2 12 49]	2288	19.74	2549	23.78	2778	24.38	–	–	2040	21.91	2288	22.82	1679	19.73
right post central gyrus	[50 26 17]	11374	-21.10	2426*	-15.95	2818*	-16.81	–	–	1640*	-13.32	4205*	-17.16	3228*	-15.95
anterior congulate cortex		18995	-23.40	18432	-21.71	18174	-21.45	12897	-20.5	14199	-22.41	9489	-20.43	2069	-15.93
posterior cingulate cortex		22807	-22.32	13645	-22.03	13937	-21.81	8591	-20.9	10741	-19.85	9867	-19.52	1933	-15.64

Table 6.1: *Activation volumes and t-scores at t > 13.00. Note that left hemispheric activation in inferior frontal and intraparietal sulci appear as one cluster in the multi-echo data and are shown as one value (italic font in table). Clusters detected at t > 10 are marked by *.*

Moreover, the correlation matrix and associated *p*-values were determined for the four echo time courses, separately for each voxel in the two ROIs (again using the initial resting state period). The results for all three subjects can be found in Table 6.2, showing the average values over each ROI. The dominant correlation values are below 0.2 which is considered 'small'; the highest average correlation was 0.34 (for ACC in subject 2, correlation between first and second echo; corresponding *p*-value 0.23).

It is also evident that timecourses acquired adjacent in time correlate most, partly with the exception of subject 3.

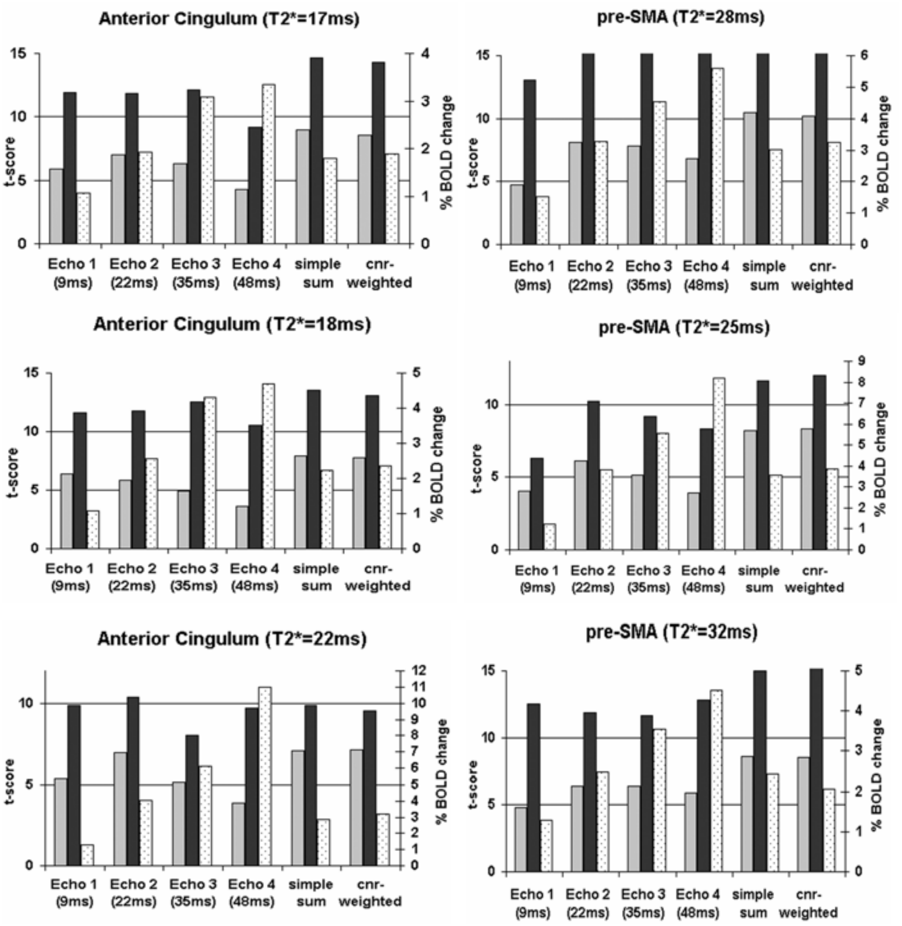

Figure 6.6: *Echo time dependence of activation in the three un-smoothed sets of single subject data, shown separately for the individual echoes, simply summed and CNR-weighted data: Average and maximum t-score, and percent BOLD signal change in ACC (top) and pre-SMA (bottom), for the ROI defined by the super-threshold activation (t > 6) in the CNR-weighted data. For details see text.*

Overall, the results do not suggest a pronounced correlation between the different echo time courses. Not surprisingly, much larger correlation values are seen in the combined data, as these result from summation of the individual echo time courses. A low degree of correlation is the prerequisite for useful multi-echo experiments, and explains why CNR gains as shown here can be achieved.

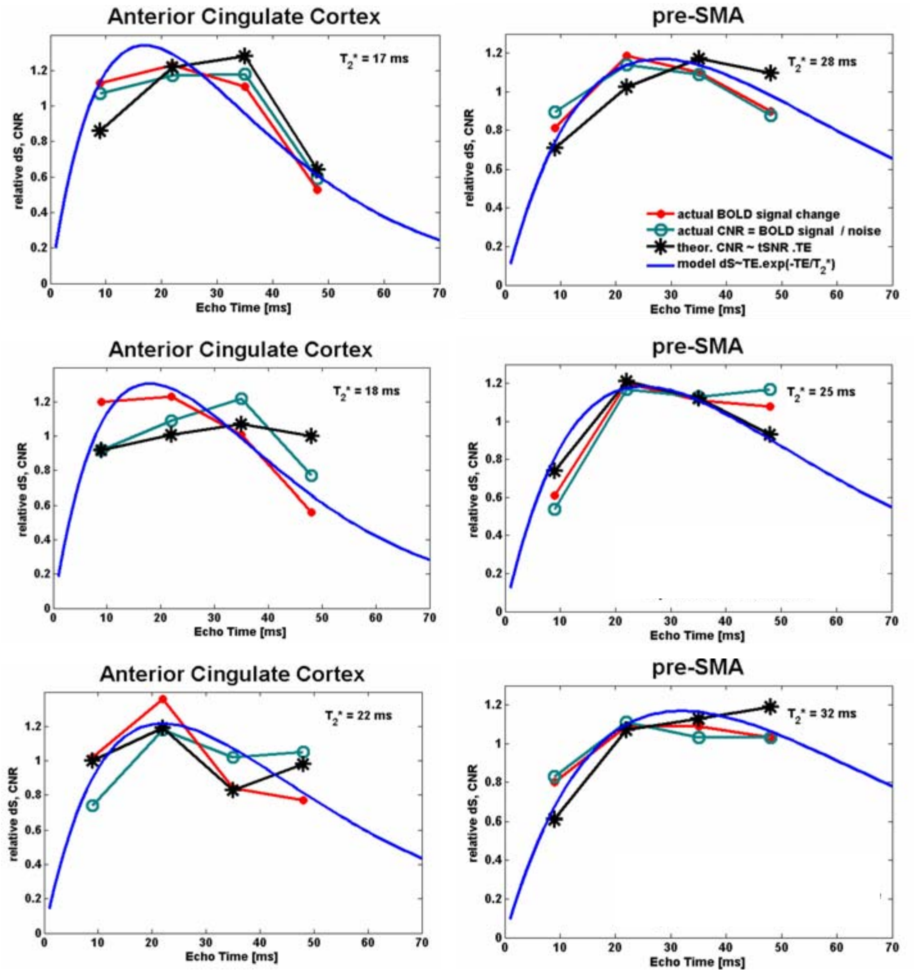

Figure 6.7 *(see Appendix for colour version): Echo time dependencies of: model BOLD contrast as TE · exp(-TE/T$_2$*) (solid line), observed absolute BOLD signal change (full circles), actual BOLD CNR as ratio of observed absolute signal change and measured temporal noise (open circles), and theoretical CNR calculated as measured tSNR · TE (asterisk); each curve is normalized to yield a sum of 4 (i.e. an average value of unity) when adding their values at the four echo time points. The 'theoretical CNR' curve (asterisk) is used to obtain the summation weights in CNR-weighted echo summation (albeit in a voxelwise manner, shown here is the ROI average). Its clear departure from the 'actual CNR' for the shorter echo times explains why CNR weighting performs comparable to, or slightly less well than simple echo summation.*

Subject 1

Anterior Cingulate Cortex (T2* = 17ms)

separate analysis at |t| ≥ 6, cluster ≥ 2

	# voxels	dS (%)	dS (abs)	max t-score
Echo 1 (9ms)	18	1.13	11.54	11.95
Echo 2 (22ms)	**27**	2.35	14.18	11.84
Echo 3 (35ms)	18	3.59	12.96	12.13
Echo 4 (48ms)	2	7.28	15.69	9.18
simple sum	31	1.76	37.42	14.62
CNR-weighted	**32**	1.89	30.25	14.31

analysis in ROI defined by activation in CNR-weighted timecourse at |t| ≥ 6, cluster ≥ 2 (32 voxels)

average t-score	t-score relative to max	max t-score	dS (%)	dS (abs)	noise	largest correlation (with echo)	p value for noise correlation	actual CNR (dS/noise)	actual CNR relative to max	tSNR
5.92	**0.84**	11.95	1.06	10.92	18.41	0.13 (3)	0.30	0.59	**0.90**	56.68
7.01	**1.00**	11.84	1.93	11.80	18.19	0.17 (3)	0.32	0.65	**0.99**	32.86
6.30	**0.90**	12.13	3.08	10.66	16.23	0.17 (2)	0.32	0.66	**1.00**	21.73
4.30	**0.61**	9.18	3.35	5.14	15.67	0.16 (3)	0.36	0.33	**0.50**	7.98
9.00	**1.28**	14.62	1.79	38.30	40.61	0.58 (3)	0.09	0.94	**1.44**	54.13
8.56	**1.22**	14.31	1.89	37.82	42.23	0.60 (4)	0.05	0.90	**1.36**	48.97

pre-SMA (T2* = 28ms)

separate analysis at |t| ≥ 6, cluster ≥ 2

	# voxels	dS (%)	dS (abs)	max t-score
Echo 1 (9ms)	8	2.78	21.93	13.04
Echo 2 (22ms)	16	4.65	24.28	19.99
Echo 3 (35ms)	**21**	5.85	19.94	17.10
Echo 4 (48ms)	15	7.85	20.00	15.30
simple sum	29	3.13	58.95	23.25
CNR-weighted	**31**	3.23	47.66	22.48

analysis in ROI defined by activation in CNR-weighted timecourse at |t| ≥ 6, cluster ≥ 2 (31 voxels)

average t-score	t-score relative to max	max t-score	dS (%)	dS (abs)	noise	largest correlation (with echo)	p value for noise correlation	actual CNR (dS/noise)	actual CNR relative to max	tSNR
4.75	**0.59**	13.04	1.53	11.87	14.41	0.28 (2)	0.36	0.82	**0.79**	58.77
8.10	**1.00**	19.99	3.26	17.34	16.54	0.32 (3)	0.29	1.05	**1.00**	34.75
7.82	**0.97**	17.10	4.53	16.07	16.02	0.33 (4)	0.32	1.00	**0.96**	24.97
6.80	**0.84**	15.30	5.59	13.13	16.26	0.33 (3)	0.33	0.81	**0.77**	17.04
10.47	**1.29**	23.25	3.02	57.31	42.35	0.73 (2)	0.01	1.35	**1.29**	52.14
10.20	**1.26**	22.48	3.23	59.58	45.21	0.75 (4)	0.02	1.32	**1.26**	47.87

Subject 2

Anterior Cingulate Cortex (T2* = 18ms)

separate analysis at |t| ≥ 6, cluster ≥ 2

	# voxels	dS (%)	dS (abs)	max t-score
Echo 1 (9ms)	**30**	1.46	10.07	11.58
Echo 2 (22ms)	22	2.52	11.82	11.74
Echo 3 (35ms)	10	5.20	14.67	12.51
Echo 4 (48ms)	6	6.52	13.86	10.55
simple sum	32	2.14	32.24	13.56
CNR-weighted	**34**	2.36	25.14	13.05

analysis in ROI defined by activation in CNR-weighted timecourse at |t| ≥ 6, cluster ≥ 2 (34 voxels)

average t-score	t-score relative to max	max t-score	dS (%)	dS (abs)	noise	largest correlation (with echo)	p value for noise correlation	actual CNR (dS/noise)	actual CNR relative to max	tSNR
6.40	**1.00**	11.58	1.07	8.59	17.53	0.34 (2)	0.23	0.49	**0.76**	38.98
5.81	**0.91**	11.74	2.56	8.76	15.01	0.34 (1)	0.23	0.58	**0.90**	17.39
4.95	**0.77**	12.51	4.30	7.25	11.17	0.24 (2)	0.23	0.65	**1.00**	11.58
3.58	**0.56**	10.55	4.69	3.97	9.65	0.21 (3)	0.34	0.41	**0.63**	7.90
7.89	**1.23**	13.56	2.24	32.14	36.78	0.68 (2)	0.03	0.87	**1.35**	31.44
7.78	**1.22**	13.05	2.36	31.43	36.26	0.62 (1)	0.10	0.87	**1.34**	29.19

pre-SMA (T2* = 25ms)

separate analysis at |t| ≥ 6, cluster ≥ 2

	# voxels	dS (%)	dS (abs)	max t-score
Echo 1 (9ms)	2	2.06	9.91	5.69
Echo 2 (22ms)	5	5.37	15.22	10.22
Echo 3 (35ms)	5	6.57	12.73	9.22
Echo 4 (48ms)	**8**	7.20	11.30	9.54
simple sum	11	3.55	38.25	11.64
CNR-weighted	**11**	3.86	40.20	12.05

analysis in ROI defined by activation in CNR-weighted timecourse at |t| ≥ 6, cluster ≥ 2 (11 voxels)

average t-score	t-score relative to max	max t-score	dS (%)	dS (abs)	noise	largest correlation (with echo)	p value for noise correlation	actual CNR (dS/noise)	actual CNR relative to max	tSNR
4.06	**0.66**	6.29	1.24	5.76	12.44	0.19 (2)	0.32	0.46	**0.46**	28.25
6.10	**1.00**	10.22	3.81	11.41	11.46	0.19 (1)	0.32	1.00	**1.00**	18.79
5.15	**0.84**	9.22	5.56	10.52	10.96	0.19 (2)	0.44	0.96	**0.96**	10.93
3.91	**0.64**	8.31	8.20	10.21	10.27	0.11 (3)	0.40	0.99	**1.00**	6.67
8.21	**1.34**	11.64	3.55	38.25	25.40	0.63 (2)	0.03	1.51	**1.51**	28.51
8.33	**1.37**	12.05	3.86	40.20	26.66	0.58 (4)	0.06	1.51	**1.51**	25.57

Subject 3

Anterior Cingulate Cortex (T2* = 22ms)

separate analysis at |t| ≥ 6, cluster ≥ 2

	# voxels	dS (%)	dS (abs)	max t-score
Echo 1 (9ms)	15	7.52	32.42	**9.89**
Echo 2 (22ms)	**16**	5.32	21.70	**10.40**
Echo 3 (35ms)	10	8.46	36.30	**9.14**
Echo 4 (48ms)	2	15.91	23.63	**9.70**
simple sum	17	3.61	48.51	**9.88**
CNR-weighted	**17**	3.14	44.73	**9.56**

analysis in ROI defined by activation in CNR-weighted timecourse at |t| ≥ 6, cluster ≥ 2 (17 voxels)

average t-score	t-score relative to max	max t-score	dS (%)	dS (abs)	noise	largest correlation (with echo)	p value for noise correlation	actual CNR (dS/noise)	actual CNR relative to max	tSNR
5.37	**0.77**	9.89	1.26	11.69	21.05	0.15 (2)	0.32	0.56	**0.63**	38.849
6.97	**1.00**	10.40	4.05	15.62	17.67	0.15 (1)	0.32	0.88	**1.00**	17.96
5.16	**0.74**	8.03	6.13	9.65	12.66	0.04 (1)	0.43	0.76	**0.86**	7.85
3.85	**0.55**	9.70	10.99	8.86	11.32	0.08 (2)	0.43	0.78	**0.89**	6.78
7.09	**1.02**	9.88	2.88	44.40	35.11	0.65 (1)	0.08	1.26	**1.43**	37.03
7.10	**1.02**	9.56	3.19	45.39	33.87	0.61 (1)	0.13	1.34	**1.52**	34.69

pre-SMA (T2* = 32ms)

separate analysis at |t| ≥ 6, cluster ≥ 2

	# voxels	dS (%)	dS (abs)	max t-score
Echo 1 (9ms)	11	2.50	19.57	12.53
Echo 2 (22ms)	17	3.58	20.12	11.84
Echo 3 (35ms)	**19**	3.98	17.90	11.68
Echo 4 (48ms)	16	5.77	18.00	12.82
simple sum	38	2.45	50.59	14.99
CNR-weighted	**39**	2.06	41.80	15.19

analysis in ROI defined by activation in CNR-weighted timecourse at |t| ≥ 6, cluster ≥ 2 (39 voxels)

average t-score	t-score relative to max	max t-score	dS (%)	dS (abs)	noise	largest correlation (with echo)	p value for noise correlation	actual CNR (dS/noise)	actual CNR relative to max	tSNR
4.81	**0.75**	12.53	1.30	10.28	12.11	0.19 (4)	0.44	0.85	**0.75**	68.10
6.40	**0.99**	11.84	2.47	14.01	12.37	0.19 (4)	0.46	1.13	**1.00**	48.71
6.43	**1.00**	11.68	3.54	13.97	13.20	0.17 (4)	0.51	1.06	**0.93**	32.31
5.90	**0.92**	12.82	4.52	13.19	12.50	0.19 (2)	0.46	1.06	**0.93**	24.93
8.63	**1.34**	14.99	2.44	49.88	30.47	0.58 (3)	0.14	1.64	**1.44**	70.87
8.54	**1.33**	15.19	2.06	49.30	30.49	0.56 (3)	0.15	1.62	**1.43**	63.96

Table 6.2: *Detailed analysis of functional activation in the unsmoothed single-subject data. Two regions of interest, anterior cingulate cortex (fitted T_2^* = 17 ms) and pre-SMA (T_2^* = 28 ms) are considered.*

Discussion

In this study the value of single-shot multi-echo EPI acquisitions at 7 T is investigated. The results demonstrate that BOLD fMRI measurements with GE-EPI benefit from multi-echo sampling even at field strengths as high as 7 T. This is confirmed by simulations and CNR estimates obtained from resting state data, and a functional Stroop experiment.

According to expectations, the improvement in sensitivity predicted by the CNR calculations are lower than those found at 3 T (for CNR weighting 14 ± 6% at 7 T vs. 25 ± 13% at 3 T (Poser et al. 2006)). This is due to the short grey matter T_2* relaxation time of approximately 25 ms at 7 T. Given the typical duration of the EPI readout train even with parallel acceleration, only a few echoes can be acquired in relative proximity to the 'preferred' echo time (TE ~ T_2*); extending the readout by additional echoes at later TE would increase the total sampling time, yield minimal further benefit and increase TR. It must thus be viewed as a very positive finding that the realised reduction in image distortion, here by a factor of 3, can be obtained not only without loss, but even with a gain in functional sensitivity. The group results of the colour-word interference Stroop experiments are in good agreement with the CNR estimates obtained form the resting state data. Larger gains are seen in the superior brain with prominent grey matter T_2* values of about 25 ms or more (Peters et al. 2007): here, considerable BOLD signal contributions clearly come for more than two echoes, as is evident from Figures 6.4, 6.5 and 6.6. Moreover, the data from the activation study also suggest superiority of the multi-echo acquisitions as compared to the single echo for the majority of the detected activation clusters, albeit the potential constraints due to intra- and inter-subject variance that are inherent to fMRI group studies may however remain (Aguirre et al. 1998). An interesting result that differs from the previous findings at 3 T is the discrepancy between the performance for simple and weighted summation as predicted on the basis of CNR estimates, and the actually observed *t*-scores and activation sizes: In most, but not all, activation clusters that were detected at the group level the CNR-weighted summation outperforms simple echo combination, even though the additional gains are small. The amount of activation that is seen at the very short and very long TEs can explain why simple echo combination is more beneficial than suggested by the simulations and sensitivity calculations on the resting state data. There are three factors that likely play role here: First, it is clear from analysis on the single-subject data that the CNR weighting does not fully take into account the actual sensitivity at each TE, leading to situations where simple summation with equal weights is more appropriate. Second, BOLD-like physiological noise that scales with the signal changes upon activation in the parenchyma (Kruger and Glover 2001; Van de Moortele et al. 2008). Third, activation related changes in intravascular T_2 may give a short-TE contribution to the BOLD: Although the intravascular compartment is small, the T_2 related signal change that results from the change in blood deoxy-haemoglobin levels is relatively large. While the net signal change may hence be small, the physiological

noise originates mainly from the much larger parenchymal department. The latter two mechanisms both serve to effectively broaden the TE dependence of the BOLD sensitivity, but on the basis of the present data it would not be possible to discern their relative or absolute contribution.
In practice, the findings imply that simple summation (or possibly a summation with a global (Weiskopf et al. 2005) or slice dependent weighting factor (Stocker et al. 2006)) is an acceptable procedure at 7 T, certainly from the pragmatic point of view: This considerably simplifies the data processing and moreover, echo combination can easily be performed ‘online’ during data acquisition, thereby drastically reducing data storage requirements.

The calculation of correlation coefficients for the different TE timecourses indicated a rather low degree of correlation. While obviously the correlation has to be < 1 (ideally $\ll 1$) as otherwise no sensitivity increases could possibly have resulted from echo combination, the correlation values obtained nevertheless provide interesting additional insight. Given the spatial resolution and field strength used in this study, it is safe to assume that the data were acquired in the domain of dominant physiological noise where ‘image’ and ‘system’ noise play only a marginal role (Triantafyllou et al. 2005). The observation of the low degree of correlation leads to two interpretations. First, coherent S_0 fluctuations cannot be the dominant type of physiological noise in our data, and hence TE-dependent BOLD-like noise resulting from effective fluctuations in T_2* is the dominant source of physiological noise. Second, this BOLD-like noise is not strongly coherent over TE, so therefore the timescale of the BOLD-like noise appears to be shorter than the inter-echo time (here 13 ms). From this it should follow that single-shot ME- EPI will always be beneficial, also in the typical situation where physiological fluctuations constitute the main source of variance. One possible explanation for this somewhat surprising result might be that the amplitude of the BOLD-like noise in a given voxel at a particular time is determined by the vector addition of all contributions from within that voxel, which may experience local variation in the static magnetic field, and some of which may experience velocity dependent phase shifts. Thus while it is unlikely that the T_2* values as such vary significantly during TE, it may well be that their influence on the signal magnitude changes over time.

ME-EPI will for practical reasons almost always require the use of parallel acceleration, and so consideration of the noise introduced by the parallel reconstruction process is important. Several studies have found the detrimental effect of parallel imaging on fMRI time series to be rather small (de Zwart et al. 2002a; Preibisch et al. 2003) such that the obvious benefits (e.g. distortion reduction, acoustic noise reduction, large matrix sizes) dominate; but this requires a reasonable choice of acceleration factor which depends on the number of coil elements and their spatial arrangement. It has been shown by consideration of the properties of MR signal propagation, that high field and parallel imaging are highly complementary. Much smaller *g*-factors will ensue for the same object at high field, for comparable coils and equal undersampling (Ohliger et al. 2003; Wiesinger et al. 2006). The relative SNR penalty of using parallel undersampling is thus considerably lower at high field, or alternatively, it will be possible to achieve higher acceleration factors at the same cost. Commercially available coils with ever-increasing numbers of channels and continuously improved algorithms for parallel image reconstruction hold promise for higher acceleration factors than used here, thereby permitting the acquisition of more echoes closer to the optimal echo time. This way one can expect further reductions in distortion, and likely also further improvements in functional sensitivity.

In summary, experiments were performed to test the applicability and benefit of parallel-accelerated ME-EPI acquisitions at 7 T. Using theoretical considerations, a method based on temporal SNR in resting state data to predict the functional sensitivity, as well as a realistic functional stimulation paradigm on 7 subjects we demonstrate that (a) distortion and dropout artefacts are drastically reduced thanks to the shortened EPI readout train, and inclusion of shorter TE signal respectively; and that (b) functional sensitivity is not compromised, but rather increases.
The multi-echo method described here and previously is easy to implement, does not necessarily require any advanced data processing steps, and is fully compatible with *post-hoc* distortion correction schemes. We therefore conclude that if not prohibited by the demand for very large matrix sizes / high spatial resolution, accelerated multi-gradient echo EPI acquisition should be the method of choice over conventional GE-EPI for fMRI also at 7 T.

Acknowledgements

The work presented here was supported by the Dutch Technical Science Foundation (STW) with grant NGT.6154. The authors would like to thank Markus Barth and Pieter Buur for useful discussions and helpful comments during the preparation of the manuscript, and Siemens for providing the source codes of the product sequence and reconstruction software on which the multi echo implementation is based.

References

Aguirre GK, Zarahn E, D'Esposito M. (1998) The variability of human, BOLD hemodynamic responses. *Neuroimage* 8:360-369

Bodurka J, Ye F, Petridou N, Murphy K, Bandettini PA. (2007) Mapping the MRI voxel volume in which thermal noise matches physiological noise--implications for fMRI. *Neuroimage* 34:542-549

Chang H, Fitzpatrick JM. (1992) A technique for accurate magnetic resonance imaging in the presence of field inhomogeneities. *IEEE Trans Med Imaging* 11:319-329

Chen NK, Wyrwicz AM. (1999) Correction for EPI distortions using multi-echo gradient-echo imaging. *Magn Reson Med* 41:1206-1213

Cusack R, Brett M, Osswald K. (2003) An Evaluation of the Use of Magnetic Field Maps to Undistort Echo-Planar Images. *NeuroImage* 18:127-142

de Zwart JA, van Gelderen P, Kellman P, Duyn JH. (2002a) Application of sensitivity-encoded echo-planar imaging for blood oxygen level-dependent functional brain imaging. *Magn Reson Med* 48:1011-1020

de Zwart JA, van Gelderen P, Kellman P, Duyn JH. (2002b) Reduction of gradient acoustic noise in MRI using SENSE-EPI. *Neuroimage* 16:1151-1155

Gorno-Tempini ML, Hutton C, Josephs O, Deichmann R, Price C, Turner R. (2002) Echo time dependence of BOLD contrast and susceptibility artefacts. *Neuroimage* 15:136-142

Gowland PA, Bowtell R. (2007) Theoretical optimization of multi-echo fMRI data acquisition. *Phys Med Biol* 52:1801-1813

Griswold MA, Jakob PM, Heidemann RM, Nittka M, Jellus V, Wang J, Kiefer B, Haase A. (2002) Generalized autocalibrating partially parallel acquisitions (GRAPPA). *Magn Reson Med* 47:1202-1210

Hagberg GE, Indovina I, Sanes JN, Posse S. (2002) Real-time quantification of T(2)(*) changes using multiecho planar imaging and numerical methods. *Magn Reson Med* 48:877-882

Hoogenraad FG, Pouwels PJ, Hofman MB, Reichenbach JR, Sprenger M, Haacke EM. (2001) Quantitative differentiation between BOLD models in fMRI. *Magn Reson Med* 45:233-246

Hutton C, Bork A, Josephs O, Deichmann R, Ashburner J, Turner R. (2002) Image Distortion Correction in fMRI: A Quantitative Evaluation. *NeuroImage* 16:217-240

Jezzard P, Balaban RS. (1995) Correction for geometric distortion in echo planar images from B0 field variations. *Magn Reson Med* 34:65-73

Kruger G, Glover GH. (2001) Physiological noise in oxygenation-sensitive magnetic resonance imaging. *Magn Reson Med* 46:631-637

Ladd ME. (2007) High-field-strength magnetic resonance: potential and limits. *Top Magn Reson Imaging* 18:139-152

Lehericy S, Ugurbil K, Van de Moortele P-F. (2006) Echo time dependence of basal ganglia activation at 3T during motor task. In: *Proceedings 14th Scientific Meeting, International Society for Magnetic Resonance in Medicine*, Seattle, p 2825

Metzler A, Barth M, Roell S, Klarhoefer M, Leibfritz D, Moser E. (1998) Echo time dependence of brain activation measured with single shot, high resolution, multiple echo spiral imaging. In: *Proceedings of the 6th Annual Meeting of ISMRM*, Sydney, p 1458

Ohliger MA, Grant AK, Sodickson DK. (2003) Ultimate intrinsic signal-to-noise ratio for parallel MRI: electromagnetic field considerations. *Magn Reson Med* 50:1018-1030

Parkes LM, Schwarzbach JV, Bouts AA, Deckers RH, Pullens P, Kerskens CM, Norris DG. (2005) Quantifying the spatial resolution of the gradient echo and spin echo BOLD response at 3 Tesla. *Magn Reson Med* 54:1465-1472

Peters AM, Brookes MJ, Hoogenraad FG, Gowland PA, Francis ST, Morris PG, Bowtell R. (2007) T2* measurements in human brain at 1.5, 3 and 7 T. *Magn Reson Imaging* 25:748-753

Poser BA, Versluis MJ, Hoogduin JM, Norris DG. (2006) BOLD contrast sensitivity enhancement and artefact reduction with multiecho EPI: Parallel-acquired inhomogeneity-desensitized fMRI. *Magn Reson Med* 55:1227-1235

Posse S, Wiese S, Gembris D, Mathiak K, Kessler C, Grosse-Ruyken ML, Elghahwagi B, Richards T, Dager SR, Kiselev VG. (1999) Enhancement of BOLD-contrast sensitivity by single-shot multi-echo functional MR imaging. *Magn Reson Med* 42:87-97

Preibisch C, Pilatus U, Bunke J, Hoogenraad F, Zanella F, Lanfermann H. (2003) Functional MRI using sensitivity-encoded echo planar imaging (SENSE-EPI). *Neuroimage* 19:412-421

Preibisch C, Volz S, Anti S, Deichmann R. (2008) Exponential excitation pulses for improved water content mapping in the presence of background gradients. *Magn Reson Med* 60:908-916

Pruessmann KP, Weiger M, Scheidegger MB, Boesiger P. (1999) SENSE: sensitivity encoding for fast MRI. *Magn Reson Med* 42:952-962

Shmuel A, Yacoub E, Chaimow D, Logothetis NK, Ugurbil K. (2007) Spatio-temporal point-spread function of fMRI signal in human gray matter at 7 Tesla. *Neuroimage* 35:539-552

Song AW, Wong EC, Tan SG, Hyde JS. (1996) Diffusion weighted fMRI at 1.5 T. *Magn Reson Med* 35:155-158

Speck O, Hennig J. (1998) Functional imaging by I0- and T2*-parameter mapping using multi-image EPI. *Magn Reson Med* 40:243-248

Speck O, Stadler J, Zaitsev M. (2008) High resolution single-shot EPI at 7T. *Magma* 21:73-86

Stocker T, Kellermann T, Schneider F, Habel U, Amunts K, Pieperhoff P, Zilles K, Shah NJ. (2006) Dependence of amygdala activation on echo time: results from olfactory fMRI experiments. *Neuroimage* 30:151-159

Triantafyllou C, Hoge RD, Krueger G, Wiggins CJ, Potthast A, Wiggins GC, Wald LL. (2005) Comparison of physiological noise at 1.5 T, 3 T and 7 T and optimization of fMRI acquisition parameters. *Neuroimage* 26:243-250

Van de Moortele P-F, Ugurbil K, Lehericy S. (2008) Is T2* always the optimum Echo Time in BOLD fMRI? Challenging a commonconcept with a new Contrast to Noise Ratio BOLD model. In: *Proceedings 16th Scientific Meeting, International Society for Magnetic Resonance in Medicine*, Toronto, p 2464

Weiskopf N, Klose U, Birbaumer N, Mathiak K. (2005) Single-shot compensation of image distortions and BOLD contrast optimization using multi-echo EPI for real-time fMRI. *Neuroimage* 24:1068-1079

Wiesinger F, Van de Moortele PF, Adriany G, De Zanche N, Ugurbil K, Pruessmann KP. (2006) Potential and feasibility of parallel MRI at high field. *NMR Biomed* 19:368-378

Yacoub E, Shmuel A, Pfeuffer J, Van De Moortele PF, Adriany G, Andersen P, Vaughan JT, Merkle H, Ugurbil K, Hu X. (2001) Imaging brain function in humans at 7 Tesla. *Magn Reson Med* 45:588-594

Zaitsev M, Hennig J, Speck O. (2004) Point spread function mapping with parallel imaging techniques and high acceleration factors: fast, robust, and flexible method for echo-planar imaging distortion correction. *Magn Reson Med* 52:1156-1166

Zeng H, Constable RT. (2002) Image distortion correction in EPI: comparison of field mapping with point spread function mapping. *Magn Reson Med* 48:137-146

Zhang R, Cox RW, Hyde JS. (1997) The effect of magnetization transfer on functional MRI signals. *Magn Reson Med* 38:187-192

Zysset S, Muller K, Lohmann G, von Cramon DY. (2001) Color-word matching stroop task: separating interference and response conflict. *Neuroimage* 13:29-36

Chapter 7 Fast spin echo sequences for BOLD functional MRI

Abstract

At higher field strengths, spin echo (SE) functional MRI (fMRI) is an attractive alternative to gradient echo (GE) as the increased weighting towards the microvasculature results in intrinsically better localisation of the BOLD signal. Images are free of signal voids but the commonly used echo planar imaging (EPI) sampling scheme causes geometric distortions, and T_2* effects often contribute considerably to the signal changes measured upon brain activation. Multiply refocused SE sequences such as fast spin echo (FSE) are essentially artefact free but their application to fast fMRI is usually hindered due to high energy deposition, and long sampling times. In the work presented here, a combination of parallel imaging and partial Fourier acquisition is used to shorten FSE acquisition times to near those of conventional SE-EPI, permitting sampling of 8 slices (matrix 64 x 64) per second. Signal acquisition is preceded by a preparation experiment that aims at increasing the relative contribution of extravascular dynamic averaging to the BOLD signal. Comparisons are made with conventional SE-EPI using a visual stimulation paradigm. While the observed signal changes are approximately 30% lower, most likely due to the absence of T_2* contamination, activation size and *t*-scores are comparable for both methods, suggesting that HASTE fMRI is a viable alternative, particularly if distortion free images are required. Our data also indicate that the BOLD post-stimulus undershoot is most probably attributable to persistent elevated oxygen metabolism rather than to delayed vascular compliance.

Poser BA, Norris DG. Magn Reson Mater Phy 20(1): 11-17; 2007

Introduction

Echo Planar Imaging (EPI) (Mansfield 1984) is commonly used for functional MRI (fMRI). It finds application in most methods for blood oxygenation level dependent (BOLD) fMRI (Ogawa et al. 1990) as well as other functional imaging sequences such as arterial spin labelling (ASL) (Williams et al. 1992) or vascular space occupancy (VASO) (Lu et al. 2003) fMRI. For BOLD fMRI, gradient echo (GE) EPI is popular as whole-brain images with high functional contrast to noise (CNR) can typically be acquired at a sufficiently high temporal resolution to adequately sample the BOLD response. An attractive alternative for fMRI at high field strengths is provided by spin echo (SE) based T_2 contrast, which arises from changes in extravascular dynamic averaging and intravascular changes in the effective T_2 of blood, both associated with the BOLD effect. Signal attenuation due to dynamic averaging is diffusion-induced and, in contrast to static dephasing effects in the field inhomogeneities around larger vessels, is not refocused in the spin echo experiment as it is a random process. At higher field strengths, this leads to an intrinsically better spatial specificity, as the relative contribution of the intravascular compartment is reduced, and the signal is weighted towards the microvasculature, that is expected to be closer to the ’true’ site of neuronal activity (Duong et al. 2003; Lee et al. 1999; Parkes et al. 2005; Yacoub et al. 2003; Yacoub et al. 2005; Zhao et al. 2004). While at 1.5 T the intravascular contribution to the SE fMRI signal dominates (Oja et al. 1999), the intravascular signal nearly vanishes at ultra-high field strength such at 9.4 T (Lee et al. 1999). At 3 T still approximately half of the functional signal change is of intravascular origin (Jochimsen et al. 2004; Norris et al. 2002), but the increased specificity of SE over GE could be demonstrated (Thulborn et al. 1997). Quantitative measurement of the spatial extent of the BOLD response (Parkes et al. 2005) showed a 13% narrower point spread function for SE-EPI, albeit at the cost of a factor of 3 reduction in functional CNR. An additional advantage of SE imaging is its insensitivity to through-plane susceptibility gradients which can result in substantial signal voids in GE images. It was shown in ref. (Norris et al. 2002) that parts of the inferior prefrontal brain activation associated with cognitive tasks could be imaged with SE-EPI, but not GE-EPI. However, SE-EPI suffers from in-plane distortions, and some T_2*-weighting will remain caused by the long EPI readout of typically 40 ms (Birn et al.; Duong et al. 2002). The severity of T_2* related artefacts increases rapidly with field strength due to the shortened relaxation time. As pointed out in ref. (Duong et al. 2002) T_2* effects can further lead to a broadening of the PSF, causing the effective spatial resolution to be less than the voxel size in regions of short T_2*, particularly at higher field strengths (4 T and 7 T) as used in their study. BOLD fMRI with pure T_2 contrast, and with no EPI artefacts, can be performed by using a multiply-refocused sequence, such as fast spin echo (FSE). This was demonstrated in an early study at 1.5 T (Constable et al. 1994) with a fully sampled multi-shot FSE sequence at relatively high in-plane resolution (1.6 x 3.2 mm^2). The resulting long repetition time (TR) of > 20 s for 5 slices, however, only allowed use of very long block stimuli. At the field strength of 1.5 T the FSE sequence was mainly sensitive to intravascular BOLD effects, but it was suggested in (Constable et al. 1994) that by adjusting the echo spacing the sensitivity could be tuned towards a specific range of vessel sizes. At 3 T, the increased contribution of extravascular dynamic averaging effects can be utilised. If for a given TE the echo train for signal acquisition is preceded by a preparation period with a long refocusing interval, the relative contribution from the extravascular compartment, and thus the more desirable portion of the BOLD contrast can be increased. As in SE-EPI, the centre of *k*-space should be acquired at a TE approximately equal to T_2. Sampling times can be made compatible with the requirements for fast fMRI by the use of partial Fourier and parallel imaging. By following this sampling strategy, repetition times comparable to that of SE-EPI can be realised (see Methods section). Acquisition rates of 8 slices per second can be achieved, permitting good sampling of the BOLD response with near whole brain coverage in about 3 s.

In this paper, the value of such an approach is investigated, and comparisons are made with the more conventional, singly-refocused SE-EPI sequence (some authors also refer to the spin echo in this context as the Hahn spin echo). To facilitate a conservative comparison of functional sensitivity, full *k*-space acquisition is used for SE-EPI.

Methods

Data acquisition

Two practical problems must be overcome to make fast multi-slice experiments viable as an alternative to SE-EPI. First, image acquisition times should ideally not exceed those of a conventional SE-EPI experiment. Second, the energy deposition of the refocusing pulses must not exceed specific absorption rate (SAR) limits; yet a high enough signal to noise (SNR) must be achieved at sufficient spatial resolution. Both constraints may be addressed by using a combination of partial Fourier (PF) imaging, and parallel imaging such as SMASH (Sodickson et al. 1999), SENSE (Pruessmann et al. 1999) or GRAPPA (Griswold et al. 2002).

To reduce total acquisition time we implemented the HASTE sequence with linear ascending phase-encoding (half-Fourier acquisition single shot turbo SE) sampling scheme with acceleration factor 4 and 7/8 PF. The first echo is refocused at 50 ms by a three-lobed 180° selective *sinc* pulse. All following pulses are 2 ms single-lobed *sinc* pulses. Sampling starts on the partially acquired side of *k*-space. Echo spacing was adjusted such that the *k*-space centre is acquired at the 'target' TE of 80 ms (at 3 T), giving an inter-echo TE of 6.5 ms. Under the conservative assumption of a tissue T_2 of 80 ms the line-broadening in this sequence caused by transverse relaxation is less than one pixel. The sequence is shown schematically in Fig. 7.1. Images were reconstructed offline in Matlab (The MathWorks, Inc., USA) using SENSE (Pruessmann et al. 1999) reconstruction. Sensitivity maps were calculated from separate moderately smoothed (FWHM 3 pixels) full resolution FLASH scans, using a third order polynomial fit for extrapolation beyond the edge of the object. Acquisition parameters were: matrix size 64 x 64, FoV = 224 mm, voxel size 3.5 x 3.5 x 5 mm^3, TR = 2 s, pixel bandwidth 300 Hz, effective echo train length of 14 *k*-space lines and T_{acq} = 130 ms per slice. Five slices covering the visual cortex were acquired. Fully sampled SE- and GE-EPI measurements were made using a singly-refocused double-echo sequence, with the same geometric parameters as for HASTE and at a bandwidth of 2700 Hz / pixel. For the EPI sequence, this resulted in a total acquisition time T_{acq} = 120 ms per slice. Images were reconstructed online using the product image reconstruction. All data were acquired on a 3 T Siemens Magnetom Trio system (Siemens Medical Solutions, Erlangen, Germany) using the product 8-channel head coil.

Stimulus Material and Subjects

Visual stimuli consisting of 30 s rest followed by 21 s of 8 Hz inverting black and white checkerboards were shown using Presentation software (Neurobehavioral Systems, Inc., USA). Each experimental run lasted 6 min (180 images). Scan order was alternated between sessions. Six subjects with normal or corrected-to-normal vision were scanned, after having given written consent according to local regulations.

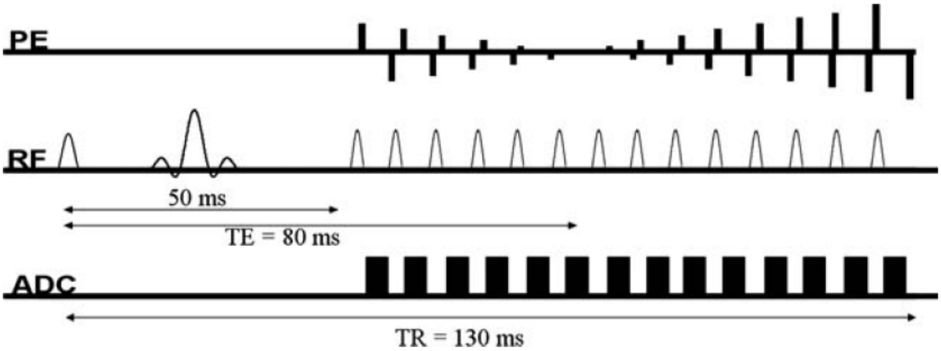

Figure 7.1: *Schematic of the HASTE sequence used for the activation studies. The initial 50 ms period sensitises for BOLD contrast by allowing dynamic averaging. Using a combination of 4-fold accelerated SENSE and 7/8 partial Fourier only 14 k-space lines are sampled, reducing total slice acquisition time to 130 ms, close to that of a typical SE-EPI experiment.*

Data Processing and Analysis

Linear trend removal and high-pass filtering of all time courses was done in Brainvoyager 2000 (Brain Innovation, The Netherlands). *t*-tests were performed at $p < 0.0001$ (all p values uncorrected for small volumes). Mean and maximum *t*-scores, as well as count of active voxels were noted. Functional CNR was calculated for each subject as the average signal change divided by the mean error on the average stimulus response curve. In addition, a spatial map of pixel-wise temporal SNR (tSNR) was calculated in one dataset to assess the effect of parallel imaging on temporal stability.

Results

Stable SENSE reconstruction of the T_2 prepared HASTE images could be achieved despite the high acceleration factor. Only in some cases could weak residual fold-over be observed. Fig. 7.2 shows GE-EPI, SE-EPI and HASTE images for comparison. Fig. 7.3 (a) and (b) show corresponding slices from SE-EPI and HASTE experiments in one functional subject. The activation overlay represents *t*-scores at $p < 0.0001$. Temporal SNR of the two pre-processed time courses is shown in Fig. 7.3 (c) and (d). In the occipital cortex, tSNR of HASTE is comparable to that of SE-EPI, but lower in other regions. The spatial noise variation not only shows the expected dependence on tissue type, but also clearly resembles that of the *g*-map (Fig. 7.3 (e)). The *g*-factor is the coil geometry related noise increase caused by the use of parallel imaging (Pruessmann et al. 1999). Figure 7.3 (f) illustrates that the visual cortex is not strongly affected by *g*-noise; typical values here are between 2.0 and 2.6. Higher values of to up to 6 were observed in central brain regions.

The average ($n = 6$) BOLD response curves for SE-EPI and HASTE measurements are shown in Fig. 7.4 (top). The time evolution of both curves is identical, however, the maximum signal change in SE-EPI (1.88%) is higher than in the HASTE measurement (1.33%), at comparable baseline intensities. Both methods show that about 9 s is required for the signal to return to baseline, followed by a BOLD undershoot. Normalising the activation timecourses shows that both main response and undershoot of HASTE are proportionately reduced compared to SE-EPI, and the curves are almost perfectly aligned (not shown).

At $p < 0.0001$, average activation volumes are comparable in SE-EPI (332 voxels) and HASTE (305 voxels). Averages of mean and maximum *t*-scores in the HASTE measurements are 7.25 ± 0.37 and 16.42 ± 1.86, respectively, and 7.35 ± 0.32 and 16.12 ± 1.72 respectively for SE-EPI. Considering only voxels active in both scans yields a similar picture, with 7.81 ± 0.75 and 16.30 ± 2.04 for HASTE, and 7.99 ± 0.59 and 16.01 ± 1.87 for SE-EPI. Differences in *t*-scores are not significant (permutation test, $p < 0.05$) and much smaller than the natural variation between subjects. Calculation of functional CNR yields 16.55 (noise 0.12) for SE-EPI, and 11.19 (noise 0.11) for HASTE; this means that the differences in sensitivity can be explained by the differences in signal change amplitude alone.

Discussion

Considering the acquisition parameters used and the *g*-factors observed in the occipital lobe, ‘within-image’ SNR of HASTE would be expected to be approximately 30% lower than that of SE-EPI. The observation of comparable effective temporal SNR of both methods (in the visual areas) is attributable to the contribution of physiological noise which markedly reduces the relative effect of image noise, and thus the use of parallel imaging on temporal stability (de Zwart et al. 2002).

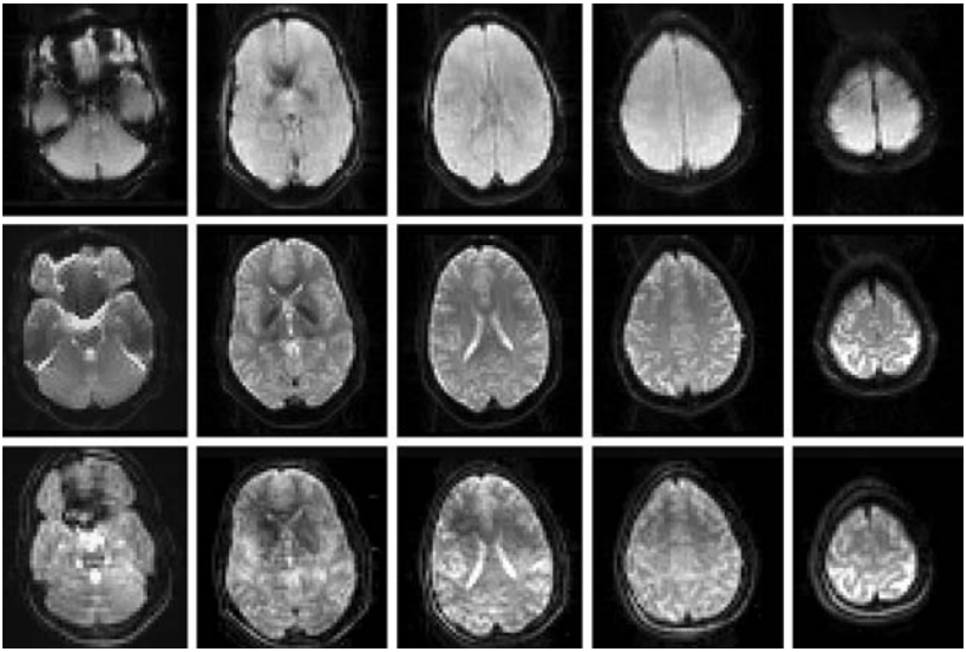

Figure 7.2: *Five brain slices spanning from inferior to superior brain, acquired with GE-EPI (top), SE-EPI (middle) and T_2-prepared HASTE (bottom). The signal voids due to through-plane dephasing that are clearly present in the GE-EPI are absent in SE-EPI, but in-plane distortions remain and are particularly severe in the inferior brain. In both cases Nyquist ghosting can be observed. These EPI artefacts are not present in the HASTE images, however the effect of coil sensitivity variations (e.g. in the left frontal regions) appears more pronounced. Traces of weak residual foldover that resembles the pattern of the g-map (see Fig. 7.3 (e)) can be seen in the third and fourth slices. In no instance, however, did this result in a projection of artefactual visual activation into other brain areas.*

In central brain areas, however, much higher *g*-factors and the reduced tSNR suggest that functional sensitivity would be compromised. The *g*-noise can be reduced by a choosing lower acceleration factor and/or different coil array, as the *g*-maps are uniquely related to the combination of coil geometries with acceleration factor *a*, and *g*-values rapidly grow with the number of pixels overlapping in the foldover (cf. Fig. 7.3). While a protocol with acceleration factor 3 might therefore produce a ‘more benign’ *g*-map, it would not have allowed meeting our demands on T_{acq} and target TE of 80 ms, and required use of ambitious PF (< 60%) if the number of refocusing pulses were to be kept constant. On future systems this is will not be an issue as the rapidly growing number of coil elements (Wiggins et al.) can yield much higher SNR: The *g*-noise penalty for acceleration factors much smaller than the number of coils would be much lower than for the *g*-factors observed here. Furthermore, *k*-space based reconstruction (e.g. GRAPPA or SMASH) would yield spatially almost invariant noise distributions, which might be regarded as favourable in an fMRI setup.

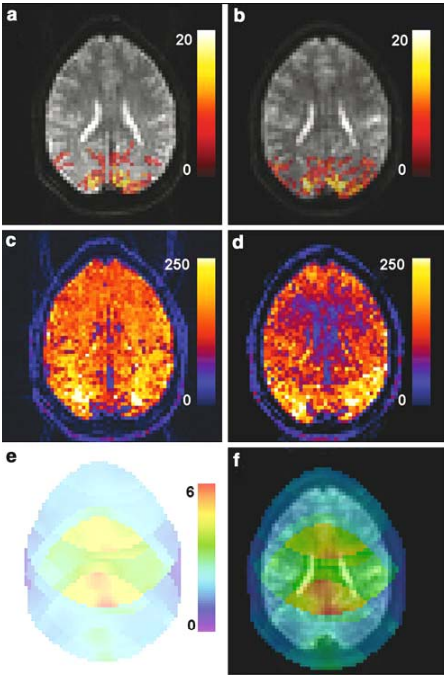

***Figure** 7.3(see Appendix for colour version): Typical SE-EPI (a) and HASTE (b) images with activation overlays at $p < 0.0001$ (colour scale represents t-scores). Subfigures (c) and (d) show tSNR maps of the SE-EPI and HASTE data, respectively. Spatial variation in the latter resembles that of the g-map (e). The overlay of g-map on HASTE image (f) illustrates that visual areas are not strongly affected by g-noise.*

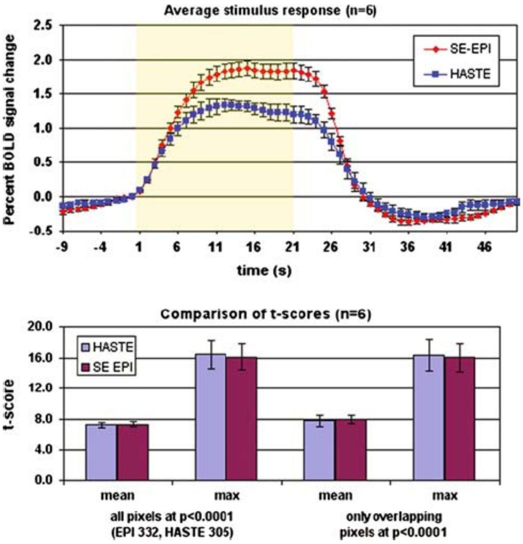

***Figure 7.4:** Results of SE-EPI and HASTE BOLD measurements. Top: Stimulus response curve considering all active pixels, averaged over subjects (error bars = SEM over subjects, they reflect variation in signal change across subjects, but not sensitivity). Note that the average response curves of individual subjects were not normalised prior to averaging to allow comparison of the amplitude of the signal change between HASTE and EPI. The shaded region marks the 21 s stimulation period. Bottom: Mean and maximum t-scores at $p < 0.0001$ (subject average, error bars = SD). For the calculation of overlapping pixels the distortion was assumed to be negligible.*

Magnetisation transfer effects due to off-resonance power deposition posed no problem for the five-slice experiment in this study, but could potentially lead to signal attenuation and SNR reduction for short TR and/or longer refocusing pulse trains (Melki and Mulkern 1992). Substantial power reductions with only moderate SNR loss could be achieved by use of variable flip-angle schemes (Le Roux and Hinks 1993), and help improve fast multi-slice experiments.

A clear advantage of HASTE is the absence of inhomogeneity artefacts, yielding images that are free of both dropout and distortion. The latter allows precise mapping from functional to anatomical data, and can further be expected to be beneficial for group studies. It was shown in ref. (Cusack et al. 2003) that the application of post-hoc distortion correction to EPI data not only improves coregistration with the anatomical images, but also that group statistics on functional studies improved considerably. HASTE acquisitions should yield the same benefits, without the difficulties associated with correction methods that rely on the use of separately acquired reference data such as field maps.

In our implementation of the HASTE sequence, the signal acquisition is preceded by a preparation experiment for dynamic averaging that lasts 50 ms. Ideally, the sequence would refocus the first echo at the optimal TE of 80 ms to maximise the dynamic averaging contribution, followed by centre-out acquisition of *k*-space, but at the price of a much longer total acquisition time. The compromise was chosen to achieve comparable slice acquisition times for SE-EPI and HASTE and permit a conservative comparison of the two methods. While we chose to use conventional SE-EPI without *k*-space undersampling for an unbiased assessment of relative functional sensitivities, SE-EPI readout times could also have been reduced by using factor a parallel undersampling. This would have resulted in a $g \cdot \sqrt{a}$ fold SNR penalty, and hence sensitivity reduction in favour of HASTE, but the benefit of a-fold reduction in EPI distortion / T_2* blurring.

The presence of T_2* decay during the long readout train can be expected to contribute considerably to the functional signal changes in SE-EPI (Birn et al.; Duong et al. 2002). This most likely explains the majority of the observed difference between SE-EPI and HASTE. Phantom studies at 1.5 T have shown that up to 37% of the SE signal changes can arise due to static dephasing (Birn and Bandettini). In vivo data at higher fields suggest an even larger contribution of T_2* effects, approximately 60% (Keilholz et al. 2005). The amount of T_2* contribution depends on the spatial features of the activated areas, and would be largest for activation with higher spatial frequency components. Quantification of this effect is hence object dependent and beyond the scope of this paper.

A difference between SE-EPI and HASTE based T_2 contrast is also likely to arise due to differences in refocusing interval: A standard SE-EPI protocol for fMRI will have a single refocusing pulse for TE 80 ms, but our HASTE implementation has a spin echo preparation experiment with TE 50 ms, followed by multiple refocusing pulses, with the *k*-space centre at TE 80 ms. In partially oxygenated blood the proton exchange between erythrocytes and blood plasma, or diffusion in the local fields gradients arising from the presence of deoxy-haemoglobin, results in a shortening of the effective intravascular T_2 with increasing deoxy-haemoglobin levels and increasing refocusing interval in CPMG sequences (Bartha et al. 2002; Stefanovic et al. 2003). This effect in itself forms the basis of the recently proposed VERVE fMRI contrast mechanism (Stefanovic and Pike 2005). The rapid refocusing in the HASTE acquisitions thus implies elongation of the intravascular T_2 compared to SE-EPI, where only a single refocusing pulse is applied, and hence a reduction in the functional sensitivity to intravascular signal changes. Similarly, increasing the number of refocusing pulses reduces the dynamic averaging contribution. Consequently both functional contrast mechanisms that contribute to spin-echo BOLD will be somewhat reduced in effect by the addition of extra refocusing pulses. It is difficult to assess the significance of this sensitivity loss, but as the difference in sensitivity between SE-EPI and HASTE in the present study is

consistent with the literature regarding the T_2* sensitivity of SE-EPI (Birn and Bandettini; Keilholz et al.), it may be expected to be small.
A potential source of functional contrast is inflow effects. These could in principle explain some of the discrepancy in signal change if they contribute differently to the two methods. However, inflow should contribute little given the SE-EPI acquisition parameters (Yacoub et al. 2005), and be similar as the same TR of 2 s is used in both sequences.

An interesting question is raised by the fact that such a pronounced undershoot is observed in the SE data, particularly the HASTE. While it is generally accepted that the post-stimulus undershoot is in some way caused by the complex temporal relationship between the parameters cerebral blood volume (CBV), blood flow (CBF) and oxygen consumption ($CMRO_2$), there are two main types of explanation. First, the 'Balloon model' family (Buxton et al. 1998; Mandeville et al. 1999) which assumes a strong coupling between $CMRO_2$ and CBF, but a temporally varying relationship between of CBV and CBF. According to this model, following stimulation, delayed vascular compliance causes CBV to return to baseline more slowly than CBF and $CMRO_2$, leading to a negative BOLD signal. The second type of explanation postulates a decoupling of CBF and $CMRO_2$: the undershoot is then caused by post-stimulus oxygen consumption that remains elevated even after CBF has returned to baseline (Lu et al. 2004).

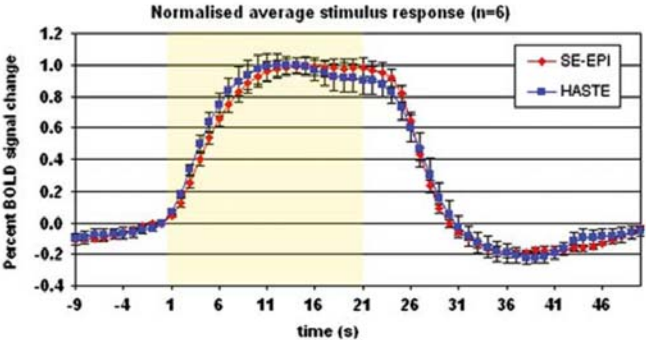

Figure 7.5 *(see Appendix for colour version): Normalisation of the curves shown in Fig. 7.4 results in both response curves being perfectly aligned, showing that HASTE sensitivity in the main and undershoot response scales by the same factor compared to SE-EPI.*

We observed no difference between the normalised response curves of SE-EPI and HASTE, meaning that any T_2* effects present in the SE-EPI data equally affect both main BOLD signal and undershoot. These curves are shown in Fig. 7.5. Comparison of the normalised activation timecourses with the GE-EPI data (not shown) which were simultaneously acquired with the SE-EPI also showed no difference in the undershoot. This suggests that the same combination of mechanisms must be contributing to both the main BOLD signal and the post-stimulus undershoot. The Balloon model (Buxton et al. 1998) predicts that the undershoot is largely due to extravascular static dephasing around the larger (downstream) vessels. An undershoot in the BOLD signal could, however, also be the result of intravascular T_2 changes as would result from sustained post-stimulus oxygen metabolism. Static dephasing effects are refocused by the SE experiment and, so if the standard Balloon model hypothesis were true, then the undershoot would have to be reduced in magnitude relative to the main response. Observation of the same signal contribution to both parts of the BOLD response thus rather excludes the interpretation of the undershoot as a downstream static dephasing effect, leaving changes in deoxy-haemoglobin concentration as the more likely explanation. Such post-stimulus elevation in deoxy-haemoglobin could be the result of ongoing oxygen metabolism after the return of CBV and CBF back to baseline, as suggested by Lu et al (Lu et al. 2004). That elevated CBV alone cannot be the cause for a post-stimulus signal decrease has recently been reported by Yacoub et al (Yacoub et al. 2006).

In conclusion, the application of fast spin echo sequences to fMRI was investigated. BOLD activation was robustly detected by HASTE acquisitions preceded by a preparation experiment for dynamic averaging. While the functional CNR in the occipital lobe was ~30% lower than for a conventional SE-EPI acquisition of approximately equal TR, the absence of image artefacts makes HASTE a viable alternative where distortion free images are required.

Acknowledgements

The work presented in this paper was supported by STW (Dutch Science Foundation) grant NGT.6154. The authors thank Markus Barth for useful discussions, and Markus Klarhöfer for providing Matlab code on which the SENSE reconstruction was based.

References

Bartha R, Michaeli S, Merkle H, Adriany G, Andersen P, Chen W, Ugurbil K, Garwood M. (2002) In vivo 1H2O T2+ measurement in the human occipital lobe at 4T and 7T by Carr-Purcell MRI: detection of microscopic susceptibility contrast. *Magn Reson Med* 47:742-750

Birn RM, Bandettini PA. The Effect of T2' Changes on Spin-Echo EPI-derived Brain Activation Maps, In: Proceedings of the 10th Annual Meeting of ISMRM, Honululu, Hawai, USA, 2002. Abstract 1324

Birn RM, Bodurka JA, Petridou N, Bandettini PA. Experimental determination of the effect of T2' changes in spin-echo EPI, In: Proceedings of the 12th Annual Meeting of ISMRM, Kyoto, Japan, 2004. Abstract 997

Buxton RB, Wong EC, Frank LR. (1998) Dynamics of blood flow and oxygenation changes during brain activation: the balloon model. *Magn Reson Med* 39:855-864

Constable RT, Kennan RP, Puce A, McCarthy G, Gore JC. (1994) Functional NMR imaging using fast spin echo at 1.5 T. *Magn Reson Med* 31:686-690

Cusack R, Brett M, Osswald K. (2003) An Evaluation of the Use of Magnetic Field Maps to Undistort Echo-Planar Images. *NeuroImage* 18:127-142

de Zwart JA, van Gelderen P, Kellman P, Duyn JH. (2002) Application of sensitivity-encoded echo-planar imaging for blood oxygen level-dependent functional brain imaging. *Magn Reson Med* 48:1011-1020

Duong TQ, Yacoub E, Adriany G, Hu X, Ugurbil K, Kim SG. (2003) Microvascular BOLD contribution at 4 and 7 T in the human brain: gradient-echo and spin-echo fMRI with suppression of blood effects. *Magn Reson Med* 49:1019-1027

Duong TQ, Yacoub E, Adriany G, Hu X, Ugurbil K, Vaughan JT, Merkle H, Kim SG. (2002) High-resolution, spin-echo BOLD, and CBF fMRI at 4 and 7 T. *Magn Reson Med* 48:589-593

Griswold MA, Jakob PM, Heidemann RM, Nittka M, Jellus V, Wang J, Kiefer B, Haase A. (2002) Generalized autocalibrating partially parallel acquisitions (GRAPPA). *Magn Reson Med* 47:1202-1210

Jochimsen TH, Norris DG, Mildner T, Moller HE. (2004) Quantifying the intra- and extravascular contributions to spin-echo fMRI at 3 T. *Magn Reson Med* 52:724-732

Keilholz S, Silva A, Duyn J, Koretsky A. The Contribution of T 2* to Spin-Echo EPI: Implications for High-Field fMRI Studies, In: Proceedings of the 13th Annual Meeting of ISMRM, Miami, FL, USA, 2005. Abstract 32

Le Roux P, Hinks RS. (1993) Stabilization of echo amplitudes in FSE sequences. *Magn Reson Med* 30:183-190

Lee SP, Silva AC, Ugurbil K, Kim SG. (1999) Diffusion-weighted spin-echo fMRI at 9.4 T: microvascular/tissue contribution to BOLD signal changes. *Magn Reson Med* 42:919-928

Lu H, Golay X, Pekar JJ, van Zijl PCM. (2003) Functional magnetic resonance Imaging based on changes in vascular space occupancy. *Magnetic Resonance in Medicine* 50:263-274

Lu HZ, Golay X, Pekar JJ, van Zijl PCM. (2004) Sustained poststimulus elevation in cerebral oxygen utilization after vascular recovery. *Journal of Cerebral Blood Flow and Metabolism* 24:764-770

Mandeville JB, Marota JJ, Ayata C, Zaharchuk G, Moskowitz MA, Rosen BR, Weisskoff RM. (1999) Evidence of a cerebrovascular postarteriole windkessel with delayed compliance. *J Cereb Blood Flow Metab* 19:679-689

Mansfield P. (1984) Real-time echo-planar imaging by NMR. *Br Med Bull* 40:187-190

Melki PS, Mulkern RV. (1992) Magnetization transfer effects in multislice RARE sequences. *Magn Reson Med* 24:189-195

Norris DG, Zysset S, Mildner T, Wiggins CJ. (2002) An investigation of the value of spin-echo-based fMRI using a Stroop color-word matching task and EPI at 3 T. *Neuroimage* 15:719-726

Ogawa S, Lee TM, Kay AR, Tank DW. (1990) Brain magnetic resonance imaging with contrast dependent on blood oxygenation. *Proc Natl Acad Sci U S A* 87:9868-9872

Oja JM, Gillen J, Kauppinen RA, Kraut M, van Zijl PC. (1999) Venous blood effects in spin-echo fMRI of human brain. *Magn Reson Med* 42:617-626

Parkes LM, Schwarzbach JV, Bouts AA, Deckers RH, Pullens P, Kerskens CM, Norris DG. (2005) Quantifying the spatial resolution of the gradient echo and spin echo BOLD response at 3 Tesla. *Magn Reson Med* 54:1465-1472

Pruessmann KP, Weiger M, Scheidegger MB, Boesiger P. (1999) SENSE: sensitivity encoding for fast MRI. *Magn Reson Med* 42:952-962

Sodickson DK, Griswold MA, Jakob PM. (1999) SMASH imaging. *Magn Reson Imaging Clin N Am* 7:237-254, vii-viii

Stefanovic B, Pike GB. (2005) Venous refocusing for volume estimation: VERVE functional magnetic resonance imaging. *Magn Reson Med* 53:339-347

Stefanovic B, Sled JG, Pike GB. (2003) Quantitative T2 in the occipital lobe: the role of the CPMG refocusing rate. *J Magn Reson Imaging* 18:302-309

Thulborn KR, Chang SY, Shen GX, Voyvodic JT. (1997) High-resolution echo-planar fMRI of human visual cortex at 3.0 tesla. *NMR Biomed* 10:183-190

Wiggins G, Potthast A, Triantafyllou C, Lin F, Benner T, Wiggins C, Wald L. A 96-channel MRI-system with 23- and 90-channel phase array head coils at 1.5T, In: Proceedingsof the 13th Annual Meeting of ISMRM, Miami, FL, USA, 2005. Abstract 671

Williams DS, Detre JA, Leigh JS, Koretsky AP. (1992) Magnetic resonance imaging of perfusion using spin inversion of arterial water. *Proc Natl Acad Sci U S A* 89:212-216

Yacoub E, Duong TQ, Van De Moortele PF, Lindquist M, Adriany G, Kim SG, Ugurbil K, Hu X. (2003) Spin-echo fMRI in humans using high spatial resolutions and high magnetic fields. *Magn Reson Med* 49:655-664

Yacoub E, Ugurbil K, Harel N. (2006) The spatial dependence of the poststimulus undershoot as revealed by high-resolution BOLD- and CBV-weighted fMRI. *J Cereb Blood Flow Metab* 26:634-644

Yacoub E, Van De Moortele PF, Shmuel A, Ugurbil K. (2005) Signal and noise characteristics of Hahn SE and GE BOLD fMRI at 7 T in humans. *Neuroimage* 24:738-750

Zhao F, Wang P, Kim SG. (2004) Cortical depth-dependent gradient-echo and spin-echo BOLD fMRI at 9.4T. *Magn Reson Med* 51:518-524

Chapter 8 Investigation into the origin of the BOLD post-stimulus undershoot using T_2-weighted fMRI

Abstract

As a consequence of neural stimulation the blood oxygenation-level dependent (BOLD) contrast in gradient-echo echo-planar imaging (GE-EPI) based functional MRI leads to an increased MR signal in activated brain regions. Following this, a BOLD signal undershoot below baseline is generally observed with GE-EPI. The origin of this undershoot has been the focus of many investigations using fMRI and optical modalities, but the underlying mechanisms remain disputed.

Here, we investigate the BOLD undershoot following visual stimulation by using a purely T_2-weighted fMRI sequence at 1.5 T and 3 T. By taking advantage of the field strength-dependency of the T_2 BOLD contrast, and complete absence of static dephasing effects due to the pure spin echoes, one can draw conclusions about the origin of the BOLD undershoot, and test the hypotheses in the literature.

We observe a significant undershoot at both field strengths, with constant undershoot-to-main response ratio. This provides compelling evidence that the undershoot is caused by BOLD changes due to elevated post-stimulus deoxy-haemoglobin concentration. ‘Delayed vascular compliance’ as suggested by the well-known Balloon and Windkessel models does not appear capable of explaining the undershoot. Our results also suggest that blood volume changes in arterioles and capillaries, for which there is consistent evidence from optical imaging studies, cannot alone cause the undershoot. This has important implications for models of neurovascular response and provides further support for the decoupling of changes in the rate of oxygen metabolism and blood flow. In addition, the hypothesis of an ‘arteriolar balloon’ is introduced, that potentially explains the undershoot timecourse.

Poser BA, van Mierlo E, Norris DG. *(in revision)*

Introduction

In gradient-echo (GE) based functional MRI (fMRI) the positive main blood oxygenation level dependent (BOLD) signal response is typically followed by a period in which the signal falls below baseline after the end of stimulation (Buxton et al. 1998; Frahm et al. 2008; Frahm et al. 1996; Jones 1999; Kwong et al. 1992; Mandeville et al. 1999; Yacoub et al. 2006; Zhao et al. 2007). This period is commonly referred to as the BOLD post-stimulus undershoot, and can persist up to one minute after cessation of the stimulus (Frahm et al. 1996). The BOLD response arises due to a combination of physiological changes upon neuronal activation, namely changes in cerebral blood flow (CBF), cerebral blood volume (CBV) and cerebral metabolic rate of oxygen consumption ($CMRO_2$). While the existence of the post-stimulus BOLD undershoot is undisputed, it is far from clear which mechanism, or combination of mechanisms causes it. Numerous studies have been performed to investigate the origin of the effect, and there are several models and hypotheses discussed in the literature that provide plausible explanations for it (Buxton et al. 1998; Frahm et al. 2008; Frahm et al. 1996; Hoge et al. 1999; Jones 1999; Lu et al. 2004; Mandeville et al. 1999; Turner and Thomas 2006; Uludag et al. 2004; Yacoub et al. 2006).

We propose in this study that the models can be tested by performing fMRI experiments with a purely T_2-weighted (spin echo) MR pulse sequence (Poser and Norris 2007a) at the two main magnetic field strengths of 1.5 and 3 T.

There are two T_2 contrast mechanisms that contribute to the BOLD signal change: First, changes in the effective intravascular T_2 relaxation time which directly depends on the deoxy-haemoglobin concentration (Kennan et al. 1994). This contribution is spatially relatively unspecific, as it is common to all post-capillary vessels, and to some extent the capillaries. Second, spin dephasing effects caused by random spin diffusion in the magnetic field gradients about the microvasculature (Ogawa et al. 1993). This extravascular dynamic averaging causes signal changes around micro-vessels, which are expected to yield a high spatial specificity as they originate closer to the site of neuronal activation. At 1.5 T nearly 100% of the positive spin echo (SE) BOLD signal change is of intravascular origin (Constable et al. 1994; Jones 1999; van Zijl et al. 1998). At 3 T, this contribution is reduced to about 50% (Jochimsen et al. 2004; Norris et al. 2002); the remainder is due to dynamic dephasing in the microvasculature. The increased spatial specificity of T_2-weighted fMRI with SE-EPI, as compared to T_2*-weighted fMRI with GE-EPI, typically makes SE-EPI the method of choice for applications on both humans and animals at very high main magnetic field strengths of 7 T and above, and could also be demonstrated in the human at 3 T (Norris et al. 2002; Parkes et al. 2005). The use of SE-EPI implies a potentially significant T_2*-weighting due to the long EPI readout the degree of which will depend on the spatial frequencies present in the activation area. This can be avoided by the use of pure SE sequences (Constable et al. 1994; Poser and Norris 2007a), such as a Fast Spin Echo sequence.

The field strength dependence of the T_2 contrast can be exploited in a straightforward, yet very robust manner to investigate the origin of the BOLD undershoot: Conclusions can be drawn both from the occurrence of an undershoot, and the ratio of the undershoot to the main BOLD response at the two different field strengths. In the following we will first briefly summarise the existing models for the post-stimulus undershoot, and then describe how these can be tested.

Models for the post-stimulus BOLD undershoot

Delayed vascular compliance

One of the most prominent models is the Balloon Model (Buxton et al. 1998), which is based on data obtained from anaesthetised rats receiving electrical forepaw stimulation. CBV measurements with MION contrast agent showed a slow post-stimulus return of CBV in comparison to CBF and $CMRO_2$. According to this model, a temporal post-stimulus decoupling of CBF and CBV causes a relatively slower return of venous CBV to baseline. This is postulated to arise from the vaso-mechanical properties of the venous vessels: Upon neuronal activation, the local increase in blood flow, and therefore blood pressure, causes vaso-dilation in the venous bed which is largely accountable for the rise in CBV during activation. Following cessation of the stimulus, the passive process of re-contraction lasts longer than the return of CBF back to baseline. This is often referred to as *delayed vascular compliance*. The consequence is a temporal ‘mismatch’ between CBV and CBF. A similar mechanism for the undershoot was proposed by (Mandeville et al. 1999), based on the same data. The post-stimulus undershoot was attributed to a ‘post-capillary Windkessel’ that accommodates an elevated blood volume beyond the period of increased blood flow. Both Balloon and Windkessel models thus interpret the undershoot as a consequence of the mechanical characteristics of the vasculature rather than the physiological or metabolic processes directly associated with the neuronal activation.

It could be shown that the Balloon model can be successfully adapted from rodent data (Buxton et al. 1998) to human data at both 1.5 T (Feng et al. 2001; Friston et al. 2000), and 3 T (Mildner et al. 2001; Obata et al. 2004) yielding parameters within physiologically plausible ranges. A modification of the Windkessel model incorporating a delayed compliance was proposed by (Kong et al. 2004) to improve the description of the post-stimulus vaso-dynamics. The Balloon model calculations in (Obata et al. 2004) however show that a substantial variation in the $CMRO_2$ and CBV responses can yield very similar CBF and BOLD responses: a good model fit to the experimental data hence does not necessarily imply that the model is thereby validated given the large number of degrees of freedom associated with it.

Given that venous CBV accounts for 60 - 80% of the total blood volume (Lee et al. 2001), and the lack of a suitable model for capillary hyperaemia, the observed CBV changes were for a long time attributed to the post-capillary / venous compartment, an interpretation that agrees well with the hypothesis of the delayed compliance models.

Sustained elevation of $CMRO_2$

A second plausible explanation for the post-stimulus undershoot is a sustained increase in oxygen consumption after blood flow has returned to baseline. Continued oxygen metabolism after cessation of neuronal activation and at baseline CBF would result in an increase in the amount of deoxy-haemoglobin in the venous capillaries and draining vessels. This mechanism was suggested in early work by the Göttingen group (Frahm et al. 1996). Evidence that CBV can return to baseline simultaneously with BOLD, and hence by implication CBF, was provided in MION-weighted cat studies by (Harel et al. 2002), and more recently (Nagaoka et al. 2006) who investigated $CMRO_2$ changes in the absence of CBV changes under hypotension. MR studies using the recently developed VASO technique (Lu et al. 2003) report similar findings. The first of these (Lu et al. 2004) shows a strong BOLD undershoot after both CBV and CBF have returned to baseline, a result that has since been supported by other VASO studies (Donahue et al. 2008; Gu et al. 2005; Poser and Norris 2007b). A VASO study into the undershoot under hypoxic conditions (Tuunanen et al. 2006) demonstrates that CBV is at resting state level during the BOLD undershoot period. Also functional bolus tracking experiments revealed the expected change in CBV during the main BOLD response but not during the undershoot (Frahm et al. 2008). These again support a metabolic rather than haemodynamic mechanism for the undershoot.

Functional near-infrared spectroscopy (fNIRS) studies (Jasdzewski et al. 2003; Schroeter et al. 2006) reported a decrease in oxy-haemoglobin and increase in deoxy-haemoglobin that accompany the BOLD undershoot; notably, total haemoglobin as a measure of CBV returned to baseline immediately after the end of stimulation. In agreement with this, measurements of tissue oxygen tension showed a clear post-stimulus pO_2 undershoot (Ances et al. 2001), while CBF as measured with laser-Doppler flowmetry quickly returned to baseline (Ances et al. 2001). These non-MR studies thus show that deoxy-haemoglobin remains increased after total haemoglobin (CBV) and oxy-haemoglobin (CBF) has returned to baseline, suggesting an accumulation of deoxy-haemoglobin in the tissue as would be the result of post-stimulus prolonged oxygen metabolism, rather than a CBV effect.

A mechanism by which $CMRO_2$ remains elevated for a considerable duration post-stimulus seems physiologically plausible, as oxygen is required to re-establish ionic concentration gradients that discharge during neuronal activation. This restoration process which is thought to account for most of the brain energy demand (Attwell and Laughlin 2001) has been shown to last 30 to 40 seconds following the offset of stimulation (Brockhaus et al. 1993), in very good agreement with the typical duration of the BOLD undershoot.

CBV changes in capillaries

There is a growing body of evidence that a large proportion, if not all, of the CBV change takes place in the arterioles and capillaries. This is particularly reported in the recent optical imaging literature (Berwick et al. 2005; Devor et al. 2003; Devor et al. 2007; Hillman et al. 2007; Vanzetta et al. 2005; Villringer et al. 1994). These studies report a change in total haemoglobin, and by implication in CBV, in the parenchyma upon activation. Using a novel depth-resolved (3-D) optical imaging technique with simultaneous recording of oxy-, deoxy- and total haemoglobin (Hillman et al. 2007) could show significant stimulus related increases in parenchymal total haemoglobin concentration that match the observed arteriolar dilation; very small total haemoglobin changes are reported for the venous side, in the absence of measurable venous volume changes. Instead, it appeared that the flow increase in the veins concomitant with arteriolar CBV change manifests as change only in the venous flow speed.

Also in recent animal MR studies by Kim et al. it was observed that the majority of total CBV change upon neuronal activation originates from changes in arterial (and not venous) CBV (Jin and Kim 2008; Kim et al. 2007). The CBV response to visual stimulation in the human observed by (Wu et al. 2008) slightly leads the BOLD response, indicative of a fast arterial CBV increase while the BOLD signal by its nature originates largely from the vasculature downstream of the site of neuronal activation.

No satisfactory explanation for how the parenchyma can accommodate the observed increases in haemoglobin following arteriolar dilation has to date been proposed in the literature, which is why many models assume an invariant capillary CBV and total haemoglobin (Buxton et al. 1998; Mandeville et al. 1999). While CBV changes clearly occur somewhere in the vasculature, it is often somewhat carelessly assumed that space for the activation related CBV increase can in some way be found in the brain. The rise in CBV associated with a strong and sustained stimulus, such as visual stimulation, could lead to a pressure increase with fatal consequences if not (at least in part) compensated by a corresponding volume decrease of another compartment. Recently a mechanism was proposed that could explain how the observed parenchymal CBV changes are physiologically feasible (Turner and Thomas 2006). According to this mechanism, the endothelium of the capillaries acts as an exchange pool from which water molecules can diffuse into the intra-capillary space, thereby leading to a volume increase of the blood pool without need for a bulk volume change. While the Turner-Thomas model does not primarily aim at explaining the BOLD undershoot it does however incidentally suggest that the undershoot could originate as a CBV effect in the capillaries, where the endothelium accounts for up to 20% of the intra-capillary space and would then act as an equivalent of the ‘post-capillary Windkessel’: If the return of the capillary diameter to baseline is driven by osmotic gradients then the time constants associated with it are likely slow and may match the typical order of the BOLD undershoot (Turner and Thomas 2006). Furthermore, the CBV recovery in the parenchyma would be expected to last longer than that of CBF (in analogy to the delayed venous compliance), and larger draining vessels should not undergo a volume change. Further downstream, the relative contribution of the single-layered endothelium to the total vessel volume rapidly drops with increasing vessel diameter, arguing for a very good localisation of the undershoot to the site of neuronal activation.

Hypotheses on MR signal changes for purely T_2-weighted fMRI

Delayed vascular compliance
If the undershoot is the result of a decoupling of CBV and CBF in the downstream vasculature as suggested in the Balloon model, then the standard interpretation is that it can be explained by extravascular static dephasing that takes place around the larger draining veins; there would be no intravascular contribution as both CBF and $CMRO_2$ will have returned to their baseline values. Static dephasing is exclusively a T_2* effect. If a pure SE sequence is used, then all static dephasing effects are refocused and only T_2 contrasts remain. Therefore if the delayed vascular compliance model is correct then no undershoot should be seen in pure SE data at *either* field strength.

Sustained elevation of $CMRO_2$
Continued increased oxygen consumption after the end of stimulation, and the return of both CBV and CBF to baseline would result in an increase in the amount of deoxy-haemoglobin. This would cause a reduction in the intravascular T_2 of blood, and at 3 T an increase in extravascular dynamic dephasing: both mechanisms would contribute to the lower MR signal during the undershoot. The undershoot would thus be a 'negative' BOLD effect and arise from the same combination of contrast mechanisms as the main positive BOLD signal change. Hence an undershoot should also be seen in T_2-weighted data at *both* field strengths. While signal changes at 3 T would be expected to be considerably larger than at 1.5 T due to the additional contribution of extravascular dynamic averaging effects, the ratio of main BOLD effect to undershoot should be constant across field strengths.

CBV changes in capillaries
If there is no volume change on the venous side and only the capillaries expand upon activation as reported in the optical imaging literature, then once $CMRO_2$ and CBF, and thus venous T_2 have returned to baseline after stimulus cessation, any observed signal contributions to the SE BOLD undershoot would arise from the prolonged volume change in the capillaries, and be due to dynamic averaging, and possibly changes in capillary T_2.
This would lead to the observation of an undershoot in SE BOLD at 3 T. In the absence of additional post-capillary / venous T_2 changes, the negligible signal contribution from dynamic averaging effects at 1.5 T however, would lead to a strongly reduced or absent undershoot at 1.5 T. If the 'collapse' of the endothelium

is the mechanism for the CBV change in accordance with the Turner-Thomas hypothesis, and its recovery after the cessation of the stimulus results in the implied temporal CBV-CBF decoupling, then for a MR pulse sequence with only T_2 contrast this implies that dynamic averaging about the capillaries should generate an undershoot at 3 T, but not at 1.5 T.

A post-stimulus elevated CBV in the capillary bed that persisted after the return of $CMRO_2$ and CBF to baseline would necessarily lead to a local reduction of blood flow velocity in the expanded capillaries. Under the common premise that $CMRO_2$ is the product of blood flow and oxygen extraction fraction (OEF), an increase in OEF would ensue even at baseline $CMRO_2$. The consequence would then be a post-stimulus accumulation of deoxy-haemoglobin in the capillaries, but not in the post-capillary vessels, which would lead to an undershoot at 3 T, but not at 1.5 T.

The models and their respective outcomes for the SE BOLD experiments are summarised schematically in Fig. 8.1.

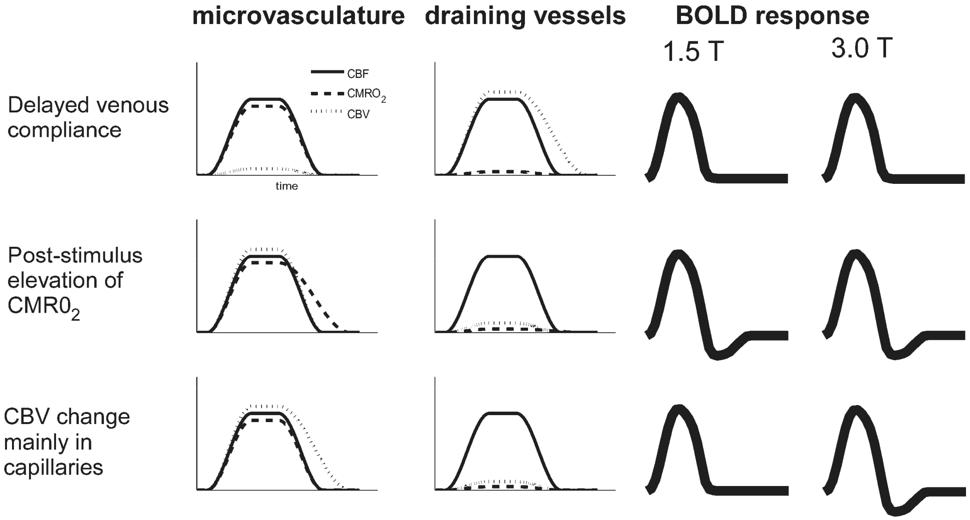

Figure 8.1: *Schematic summary of the CBF, CBV and $CMRO_2$ timecourses associated with the different models for the undershoot, and the T_2-weighted BOLD response that would be expected for each of them at 1.5 T and 3 T.*

Materials and Methods

Experiments were performed on 1.5 T Avanto and 3 T Trio TIM systems (Siemens, Erlangen, Germany), using the product 32-channel head coils at both field strengths. A purely T_2-weighted HASTE fMRI sequence was used as previously described (Poser and Norris 2007a). In short, the sequence refocuses the first spin echo at a TE of 50 ms to allow for dynamic averaging, followed by a rapid, linearly ascending, HASTE readout. The *k*-space centre is acquired at the target TE of 80 ms to optimise sensitivity for the grey matter signal. A schematic of the sequence is shown in Fig. 8.2. As grey matter T_2 is similar at both fields, identical acquisition parameters were used. Six slices were acquired with a TR of 2 s and resolution 3.5 x 3.5 x 5 mm^3 (matrix size 64 x 64, no slice gap). To shorten the echo train length and reduce power deposition, factor four parallel acceleration with GRAPPA image reconstruction was employed. Fat saturation was used. Each measurement lasted ten minutes, yielding 300 data points. For further details see (Poser and Norris 2007a). As an additional reference experiment to simultaneously acquire T_2* and T_2-weighted signal timecourses at 3 T, we used a combined dual-echo GE- and SE-EPI sequence, with TE = 23 ms and 80 ms, respectively, BW = 1960 Hz / px, 150 time points (5 minutes scan time), but otherwise identical geometric parameters. The vendor provided 'AutoAlign' scan was performed at the beginning of each of the two sessions to ensure identical slice positioning at both field strengths, and to yield the same anatomical coverage for all subjects.

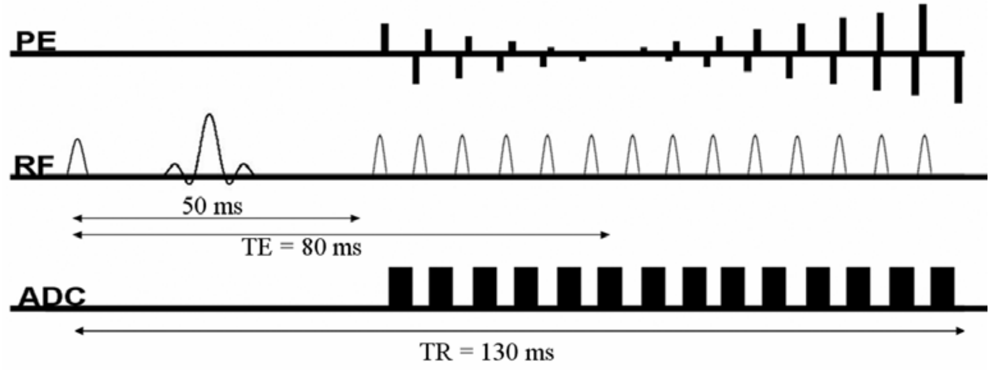

Figure 8.2: *T_2-weighted HASTE fMRI sequence used in this study. To allow dynamic averaging to take place, the preparation experiment forms the first echo at a TE of 50 ms. The k-space centre is acquired at a TE of 80 ms to maximise functional BOLD contrast.*

At each field strength, measurements were made on the same 14 subjects with normal or corrected-to-normal vision. Prior to the experiments informed consent was obtained in writing according to local regulations. The stimulus consisted of a black-and-white flickering checkerboard (frequency 10 Hz) which was presented in blocks of 20 s 'on' / 40 s 'off' using VSG (ViSaGe, Cambridge Research Systems, Rochester, England) stimulation equipment which was controlled using the CRS Toolbox for Matlab. The long rest period was chosen to allow full BOLD signal recovery. Throughout both 'on' and 'off' blocks, subjects were instructed to maintain fixation on a small cross that underwent random colour changes, to which they had to respond by button presses.

Data pre-processing and analysis were performed with Brainvoyager 2000 (BrainInnovation, Maastricht, The Netherlands) and custom-written software implemented in Matlab. Pre-processing included 3D motion correction and removal of linear intensity drifts. No other temporal or spatial smoothing was applied. Two of the 14 subjects were excluded from the analysis due to strong discontinuities in the signal timecourse, apparently caused by abrupt subject motion in the through-plane direction which was not properly detected nor 'corrected' by the 3D algorithm due the limited volume coverage in the slice direction. For the remaining subjects, the detected motion was well below one voxel.

For statistical analysis of the T_2-weighted data, *t*-tests were performed on the individual subjects, with the significance threshold set to $p < 0.01$. Activation timecourses were extracted as the average stimulus response of the voxels that met the activation criterion at *both* static magnetic field strengths. The baseline level was taken as the average signal of the three time points preceding stimulus onset.

The average stimulus response across subjects was calculated as the normalised event-related average of the individual response curves to ensure equal weighting of each subject. The undershoot-to-main response ratio was then determined from the average BOLD response curve, by computing the ratio of the integrals as the 'area under' the main response (Int_{mr}) and undershoot response (Int_{ur}).

To investigate a possible spatial dependence of the undershoot behaviour, the activated voxels in each subject were sorted according to percent signal change in the positive part of the BOLD response in the pure spin-echo data. Since the spatial resolution of the fMRI experiment is too limited for a detailed spatial analysis, the 25% of voxels with the highest signal change were, as an approximation, taken as voxels where the signal change would be dominated by larger draining vessels. The undershoot-to-main response ratio in the group average of these voxels was compared to that of the remaining 75% of voxels, which were assumed to contain mainly tissue.

The additional GE- and SE-EPI measurements acquired at 3 T were analysed by performing *t*-tests at $p < 0.0001$; the overlap of the activation maps thus obtained was then used as ROI for both data sets. Again, the resulting individual subject time courses were normalised prior to averaging.

Results

A pronounced undershoot is clearly observed in the subject average at both field strengths, as can be seen by reference to the left panel of Fig. 8.3. With 1.17% and 1.61% signal changes at 1.5 T and 3 T respectively, the average percentage BOLD response is considerably larger at 3 T. This agrees with the expectation of an additional contribution from dynamic averaging effects at the higher field strength.

The undershoot-to-main response ratio ($\mathrm{ratio}_{ur/mr}$) at 1.5 T and 3 T is 0.20 ± 0.07 and 0.22 ± 0.05, respectively. Here, the error in the ratio (σ_{ratio}) was calculated as $\sigma_{ratio} / \mathrm{ratio}_{ur/mr} = \sigma_{mr} / \mathrm{Int}_{mr} + \sigma_{ur} / \mathrm{Int}_{ur}$, where σ_{mr} and σ_{ur} are additional integral increments obtained by including the SEM on each point in the curves in the integral calculation for the main response (mr) and the undershoot (ur) respectively. The normalised timecourses are shown in the right panel of Fig. 8.3, which illustrates clearly that the signal timecourses have essentially identical characteristics at both field strengths. Moreover, the GE- and SE-EPI data that were acquired with the double echo sequence at 3 T also show an identical timecourse behaviour (Fig. 8.4), in the ROI defined by the commonly activated voxels ($p < 0.001$). Since simultaneous acquisition was used, very reliable quantitative comparisons can be made, despite the fact that some degree of T_2*-weighting can be expected also in the SE-EPI data.

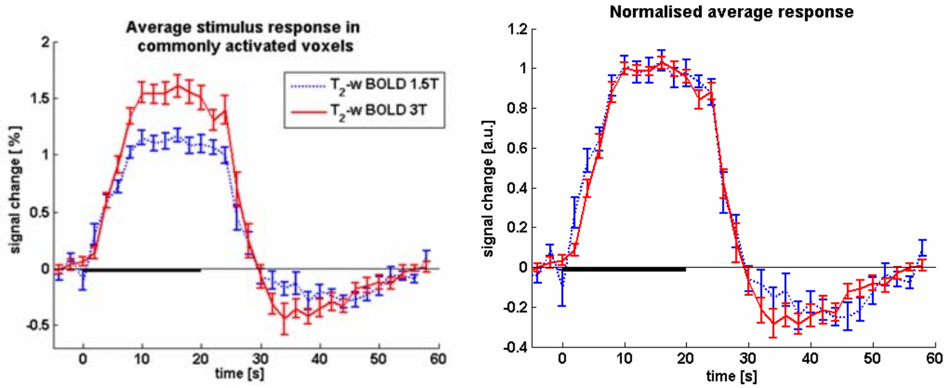

Figure 8.3: *BOLD signal changes at 1.5 and 3 T as measured with pure T_2 contrast, averaged over subjects ($N = 12$). A post-stimulus BOLD undershoot is clearly present at both field strengths. The average percent signal change at 1.5 T (1.17%) is much lower than at 3 T (1.61%), as would be expected due to the additional contribution of dynamic averaging effects at the higher field strength. The panel and the right shows the normalised T_2-weighted BOLD response curves overlaid, illustrating the essentially identical timecourse at both fields. In the individual subject response curves baseline was taken as the average of the five seconds proceeding stimulus onset; the individual curves were then normalised prior to averaging to ensure equal weighting. Error bars show SEM over subjects. The 20 s stimulation period is indicated by the solid black line on the time axis.*

The comparison of undershoot-to-main response ratio in ‘vessel’ versus ‘tissue’ voxels at 1.5 T yields an undershoot-to-main response ratio of 0.12 ± 0.06 and 0.23 ± 0.07 for ‘vessel’ and ’tissue’ voxels, respectively. At 3 T, the corresponding ratios are 0.10 ± 0.04 and 0.26 ± 0.04, respectively. The corresponding signal timecourses are shown in Fig. 8.5. Clusters of ‘vessel’ voxels are found particularly near the sagittal sinus and the cortical surface as would be expected. An example for the segmentation of ‘tissue’ and ‘vessels’ for one subject is shown in Fig. 8.6. When changing the threshold so as to separate out much less than 25% of voxels, an increasing tendency is observed that indicates a reduced undershoot-to-main response ratio for the few voxels exhibiting the largest signal change.

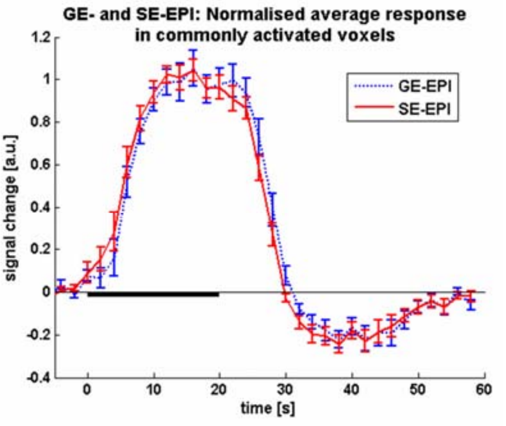

Figure 8.4: *Average normalised stimulus response curves as simultaneously measured at 3 T using the double echo GE- and SE-EPI sequence. No difference in temporal characteristics is observed between the two methods.*

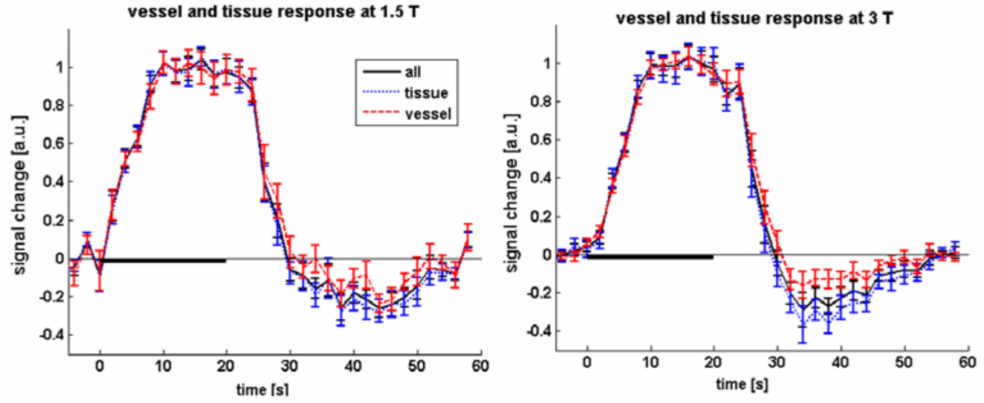

Figure 8.5: *Average normalised stimulus response for the different compartments at 1.5 T (left panel) and 3 T (right panel), separated on the basis of signal change. Timecourses for the 'tissue' and 'vessel' voxels are shown in blue and red, respectively. The solid black curves show the average over all active voxels.*

Discussion

No generally accepted consensus has been reached in the literature as to what causes the BOLD post-stimulus undershoot, in part because the haemo-dynamics within the different vascular compartments remain disputed. We propose here that origin of the undershoot can be pinpointed by using fMRI with pure T_2 contrast.

We observed a pronounced BOLD undershoot in the T_2-weighted data at both 1.5 T and 3 T. The temporal characteristics and ratios of main BOLD-response to undershoot are very similar. This points towards a BOLD mechanism for the undershoot in which exactly the same combination of contrast mechanisms is active during the main-BOLD and undershoot BOLD responses. In further support of this, we observed no difference in the temporal characteristics and undershoot-to-main response ratio of GE- and SE-EPI BOLD responses at 3 T, implying that T_2 and T_2* contrasts give identical BOLD response curves with regard to these parameters. A clear BOLD undershoot in SE-EPI can also be seen at 1.5 T, as is, for instance evident from the work of (Jones 1999); albeit this may also in part be attributable to residual T_2* contributions.

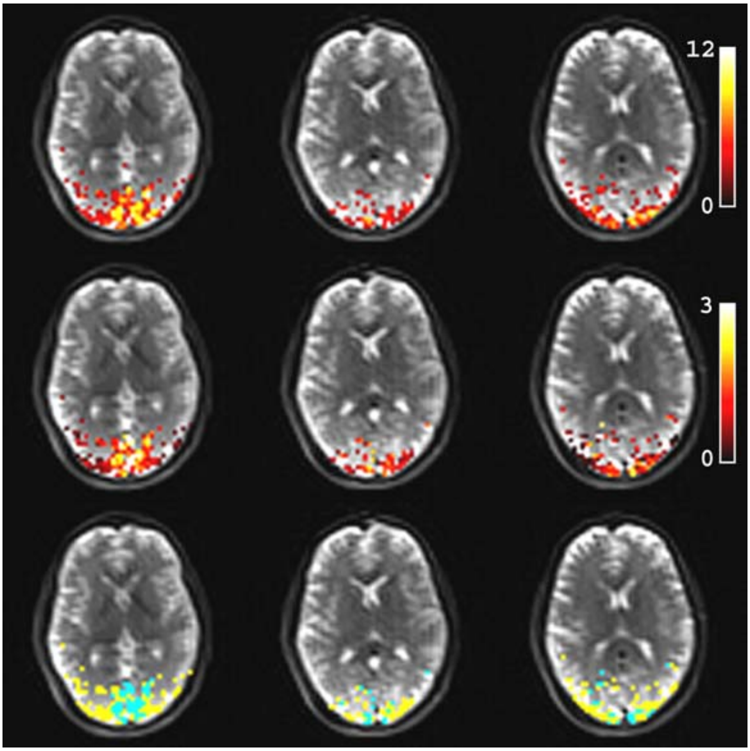

Figure 8.6 *(see Appendix for colour version): Example of activation maps from one subject at 3 T, overlaid on three slices of the corresponding T_2-weighted HASTE images (top row). Also shown are the percent signal changes (middle row), and the vessel-tissue segmentation map (bottom row). For the latter, active voxels were subdivided into 'tissue' and 'vessel' voxels by sorting them according to positive percent signal change. The top 25% were considered voxels with a large contribution from draining vessels, depicted in green. The remaining 75% were taken as tissue voxels, depicted in yellow.*

The fact that the shape of the BOLD response curves does not change as a function of field strength, despite the differing contrast mechanisms that contribute to the signal, leads to the conclusion that the measured curves are proportional to the timecourse of deoxy-haemoglobin content.

Looking into a possible dependence of the undershoot on the venous volume revealed that a stronger undershoot occurring in the putative tissue compartment.

The ratio for each compartment is not significantly different at both field strengths. At the spatial resolution of typical fMRI on which our interest is focused, however, a detailed separation of voxels by tissue and vessel content is clearly only approximate. We therefore chose an approximation by which voxels were rated according to the (positive) BOLD signal change. For an increasingly smaller fraction of voxels with the largest vessels there is a tendency towards a reduced undershoot. This may not be surprising as the largest vessels will also drain brain tissue that was not activated by the stimulus, and which (under the assumption of post-stimulus elevated $CMRO_2$) therefore carry blood with a smaller post-stimulus deoxy-haemoglobin concentration. Clearly, the vast majority of voxels did show a post-stimulus undershoot, independent of field strength.

It should be concluded from our observations that the undershoot arises due to changes in the amount of intravascular deoxy-haemoglobin, and not a temporal CBV-CBF decoupling. If the undershoot seen in GE-EPI were solely caused by the vaso-mechanical effects postulated by the Balloon and Windkessel models, the undershoot should have been absent in the pure spin-echo data.

If one considers parenchymal CBV changes, for instance by the mechanism of endothelial water exchange described by Turner and Thomas, then a more pronounced undershoot compared to 1.5 T should have been seen at 3 T as a result of dynamic averaging about the microvasculature. At 1.5 T the absence of a contribution of dynamic averaging effects would have resulted in the observation of no (or a strongly reduced) undershoot.

Our findings thus provide evidence for an increased deoxy-haemoglobin level even after the return of CBV and CBF to baseline and are consistent with the notion of continued elevation in oxygen metabolism.

A similar conclusion has previously been reached by other authors (Donahue et al. 2008; Lu et al. 2004), based on MR experiments that were aimed at directly but separately measuring the different physiological parameters GE-BOLD, CBV and CBF. Such an approach clearly has the advantage that each parameter can be studied separately, but requires the combination of data acquired with methods of differing sensitivity. Using an entirely different approach with only a single type of MR pulse sequence we have been able to draw the same conclusion. Furthermore, the previous data were obtained at a field strength of 1.5 T, thus without being sensitive to the BOLD contribution of extravascular dynamic averaging around the capillaries: in our experiments at 3 T we assume from the literature that 50% of the signal originates from the microvasculature, allowing evaluation of the capillary contributions. Our conclusions are in agreement with the recent MR findings from Frahm et al.'s bolus tracking fMRI experiments (Frahm et al. 2008).

A prominent and important temporal feature of the BOLD response should be noted here that merits further investigation in this context. Under the hypothesis that CBV and CBF return to baseline quickly and simultaneously, while $CMRO_2$ remains elevated, one would expect a rapid rise in deoxy-haemoglobin, leading to a fast BOLD signal drop into the undershoot. Such a sharp signal decrease however is not typically observed in published data. Also from our experimental results we estimate that the undershoot 'peaks' only approximately 10 – 15 s after stimulus offset.

This suggests that the undershoot is delayed by another mechanism that counteracts the $CMRO_2$ related accumulation of deoxy-haemoglobin, and which is moreover also field strength independent.

A plausible explanation for the observed timecourse of the BOLD in presence of sustained post-stimulus oxygen metabolism can be as follows.

In contrast to Buxton's original Balloon model (Buxton et al. 1998), we propose a ballooning effect that takes place in the arteriolar rather than venous compartment. The consequence of such an arteriolar balloon would be that oxygenated blood flows out of the balloon after stimulus cessation and hence elevates the blood velocity in the capillary bed for some time after the return of blood inflow f_{in} to baseline. Blood outflow f_{out} from the balloon would thus follow f_{in} with some delay that would depend on the vaso-mechanical properties of the arteriolar balloon, in an analogous manner to Buxton's venous balloon. The resulting washout would cause a lower deoxy-haemoglobin content in both capillary and venous bed than would have ensued from continued post-stimulus $CMRO_2$ alone, thereby slowing down the transition into the undershoot until the balloon is deflated and the arteriolar diameter has returned to baseline. Convincing evidence for vessel dilation in the arteriolar compartment can be found in the optical imaging literature; both Devor et al. and Hillman et al. (Devor et al. 2007; Hillman et al. 2007) for instance report arteriolar (but clearly not venous) diameter changes that agree very well with the measured venous flow speed (Hillman et al. 2007). This agrees with the MR results of (Kim et al. 2007) which show arterial CBV to be by far the main contributor to total blood volume changes.

Typically, functional perfusion studies report a relatively rapid baseline return of measured CBF. Since arterial spin labelling techniques however are mainly sensitive to the inflow of freshly labelled blood this does not exclude the possibility of a continued elevated flow of oxygenated blood through the capillaries from an arterial balloon.

To test the plausibility of the 'delayed arteriolar compliance' hypothesis as an explanation for the slow transition to the undershoot we constructed an arteriolar balloon by adapting the rate equations of the original Balloon model. The two modifications are that a) the explicit dependence of deoxy-haemoglobin on venous CBV is removed and b) the *outflow* from the balloon both supplies and drains the capillary bed. The relationship describing the rate of change on CBV remains unaltered. The resulting pair of coupled differential equations is thus

$$\frac{dq}{dt} = \frac{1}{\tau_0}\left[CMRO_2(t) - f_{out}(v) \cdot q(t)\right] \qquad [8.1]$$

$$\frac{dv}{dt} = \frac{1}{\tau_0}\left[f_{in}(t) - f_{out}(v)\right], \qquad [8.2]$$

where

$$f_{out}(v) = v^{\frac{1}{\alpha}} + \tau_v \frac{dv}{dt}. \qquad [8.3]$$

In these dimensionless mass equations the dynamic variables $f_{in}(t)$ for inflow into the balloon, $f_{out}(v)$ for outflow from the balloon, $q(t)$ for deoxy-haemoglobin content and $CMRO_2(t)$ are normalised to their respective values at baseline. The constant parameters are the transit time through the balloon τ_0, the viscoelastic time constant for the balloon τ_v which characterises the time scale for the volume change, and the Grubb exponent α for the flow-volume relationship $v = f^{\alpha}$. For the calculations, we assume a $CMRO_2(t)$ which after stimulus offset decreases linearly from its plateau value to baseline over the duration of the undershoot, similar to the $CMRO_2$ curve obtained experimentally in the Lu study (Lu et al. 2004). The other parameters are set to typical literature values: $\tau_0 = 2$ s, $\tau_v = 6$ s (estimated from (Hillman et al. 2007)), ramp-up/down time for f_{in} and $CMRO_2$ of 7 s, $\Delta f_{in} = 55\%$ and Grubb exponent $\alpha = 0.4$.

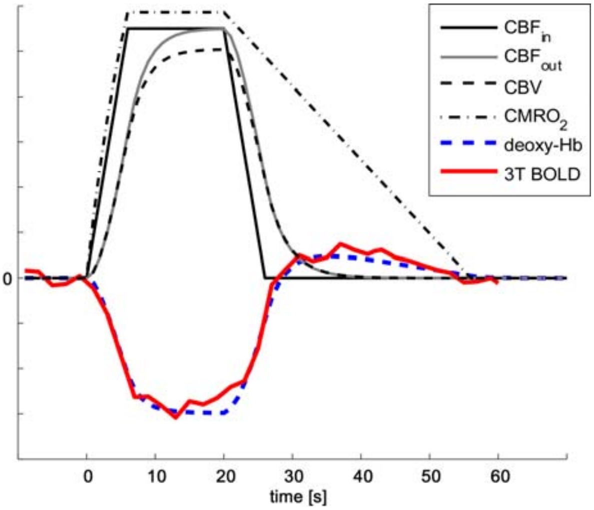

Figure 8.7: *Time evolution of the parameters in the 'arteriolar balloon' model. CBF_{in} and $CMRO_2$ are the input parameters, where CBF_{in} is modelled as a trapezoidal function and $CMRO_2$ takes an assumed form that after stimulus offset ramps down linearly over the duration of the observed undershoot. The resulting arteriolar outflow CBF_{out} (i.e. the inflow into the capillaries) depends on CBV, the volume of the arteriolar balloon. The experimentally measured response (T_2-weighted BOLD at 3 T, shown inverted) very closely follows the modelled deoxy-haemoglobin response to a 20 s stimulus; this demonstrates the plausibility of arteriolar ballooning as explanation for the observed latency of the undershoot in the presence of sustained post-stimulus elevation of $CMRO_2$. Curves were arbitrarily rescaled for display. For details on model parameters see text.*

Figure 8.7 illustrates the temporal evolution of the model input parameters, f_{in} and $CMRO_2$, as well as the model output timecourses of f_{out}, arteriolar CBV, and deoxy-haemoglobin content. As the experimentally obtained T_2 BOLD curves are proportional to the deoxy-haemoglobin time course, this alleviates the need to determine the weighting parameters necessary for the computation of the BOLD signal change, and thereby facilitates a direct comparison with the modelled deoxy-haemoglobin response. Figure 8.7 also shows the model deoxy-haemoglobin timecourse, and the experimental signal response at 3 T for comparison.

For the set of typical model parameters, the response predicted by the 'arteriolar balloon model' agrees very well with the experimental data. The model calculations thus demonstrate the plausibility of a mechanism by which the BOLD undershoot is caused by sustained elevation in $CMRO_2$, and its temporal characteristics are determined by a delayed compliance effect on the inflow side.

Conclusions

In this work, we have presented a straightforward way of investigating the BOLD undershoot with a purely T_2-weighted fMRI sequence, and by taking advantage of the field-strength dependence of contributions to the BOLD contrast. The attractiveness of the approach lies in the fact that clear insights can be gained without the need for more complicated techniques. Our data strongly point towards a sustained elevation in deoxy-haemoglobin level as the source of the post-stimulus undershoot; blood flow and oxygen consumption are hence decoupled from each other. It appears from these data that neither parenchymal nor venous CBV changes alone can universally explain the undershoot. In addition to the finding of $CMRO_2$ as the cause of the undershoot, we present a hypothesis that can explain the observed shape of the undershoot by delayed compliance of an arteriolar balloon.

Acknowledgements

The work presented in this paper was supported by STW (Dutch Technical Science Foundation) project NGT.6154. The authors would like to thank Siemens Medical Solutions in Erlangen, Germany for very kindly providing the two 32-channel head coils, Markus Barth helping out with the data acquisition and for useful discussions throughout the project, and Oliver Langner for preparing the stimulus material.

References

Ances BM, Buerk DG, Greenberg JH, Detre JA. (2001) Temporal dynamics of the partial pressure of brain tissue oxygen during functional forepaw stimulation in rats. *Neurosci Lett* 306:106-110

Attwell D, Laughlin SB. (2001) An energy budget for signaling in the grey matter of the brain. *J Cereb Blood Flow Metab* 21:1133-1145

Berwick J, Johnston D, Jones M, Martindale J, Redgrave P, McLoughlin N, Schiessl I, Mayhew JE. (2005) Neurovascular coupling investigated with two-dimensional optical imaging spectroscopy in rat whisker barrel cortex. *Eur J Neurosci* 22:1655-1666

Brockhaus J, Ballanyi K, Smith JC, Richter DW. (1993) Microenvironment of respiratory neurons in the in vitro brainstem-spinal cord of neonatal rats. *J Physiol* 462:421-445

Buxton RB, Wong EC, Frank LR. (1998) Dynamics of blood flow and oxygenation changes during brain activation: the balloon model. *Magn Reson Med* 39:855-864

Constable RT, Kennan RP, Puce A, McCarthy G, Gore JC. (1994) Functional NMR imaging using fast spin echo at 1.5 T. *Magn Reson Med* 31:686-690

Devor A, Dunn AK, Andermann ML, Ulbert I, Boas DA, Dale AM. (2003) Coupling of total hemoglobin concentration, oxygenation, and neural activity in rat somatosensory cortex. *Neuron* 39:353-359

Devor A, Tian P, Nishimura N, Teng IC, Hillman EM, Narayanan SN, Ulbert I, Boas DA, Kleinfeld D, Dale AM. (2007) Suppressed neuronal activity and concurrent arteriolar vasoconstriction may explain negative blood oxygenation level-dependent signal. *J Neurosci* 27:4452-4459

Donahue MJ, Stevens RD, de Boorder M, Pekar JJ, Hendrikse J, van Zijl PC. (2008) Hemodynamic changes after visual stimulation and breath holding provide evidence for an uncoupling of cerebral blood flow and volume from oxygen metabolism. *J Cereb Blood Flow Metab*

Feng CM, Liu HL, Fox PT, Gao JH. (2001) Comparison of the experimental BOLD signal change in event-related fMRI with the balloon model. *NMR Biomed* 14:397-401

Frahm J, Baudewig J, Kallenberg K, Kastrup A, Merboldt KD, Dechent P. (2008) The post-stimulation undershoot in BOLD fMRI of human brain is not caused by elevated cerebral blood volume. *Neuroimage* 40:473-481

Frahm J, Kruger G, Merboldt KD, Kleinschmidt A. (1996) Dynamic uncoupling and recoupling of perfusion and oxidative metabolism during focal brain activation in man. *Magn Reson Med* 35:143-148

Friston KJ, Mechelli A, Turner R, Price CJ. (2000) Nonlinear responses in fMRI: the Balloon model, Volterra kernels, and other hemodynamics. *Neuroimage* 12:466-477

Gu H, Stein EA, Yang Y. (2005) Nonlinear responses of cerebral blood volume, blood flow and blood oxygenation signals during visual stimulation. *Magn Reson Imaging* 23:921-928

Harel N, Lee SP, Nagaoka T, Kim DS, Kim SG. (2002) Origin of negative blood oxygenation level-dependent fMRI signals. *J Cereb Blood Flow Metab* 22:908-917

Hillman EM, Devor A, Bouchard MB, Dunn AK, Krauss GW, Skoch J, Bacskai BJ, Dale AM, Boas DA. (2007) Depth-resolved optical imaging and microscopy of vascular compartment dynamics during somatosensory stimulation. *Neuroimage* 35:89-104

Hoge RD, Atkinson J, Gill B, Crelier GR, Marrett S, Pike GB. (1999) Stimulus-dependent BOLD and perfusion dynamics in human V1. *Neuroimage* 9:573-585

Jasdzewski G, Strangman G, Wagner J, Kwong KK, Poldrack RA, Boas DA. (2003) Differences in the hemodynamic response to event-related motor and visual paradigms as measured by near-infrared spectroscopy. *Neuroimage* 20:479-488

Jin T, Kim SG. (2008) Improved cortical-layer specificity of vascular space occupancy fMRI with slab inversion relative to spin-echo BOLD at 9.4 T. *Neuroimage* 40:59-67

Jochimsen TH, Norris DG, Mildner T, Moller HE. (2004) Quantifying the intra- and extravascular contributions to spin-echo fMRI at 3 T. *Magn Reson Med* 52:724-732

Jones RA. (1999) Origin of the signal undershoot in BOLD studies of the visual cortex. *NMR Biomed* 12:299-308

Kennan RP, Zhong J, Gore JC. (1994) Intravascular susceptibility contrast mechanisms in tissues. *Magn Reson Med* 31:9-21

Kim T, Hendrich KS, Masamoto K, Kim SG. (2007) Arterial versus total blood volume changes during neural activity-induced cerebral blood flow change: implication for BOLD fMRI. *J Cereb Blood Flow Metab* 27:1235-1247

Kong Y, Zheng Y, Johnston D, Martindale J, Jones M, Billings S, Mayhew J. (2004) A model of the dynamic relationship between blood flow and volume changes during brain activation. *J Cereb Blood Flow Metab* 24:1382-1392

Kwong KK, Belliveau JW, Chesler DA, Goldberg IE, Weisskoff RM, Poncelet BP, Kennedy DN, Hoppel BE, Cohen MS, Turner R, et al. (1992) Dynamic magnetic resonance imaging of human brain activity during primary sensory stimulation. *Proc Natl Acad Sci U S A* 89:5675-5679

Lee SP, Duong TQ, Yang G, Iadecola C, Kim SG. (2001) Relative changes of cerebral arterial and venous blood volumes during increased cerebral blood flow: implications for BOLD fMRI. *Magn Reson Med* 45:791-800

Lu H, Golay X, Pekar JJ, van Zijl PCM. (2003) Functional magnetic resonance Imaging based on changes in vascular space occupancy. *Magn Reson Med* 50:263-274

Lu HZ, Golay X, Pekar JJ, van Zijl PCM. (2004) Sustained poststimulus elevation in cerebral oxygen utilization after vascular recovery. *Journal of Cerebral Blood Flow and Metabolism* 24:764-770

Mandeville JB, Marota JJ, Ayata C, Zaharchuk G, Moskowitz MA, Rosen BR, Weisskoff RM. (1999) Evidence of a cerebrovascular postarteriole windkessel with delayed compliance. *J Cereb Blood Flow Metab* 19:679-689

Mildner T, Norris DG, Schwarzbauer C, Wiggins CJ. (2001) A qualitative test of the balloon model for BOLD-based MR signal changes at 3T. *Magn Reson Med* 46:891-899

Nagaoka T, Zhao F, Wang P, Harel N, Kennan RP, Ogawa S, Kim SG. (2006) Increases in oxygen consumption without cerebral blood volume change during visual stimulation under hypotension condition. *J Cereb Blood Flow Metab* 26:1043-1051

Norris DG, Zysset S, Mildner T, Wiggins CJ. (2002) An investigation of the value of spin-echo-based fMRI using a Stroop color-word matching task and EPI at 3 T. *Neuroimage* 15:719-726

Obata T, Liu TT, Miller KL, Luh WM, Wong EC, Frank LR, Buxton RB. (2004) Discrepancies between BOLD and flow dynamics in primary and supplementary motor areas: application of the balloon model to the interpretation of BOLD transients. *Neuroimage* 21:144-153

Ogawa S, Menon RS, Tank DW, Kim SG, Merkle H, Ellermann JM, Ugurbil K. (1993) Functional brain mapping by blood oxygenation level-dependent contrast magnetic resonance imaging. A comparison of signal characteristics with a biophysical model. *Biophys J* 64:803-812

Parkes LM, Schwarzbach JV, Bouts AA, Deckers RH, Pullens P, Kerskens CM, Norris DG. (2005) Quantifying the spatial resolution of the gradient echo and spin echo BOLD response at 3 Tesla. *Magn Reson Med* 54:1465-1472

Poser BA, Norris DG. (2007a) Fast spin echo sequences for BOLD functional MRI. *Magn Reson Mater Phy* 20:11-17

Poser BA, Norris DG. (2007b) Measurement of activation-related changes in cerebral blood volume: VASO with single-shot HASTE acquisition. *Magn Reson Mater Phy*

Schroeter ML, Kupka T, Mildner T, Uludag K, von Cramon DY. (2006) Investigating the post-stimulus undershoot of the BOLD signal--a simultaneous fMRI and fNIRS study. *Neuroimage* 30:349-358

Turner R, Thomas D. (2006) Cerebral Blood Volume: Measurement and Change. In: *Proceedings 14th Scientific Meeting, International Society for Magnetic Resonance in Medicine*, Seattle, p 2771

Tuunanen PI, Vidyasagar R, Kauppinen RA. (2006) Effects of mild hypoxic hypoxia on poststimulus undershoot of blood-oxygenation-level-dependent fMRI signal in the human visual cortex. *Magn Reson Imaging* 24:993-999

Uludag K, Dubowitz DJ, Yoder EJ, Restom K, Liu TT, Buxton RB. (2004) Coupling of cerebral blood flow and oxygen consumption during physiological activation and deactivation measured with fMRI. *Neuroimage* 23:148-155

van Zijl PC, Eleff SM, Ulatowski JA, Oja JM, Ulug AM, Traystman RJ, Kauppinen RA. (1998) Quantitative assessment of blood flow, blood volume and blood oxygenation effects in functional magnetic resonance imaging. *Nat Med* 4:159-167

Vanzetta I, Hildesheim R, Grinvald A. (2005) Compartment-resolved imaging of activity-dependent dynamics of cortical blood volume and oximetry. *J Neurosci* 25:2233-2244

Villringer A, Them A, Lindauer U, Einhaupl K, Dirnagl U. (1994) Capillary perfusion of the rat brain cortex. An in vivo confocal microscopy study. *Circ Res* 75:55-62

Wu CW, Chuang KH, Wai YY, Wan YL, Chen JH, Liu HL. (2008) Vascular space occupancy-dependent functional MRI by tissue suppression. *J Magn Reson Imaging* 28:219-226

Yacoub E, Ugurbil K, Harel N. (2006) The spatial dependence of the poststimulus undershoot as revealed by high-resolution BOLD- and CBV-weighted fMRI. *J Cereb Blood Flow Metab* 26:634-644

Zhao F, Jin T, Wang P, Kim SG. (2007) Improved spatial localization of post-stimulus BOLD undershoot relative to positive BOLD. *Neuroimage* 34:1084-1092

Chapter 9 Measurement of activation-related changes in cerebral blood volume: VASO with single-shot HASTE acquisition

Abstract

The recently developed Vascular Space Occupancy (VASO) fMRI technique is gaining popularity as it facilitates the measurement of cerebral blood volume (CBV) changes concomitant with brain activation, without the use of contrast agents. Thus far, VASO fMRI has only been used in conjunction with a GE-EPI (gradient-echo echo planar imaging) sequence, which is proceeded by an inversion recovery (IR) experiment to selectively null the blood signal. The use of GE-EPI has potential disadvantages: (a) the non-zero TE may lead to BOLD contamination and (b) images suffer from the EPI-typical inhomogeneity artefacts. Here, we propose the use of VASO based on an IR-HASTE (inversion recovery half-Fourier acquisition single-shot turbo spin echo) sequence. Results from a visual stimulation study (n = 8) at 3 T show a 43% higher functional contrast-to-noise (CNR) of HASTE compared to EPI, with a strongly increased count of active voxels at the same significance threshold. Sensitivity to inflow effects was investigated and found to be similar for both methods. As HASTE VASO yields essentially artefact free images, it appears to be the method of choice for measuring relative CBV changes with VASO.

Poser BA, Norris DG. Magn Reson Mater Phy 20(2): 63-67; 2007

Introduction

The Vascular Space Occupancy (VASO) technique (Lu et al. 2003) has proven valuable for measuring relative changes in cerebral blood volume (CBV) upon brain activation. The original method was implemented with a standard echo-planar imaging (EPI) sequence (Lu et al. 2003), preceded by a non-selective adiabatic inversion pulse. The inversion time (TI) is chosen such that the blood magnetisation is passing the zero-point at the moment of excitation; CBV increases as a result of increased brain activation, therefore leading to a negative signal change in VASO as a larger fraction of the tissue volume is taken up by blood.

Employment of EPI-based acquisitions may result in T_2* blurring and geometric distortions, and thereby a potential reduction in spatial specificity. Furthermore, the echo time (TE) should be as short as possible (ideally zero) to avoid any BOLD-like signal contributions, but the duration of the EPI readout often requires a TE above 10 ms even at standard spatial resolution and matrix size. Shorter TEs can only achieved by use of a very high acquisition bandwidth or accelerated parallel acquisition techniques, thereby incurring SNR penalties, or segmented acquisitions at the cost of temporal resolution. If the TE is too long this can lead to contamination of the VASO signal by the positive, and thus opposite, BOLD signal change, especially at the more and more routinely used higher field strengths. The TE dependence of the VASO signal has been observed in multi-echo EPI measurements (Lu and van Zijl 2005). Such measurements have been used for extrapolating the VASO signal to zero TE, and predicting extravascular parenchymal BOLD effects and oxygen extraction fractions (Lu and van Zijl 2005); however, acquisitions at a single short TE would generally be favourable. One way to achieve this is the use of a spiral-out sampling scheme which allows minimal TE, but will still suffer from some measure of T_2* contamination. With the inherently low signal levels in VASO images, due to the inversion recovery (IR) preparation and therefore considerable reduction of the tissue signal, the method has a much reduced sensitivity compared to BOLD fMRI. Improvement of the functional sensitivity of VASO is hence desirable.

The impact of blood flow effects has been reported for EPI-based VASO (Donahue et al. 2006). The VASO method relies on the assumption of steady-state conditions, while in reality the inflow of fresh spins from outside the inversion volume effectively makes the TI too short. The result is a larger negative signal change than would be observed in the steady state. It was demonstrated at high spatial resolution that typical short-TR VASO measurements therefore show a considerably larger effect than long-TR measurements.

In this paper, we investigate the application of the HASTE (half-Fourier acquisition single-shot turbo spin echo) sequence to VASO fMRI. HASTE (Kiefer et al. 1994) is a half-Fourier, single-shot RARE / FSE sequence (Hennig et al. 1986; Norris et al. 1992). It consists of a train of RF refocusing pulses which, following excitation, repeatedly form a spin echo half-way between the refocusing pulses. These echoes are acquired with different phase encoding gradients to cover just more than half of *k*-space. The unrecorded lines are generated by Hermitian conjugation of the acquired lines. The resulting complex image undergoes Margosian phase correction, using a low resolution phase map that is extracted from the fully-covered central portion of *k*-space. Being a spin echo sequence, the advantage of HASTE is that yields pure T_2 contrast. As tissue T_2 is much longer than T_2*, and at short TE the BOLD changes related to T_2 are considerably less than those related to T_2*, a short TE readout using HASTE should suppress BOLD contributions almost entirely. At the same time, such T_2-weighted images are essentially free of susceptibility artefacts. Results from an activation study using a visual stimulation paradigm are compared to conventional EPI based VASO. Differences in the sensitivity to inflow effects between the two methods are also investigated.

Methods

Data acquisition

Scan parameters common to all acquisitions were: matrix size 64 x 64, FoV = 224 mm, voxel size 3.5 x 3.5 x 5 mm^3, TI = 710 ms, TR = 2 s, one slice, non-selective adiabatic inversion pulse applied with the body coil to achieve the largest possible inversion volume, and fat saturation. For the HASTE VASO measurements, an IR-HASTE sequence was used with the following features: ascending phase encoding with 36 echoes (i.e. 56% partial-Fourier, with the eight central lines used for phase correction) starting on the undersampled side of *k*-space; flip angle was 180º and a readout bandwidth of 700 Hz was used. This yields an inter-echo spacing of 3.5 ms, an actual TE of 14 ms for the central line of *k*-space, and a total echo train length of 115 ms. Conventional VASO-EPI acquisitions were made with an IR-GE-EPI sequence, using 75% partial-Fourier to shorten TE to 11 ms, and bandwidth 2700 Hz. T_2*-weighted GE-EPI BOLD scans (TE = 40 ms) were made for comparison of the activation time courses, and to extract regions of interest for subsequent analysis. Additional VASO measurements were made at TR = 5 s (TI = 1054 ms) and TR = 8 s (TI = 1116 ms) to assess inflow effects.

All data were acquired on a 3 T Siemens Magnetom Trio system (Siemens Medical Solutions, Erlangen, Germany) using the product 8-channel head coil.

Stimulus Material and Subjects

Visual stimuli consisting of 30 s rest followed by 21 s of 8 Hz inverting black and white checkerboards were shown using Presentation software (Neurobehavioral Systems, Inc., USA). Eight subjects were scanned for the main experiment at TR = 2 s, five at TR = 5 s and three at TR = 8 s. Each run lasted 6 min, with the exception of the GE-EPI measurement which lasted 3 min. All subjects had normal or corrected-to-normal vision, and gave written consent according to local regulations.

Data Processing and Analysis

Linear trend removal and high-pass filtering of all time courses was done in Brainvoyager 2000 (Brain Innovation, The Netherlands). No data smoothing was applied as part of the pre-processing. Motion correction was deliberately not used to avoid the introduction of a possible bias due to the strong signal change the stimulus induces in large portion of the slice; however, using the SPM2 realignment algorithm (http://www.fil.ion.ucl.ac.uk/spm) it was verified that the data were not affected by excessive motion (average maximum detected motion below 10% of the voxel size). For unbiased functional analysis, a ROI mask was extracted from the activation in GE BOLD scan at $p < 0.0001$. For the purpose of the ROI analysis, distortion in the EPI data was assumed to be negligible, thus permitting the activation mask from the BOLD data to be applied to both EPI and HASTE VASO data. Amplitude signal changes, and mean and maximum *t*-scores of the HASTE and EPI VASO activation timecourses were noted. For all subjects, temporal SNR (tSNR) was determined from a manually selected non-activated grey matter region in the pre-processed data (40 pixels, tSNR calculated first pixel-wise, then averaged). This was used for calculation of functional CNR, and estimation of the relative contribution of thermal and physiological noise. For the investigation of inflow effects, signal changes in HASTE and EPI VASO were extracted separately by *t*-tests (i.e. without the use of a mask).

Results

Typical EPI and HASTE VASO images with activation overlays are shown in Fig. 9.1. As can be seen from the images, the use of a pure spin echo sequence results in a higher intrinsic signal level in grey matter for HASTE than for EPI: at TR = 2 s, the mean grey matter intensities ($n = 8$) are 336 ± 30 and 202 ± 19 for HASTE and EPI, respectively, for the same receiver gain and scaling parameters in the reconstruction. With 4.38 ± 0.54 and 4.13 ± 0.58 units the average temporal noise in the non-activated grey matter ROI is nearly identical in HASTE and EPI. Purely on the basis of bandwidth considerations, i.e. taking the square root ratio of the effective ADC time which is spent acquiring the MR signal, intrinsic thermal noise in HASTE is expected to be a factor of 1.70 lower than thermal noise in EPI. Under the assumptions that non-thermal noise is of physiological origin and scales proportionately with signal strength (Kruger and Glover 2001), and that the experimentally determined temporal noise reflects the contributions of thermal (σ_{th}) and physiological (σ_{ph}) noise as $\sqrt{(\sigma_{th}^2 + \sigma_{ph}^2)}$, then the relative contribution of the two noise sources can be estimated for each method. This yields 66% physiological to 34% thermal noise for HASTE, and a corresponding ratio of 41% to 59% for EPI.

Defining the BOLD activation ($p < 0.0001$) as a neutral ROI for comparison, the VASO signal changes are 3.42 ± 1.34 for EPI and 5.18 ± 1.96 for HASTE, i.e. considerably larger for the spin-echo sequence (error bars = SD across subjects). Functional CNR was calculated as $CNR = tSNR \cdot \Delta S / S$. Given the observed noise levels, this yields a 43% higher CNR of the HASTE method. Calculation of mean *t*-scores in the same ROI yielded a subject average for 3.40 ± 1.16 for EPI and 4.78 ± 1.56 for HASTE. The ratio of 1.41 is in excellent agreement with the direct CNR measurements; this is not unexpected as *t*-scores and CNR are equivalent measures in a blocked design.

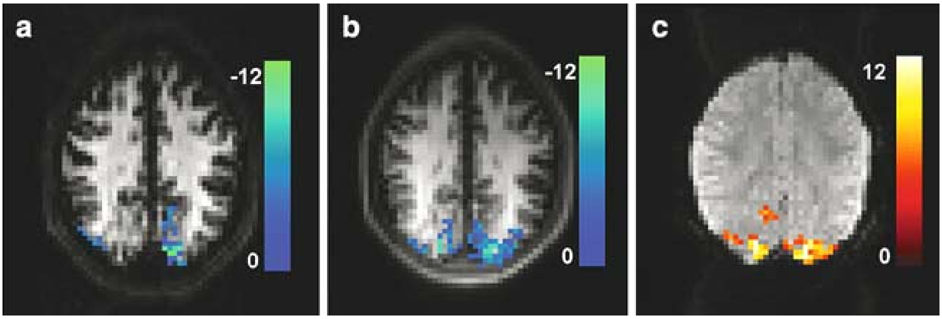

Figure 9.1 *(see Appendix for colour version): Typical EPI (a) and HASTE (b) VASO images with activation overlays (t-scores, $p < 0.0004$). Activation regions detected in the HASTE data are considerably larger, suggesting superior functional sensitivity. As a result, the activation pattern of HASTE more closely resembles that of the BOLD measurements (c). The use of pure spin echoes results in nearly factor 1.7 higher grey matter intensity in the HASTE images as compared to the EPI images.*

When analysed separately, this increased sensitivity resulted in a more than doubled count of active voxels in HASTE (61 voxels) compared to EPI (26 voxels) at the same significance threshold ($p < 0.0004$), averaged over all subjects. Visual assessment of the activation maps indicates that as a consequence the HASTE VASO activation covers a similar volume to the BOLD activation (Fig. 9.1).

Normalised stimulus response curves of the two VASO measurements, as well the BOLD response, are shown in Fig. 9.2.

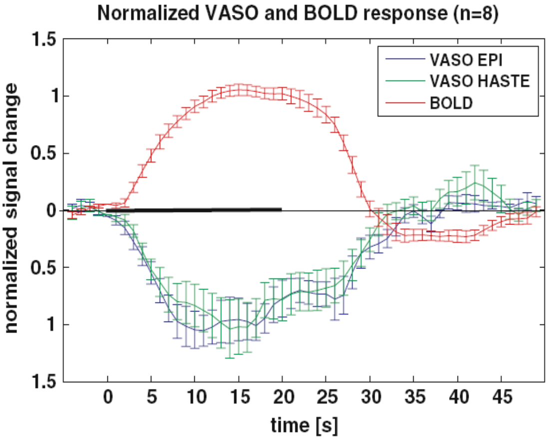

Figure 9.2 *(see Appendix for colour version): Averaged stimulus response ($n = 8$) of the EPI and HASTE VASO activation ($p < 0.0004$). Note the decline of the CBV well before the end of the stimulus; this behaviour is much less pronounced in the BOLD response. The VASO curves show a nearly identical signal time course, with a return to baseline that essentially coincides with that of the BOLD (error bars = SEM). The stimulation period is indicated by the solid line on the time axis. The baseline was taken as the average of the 5 s before stimulus onset.*

Measurements at longer TR were performed with both methods for the investigation of their sensitivity to inflow effects, and did not reveal a significant difference. The results from the present data are shown in Table 9.1. Within the limits of experimental error, mainly due to the dominant inter-subject differences, both methods appear to be equally affected.

TR[s]	**TI [ms]**	ΔS_{EPI} [a.u.]	ΔS_{HASTE} [a.u.]
2^{*}	713	5.60 ± 1.06	6.27 ± 1.50
5^{**}	1054	5.20 ± 1.26	4.66 ± 0.89
8^{***}	1116	4.12 ± 1.08	3.67 ± 0.33

Table 9.1: *VASO signal changes measured with EPI and HASTE at different TR. Within measurement errors (SD over subjects) CBV signals equally change with TR for both methods. This suggests that both are equally affected by CBF increases upon activation. Activation was thresholded at* $^{*}p<0.0004$, $^{**}p<0.0017$ *and* $^{***}p<0.01$ *to account for the reduced number of measurements available with increasing TR and to keep activation volume approximately equal for each case. All significantly activated voxels were taken into account for the calculation of signal change.*

Discussion

In the choice of sequence parameters care was taken that the HASTE echo train is sufficiently short so as not to lead to T_2 blurring along the phase-encode dimension: this might potentially lead to ‘smearing’ of high white matter signal into the low-intensity grey matter areas if the acquisition window were too long. The FWHM of the PSF due to T_2 decay is given by $\Delta f = 1 / (\pi \cdot T_2)$. Thus for typical T_2 values of approximately 80 ms (Wansapura et al. 1999) and the short readout train of approximately 115 ms, a linewidth in excess of one pixel cannot be expected. T_2 blurring may pose a problem for larger matrix sizes or higher image resolution that would require a longer echo train, but here parallel imaging techniques can be employed to shorten the readout appropriately. Particularly for longer echo trains, the use a ‘centre-out’ phase encoding scheme might be beneficial as it typically permits use of shorter TE than a linearly ascending scheme.

The possibility of blurring in HASTE due to partial Fourier sampling and imperfect Margosian phase correction was investigated by performing scans on a resolution phantom. The results (Fig. 9.3) showed very sharp images for HASTE and thus blurring could be excluded from causing an ‘artificial’ reconstruction related SNR increase in HASTE.

BOLD signal changes are expected to contribute considerably less to the T_2-weighted HASTE VASO signal than to EPI; with the short TE of 14 ms the HASTE sequence is almost entirely insensitive BOLD related signal changes which would peak at the TE of approximately 80 ms.

As is evident from the multi-echo data shown by Lu et al (Lu and van Zijl 2005), some degree of BOLD contamination can be expected for the typical grey matter T_2* of 40 ms and the TE of 11 ms used here for EPI.

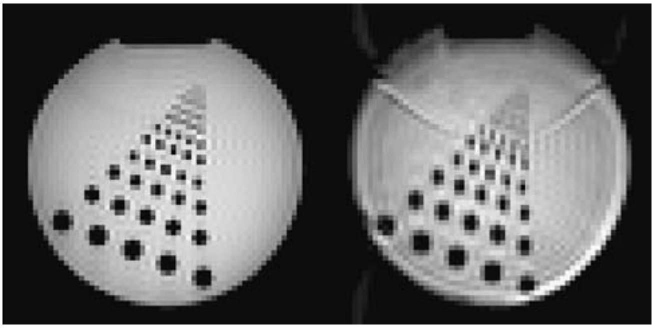

Figure 9.3: *Phantom images acquired with HASTE (left) and EPI (right) using the same parameters as for the functional experiment, but without the inversion pulse.*

The estimation of noise ratios did not distinguish between the different sources of physiological fluctuations, and possible interdependencies between them, such as a cross-correlation of noise in $T_2*(t)$ and signal intensity $S_0(t)$. This has been proposed in a more elaborate noise model (Wu and Li 2005). For the very short TEs used in this study, it is reasonable to assume that the contribution of T_2* noise to the total physiological noise (including cross-terms) can be neglected.

Considering the relative noise contributions to EPI and HASTE VASO, it appears that for the voxel size used here EPI is in the thermal noise dominated regime, whereas HASTE is physiological noise dominated (66%). If physiological noise is the major contributor to HASTE, then the relative sensitivity penalty for increasing the spatial resolution would thus be much lower than for EPI. This suggests HASTE as the more suitable method for high resolution VASO measurements. VASO scans at higher spatial resolution than currently used for BOLD would appear attractive because of the stronger microvascular weighting in VASO (Lu et al. 2003).

Despite its advantage of permitting CBV measurements without contrast agents, the fact that VASO is a single slice experiment is clearly disadvantageous in a typical routine clinical or cognitive fMRI setup. A multi-slice VASO acquisition scheme using global inversion cycling (MAGIC) (Lu et al. 2004) was successfully demonstrated at 1.5 T, taking advantage of the relatively low BOLD contribution and the fast EPI readout. As an alternative to multi-slice acquisition the SE-based approach proposed here could be extended to 3D acquisitions by using a GRASE (gradient and spin echo) scheme. This would appear attractive on the basis of SNR and image artefact considerations: reasonable slab acquisition times could be achieved by the use of parallel imaging techniques. That GRASE offers potential benefits has recently been shown by Gunther et al (Gunther et al. 2005) for perfusion imaging. For VASO, a phase encoding scheme by which T_2 and T_2* effects are separated into two different directions (Mugler 1999) should permit acquisitions with minimal BOLD contamination and high image quality.

In conclusion, the application of HASTE to VASO fMRI was investigated. EPI VASO time courses were faithfully reproduced using IR-HASTE measurements. HASTE VASO showed a 43% higher sensitivity than EPI. This results in a large increase in number of active pixels at the same significance threshold. As a consequence VASO activation maps cover a similar volume to their BOLD counterparts, rather than showing activation in only a subset of the BOLD activated pixels. This is physiologically reasonable, as BOLD activation is a result of increased CBF, which must have a corresponding increase in CBV associated with it. The data also provide further evidence of increased microvascular weighting of VASO compared to BOLD. With the additional advantage of yielding images free of susceptibility artefacts, the present results suggest that a HASTE acquisition scheme is significantly superior to EPI and should therefore be the method of choice for measuring VASO signal changes.

Acknowledgements

The work presented in this paper was supported by STW grant NGT.6154. The authors thank Markus Barth for useful discussions, and two anonymous reviewers for helpful comments.

References

Donahue MJ, Lu H, Jones CK, Edden RA, Pekar JJ, van Zijl PC. (2006) Theoretical and experimental investigation of the VASO contrast mechanism. *Magn Reson Med* 56:1261-1273

Gunther M, Oshio K, Feinberg DA. (2005) Single-shot 3D imaging techniques improve arterial spin labeling perfusion measurements. *Magn Reson Med* 54:491-498

Hennig J, Nauerth A, Friedburg H. (1986) RARE imaging: a fast imaging method for clinical MR. *Magn Reson Med* 3:823-833

Kiefer B, Grässner J, Hausmann R. Image acquisition in a second with half-Fourier-acquisition single-shot turbo spin echo, supplement to JMRI volume 4(P), abstract #436; page 86, 1994

Kruger G, Glover GH. (2001) Physiological noise in oxygenation-sensitive magnetic resonance imaging. *Magn Reson Med* 46:631-637

Lu H, Golay X, Pekar JJ, van Zijl PCM. (2003) Functional magnetic resonance Imaging based on changes in vascular space occupancy. *Magnetic Resonance in Medicine* 50:263-274

Lu H, van Zijl PC. (2005) Experimental measurement of extravascular parenchymal BOLD effects and tissue oxygen extraction fractions using multi-echo VASO fMRI at 1.5 and 3.0 T. *Magn Reson Med* 53:808-816

Lu H, van Zijl PC, Hendrikse J, Golay X. (2004) Multiple acquisitions with global inversion cycling (MAGIC): a multislice technique for vascular-space-occupancy dependent fMRI. *Magn Reson Med* 51:9-15

Mugler JP, 3rd. (1999) Improved three-dimensional GRASE imaging with the SORT phase-encoding strategy. *J Magn Reson Imaging* 9:604-612

Norris DG, Bornert P, Reese T, Leibfritz D. (1992) On the application of ultra-fast RARE experiments. *Magn Reson Med* 27:142-164

Wansapura JP, Holland SK, Dunn RS, Ball WS, Jr. (1999) NMR relaxation times in the human brain at 3.0 tesla. *J Magn Reson Imaging* 9:531-538

Wu G, Li SJ. (2005) Theoretical noise model for oxygenation-sensitive magnetic resonance imaging. *Magn Reson Med* 53:1046-1054

Chapter 10 VASO with whole-brain coverage using a Maxwell-gradient compensated single-shot 3D GRASE sequence

Abstract

The vascular space occupancy (VASO) method was recently proposed as an fMRI method that is capable of detecting activation related changes in blood volume (CBV), without the need for a blood-pool contrast agent. In the present work we introduce a new whole brain VASO technique that is based on a parallel-accelerated single-shot 3D GRASE (gradient and spin echo) readout. The GRASE VASO sequence employs a flow-compensated correction scheme for concomitant Maxwell gradients which is necessary to avoid smearing artefacts that may occur due to violation of the CPMG condition for off-resonance excitation.

Experiments with 6 minutes of visual-motor stimulation were performed on eight subjects. At $p < 0.01$, average percent signal change and *t*-score for visual stimulation were -3.11% and -8.42, respectively; activation in left and right motor cortices and supplementary motor area was detected with -2.75% and -6.70, respectively. Sensitivity and signal changes are comparable to those of EPI based single-slice VASO, as indicated by additional visual-task experiments (-3.39% and -6.93).

The method makes it possible to perform whole brain cognitive activation studies based on CBV contrast.

Poser BA, Norris DG. Magn Reson Med (*in press*); 2009

Introduction

There is great demand in the neuroscience community for a method that permits measurement of activation related changes in cerebral blood volume (CBV) without administration of harmful contrast agents, and that can hence be applied on humans. A first such method was proposed by Thomas et al (Thomas et al. 2001), but due to its relatively low sensitivity did not find widespread application. More recently, the VASO method was introduced which measures relative CBV changes in terms of 'vascular space occupancy' (Lu et al. 2003). VASO works on the basis of the inversion recovery experiment and exploits the difference in T_1 relaxation times of blood and grey matter. A non-selective inversion is performed, followed by selective excitation and acquisition of an imaging slice at exactly the time where the longitudinal magnetisation of blood passes the zero point. Hence, the blood compartment will not contribute to the measured MR signal, and consequently a decrease in signal intensity will ensue from any activation-driven increase in CBV, under the assumption that an increase in blood volume will cause a corresponding displacement of extravascular water from the voxel.

VASO was received with considerable interest. First, it uses blood as an endogenous contrast agent. Second, the activation time courses provide interesting input to modelling the haemodynamic and metabolic response (Lu et al. 2004c). And third, if task related vasodilatation is specific to the arterioles and capillaries very close to the site of neuronal activation, as indicated in the recent MR literature (Donahue et al. 2006; Kim et al. 2007; Lu et al. 2003) and underpinned by optical imaging studies (Devor et al. 2007; Hillman et al. 2007), then VASO fMRI should be characterised by a spatial specificity superior to that of the most commonly used gradient-echo BOLD fMRI (Ogawa et al. 1990): the BOLD signal derives from changes in deoxy-haemoglobin content which are by their nature downstream. Since its development, numerous studies have focused on optimising and extending the VASO method, as well as investigating the mechanisms of the VASO contrast in detail (Donahue et al. 2006; Lu et al. 2005a; Lu et al. 2005b; Lu and van Zijl 2005). While the original VASO implementation employed a gradient-echo EPI module for signal readout at short but non-zero TE (Lu et al. 2003), the criticism of potential BOLD contamination has prompted others to use a SE-EPI (Donahue et al. 2006) or FSE readout (Poser and Norris 2007). Others have extended the VASO sequence for simultaneous measurement of CBV, CBF and BOLD (Yang et al. 2004).

The major drawback of the original VASO method and aforementioned variants is that only a single slice can be acquired per inversion pulse. This results in lengthy experiments that yield very low temporal resolution and volume coverage. To address this problem which thus far limited VASO to mechanistic investigations and a few niche applications, multi-slice VASO variants were proposed, based on the 'multiple acquisitions with global inversion cycling' (MAGIC) scheme (Lu et al. 2004b) and its recent extension to whole brain coverage (Scouten and Constable 2007). These multi-slice methods, however, rely on multiple inversion pulses being applied in rapid succession, in between which a number of slices are separately

excited and acquired near, but importantly not at, the zero crossing of the blood signal. Furthermore, the signal decay during the acquisition of multiple slices causes an intensity (and thus SNR) decrease between the first and subsequent slices, hence requiring an additional acquisition in opposite slice order with subsequent averaging to compensate the effect (Lu et al. 2004b).
Recently, 3D single-shot gradient- and spin echo (3D GRASE) (Song et al. 1994) was proposed for arterial spin labeling (Gunther et al. 2005). In their work the authors demonstrate that a GRASE readout with near whole-brain coverage can yield a 2.8-fold SNR increase as compared to the conventionally used 2D-EPI, and thereby constitutes a highly efficient acquisition scheme that can drastically shorten acquisition times.

In this study we investigate whether the benefits of 3D GRASE can be translated to VASO fMRI as was previously suggested (Poser and Norris 2007). A 3D GRASE sequence is realised which employs Maxwell compensation gradients on the read axis to ensure that the CPMG condition is satisfied, and further permits use of parallel acceleration along both phase encoding directions to efficiently reduce the required echo train length, and thereby T_2 blurring.
The method is applied to an fMRI study with visual and motor stimulation, and additional experiments are performed with the typically used GE-EPI VASO sequence to verify that similar activation patterns would be obtained in visual cortex.

Methods

Sequence implementation
As in the original VASO sequence, blood nulling is achieved by means of a non-selective adiabatic inversion pulse, followed by inversion time TI such that in the steady state the longitudinal magnetisation of blood passes the zero point at the moment of excitation:

$$TI = -T_1 \ln\left(\frac{1}{2} + \frac{1}{2} e^{\frac{-TR}{T_1}}\right), \qquad [10.1]$$

(Lu et al. 2003), where T_1 is the longitudinal relaxation time of blood and TR the volume repetition time. The imaging volume is excited using a slab-selective 90º 19-lobe *sinc* pulse with 2.56 ms duration and with a high bandwidth-time product of 20.8 to yield a sharp slab profile, subsequently refocused by 180º *sinc* pulses that are surrounded by crusher gradients on the *z*-axis. During each spin echo, an entire k_x-k_y plane is acquired using an EPI readout. Phase encoding along the k_z-axis starts at $k_z = 0$ and proceeds in a centre-out fashion to minimise TE and maximise SNR. Three navigator echoes for B_0 drift and eddy current (N / 2 ghost) correction are acquired immediately after excitation, and the corrections applied in the standard manner during the product image reconstruction. To avoid blurring due to T_2 decay during the long readout train that is required for a large number of slices, parallel imaging capability was added to allow undersampling in both primary (k_y) and secondary (k_z) phase encoding directions.

In contrast to previous 3D GRASE sequences we compensate for concomitant 'Maxwell terms' that result from the strong switching of the readout gradients. According to Maxwell's equations a magnetic field gradient purely along one intended direction (e.g. x) cannot be produced, and so concomitant gradient fields along the orthogonal direction(s) will be present (Norris and Hutchison 1990). At main magnetic field B_0 the concomitant gradient field along the z-axis that is produced by a gradient G_x along the x-axis at an off-resonance position z, is given by (Norris and Hutchison 1990)

$$\Delta B(z,t) \approx \frac{z^2 G_x^2(t)}{2B_0}, \qquad [10.2]$$

and hence the associated phase accumulation over time t is

$$\theta(z) \approx \int_0^t \gamma \Delta B(z,t)dt. \qquad [10.3]$$

In the 3D-GRASE experiment, strong concomitant gradients are generated in particular by the fast alternation of the EPI readout gradients. The effect of the phase encoding 'blips' is typically two orders of magnitude smaller, and since they will not give rise to a phase shift sufficient to compromise the CPMG condition their contribution is not considered the current publication. Concomitant field gradients tend to be unproblematic for most sequences particularly at higher magnetic field, but can constitute a confound in CPMG methods such as the GRASE sequence: the rapid EPI readout is switched between all refocusing pulses, but importantly not between excitation and the first refocusing pulse. Compensation can be applied in a straightforward manner by switching 'dummy' gradients with zero effective moment but equivalent concomitant z-contribution before the first refocusing pulse (Zhou et al. 1998). Rather than the more conventional bi-polar gradient pairs, we chose tri-polar gradients that are intrinsically 'flow-compensated' and eliminate the phase change induced by constant velocity motion (Zhou et al. 1998). The complete sequence is shown schematically in Fig. 10.1.

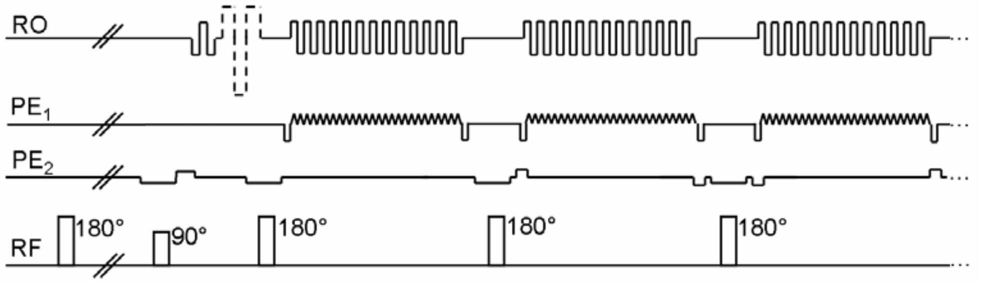

Figure 10.1: Schematic of the 3D GRASE VASO sequence. The dotted lines indicate the tri-polar Maxwell correction gradients.

MRI acquisitions

Experiments were performed on a Siemens 3 T TIM Trio scanner (Siemens Medical Solutions, Germany) equipped with the product 12-channel head coil.

The effect of the Maxwell compensation was demonstrated by acquiring images of a water-filled table tennis ball placed either at the isocentre, or 5 cm off-centre, with the following parameters: FoV = 100 x 100 x 50 mm^3, matrix 64 x 64 x 10, readout bandwidth 1860 Hz / px, slice thickness 5mm. Full sampling (TE = 60 ms) and factor 2 in-plane parallel acceleration (TE = 32 ms) were used so as to show the impact of different read gradient integrals. The phase accumulation at z = 5 cm was calculated to be 98° and 48° without and with parallel acceleration, respectively.

Two protocols were used for the functional VASO experiments, a 3D GRASE and a conventional single-slice EPI-VASO protocol for reference. Imaging parameters of the GRASE VASO protocol were: matrix size 64 x 64 x 16 (+2 for slice oversampling), effective FoV = 224 x 224 x 80 mm^3, TE = 15 ms, readout bandwidth 1700 Hz / px, factor 4 x 1 GRAPPA acceleration (56 lines over 18 partitions acquired for weight set calculation), total readout length 260 ms, TR = 2.5 s, TI = 746 ms. The high acceleration factor was chosen to shorten the GRASE readout to prevent T_2 blurring, and to allow a suitable time for T_1 relaxation prior to the next inversion. Acceleration along the primary phase encode direction was used to facilitate an axial slice orientation corresponding to the EPI-VASO scans. These were performed using an IR-GE-EPI sequence with corresponding parameters: matrix 64 x 64, one slice of 5 mm thickness, FoV = 224 x 224 mm^2, TE 9.6 ms, readout bandwidth 1700 Hz / px, factor 4 GRAPPA parallel imaging (56 reference lines) to achieve the short TE so as to reduce BOLD weighting, TR = 2.5 s, TI = 810 ms. The inversion pulse was applied using the body RF coil to achieve the largest possible inversion volume.

For GRASE acquisitions, the imaging slab was positioned so as to cover both visual and motor cortices; for the EPI measurements, a single slice with the same orientation was placed at the centre of visual cortex.

In each case the inversion time TI was calculated using Eq. 10.1 for a blood T_1 of 1627 ms (Lu et al. 2004a). In the case of GRASE however, the effective time available for T_1 relaxation is shorter than TR as a result of the multiple 180º pulses. Thus for the purpose of TI calculation in GRASE, 'TR' in Eq. 10.1 was taken as TR minus the time between excitation and the last refocusing pulse.

Functional experiments

Eight subjects (two females) gave written informed consent according to the local ethics regulations prior to study participation. All subjects had normal or corrected-to-normal vision. The functional activation paradigm consisted of a combined visual and motor activation task (visual only for EPI). Six blocks each of 30 s rest during which subjects fixated on a central cross, and 30 s of 10 Hz black-and-white flickering checkerboards were interleaved, resulting in a total duration of 6.25 minutes per run including preparation scans and reference line acquisition.

Subjects were instructed to simultaneously perform bilateral finger tapping during checkerboard blocks. Two experimental runs were performed on each of the eight subjects. Additional EPI-VASO experiments with visual stimulation were run on six of these subjects (acquisition order pseudo-randomised with the first GRASE VASO scan) to verify that the subjects show comparable VASO activation patterns to those found in the literature, e.g. (Donahue et al. 2006; Lu and van Zijl 2005; Poser and Norris 2007) and that approximately the same sensitivity was achieved as with EPI. Each run yielded 150 imaging volumes or slices, respectively. Care was taken during subject positioning to ensure subjects lay comfortably, and head motion was constrained by foam padding.

Data analysis

All data were analysed in Brainvoyager QX (BrainInnovation, Netherlands). Preprocessing included motion correction, linear trend removal and high-pass filtering. Otherwise no temporal or spatial smoothing was applied. Activation maps were computed by *t*-tests at $p < 0.01$, where the boxcar function was shifted by one TR (2.5 s) to compensate for the delayed vascular response. A cluster threshold of four voxels was applied to suppress type I errors. The average stimulus response was calculated as the average over all voxels passing both significance and cluster thresholds, separately for visual cortex and motor areas (left and right motor cortices and supplementary motor area (SMA) taken together).

Results

Imaging sequence

The effect of the Maxwell compensation can be seen in Fig. 10.2. As expected, correction is not required for a slab positioned at the isocentre, in agreement with Eq. 10.2. For off-resonance excitation, a considerable smearing is seen along the *z*-direction without application of the correction gradients (Fig. 10.2C), but not when the gradients are active (Fig. 10.2D). When reducing the read gradient switching, here application of twofold parallel acceleration, the artefact reduces by some degree (Fig. 10.2E), but is again only removed entirely by application of the compensation gradients (Fig. 10.2F).

Functional experiments

GRASE VASO activation maps (*t*-test, $p < 0.01$) of one subject overlaid on native image data are shown in Fig. 10.3. Activation in visual and motor cortices is detected robustly, as can be seen by reference to the average stimulus response curves, plotted separately for visual cortex, and left and right motor cortices and SMA.

Figure 10.4 (top) shows the GRASE VASO signal time course in visual and motor areas, averaged over all eight subjects and both experimental runs. With -2.75 ± 0.91% (mean ± SD) the average maximum VASO signal change in the motor areas (left and right motor cortices and SMA taken together) is slightly smaller than in visual cortex (-3.11 ± 1.02%). This is not surprising given that very commonly also smaller BOLD signal changes are observed in motor compared to visual cortices (c.f. results in e.g. (Scouten and Constable 2007)).The average maximum *t*-scores for the GRASE measurements are -6.70 ± 1.65 in motor areas, and -8.42 ± 1.56 in visual cortex. The corresponding mean *t*-scores in the activated regions are -3.46 ± 0.60, and -3.91 ± 0.61, respectively. Bilateral motor activation was found in all subjects, but SMA activation only seen in five at the chosen significance and cluster thresholds. All results are summarised in Table 10.1.

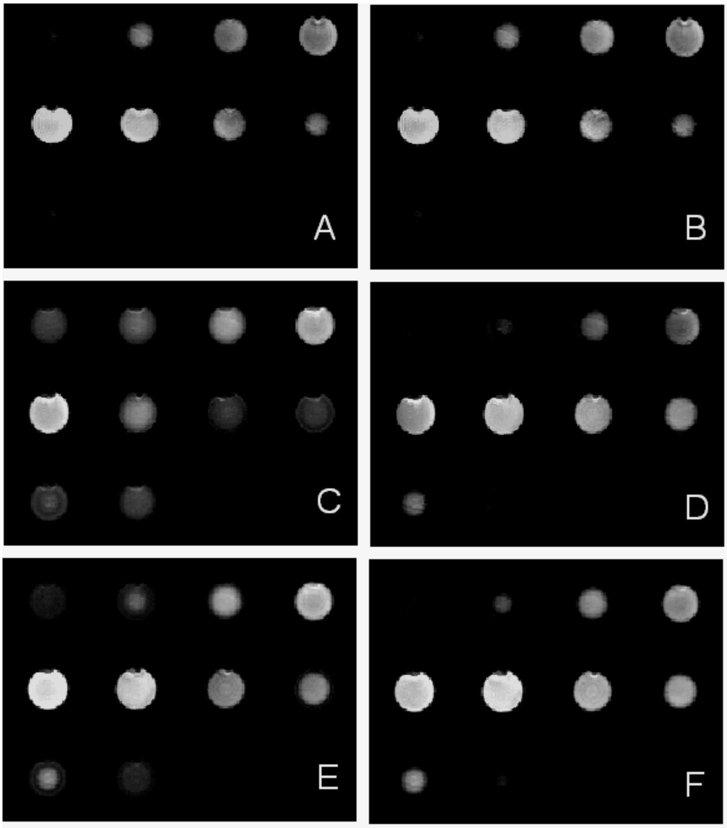

Figure 10.2: *Effect of Maxwell correction on MR images of a water-filled tennis ball placed at the isocenter (panels A and B), or 5 cm off-resonance (panels C-F). Each small image within the mosaics shows a transversal (x-y plane) view through the ball, at increasing z-coordinate from top left to bottom right. Since the ball is fully encompassed by the FoV in z-direction no signal should be seen in the outmost slices (top left, and second from left in bottom row of each panel). At z = 0 the same image quality is observed irrespective of whether the compensation gradients are enabled (B) or not (A). 5 cm off-resonance, a 'smearing' along the z-direction is present without Maxwell compensation (C), but fully removed when enabled (D). When reducing the gradient switching, here by twofold in-plane acceleration, the smearing is also reduced without correction (panel E vs. C), but again removed entirely by the Maxwell gradients (F). The images give a zoomed view for better visibility (outer 25% of x-y FoV removed).*

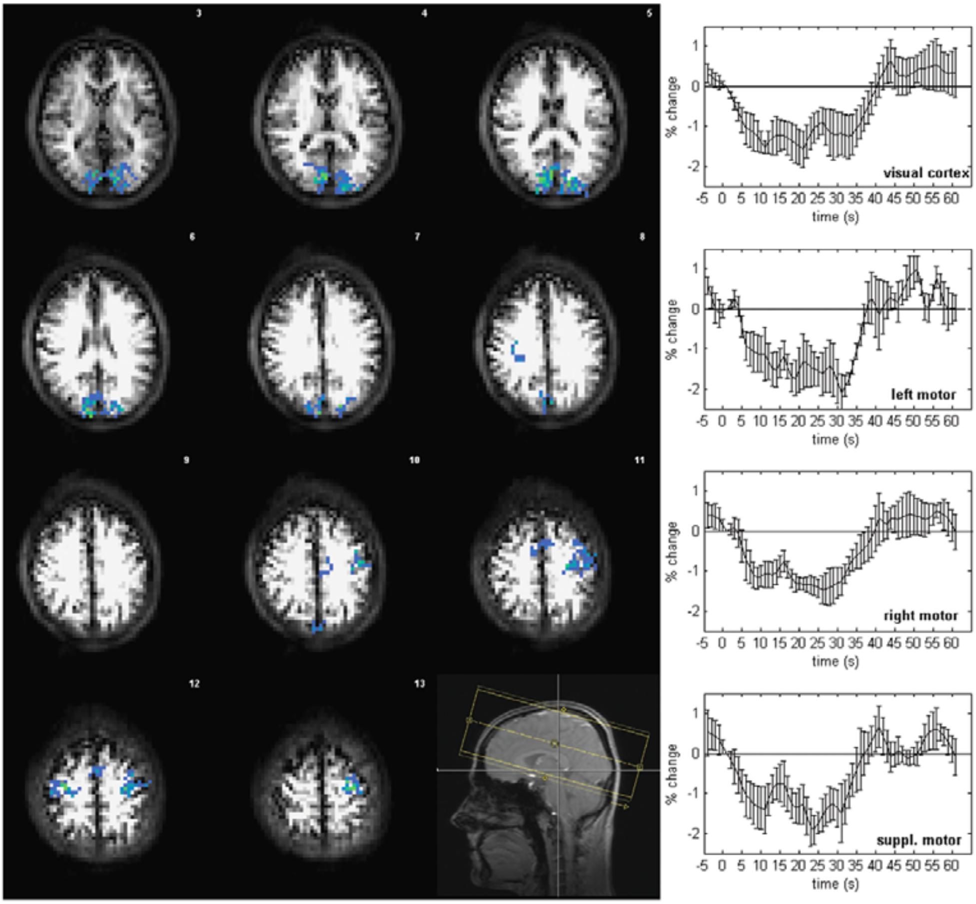

Figure 10.3 *(see Appendix for colour version): GRASE VASO activation map (t-test, p<0.01) of a single subject (subject two, first run, 150 volumes) overlaid on the native data, showing activation in visual cortex, left and right motor cortex and supplementary motor area. Also shown are the average stimulus responses in the respective ROIs, and the slab positioning.*

The EPI-VASO experiments on six of the subjects confirm that typical activation maps similar to those in previously published work are obtained (Donahue et al. 2006; Lu and van Zijl 2005; Poser and Norris 2007). The EPI-VASO timecourse is shown in Fig. 10.4 (bottom). At the same significance and cluster threshold ($p < 0.01$, 4 voxels), average EPI-VASO signal changes and maximum t-scores in the visual cortex are -3.39 ± 1.22% and -6.93 ± 1.40, respectively (corresponding mean t-scores -3.86 ± 0.63). These values compare well with those obtained for GRASE in the same six subjects from identical brain slices using only the first run (to give equal acquisition time), *viz*: -3.26 ± 1.15% signal change, an average maximum t-score of -7.91 ± 1.37 and an average mean t-score of -3.85 ± 0.89.

Note however that these results may not be directly comparable since the concurrent finger tapping during the GRASE scan might have had a modulating effect on the attention to the visual stimulus.

subject	**GRASE VASO - visual**				**GRASE VASO – motor**			
	max t-score	mean t-score	number of pixels	% signal change	max t-score	mean t-score	number of pixels	% signal change
1.1	-9.27	-3.91	392	-2.02	-6.46	-3.38	139	-1.77
1.2	-9.16	-4.31	279	-3.25	-6.53	-3.82	80	-2.01
2.1	-7.11	-3.62	170	-1.99	-6.76	-3.40	134	-1.78
2.2	-7.93	-3.86	317	-2.43	-8.00	-3.65	344	-2.43
3.1	-10.67	-4.01	234	-3.26	-7.29	-3.77	119	-3.36
3.2	-10.70	-4.08	286	-2.80	-10.19	-3.19	94	-3.33
4.1	-6.05	-3.34	119	-2.42	-6.31	-3.38	156	-2.18
4.2	-7.33	-3.77	93	-2.88	-6.07	-3.26	52	-3.24
5.1	-6.18	-3.06	188	-2.76	-5.35	-2.85	107	-2.12
5.2	-6.68	-2.91	220	-1.99	-4.48	-2.59	72	-2.29
6.1	-8.18	-3.52	327	-2.56	-4.11	-2.79	52	-3.49
6.2	-8.04	-4.06	239	-3.95	-5.72	-3.35	112	-2.18
7.1	-9.43	-4.65	377	-5.31	-7.88	-4.21	162	-3.79
7.2	-10.98	-5.49	280	-5.25	-9.77	-5.14	208	-5.13
8.1	-8.96	-4.15	257	-3.74	-6.13	-3.24	50	-2.79
8.2	-8.06	-3.87	237	-3.13	-6.09	-3.32	81	-2.07
mean	**-8.42**	**-3.91**	**251**	**-3.11 ***	**-6.70**	**-3.46**	**123**	**-2.75 ***
SD	1.56	0.61	83	1.02	1.65	0.60	74	0.91

subject	**EPI VASO - visual**				**GRASE VASO - visual**			
	max t-score	mean t-score	number of pixels	% signal change	max t-score	mean t-score	number of pixels	% signal change
1	-6.02	-4.00	15	-4.42	-8.15	-3.75	43	-2.06
2	-6.07	-3.50	21	-1.69	-7.33	-3.10	33	-2.71
3	-7.17	-3.02	20	-3.06	-5.56	-2.64	48	-2.07
4	-8.21	-4.22	36	-3.74	-8.04	-4.22	54	-4.18
5	-8.85	-4.81	43	-4.95	-9.44	-5.15	59	-4.81
6	-5.27	-3.58	23	-2.51	-8.96	-4.21	58	-3.75
mean	**-6.93**	**-3.86**	**26**	**-3.39 ***	**-7.91**	**-3.85**	**49**	**-3.26 ***
SD	1.40	0.63	11	1.22	1.37	0.89	10	1.15

Table 10.1: *Summary of results, showing maximum and mean t-scores, pixel count and percent signal change for each subject. Top: comparison of visual and motor activation in all GRASE VASO experiments (N=8). Bottom: visual activation detected in the single slice EPI VASO data (N=6); the results for the corresponding slice in the corresponding GRASE experiments are shown for reference. *Note: The mean percentage signal changes that result from first averaging individual response curves (see Fig. 10.4) are 2.77% (GRASE visual), 2.30% (GRASE motor), 3.06% (EPI visual) and 2.96% (GRASE visual, single corresponding slice). The values thus obtained are lower than the average peak signal change.*

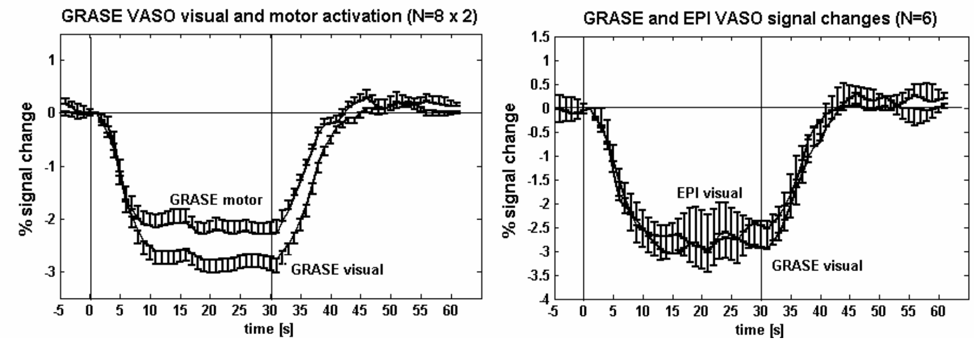

Figure 10.4: *Top: VASO responses to visual and motor stimulation as measured with GRASE, averaged over all subjects (N = 8, two experimental runs each). Apart from the small differences in percent signal change, -2.78% versus -2.30% between visual and motor cortex, respectively, the activation timecourse in the two cortical systems is extremely similar. For display, the temporal resolution was interpolated to 1 s. The 30 s stimulation period is indicated by the vertical lines. Error bars show SEM over subjects and experimental runs, and are plotted in one direction only for better visibility of the curves (up for motor, down for visual activation).*
Bottom: Timecourse of the VASO signal in visual cortex as measured by EPI-VASO (N = 6, p < 0.01). The average signal change was -3.06%. The GRASE activation in the same brain slice of the corresponding experimental runs is shown for reference (signal change -2.96%).

Discussion

A novel VASO method is presented that allows activation related CBV changes to be measured from large contiguous tissue volumes. Due to the already long TR of typical single-slice VASO and the short duration of the GRASE readout, there is no extra time penalty for the additional volume coverage. Sensory-motor stimulation experiments were performed on eight subjects with flickering checkerboard and bilateral finger tapping. Both visual and motor activation could simultaneously and robustly be detected with similar statistical power, but with larger signal changes in visual cortex. With the acquisition protocol used here, both relative signal changes and significance levels in the visual cortex were found to be very similar to those obtained with the additional EPI-VASO measurements.

In contrast to the MAGIC method (Lu et al. 2004b; Scouten and Constable 2007), the VASO scheme proposed here is based on a ‘true’ single shot 3D GRASE sequence, and so following a single inversion only one excitation is required to excite the entire imaging volume. Consequently, all partitions of the 3D volume have exactly the same ‘optimal’ CBV weighting and incomplete blood nulling as occurs in MAGIC is not a concern: slice dependent correction factors for quantification of CBV changes are hence not required (Scouten and Constable 2007). In GRASE however, one might in principle expect higher spatial frequencies along the *z*-encoding dimension to have slightly different VASO-weighting. Another positive consequence of single shot excitation and acquisition is that for a good slab profile, all slices in the volume should have the same signal intensity (and thus SNR).

In the GRASE protocol, a volume TR of 2.5 s was used, but due to the signal readout which results in multiple refocusing of the magnetisation, the effective time allowed for T_1 relaxation in the GRASE sequence is approximately 250ms shorter than TR. This was accounted for in the TI calculation by subtracting the time between excitation and last refocusing pulse from the TR value.

The most common readout for VASO is GE-EPI. Although the BOLD contribution to the measured VASO signal should be expected to be very small in a short-TE protocol such as the one used here, the use of spin echo based sequences carries potential advantages over gradient echo. First, although the blood signal is ‘invisible’, the changing blood oxygenation will in GE VASO nevertheless cause static dephasing around the vessels. In spin echo sequences these static effects are refocused, and since the intravascular signal is nulled, only dynamic averaging around the capillaries remains as a possible BOLD contributor. This effect is essentially absent at 1.5 T, and here at 3 T can be neglected as the TE of 15 ms is far shorter than the T_2 relaxation time of grey matter, ~80 ms (Wansapura et al. 1999). Second, spin echo based sequences are insensitive to through-plane signal dephasing and would therefore be the preferred choice for imaging brain regions that are prone to susceptibility artefacts. 3D-GRASE combines both advantages of spin echoes while having the same, or better, sampling efficiency.

An important benefit inherent to 3D schemes is that parallel imaging can be applied along two dimensions. Both image distortions and sampling time reduce only with in-plane acceleration. However, undersampling along the second phase encoding direction reduces sampling time and RF power deposition more efficiently because entire *z*-encoding steps are skipped. The 2D acceleration capability of the sequence was not exploited in the present experiments because 2 x 2 acceleration would have required sagittal orientation which would have made comparison with EPI VASO difficult. Another advantage of 3D methods is their only marginal sensitivity to spin-history effects caused by subject motion. These are known to have a detrimental effect on 2D-EPI. A method like VASO where the available SNR is already low will certainly benefit from the reduction of motion-induced physiological noise contributions.

Regarding the technical implementation of the GRASE sequence, we advise the use of additional gradients on the readout axis before to the first refocusing pulse, to compensate the imbalance in Maxwell terms due to the EPI readout that occurs after this pulse. This has not been reported for previous implementations of 3D GRASE with long gradient echo trains. The results demonstrate that if left uncompensated, smearing artefacts may occur due to violation of the CPMG condition under off-resonance excitation even at 3 T. The severity of the artefacts increases with the ‘amount’ of EPI gradient switching, so consequently the use of high in-plane acceleration factors will alleviate, but not entirely remove the need for Maxwell compensation. In the current implementation, the contribution of the Maxwell terms concomitant with the phase-encode gradient were neglected since their integral over half the EPI readout is an order of magnitude smaller: G_x traverses k-space many times in an alternating fashion, while G_y is merely prephased and then slowly blipped back (effectively corresponding to only one traversal); due to the square dependence on the gradient amplitude the net contribution of the *y*-gradients to the z^2 Maxwell term is typically a factor ~100 smaller. While they do not constitute a practical concern, a full compensation of the Maxwell effects would have to take their contribution into account.

In summary, we present a new VASO method which allows reliable detection of brain activation with large volume coverage. The VASO GRASE approach yields images and signal changes that are probably more straightforward to process and interpret than those generated by previously proposed multi-slice schemes. The ultimate goal of performing real cognitive stimulation tasks or resting state experiments with CBV contrast now seems within reach, opening up a whole range of interesting future possibilities. This may include benefiting from the potentially higher spatial specificity than BOLD, as well as further addressing open questions regarding the brain's haemodynamic and metabolic functioning.

Acknowledgements

We thank Markus Barth and Peter Koopmans for helpful discussions, and Matthias Günther (mediri GmbH, Heidelberg, Germany, www.mediri.de) for providing the source code of his ASL sequence which served as starting point for the GRASE VASO implementation.

References

Devor A, Tian P, Nishimura N, Teng IC, Hillman EM, Narayanan SN, Ulbert I, Boas DA, Kleinfeld D, Dale AM. (2007) Suppressed neuronal activity and concurrent arteriolar vasoconstriction may explain negative blood oxygenation level-dependent signal. *J Neurosci* 27:4452-4459

Donahue MJ, Lu H, Jones CK, Edden RA, Pekar JJ, van Zijl PC. (2006) Theoretical and experimental investigation of the VASO contrast mechanism. *Magn Reson Med* 56:1261-1273

Gunther M, Oshio K, Feinberg DA. (2005) Single-shot 3D imaging techniques improve arterial spin labeling perfusion measurements. *Magn Reson Med* 54:491-498

Hillman EM, Devor A, Bouchard MB, Dunn AK, Krauss GW, Skoch J, Bacskai BJ, Dale AM, Boas DA. (2007) Depth-resolved optical imaging and microscopy of vascular compartment dynamics during somatosensory stimulation. *Neuroimage* 35:89-104

Kim T, Hendrich KS, Masamoto K, Kim SG. (2007) Arterial versus total blood volume changes during neural activity-induced cerebral blood flow change: implication for BOLD fMRI. *J Cereb Blood Flow Metab* 27:1235-1247

Lu H, Clingman C, Golay X, van Zijl PC. (2004a) Determining the longitudinal relaxation time (T1) of blood at 3.0 Tesla. *Magn Reson Med* 52:679-682

Lu H, Donahue M, Jones C, van Zijl P. (2005a) Spatial Characteristics of VASO fMRI at Ultra-High Resolution. In: *Proceedings of the 13th Annual Meeting of ISMRM*, Miami, p 27

Lu H, Golay X, Pekar JJ, van Zijl PCM. (2003) Functional magnetic resonance Imaging based on changes in vascular space occupancy. *Magn Reson Med* 50:263-274

Lu H, Law M, Johnson G, Ge Y, van Zijl PC, Helpern JA. (2005b) Novel approach to the measurement of absolute cerebral blood volume using vascular-space-occupancy magnetic resonance imaging. *Magn Reson Med* 54:1403-1411

Lu H, van Zijl PC, Hendrikse J, Golay X. (2004b) Multiple acquisitions with global inversion cycling (MAGIC): a multislice technique for vascular-space-occupancy dependent fMRI. *Magn Reson Med* 51:9-15

Lu HZ, Golay X, Pekar JJ, van Zijl PCM. (2004c) Sustained poststimulus elevation in cerebral oxygen utilization after vascular recovery. *Journal of Cerebral Blood Flow and Metabolism* 24:764-770

Lu HZ, van Zijl PCM. (2005) Experimental measurement of extravascular parenchymal BOLD effects and tissue oxygen extraction fractions using multi-echo VASO fMRI at 1.5 and 3.0 T. *Magnetic Resonance in Medicine* 53:808-816

Norris DG, Hutchison JM. (1990) Concomitant magnetic field gradients and their effects on imaging at low magnetic field strengths. *Magn Reson Imaging* 8:33-37

Ogawa S, Lee TM, Kay AR, Tank DW. (1990) Brain magnetic resonance imaging with contrast dependent on blood oxygenation. *Proc Natl Acad Sci U S A* 87:9868-9872

Poser BA, Norris DG. (2007) Measurement of activation-related changes in cerebral blood volume: VASO with single-shot HASTE acquisition. *Magn Reson Mater Phy* 20:63-67

Scouten A, Constable RT. (2007) Applications and limitations of whole-brain MAGIC VASO functional imaging. *Magn Reson Med* 58:306-315

Song AW, Wong EC, Hyde JS. (1994) Echo-volume imaging. *Magn Reson Med* 32:668-671

Thomas DL, Lythgoe MF, Calamante F, Gadian DG, Ordidge RJ. (2001) Simultaneous noninvasive measurement of CBF and CBV using double-echo FAIR (DEFAIR). *Magn Reson Med* 45:853-863

Wansapura JP, Holland SK, Dunn RS, Ball WS, Jr. (1999) NMR relaxation times in the human brain at 3.0 tesla. *J Magn Reson Imaging* 9:531-538

Yang Y, Gu H, Stein EA. (2004) Simultaneous MRI acquisition of blood volume, blood flow, and blood oxygenation information during brain activation. *Magn Reson Med* 52:1407-1417

Zhou XJ, Tan SG, Bernstein MA. (1998) Artefacts induced by concomitant magnetic field in fast spin-echo imaging. *Magn Reson Med* 40:582-591

Chapter 11 Summary

Functional MRI has become an indispensable neuroscientific tool for probing brain function. Since its first demonstration in 1990, nearly 17.000 human and animal studies have been published with the keyword ‘fMRI’ (at the time of writing of this thesis). Most fMRI investigations today are conducted by ‘users’ from well outside the field of MR physics, with the largest user group being the cognitive neurosciences; but also clinical applications on single patients, such as pre-surgical functional brain mapping, are rapidly gaining importance. The vast majority of these studies make use of the BOLD contrast, measured with GE-EPI in very much the same manner as Bandettini and Blamire did already in 1992. Interestingly, the major improvements to routine BOLD fMRI in the last fifteen years have very clearly not been in sequence design. Instead it has largely benefited from drastic improvements in the hardware, including high field magnets, quality gradients and receiver coils, but also improvements in image reconstruction and post-processing algorithms; not to forget the battery of advanced statistical analysis techniques. This is not to suggest that MR method developers have been lethargic: a large number of exciting fMRI niche applications for specific research questions are continuously being thought up. But for routine use, 2D GE-EPI with its very remarkable functional sensitivity and acquisition speed appears hard to beat, despite its problems with susceptibility artefacts especially at high field.

It is for this reason that the first project towards this thesis was originally intended as a small improvement to the conventional EPI sequence. Parallel imaging had only just become available and been suggested as useful to fMRI (de Zwart et al. 2002a; de Zwart et al. 2002b). The implementation of a multi-echo EPI sequence was hence an obvious first step to take. While the idea of multi-echo sampling was not *per se* new, parallel imaging now permitted a realistic and potentially competitive strategy by which multiple EPI images, typically five, could be acquired within the same repetition time as a conventional EPI image. That image quality was drastically improved, both in terms of signal void and image distortions was quickly demonstrated. Next, different echo combination schemes were investigated to optimally extract the functional information from the now five times larger data volume. Three methods were implemented: simple summation, weighted summation according to the BOLD signal expected from a pixel-wise T_2* fit, and a weighted summation according to a new filter that was developed for this purpose and that weights the echo signal depending on their relative measured CNR contribution. The CNR weighting filter was found to be superior to the other techniques in subsequent SNR and CNR measurements, but even simple echo summation yielded some improvement in BOLD sensitivity compared to

conventional EPI. The superiority of the weighted summation was shown to result from the strong echo time dependence of BOLD contrast at 3 T: the more BOLD contrast a given echo contributes, the more weight it receives in the summation. These findings were confirmed in the ‘field test’ application, a comparative activation study with a cognitive Stroop task experiment. What was intended a small improvement turned out to be a considerable improvement of both image quality and BOLD sensitivity. Following upgrades on the image reconstruction hardware, a steadily increasing number of routine fMRI studies at the Donders Institute now makes use of multi-echo EPI acquisitions with a post-processing chain that has meanwhile been further advanced (Buur et al. 2008; Buur et al. in preparation; Buur et al. 2009).
When the 7 T system at the Erwin L. Hahn Institute in Essen became available nearly three years later, the even greater problem of inhomogeneity artefacts prompted a new series of parallel-accelerated multi-echo experiments. Again image quality was shown to considerably improve, as expected. The far more interesting findings however were (a) superior BOLD sensitivity compared to standard EPI scans which are often affected by strong ghosting artefacts, (b) a low echo time dependence of BOLD sensitivity in accordance with physiological noise investigations, resulting in (c) that simple summation is an equally good approach as the CNR weighting which had been found superior at 3 T. The latter finding considerably eases implementation, data storage and post-processing requirements and shall hopefully encourage other researchers to benefit from the advantages of multi-echo EPI. An additional set of very interesting observations were made at 7 T: In contradiction to the common assumption of dominant physiological noise that coherently affects all TE images, a low degree of correlation between echo time courses was observed. While the underlying mechanism of this remains to be studied more fully, this important finding by itself provides concrete evidence why multi-echo summation will always be beneficial even, or possibly in particular, in the domain of dominating physiological noise (where the experiments where performed). Many aspects of noise in fMRI still need to be studied, and multi-echo EPI might be expected to play an important role in this effort. Meanwhile, the artefact level of accelerated (multi-echo) EPI acquisitions could be much further reduced by replacing the conventional 2D slice selective sampling of EPI by 3D encoding (Poser et al. in preparation). The overall conclusion from the experiments at both 3 T and 7 T is that for EPI at typical spatial resolution multi-echo acquisitions should be the preferred choice.

The second part of the work towards this thesis was concerned with the development and application of an fMRI technique that yields images entirely free of inhomogeneity artefacts. The RARE (TSE, FSE) sequence is a prime candidate for this, however in its conventional form is far too restricted due to RF power deposition, and too slow if appreciable volume coverage is to be achieved. Again, parallel imaging came to help and a highly accelerated version of a partial-Fourier RARE sequence and SENSE reconstruction were implemented. The timing

constraints were alleviated, in principle allowing an acquisition of eight slices per second which is close to SE-EPI at optimal parameters (in practice restrictions due to SAR apply at 3 T). The inherently low BOLD sensitivity of the purely T_2 weighted sequence was increased by introducing a long first RF interval so as to allow extravascular dynamic dephasing to develop. At 3 T the BOLD signal is hence also more strongly weighted toward the microvasculature, the most favourable property of spin echo BOLD contrast at higher field. A comparative study with SE-EPI was performed using a visual stimulation task, in which it was demonstrated that the RARE BOLD sequence can be of comparable sensitivity to SE-EPI. The conclusion is hence that the RARE sequence may be chosen as alternative to SE-EPI especially if distortion free images are required.
The interesting observation of a very pronounced post-stimulus BOLD undershoot in the T_2-weighted fMRI data was interpreted as contradictory to the generally accepted Balloon model hypothesis for the undershoot, and triggered the subsequent application of the sequence to the study of this phenomenon. Taking advantage of the field strength dependence of the T_2 BOLD contributions, a large number of subjects was scanned at both 1.5 T and 3 T, in order to test three hypotheses for the mechanism underlying the undershoot. The main experimental finding was an equal undershoot to peak ratio at both fields, which excludes the Balloon model hypothesis, but also excludes a hypothesis based on parenchymal CBV changes as the sole contributor. Instead the data support the idea of the sustained oxygen metabolism model according to which $CMRO_2$ remains elevated for some time after stimulation and beyond the return of CBV and CBF to baseline. Furthermore, simulations were performed on the basis of the measured BOLD response curves, and the plausibility of a vascular ballooning mechanism on the arteriolar side as a cause of the undershoot was demonstrated. There is now a growing body of literature both from high-resolution animal MRI (Jin and Kim 2008; Kim et al. 2007; Zhao et al. 2007) and the optical imaging community (Devor et al. 2007; Hillman et al. 2007) that CBV changes to take place primarily on the supply side.

The third part of the thesis continues along the theme of spin-echo based fMRI, but inspired by the then newly introduced VASO method (Lu et al. 2003) is focused on the development and evaluation of blood volume weighted techniques. VASO is a novel technique that is sensitive to relative changes in CBV by virtue of an inversion recovery preparation for blood nulling and importantly does not require the administration of a contrast agent. First, a VASO variant was implemented on the basis of a short-TE half-Fourier RARE readout. SAR is here not a constraint as VASO is inherently a single slice method with long TR, and no parallel acquisition was required. The new VASO sequence was evaluated by comparison with the originally proposed GE-EPI VASO in a visual activation study. The results reveal larger relative signal changes in the spin echo based VASO, and furthermore a more than 40% increased activation volume at the same significance level. Inflow effects were investigated by repeated measurements at different TR and could be excluded as a reason for the positive finding. Apart from the much increased sensitivity, the RARE VASO approach is entirely distortion free, and is also considerably less sensitive to BOLD contamination, which is a concern in GE-EPI VASO due the non-zero TE. The conclusion is hence for multiple reasons that VASO with a short-TE half-Fourier RARE readout is the preferred method for the measurement of relative CBV changes, a suggestion that has meanwhile been taken onboard by other authors (Hua et al. 2009). SE-EPI based VASO has also been proposed on the basis of similar arguments (Donahue et al. 2006).

The most severe limitation of the original VASO method was put at the focus of the second project on of CBV weighted fMRI: the limited volume coverage. A multi-slice version of VASO (i.e. MAGIC) was proposed in the literature soon after the publication of the original method (Lu et al. 2004), however it comes with a number of known limitations (Lu et al. 2004; Scouten and Constable 2007). The approach chosen here was to combine VASO with a 3D GRASE readout the benefits of which had been firmly established in CBF weighted fMRI applications (Fernandez-Seara et al. 2007; Fernandez-Seara et al. 2005; Gunther et al. 2005; MacIntosh et al. 2008). A 3D GRASE sequence with short-TE centric-out phase encoding and 2D parallel imaging support was hence programmed and combined with a VASO preparation. During phantom test measurements in the implementation phase, smearing artefacts in the *z*-direction were repeatedly observed, which could eventually be ascribed to phase errors arising from concomitant Maxwell terms that gave rise to an effective phase difference before and after the first refocusing pulse. Maxwell compensating gradients were hence introduced; here a tripolar implementation is proposed to avoid the flow weighting associated with the more commonly used bipolar gradients. While being a by-product, a very crucial finding of the study was therefore that in contradiction to the often-made assumption of negligible Maxwell terms are at $B_0 > 1.5$ T, the GRASE sequence cannot be guaranteed to yield artefact free images without appropriate correction gradients.

The CBV weighted properties of the functioning sequence were evaluated by a visual-motor task on eight subjects. Near whole brain coverage was easily achieved. Maps of visual and motor activation (M1 and SMA) could be obtained in all subjects; moreover the observed signal changes and sensitivity agreed well with what is typically observed in single-slice EPI based VASO. The clear advantage of GRASE as 3D single-shot method is, in contrast to MAGIC, that there is equal CBV weighting in each slice.

This important development thus in principle enables ‘true’ cognitive fMRI experiments with CBV contrast that were previously unthinkable. Since completion of the study which was presented in Chapter 10, first CBV weighted pilot experiments have been performed with a Stroop task paradigm. The initial data indicate that brain regions corresponding to those seen in BOLD measurements can be detected in a reasonable experimental duration. If confirmed in a full study, the implications would be considerable. A very interesting application will also be the investigation of CBV fluctuations in the resting state; this may shed some light on the mechanisms underlying a phenomenon that could so far only be probed by BOLD (and only to degree by CBF) fMRI. It is in any case conceivable that GRASE VASO along with the multi-echo EPI method becomes one of the more widely applicable fMRI techniques that users of fMRI have at their disposal.

Zusammenfassung

Die funktionelle Magnetresonanztomographie (fMRT) hat sich in den vergangenen zwei Jahrzehnten zu einer für die Neurowissenschaften unentbehrlichen Bildgebungsmodalität entwickelt: Seit ihrer ersten erfolgreichen Anwendung im Jahre 1990 sind nahezu 17.000 Studien an Mensch und Tier mit dem Schlagwort ‚fMRI' veröffentlicht worden. Heutzutage wird die große Mehrheit an fMRT-Studien von wissenschaftlichen ‚Anwendern' von außerhalb der MR-Physik durchgeführt, wobei die kognitiven Neurowissenschaften die bei weitem größte Gruppe stellen. Doch auch klinische Applikationen am einzelnen Patienten, wie zum Beispiel das prä-operative Kartieren der Funktion verschiedener Hirnareale, gewinnen zunehmend an Bedeutung. Der Großteil aller fMRT-Untersuchungen basiert auf dem BOLD Kontrast[1], und verwendet dazu mit GE-EPI[2] nahezu dieselben Bildgebungsverfahren wie Bandettini und Blamire schon im Jahre 1992. Erstaunlicherweise haben die maßgeblichen Verbesserungen der BOLD fMRT als Routine-Anwendung während der vergangenen fünfzehn Jahre aber keineswegs im Bereich der Sequenzentwicklung stattgefunden. Stattdessen wurden drastische Fortschritte im Hardwarebereich erzielt, darunter die Entwicklung von Hochfeldmagneten, qualitativ hochwertigen Gradientenspulen und mehrkanaligen Empfangsspulen, aber auch im Bereich der Bildrekonstruktions- und Nachbearbeitungs-Algorithmen. Nicht zu vergessen ist hierbei das kontinuierlich wachsende Sortiment an komplexen statistischen Auswertemethoden. Dies stellt jedoch keine Trägheit seitens der Pulssequenz-Entwickler dar: eine Vielzahl interessanter fMRT Sequenzen, oft für spezifische Nischenanwendungen, wird regelmäßig veröffentlicht. Für die fMRT als Routineanwendung bei klinischen Feldstärken aber ist 2D GE-EPI mit seiner enormen Sensitivität and Akquisitions-Effizienz schwer zu übertreffen – trotz der Schwierigkeiten mit Suszeptibilitäts-Artefakten insbesondere bei den zunehmend beliebten hohen Feldstärken.

Aus diesem Grund hatte das erste Projekt dieser Arbeit zunächst eine schrittweise Verbesserung der konventionellen EPI Sequenz zum Ziel. Verschiedene Methoden zur parallelen Bildgebung waren kurz zuvor entwickelt worden und erste Studien konnten ihre Bedeutung für fMRT-Anwendungen demonstrieren (de Zwart et al. 2002a; de Zwart et al. 2002b). In dieser Hinsicht war die Implementierung der multi-echo (ME-) EPI Sequenz ein offensichtlicher erster Schritt. Während die Sequenz *per se* keine Neuerung darstellte, so erlaubte sie nun durch die Verwendung paralleler Bildgebung eine realistische und wettbewerbsfähige

---

[1] BOLD Kontrast = ‚blood oxygenation level dependent' Kontrast

[2] GE-EPI = gradient-echo echo planar imaging

Akquisitionsstrategie, durch die die Aufnahme mehrer (etwa fünf) EPI-Bilder in derselben Wiederholungszeit (TR) wie bei einer konventionellen EPI Sequenz möglich ist. Die daraus resultierenden Vorteile für die Bildqualität waren eindeutig und konnten schnell demonstriert werden, sowohl im Bezug auf Bildverzerrungen als auch die Signalauslöschungen durch Dephasierung.

Um die durch Hirnaktivierung verursachten Signaländerungen optimal darzustellen, wurden als nächstes drei verschiedene Methoden zur Echo-Summierung untersucht: (a) einfache Aufsummierung aller Echos, (b) gewichtete Summierung Pixel für Pixel entsprechend dem relativen BOLD Kontrast, der aufgrund zuvor berechneter T_2*-Karten zu erwarten ist, und (c) gewichtete Summierung Pixel für Pixel mit dem eigens dafür entwickelten PAID[3] Filter, der den relativen Beitrag der einzelnen Echos zum BOLD Kontrast abschätzt. In anschließenden SNR- und CNR-Messungen[4] erwies sich der PAID Filter als überlegen, doch selbst ungewichtete Echo-Summierung führte im Vergleich zu konventionellem EPI zu einer verbesserten BOLD Sensitivität. Der Nutzen einer gewichteten Summierung wurde auf die Abhängigkeit des BOLD Kontrasts von der Echozeit zurückgeführt: je größer das CNR eines Echos, desto stärker seine Gewichtung bei der Echo-Kombination. Dies konnte auch im Feldtest gezeigt werden, einer Aktivierungsstudie mit kognitivem Stroop-Task Experiment. Obwohl das ME-EPI ursprünglich primär als Optimierung des gebräuchlichen EPI gedacht war, erwies es sich als beachtliche Verbesserung sowohl im Hinblick auf Bildqualität als auch auf BOLD Sensitivität. Nach Upgrades der Bildrechner und Rekonstruktions-Software wird am Donders Institute nun ein stetig wachsender Anteil der fMRT Studien mit multi-echo EPI gemessen, wozu auch die Entwicklung optimierter Methoden für die Daten-Nachbearbeitung erheblich vorangetrieben wurde (Buur et al. 2008; Buur et al. in Vorbereitung; Buur et al. 2009).

Als beinahe drei Jahre später das 7 T System am Erwin L. Hahn Institute in Essen in Betrieb genommen wurde, führten wir angesichts der bei 7 T noch größeren Probleme mit Inhomogenitätsartefakten erneut ME-EPI Messungen durch. Wieder zeigte sich erwartungsgemäß eine erheblich verbesserte Bildqualität. Viel bedeutendere Ergebnisse hingegen waren, dass (a) BOLD-Sensitivität höher war als bei normalen EPI-Messungen, die oft unter starken Nyquist-Geist-Artefakten leiden, und (b) sich eine sehr geringe Echozeit-Abhängigkeit der Aktivierung ergab, im Einklang mit Berechnungen unter Einbeziehen des physiologischen Rauschens. Daraus resultiert (c), dass im Gagensatz zu den Ergebnissen bei 3 T einfache Echosummierung vergleichbar gut funktioniert wie CNR-Gewichtung. Letzteres ist aus praktischer Sicht sehr vorteilhaft, da es die Sequenz-Implementierung erheblich erleichtert, deutlich weniger Bild-Datenspeicher erfordert, und eine Anzahl von zeitaufwendigen Nachbearbeitungsschritten entfällt. Es steht zu hoffen, dass diese Vereinfachungen weitere Wissenschaftler ermutigen, sich die Vorteile von ME-EPI zunutze zu machen. Eine weitere wichtige

---

[3] PAID = parallel-acquired inhomogeneity desensitised

[4] SNR = Signal-Rausch-Verhältnis; CNR = Kontrast-Rausch-Verhältnis

Beobachtung in den 7 T Daten war, dass nur eine schwache Korrelation zwischen den Zeitverläufen der einzelnen Echos festgestellt wurde. Das ist im Widerspruch zur allgemeinen Annahme, dass sich physiologisches Rauschen kohärent auf alle Echozeiten auswirkt. Die zugrundeliegenden Mechanismen müssen in weiteren Studien genauer untersucht werden, aber die Tatsache an sich führt zu dem Schluss, dass Echosummierung immer nützlich ist, sogar (oder vielleicht gerade) in der Domäne dominierenden physiologischen Rauschens, in welcher die Experimente durchgeführt wurden. Viele Aspekte des physiologischen Rauschens in fMRT Daten müssen noch besser erforscht und verstanden werden, und es ist davon auszugehen, dass ME-EPI dabei eine wichtige Rolle spielen wird. Mittlerweile ist es uns gelungen, Artefakte der parallelen Bildgebung in (multi-echo) EPI Akquisitionen drastisch weiter zu reduzieren, indem die 2D schichtselektive Anregung durch 3D Volumenanregung mit zweifacher Phasenkodierung ersetzt wurde, was darüber hinaus eine optimale Nutzung paralleler Bildgebung gestattet (Poser et al. in Vorbereitung).

Der zweite Teil dieser Arbeit beschäftigt sich mit der Entwicklung und Anwendung einer fMRT Methode, die vollständig frei von Suszeptibilitäts-Artefakten ist. Die RARE (TSE, FSE)[5] Sequenz wäre hierfür ein guter Kandidat, ist aber in ihrer ursprünglichen Form durch hohe SAR[6]-Werte zu stark eingeschränkt, und gleichzeitig zu langsam, um in angemessener Zeit eine ausreichende Volumenabdeckung zu erzielen. Wieder kann die parallele Bildgebung hilfreich eingesetzt werden, und eine partial-Fourier RARE Sequenz sowie Rekonstruktion für Sensitivity-Enconding (SENSE) wurden implementiert. So wurden die Schwierigkeiten soweit überwunden, dass acht Schichten pro Sekunde gemessen werden können, was in etwa einer konventionellen SE-EPI Sequenz entspricht (*in vivo* kommt es aber zu zusätzlichen Einschränkungen durch SAR). Die inhärent geringe BOLD Sensitivität von rein T_2-gewichteten Sequenzen wurde durch Verlängern des ersten RF-Intervalls erhöht, so dass sich während dieser Zeitspanne eine von der Deoxyhämoglobin-Konzentration abhängige Signaldämpfung durch dynamisches Dephasieren im extravaskulären (insbesondere extrakapillaren) Raum entfalten kann. Bei 3 T ist somit das BOLD Signal stärker zu den Kapillargefäßen hin gewichtet, worin sich auch der große Nutzen und die Beliebtheit von Spin-Echo Sequenzen bei hohen Feldstärken erklärt. Ein Vergleich zu SE-EPI wurde mit Hilfe einer Aktivierungsstudie mit visueller Stimulation durchgeführt. Die Experimente ergaben, dass die RARE BOLD Sequenz eine ähnliche Sensitivität besitzt und somit eine Alternative zu SE-EPI bieten kann, insbesondere wenn verzerrungsfreie Bilder erforderlich sind.

Die überraschende Beobachtung eines ‚post-stimulus BOLD Undershoot' in den rein T_2-gewichteten Daten schien zu der weithin akzeptierten These für den

---

[5] RARE = rapid acquisition with relaxation enhancement; TSE = turbo spin echo; FSE = fast spin echo

[6] SAR = specific absorption rate

Undershoot aus Buxtons ‚Balloon oder Winkesselmodel' im Widerspruch zu stehen, und gab Anlass für weiterführende Studien, in denen das Phänomen genauer untersucht wurde.
Hierbei haben wir uns zunutze gemacht, dass die Zusammensetzung des T_2 BOLD Signals stark feldstärkenabhängig ist, und maßen eine große Anzahl Probanden bei 1.5 T und 3 T, um drei plausible Hypothesen für den BOLD Undershoot zu testen. Die Messungen ergaben ein identisches Verhältnis von Undershoot zur positiven BOLD-Antwort bei 1.5 T und 3 T, was die Hypothese des Balloon Models widerlegte, aber auch die alternative Erklärung, dass der undershoot allein durch Blutvolumensänderungen (CBV) im Parenchym verursacht wird. Stattdessen deuten die Ergebnisse auf einen über die Aktivierung hinaus anhaltenden Sauerstoffmetabolismus ($CMRO_2$) hin, der auch nach Rückgang von Blutfluss (CBF) und CBV zum Basiszustand fortdauert und dadurch nach dem Stimulus eine Akkumulierung von Deoxyhämoglobin verursacht. Des Weiteren wurden auf Basis der gemessenen BOLD Signalverläufe Simulationen durchgeführt, welche zeigten, dass auch ein vaskulärer Balloneffekt in den prä-kapillaren Arteriolen als Ursache für den Undershoot in Frage kommt. Eine stetig wachsende Zahl an Studien sowohl aus dem Bereich der hochaufgelösten fMRT an Tieren (Jin and Kim 2008; Kim et al. 2007; Zhao et al. 2007), als auch als Studien mit optischen Bildgebungsverfahren (Devor et al. 2007; Hillman et al. 2007) weist ebenfalls darauf hin, dass die CBV Änderungen primär oder gar ausschließlich auf der Versorgungsseite stattfinden.

Der dritte Teil der Arbeit verfolgt ebenfalls die Weiterentwicklung Spin-echo-basierter fMRT. Maßgeblich inspiriert durch die VASO[7] Methode (Lu et al. 2003), konzentriert er sich auf die Entwicklung und Auswertung zweier CBV-gewichteter fMRT Methoden. VASO ist eine relativ neuartige Technik, die das Messen aktivierungsabhängiger CBV Änderungen ohne Kontrastmittelgaben gestattet, indem das Blut durch eine Inversions-Vorbereitung als endogenes Kontrastmittel verwendet wird. Zunächst wurde eine VASO Variante auf Basis der half-Fourier RARE Sequenz mit kurzer Echozeit implementiert. Für VASO als Einzelschicht-Methode mit langem TR stellen hohe SAR-Werte kein Hindernis dar und die Verwendung von paralleler Beschleunigung war nicht erforderlich. In einer Aktivierungsstudie mit visueller Stimulation wurde die neue VASO Methode mit Lu's ursprünglicher GE-EPI VASO Sequenz verglichen. Die Ergebnisse zeigten größere relative Signaländerungen in der auf Spin-echo basierten Sequenz, und darüber hinaus ein etwa um 40% erhöhtes Aktivierungsvolumen bei gleicher Signifikanz. Blutfluss-Effekte wurden durch Messungen bei verschiedenen Repetitionszeiten untersucht, konnten aber als Ursache ausgeschlossen werden. Abgesehen von der höheren Sensitivität liefert die RARE VASO Methode artefaktfreie Bilder. Darüber hinaus ist sie durch den reinen T_2-Kontrast bei kurzem

---

[7] VASO = vascular space occupancy

TE weniger anfällig für Einflüsse durch das entgegengesetzt verlaufende BOLD Signal, welches bei GE-EPI VASO problematisch sein kann.

Aus den verschiedenen genannten Gründen ist also für VASO eine RARE Auslese vorzuziehen, und mittlerweile sind auch andere Autoren zur Verwendung von RARE (Hua et al. 2009), oder SE-EPI (Donahue et al. 2006) übergegangen.

Der bei weitem größte Schwachpunkt der ursprünglichen VASO Methode wurde im zweiten Projekt in Angriff genommen: die eingeschränkte Volumenabdeckung da nur eine Einzelschicht aufgenommen werden kann. Eine mehrschichtige Variante von VASO, die sogenannte MAGIC Sequenz, wurde zwar bald nach VASO vorgeschlagen (Lu et al. 2004), jedoch ist auch sie mit verschiedenen Einschränkungen verbunden (Lu et al. 2004; Scouten and Constable 2007). Der hier gewählte Ansatz sollte VASO mit den Vorzügen einer 3D GRASE Auslese verbinden, welche sich zuvor bereits in CBF-gewichteten fMRT Studien mit als nützlich erwiesen hatte (Fernandez-Seara et al. 2007; Fernandez-Seara et al. 2005; Gunther et al. 2005; MacIntosh et al. 2008). Daher wurde eine 3D GRASE Sequenz mit zentrischer Phasenkodierung in z-Richtung und kurzer Echozeit implementiert, und mit einer Inversions-Vorbereitung versehen. Bei Phantommessungen während der Implementierungsphase wurden immer wieder Schmierartefakte in Schichtrichtung beobachtet, was letztendlich auf Phasendifferenzen zurückgeführt werden konnte, die durch unbalancierte Maxwell-Terme um den ersten Refokussierpuls herum auftreten. So wurden zusätzliche x-Gradienten zur Maxwell-Kompensierung eingeführt, und um eine ungewollte Flussgewichtung durch die typischen bipolaren Gradienten zu vermeiden, wurden hier intrinsisch flusskompensierte tripolare Gradienten verwendet. Obwohl es sich hierbei um ein Nebenprodukt des GRASE VASO Studie handelt, so war das Beobachten der Maxwell-Effekte doch ein wichtiges Ergebnis, das im Widerspruch zur allgemein gemachten Annahme steht, dass die Phasenfehler bei $B_0 > 1.5$ T vernachlässigbar sind: Je nach Schichtpositionierung können mit der 3D GRASE Sequenz auch bei 3 T ohne Maxwell-Korrektur keine artefaktfreien Bilder gewährleistet werden.

Die CBV-gewichteten Eigenschaften der Sequenz wurden mit Hilfe von Visuomotor-Stimulation bei acht Probanden untersucht. Fast volle Abdeckung des Hirns wurde erreicht, und Aktivierung im visuellem und im Motor-Kortex konnte bei allen Probanden sichtbar gemacht werden. Weiterhin ähnelten die beobachteten Signaländerungen stark denen in der mit der EPI-VASO Sequenz gemessenen Einzelschicht. Der eindeutige Vorteil von 3D GRASE als ‚single-shot' Methode ist im Gegensatz zu MAGIC die schichtunabhängige CBV-Gewichtung.

Diese wichtige Weiterentwicklung der VASO Methode gestattet nun prinzipiell ‚realistische' auf CBV basierte Aktivierungsstudien, die bis dahin undenkbar waren. Seit Fertigstellung der in Kapitel 10 beschriebenen GRASE VASO Studie haben wir Messungen mit dem Stroop-Paradigma durchgeführt. Die ersten Ergebnisse deuten darauf hin, dass innerhalb akzeptabler Messzeiten mit VASO die gleichen Aktivierungen sichtbar gemacht werden können wie mit BOLD fMRT. Wenn sich dies im weiteren Verlauf bestätigt, sind die Implikationen äußerst relevant. Eine sehr interessante Fragestellung ist zum Beispiel die Untersuchung der CBV Fluktuationen im ‚resting state', womit sich Licht auf ein Phänomen werfen ließe, das bisher nur mit BOLD gewichteter fMRT (und in sehr eingeschränkter Form CBF) untersucht werden konnte.

Auf Grund der hier vorgestellten Weiterentwicklung von VASO besteht nun in jedem Fall die Möglichkeit, dass funktionelle CBV Studien neben ME-EPI EPI eine der weiter verbreiteten fMRT-Methoden werden, und Anwendern zur Verfügung stehen um weitergehende, nicht-invasive Einblicke in die Funktionsweise des Gehirns zu gewinnen.

Samenvatting

De functionele magnetische resonantie beeldvorming (functional magnetic resonance imaging; fMRI) heeft zich in de afgelopen twee decennia ontwikkeld tot een voor de neurowetenschappen onmisbare beeldvormingsmodaliteit. Sinds de eerste succesvolle toepassing in 1990 zijn bijna 17.000 studies bij mens en dier met het keyword 'fMRI' gepubliceerd. Tegenwoordig worden de meeste fMRI studies gedaan door wetenschappers van buiten het domein van de MR fysica. De cognitieve neurowetenschappen vormen veruit de grootste groep. Echter, klinische toepassingen op individuele patiënten, zoals de preoperatieve *mapping* van de functie van verschillende hersenengebieden, worden steeds belangrijker. De meerderheid van alle fMRI studies is gebaseerd op het BOLD contrast[1] en wordt gemeten met GE-EPI[2], op grotendeels dezelfde wijze als Bandettini en Blamire dit deden in 1992. Interessant is dat de aanzienlijke verbeteringen van standaard BOLD fMRI in de afgelopen vijftien jaar zeker niet te danken zijn aan de ontwikkeling van verbeterde sequenties. Integendeel, de methode heeft vooral geprofiteerd van spectaculaire vooruitgang in de hardware, inclusief de ontwikkeling van sterkere magneten, hoogwaardiger gradiënten en meerkanaalsspoelen. Ook de belangrijke vooruitgang op het gebied van beeldreconstructie en *postprocessing* algoritmen en niet te vergeten het continu groeiende aanbod van geavanceerde methoden voor statistische analyse speelden een belangrijke rol. Dit wil echter niet zeggen dat de ontwikkeling van pulssequenties heeft stilgestaan; er komen zeer regelmatig interessante fMRI sequenties bij, vaak voor specifieke onderzoeksvragen. Echter, voor routinematig gebruik van fMRI op klinische veldsterktes is 2D GE-EPI, met zijn enorme gevoeligheid en acquisitiesnelheid, moeilijk te verslaan – ondanks problemen met susceptibiliteitsartefacten die vooral voorkomen bij hoge veldsterktes.

Om deze reden was het eerste project van dit proefschrift oorspronkelijk bedoeld als een kleine aanpassing van de conventionele EPI sequentie. Verschillende methoden voor parallelle beeldvorming waren net beschikbaar en er werd gesuggereerd dat ze relevant zouden zijn voor fMRI toepassingen (de Zwart et al., 2002a; de Zwart et al., 2002b). In dit verband was de implementatie van een multi-echo EPI sequentie een logische eerste stap. Hoewel het idee van multi-echo dataverzameling op zichzelf niet nieuw was, vormde parallelle beeldvorming een reële en wellicht concurrerende strategie in vergelijking met conventionele EPI, omdat meerdere EPI afbeeldingen (meestal vijf) verworven konden worden in dezelfde repetitie tijd (TR). Dat hierdoor de kwaliteit van de beelden met

---

[1] BOLD contrast = ‚blood oxygenation level dependent' contrast

[2] GE-EPI = gradient-echo echo planar imaging

betrekking tot signaalverlies en beeldvervormingen, was al snel aangetoond. Vervolgens werden verschillende technieken voor echocombinatie onderzocht opdat de functionele informatie optimaal kon worden geëxtraheerd uit het nu vijf keer zo grote data volume. Drie methoden werden geïmplementeerd: (a) eenvoudige sommatie, (b) sommatie gewogen volgens het voor ieder voxel verwachte BOLD signaal uit een T_2^* *fit* en (c) sommatie gewogen volgens het nieuwe PAID[3] filter, dat voor dit doel was ontwikkeld en dat het echosignaal (ook weer voor ieder voxel) weegt op basis van zijn relatief gemeten CNR bijdrage. Het CNR weegfilter bleek superieur ten opzichte van de andere technieken in daaropvolgende SNR- en CNR[4]-metingen. Echter, zelfs eenvoudige echo sommatie verbeterde de BOLD sensitiviteit in vergelijking met conventionele EPI. De superioriteit van de gewogen sommatie komt voort uit een sterke afhankelijkheid van echo tijd van BOLD contrast op 3 T: hoe meer BOLD contrast een echo bijdraagt, hoe zwaarder het gewicht in de sommatie. Dit werd bevestigd in een vergelijkende studie met een cognitief *Stroop* experiment. Wat in eerste instantie was bedoeld als een kleine aanpassing bleek een behoorlijke verbetering in zowel beeldkwaliteit als BOLD sensitiviteit. Na een *upgrade* van de beeldreconstructie hardware maakt een groeiend aantal fMRI studies in het Donders Institute gebruik van multi-echo EPI acquisitie in combinatie met *postprocessing* methoden die nog voortdurend verder ontwikkeld worden (Buur et al. 2008; Buur et al. in voorbereiding; Buur et al. 2009).

Toen bijna drie jaar later het 7 T systeem in Essen in gebruik werd genomen, , resulteerden nog grotere problemen met inhomogeniteitsartefacten in een nieuwe reeks multi-echo experimenten. Zoals verwacht verbeterde de beeldkwaliteit wederom sterk. Interessant was echter dat (a) de BOLD sensitiviteit sterk superieur was in vergelijking met conventionele EPI scans, die vaak onder sterke *Nyquist-ghost* artefacten lijden, (b) de BOLD gevoeligheid in slechts zeer kleine mate afhankelijk was van de echotijd, in overeenstemming met berekeningen voor fysiologische ruis, met als gevolg dat (c) eenvoudige sommatie een even goede benadering is als de CNR-gewogen sommatie, in tegenstelling tot de 3 T resultaten. Deze laatste bevinding vereenvoudigt de implementatie, dataopslag en het aantal *postprocessing* stappen, en zal hierdoor hopelijk andere onderzoekers aanmoedigen om te profiteren van de voordelen van multi-echo EPI. Meer interessante observaties werden gedaan in de 7 T data: in tegenstelling tot de algemene veronderstelling dat fysiologisch coherente ruis alle TE afbeeldingen beïnvloedt werd slechts een zwakke correlatie tussen de signalen in verschillende echotijden gevonden. Hoewel de onderliggende mechanismen verder onderzocht moeten worden, vormt deze bevinding op zich concreet bewijs dat multi-echo sommatie altijd nuttig is, zelfs (of misschien voornamelijk) in omstandigheden waarin fysiologische ruis dominant is, zoals ook hier het geval was. Veel aspecten van fysiologische ruis in fMRI moeten beter onderzocht en begrepen worden, en multi-echo EPI zou hierbij een belangrijke rol kunnen spelen. Ondertusen kunnen het

---

[3] PAID = parallel-acquired inhomogeneity desensitised

[4] SNR = signal-ruis verhouding, CNR = contrast-ruis verhouding

aantal en de ernst van artefacten van versnelde (multi-echo) EPI acquisities verder worden aangepakt door de conventionele 2D selectieve excitatie van EPI te vervangen door 3D volume excitatie (Poser et al. in voorbereiding). De conclusie van de experimenten op zowel 3 T als 7 T is dat voor EPI met een gangbare spatiële resolutie, multi-echo acquisitie de voorkeur zou moeten krijgen.

Het tweede deel van dit proefschrift betrof de ontwikkeling en toepassing van een fMRI techniek die volledig vrij is van inhomogeniteits-artefacten. De RARE (TSE, FSE)[5] sequentie is hiervoor een geschikte kandidaat, hoewel deze in oorspronkelijke vorm sterk wordt beperkt door het benodigde RF vermogen en bovendien te traag is om voldoende volume te beslaan. Ook hier bood parallele beeldvorming uitkomst en een sterk versnelde versie van een half-Fourier RARE sequentie met *sensitivity encoding* (SENSE) reconstructie werd geïmplementeerd. De beperkingen met betrekking tot timing werden overwonnen waardoor in principe acquisitie van 8 *slices* per seconde mogelijk werd, vergelijkbaar met SE-EPI met optimale parameters (in de praktijk wordt de methode op 3 T echter beperkt door de SAR[6] limiet). De inherent lage BOLD gevoeligheid van zuiver T_2-gewogen sequenties werd vergroot door verlenging van het eerste RF interval, zodat extravasculair dynamisch defasering zich kon ontwikkelen. Op 3 T wordt het BOLD signaal van de haarvaten relatief zwaarder gewogen, hetgeen het grootste voordeel van spin-echo sequenties bij hoge veldsterktes vormt. Een vergelijkende studie met SE-EPI werd uitgevoerd met visuele stimulatie, waarin werd gedemonstreerd dat de sensitiviteit van de RARE BOLD sequentie vergelijkbaar is met de sensitiviteit van SE-EPI. Hiermee biedt het goed alternatief, in het bijzonder wanneer afbeeldingen zonder vervormingen vereist zijn.

De verrassende observatie van een post-stimulus BOLD *undershoot* in de zuiver T_2-gewogen fMRI data leek tegenstrijdig met het algemeen geaccepteerde *Balloon* Model voor de *undershoot* van Buxton en gaf aanleiding tot een vervolgstudie waarin dit verschijnsel werd onderzocht. Hierbij werd gebruik gemaakt van de afhankelijkheid van de veldsterkte van de samenstelling van T_2 BOLD signaal. Een groot aantal vrijwilligers werd gescand op zowel 1.5 T als 3 T, om op die manier drie plausibele hypothesen voor de *undershoot* te testen. De belangrijkste bevinding was dat er gelijke *undershoot to peak* ratio's waren voor beide veldsterktes. Dit sluit zowel het Balloon model alsook de hypothese gebaseerd op alleen veranderingen van het bloed volume (CBV) in het parenchym uit. De resultaten steunen echter een hypothese die is gebaseerd op een verlengd zuurstofmetabolisme ($CMRO_2$) na stimulatie, en zelfs tot na terugkeer van CBV en bloed *flow* (CBF) naar uitgangswaarden. Bovendien werden simulaties uitgevoerd op basis van de gemeten BOLD respons curven en de plausibiliteit van een vasculair ballon effect aan arteriële zijde als oorzaak van de *undershoot* werd aangetoond. Een groeiend aantal studies, gebruik makend van zowel fMRI met

---

[5] RARE = rapid acquisition with relaxation enhancement, TSE = turbo spin echo, FSE = fast spin echo

[6] SAR = specific absorption rate

hoge resolutie bij dieren (Jin and Kim 2008; Kim et al. 2007; Zhao et al. 2007) als van optische beeldvorming (Devor et al., 2007, Hillman et al., 2007), laten zien dat veranderingen in CBV vooral plaats vinden aan de arteriële zijde.

Het derde deel van dit proefschrift bouwt voort op het thema van *spin echo based fMRI*, ditmaal geïnspireerd door de toen net geïntroduceerde VASO[7] methode (Lu et al., 2003) en was gericht op de ontwikkeling en evaluatie van CBV-gewogen technieken. VASO is een relatief nieuwe techniek die gevoelig is voor de relatieve veranderingen in CBV, waarbij bloed als een endogeen contrast middel gebruikt wordt door middel van een *inversion recovery* experiment. Eerst werd een VASO variant geïmplementeerd gebaseerd op een half-Fourier RARE sequentie met een korte TE. Omdat VASO een *single-slice* methode is met een lange TR wordt de methode niet beperkt door SAR en is parallelle acquisitie niet noodzakelijk. De nieuwe VASO sequentie werd vergeleken met de GE-EPI VASO methode van Lu et al. in een studie met visuele stimulatie; de resultaten toonden grotere relatieve veranderingen in signaal in de VASO sequentie die was gebaseerd op spin-echo. Bovendien nam het activatie volume toe met meer dan 40% bij eenzelfde significantie niveau. *Inflow* effecten werden onderzocht door de metingen herhalen met diverse repetitietijden en konden worden uitgesloten als oorzaak. Behalve de veel hogere gevoeligheid is de RARE VASO methode ook vrij van vervormingen en beduidend minder gevoelig voor BOLD contaminatie dan GE-EPI VASO. Samengevat heeft de half-Fourier RARE VASO methode met korte TE de voorkeur het meten van relatieve veranderingen in CBV. Deze suggestie is inmiddels overgenomen door andere auteurs (Hua et al. 2009). Ook SE-EPI VASO is voorgesteld op basis van soortgelijke argumenten (Donahue et al., 2006).

De grootste belemmering van de oorspronkelijke VASO methode werd de focus van het tweede project voor CBV-gewogen fMRI: de beperkte dekking van volume. Een *multi-slice* versie van VASO, de zogenaamde MAGIC sequentie werd kort na de publicatie van VASO voorgesteld (Lu et al., 2004). Deze sequentie heeft echter een aantal beperkingen (Lu et al., 2004; Scouten en Constable 2007). In dit proefschrift werd VASO daarom gecombineerd met de voordelen van een 3D GRASE *readout* welke zich al in CBF-gewogen fMRI studies had bewezen (Fernandez-Seara et al., 2005, Fernandez-Seara et al., 2007; Gunther et al 2005; MacIntosh et al., 2008). Een 3D GRASE sequentie met centrische fasecodering in de z-richting, korte TE en 2D parallelle beeldvorming werd geïmplementeerd en gecombineerd met de VASO voorbereiding. Bij fantoommetingen tijdens de implementatiefase werden herhaaldelijk *smearing* artefacten in de *z*-richting waargenomen, die uiteindelijk werden toegeschreven aan een faseverschil als gevolg van ongebalanceerde Maxwell termen die optreden voor en na de eerste *refocusing* puls. Daarom werd een extra *x*-gradiënt ingevoerd om voor de ontstane Maxwell termen te compenseren. Een tripolaire gradiënt werd gebruikt ter voorkoming van *flow* effecten die vaak worden gezien bij de veelgebruikte

---

[7] VASO = vascular space occupancy

bipolaire gradiënten. Hoewel een bijproduct, dit is het een belangrijk resultaat, aangezien het de algemene veronderstelling dat Maxwell termen verwaarloosbaar zijn voor $B_0 > 1.5$ T tegenspreekt. Zonder geschikte correctiegradiënten kunnen artefactvrije afbeeldingen niet worden gegarandeerd met de GRASE sequentie.

De CBV-gewogen eigenschappen van de sequentie werden onderzocht met behulp van visuele en motorische stimulatie van acht proefpersonen. Bijna volledige dekking van het brein werd eenvoudig bereikt en *maps* van visuele en motor activaties (M1 en SMA) konden worden verkregen van alle proefpersonen. De waargenomen signaalveranderingen en sensitiviteit kwamen in grote mate overeen met die in *single-slice* EPI-VASO. Het grote voordeel van de 3D GRASE *single-shot* methode is dat, in tegenstelling tot MAGIC, CBV in elke *slice* gelijk gewogen wordt.

Deze belangrijke ontwikkeling maakt cognitieve fMRI experimenten met CBV contrast mogelijk die voorheen ondenkbaar waren. Na de voltooiing van de studie gepresenteerd in hoofdstuk 10 zijn de eerste CBV-gewogen experimenten uitgevoerd met een *Stroop* paradigma. De eerste resultaten wijzen erop dat binnen een aanvaardbare experimentele duur hersenregio's worden gedetecteerd die overeenkomen met BOLD metingen. Als deze bevinding wordt bevestigd in een volledige studie heeft dit aanzienlijke implicaties. Het zou interessant zijn om CBV-fluctuaties in rusttoestand te onderzoeken. Dit zou licht kunnen werpen op mechanismen die ten grondslag liggen aan een fenomeen dat tot nu toe alleen met BOLD (en in zeer beperkte mate CBF) fMRI kan worden onderzocht. Het is hoe dan ook denkbaar dat GRASE VASO samen met multi-echo EPI een van de breed inzetbare fMRI technieken wordt die 'gebruikers' van fMRI tot hun beschikking hebben.

References

Buur P, Hesse C, Norris D. (2008) Separating BOLD activation from stimulus-correlated motion by means of linear source extraction applied to multi-echo data. In: *Proceedings 16th Scientific Meeting, International Society for Magnetic Resonance in Medicine*, Toronto, p 2491

Buur PF, Hesse CW, Norris DG. (in preparation) Optimal data analysis for multi-echo fMRI: preprocessing and echo combination

Buur PF, Poser BA, Norris DG. (2009) A dual echo approach to removing motion artefacts in fMRI time series. *NMR Biomed*

de Zwart JA, van Gelderen P, Kellman P, Duyn JH. (2002a) Application of sensitivity-encoded echo-planar imaging for blood oxygen level-dependent functional brain imaging. *Magn Reson Med* 48:1011-1020

de Zwart JA, van Gelderen P, Kellman P, Duyn JH. (2002b) Reduction of gradient acoustic noise in MRI using SENSE-EPI. *Neuroimage* 16:1151-1155

Devor A, Tian P, Nishimura N, Teng IC, Hillman EM, Narayanan SN, Ulbert I, Boas DA, Kleinfeld D, Dale AM. (2007) Suppressed neuronal activity and concurrent arteriolar vasoconstriction may explain negative blood oxygenation level-dependent signal. *J Neurosci* 27:4452-4459

Donahue MJ, Lu H, Jones CK, Edden RA, Pekar JJ, van Zijl PC. (2006) Theoretical and experimental investigation of the VASO contrast mechanism. *Magn Reson Med* 56:1261-1273

Fernandez-Seara MA, Wang J, Wang Z, Korczykowski M, Guenther M, Feinberg DA, Detre JA. (2007) Imaging mesial temporal lobe activation during scene encoding: Comparison of fMRI using BOLD and arterial spin labeling. *Human Brain Mapping* 28:1391-1400

Fernandez-Seara MA, Wang Z, Wang JJ, Rao HY, Guenther M, Feinberg DA, Detre JA. (2005) Continuous arterial spin labeling perfusion measurements using single shot 3D GRASE at 3 T. *Magnetic Resonance in Medicine* 54:1241-1247

Gunther M, Oshio K, Feinberg DA. (2005) Single-shot 3D imaging techniques improve arterial spin labeling perfusion measurements. *Magn Reson Med* 54:491-498

Hillman EM, Devor A, Bouchard MB, Dunn AK, Krauss GW, Skoch J, Bacskai BJ, Dale AM, Boas DA. (2007) Depth-resolved optical imaging and microscopy of vascular compartment dynamics during somatosensory stimulation. *Neuroimage* 35:89-104

Hua J, Donahue MJ, Zhao JM, Grgac K, Huang AJ, Zhou J, van Zijl PCM. (2009) Magnetization transfer enhanced vascular-space-occupancy (MT-VASO) functional MRI. *Magn Reson Med*

Jin T, Kim SG. (2008) Improved cortical-layer specificity of vascular space occupancy fMRI with slab inversion relative to spin-echo BOLD at 9.4 T. *Neuroimage* 40:59-67

Kim T, Hendrich KS, Masamoto K, Kim SG. (2007) Arterial versus total blood volume changes during neural activity-induced cerebral blood flow change: implication for BOLD fMRI. *J Cereb Blood Flow Metab* 27:1235-1247

Lu H, Golay X, Pekar JJ, van Zijl PCM. (2003) Functional magnetic resonance Imaging based on changes in vascular space occupancy. *Magn Reson Med* 50:263-274

Lu H, van Zijl PC, Hendrikse J, Golay X. (2004) Multiple acquisitions with global inversion cycling (MAGIC): a multislice technique for vascular-space-occupancy dependent fMRI. *Magn Reson Med* 51:9-15

MacIntosh BJ, Pattinson KTS, Gallichan D, Ahmad I, Miller KL, Feinberg DA, Wise RG, Jezzard P. (2008) Measuring the effects of remifentanil on cerebral blood flow and arterial arrival time using 3D GRASE MRI with pulsed arterial spin labelling. *Journal of Cerebral Blood Flow and Metabolism* 28:1514-1522

Poser BA, Koopmans PA, Witzel T, Wald LL, Barth M. (in preparation) Three dimensional EPI at high fields

Scouten A, Constable RT. (2007) Applications and limitations of whole-brain MAGIC VASO functional imaging. *Magn Reson Med* 58:306-315

Zhao F, Jin T, Wang P, Kim SG. (2007) Improved spatial localization of post-stimulus BOLD undershoot relative to positive BOLD. *Neuroimage* 34:1084-1092

Acknowledgements

The work towards this thesis was not accomplished in a day. In fact, the adventure lasted a fair few days (and nights), and it would never have been possible without the help und support of many people.

First and foremost, I wish to thank my supervisor David Norris. For taking me onboard as a PhD student. For always being accessible and having time to discuss ideas, progress and problems literally whenever I walked by his office. For always being so full of new ideas, which in turn quite often made him walk down to my office. For his ambition to always push the limits, which sometimes let me get stuck. For his unlimited (and luckily contagious!) enthusiasm, especially when I *was* stuck. For always knowing what I was up to. For always returning draft manuscripts within two days. For his constructive criticism. For being so incredibly organised. For hating to see ‘man minutes go down the drain’. For lunchtime runs. For Christmas drinks. For repeatedly pointing out that private life is at least as important as work. And of course for giving me the opportunity to continue my research in Essen and Nijmegen, and supporting my future plans whatever exactly they will turn out to be. David, it has been good to work under your supervision and guidance and I am grateful for all that I could learn during this time in your group.

I want to thank the entire Donders Family for their help, the discussions, brainstorming and breeding of new ideas, be it in meetings, in the corridor, on the coffee room couch or over some beers. I really enjoyed and benefited from this amazing environment with its culture of altruistic knowledge sharing, mutual interest and helping each other wherever possible. Surely it will be difficult to find another place where so many friendly, interested, interesting, good-looking, smart and intelligent people from such diverse scientific and personal backgrounds work together and ‘synergise’ as I have experienced during my time in Nijmegen. The distinction between work and free-time was often lost, and there will also be many good memories of the non-scientific activities; running club, movie club, frisbee, Batavierenrace, ping-pong, stamppot nights, games nights, FADs, etc. etc. Special thanks in this category go to my fellow lunchtime runners, Christine, David, René, Mattijs, Jan and Stan; and thanks, Marlieke, for putting up with my table tennis incompetence!

Very big thanks go out to the MR group, in particular Laura Parkes who kick-started me in my early days, statistics wiz kid Hubert Fonteijn, multi-echo expert and victim Pieter Buur, high-res and Matlab guy Peter Koopmans, and my personal senior advisor and next door neighbour Markus Barth. Thanks Emily for excellent coffee and the Dutch translation of the Summary chapter.

And I thank Paul Gaalman, for all his knowledgeable help in the MR lab, for letting me have countless ten-minute-in-between timeslots for trying yet another buggy sequence, and then forgiving me when I left the systems in a funny state or didn't fill in the logbook. Thanks also for the occasional piece of personal advice. The Donders wouldn't work the same without you in many ways.

My roommates Rogier, Markus, Hanneke, Ali, Giosuè, Erno, Irina, Stan, Anke and Hanneke, I've enjoyed sharing office with you. I'm grateful to R&M for teaching me how to verbally and physically communicate with disobedient computers, I still practice every day. In ironically perfect synchrony with the cycle of PhD life the room changed over the years from a beehive to an oasis of calm.

I thank the Admin and Technical Groups for providing the incredibly efficient and reliable infrastructure which essentially takes away all the annoying overhead and allows us scientists to do our science. Thanks to Marek for shouting 'Morning Ben', René for rescuing gigabytes of accidentally deleted data, and Tildie for being way more than just the good heart of the Centre.

I also thank my colleagues in Essen. After years of scanning heads to find blobs in rather blurry fMRI data, I realised that MR can also be used to make sharp images of other parts of the body, and even to see what's wrong inside! I keep being intrigued by your wire-bending and coil building skills. Thanks especially to Stefan 1, Oliver and Stephan 2 for your help with the system when ten reboots didn't help. And thanks to whoever paid all the helium for paying for all the helium…

After some years it's difficult to see the role of special people from the right perspective, but I feel I should thank at least a few.

Sabine, already on this super-rainy 'dagje uit' I knew you'd make a good country- and soul mate, even though our schizophrenic lives often limited our encounters to the Tuesday movies. It's a real shame your time at the Donders was so short, and even more so that I'm utterly useless at keeping contact. So I really look forward to seeing you and your family in summer!

Carinne, why did you finish your PhD and leave already after four years!? (Is this how it should be?) The times with you were really great fun, I surely did enjoy working and drinking whiskies together. We've caused some confusion along the way, but I'm really glad we manage to stay in touch and that I find you happier than ever!

Markus, thank you for being my senior advisor, weekly deriving with me from first principles what SNR means and teaching me all these k-space words in my own language (and some others in yours). It's been really nice working with you on the 3D project, and I hope we'll do much more together in future. I equally enjoyed our post-conference trips (how many MR-physicists fit in an American oven?).

Christine, you are amazing, adorable, uncomplicated. Thanks for all these uncountable runs even in the shittiest of weathers. I've always enjoyed your company, for the main part because it's simply nice; but you won't guess how much support and motivation it has given me when things were frustrating especially in the last two years. You've found the good mix of work, fun, sports

and beers that I'm still looking for. Maybe one day I'm fit enough to cycle up a mountain with you – and if not we can always try sailing again ;-)
Pieter, it's great you've been doing so much stuff on the multi-echo that I would never have had the time nor patience to do. It has made me feel a little guilty at times, but without your efforts nobody would be able to use this 'simplest' (haha) yet most useful thing that has come out of this thesis. Thanks for your numerous social initiatives, the dinners at your place, and letting me lodge in your apartment so many times. And of course for being my Paranimf!

Working at the Donders Centre has been a huge privilege, and thanks to many, my time here in Nijmegen will surely be difficult to top. It often felt like I was jumping between two separate worlds connected by little more than the Autobahn, but I never underrated the role of my friends and family up North. I therefore thank Steff, Kai, Joe and Carsten for their almost unconditional friendship and apologise for so often keeping my whereabouts secret especially in the first few years. The same goes for my sisters, Johanna and Katharina, thank you both for your understanding.
Gaby and Wolfgang, I'm happy to be so completely absorbed into your family which makes Heikendorf a double home for me. And yes, I can imagine what you felt when I lured your daughter to Düsseldorf... I appreciate your interest in what I'm doing, and of course thank you, Gaby, for always trying so hard to keep me warm, dry and fed.
Mami und Papi, what more could I ever have wished for than growing up in a loving and caring environment as we did, always being given so many opportunities to learn and explore. From the beginning you fostered an interest in the world, in people, in things and how they work (and if they didn't, in how to fix them). I'm endlessly grateful for that, and this is where it all started. I regret I didn't share more of my daily life with you and know your disappointment when I left so many questions unanswered.

And last but not least, my dearest wife Wiebke. Thank you for always being there for me, for all your support and encouragement, your patience, your trust, and your love. Mit keinen Worten dieser Welt könnte ich beschreiben, was Du mir bedeutest. Es ist wunderbar, dass es Dich gibt und ich freue mich riesig auf unsere gemeinsame Zukunft als ein Wir!

List of publications

Journal Articles

Poser BA, Versluis MJ, Hoogduin JM, Norris DG. *BOLD contrast sensitivity enhancement and artefact reduction with multiecho EPI: Parallel-acquired inhomogeneity-desensitised fMRI*. Magn Reson Med 55(6): 1227-1235; 2006

Poser BA, Norris DG. *Fast spin echo sequences for BOLD functional MRI*. Magn Reson Mater Phy 20(1): 11-17; 2007

Poser BA, Norris DG. *Measurement of activation-related changes in cerebral blood volume: VASO with single-shot HASTE acquisition.* Magn Reson Mater Phy 20(2): 63-67; 2007

Poser BA, Norris DG. *Investigating the benefits of multi-echo EPI for fMRI at 7 Tesla*. Neuroimage 45(4):1162-72; 2009

Buur PF, **Poser BA**, Norris DG. *A dual echo approach to removing motion artefacts in fMRI time series*. NMR Biomed (in press); 2009

Poser BA, Norris DG. *3D single-shot VASO using a Maxwell-gradient compensated GRASE sequence*. Magn Reson Med (in press); 2009

Poser BA, Norris DG. *Exploring the post-stimulus undershoot with spin-echo fMRI: implications for models of neurovascular response*. (in revision)

Poser BA, Koopmans PA, Witzel T, Wald LL, Barth M. *Three dimensional EPI at high fields*. (in preparation)

Conference Proceedings and Invited Talks

Poser BA, Versluis MJ, Hoogduin JM, Norris DG. *BOLD Contrast Sensitivity Enhancement and Artefact Reduction with Parallel-Acquired Inhomogeneity Desensitized (PAID) fMRI.* In: Proceedings of the13th Scientific Meeting, International Society for Magnetic Resonance in Medicine, Miami, p 1542; 2005

Poser BA, Norris DG. *BOLD Contrast Sensitivity Enhancement and Artefact Reduction with Parallel-Acquired Inhomogeneity Desensitized (PAID) fMRI.* In: Proceedings to HBM, Toronto p500; 2005

Poser BA, Norris DG. *Simple and reliable method for assessment of relative BOLD contrast sensitivity in GE-EPI based fMRI acquisition schemes*. In: Proceedings to HBM Toronto, Toronto, p 511; 2005

Piekema C, **Poser BA**, Fernandez G, Norris DG. *MTL study with Multi-Echo PAID fMRI at 3T*. In: Proceedings to HBM, Toronto, p 610; 2005

Poser BA, Norris D. *HASTE sequences for functional MRI: BOLD and VASO*. In: Proceedings of the 14th Annual Meeting of ISMRM, Seattle, p 416; 2006

van Leeuwen TM, Lamers M, Petersson KM, Rietveld T, Gussenhoven C, **Poser BA**, Hagoort, P. Prosody and information structure: An fMRI study. In: Proceedings to 12th Annual Conference on Architectures and Mechanisms for Language Processing (AMLaP), Nijmegen, 2006

Poser BA, Barth M, Norris D. *Evidence for functional activation in fusiform face area and amygdala using high-resolution single-shot GE-EPI at 7 T*. In: Proceedings of ISMRM High Field Workshop, Asilomar, California, p 60; 2007

Poser BA, Norris DG. *On bursting balloons and collapsing endothelia: what does cause the BOLD undershoot?* In: Proceedings of the 15th Annual Meeting of ISMRM, Berlin, p 26; 2007

van Leeuwen TM, Lamers M, Petersson KM, Rietveld T, Gussenhoven C, **Poser BA**, Hagoort, P. *Prosody and information structure: An fMRI study.* In: Proceedings to Cognitive Neuroscience Society 14th Annual meeting, New York, 2007

Poser BA. *Ultra-high Field Whole-Body Human Imaging - Looking back on the first year at the Erwin L Hahn Institute in Essen*. Invited talk, Oxford Centre for Functional MRI of the Brain (FMRIB), Oxford, November 23, 2007

van Leeuwen TM, Lamers M, Petersson KM, Rietveld T, Gussenhoven C, **Poser BA**, Hagoort, P.. *Prosody and information structure: An fMRI study*. In: proceedings to Workshop Prosody and information structure (Internationalization project 'Forms and Functions of Prosodic Structure'), Ravenstein, 2008

Poser BA, Norris DG. *PAID fMRI at 7T - investigating the benefits of multi-echo EPI at high field*. In: Proceedings to the first Annual Meeting of the BeNeLux Chapter of ISMRM, Nijmegen; 2007

Poser BA, Barth M, Norris D. *Evidence for functional activation in fusiform face area and amygdala using high-resolution single-shot GE-EPI at 7 T*. In: Proceedings to the first Annual Meeting of the BeNeLux Chapter of ISMRM, Nijmegen; 2007

Poser BA, Norris DG. *PAID fMRI at 7T - investigating the benefits of multi-echo EPI at high field*. In: Proceedings of the 16th Scientific Meeting, International Society for Magnetic Resonance in Medicine, Toronto, p 3562; 2008

Poser BA, Norris D. *Plausibility of Delayed Arteriolar Compliance as Cause of the BOLD Post-Stimulus Undershoot in Presence of Post-Stimulus Elevation in CMRO2: The Arterial Balloon Model.* In: Proceedings 16th Scientific Meeting, International Society for Magnetic Resonance in Medicine, Toronto, p 2350; 2008

Poser BA, Guenther M, Norris D. *BOLD fMRI using T_2* weighted selective parity single shot 3D GRASE imaging*. In: Proceedings of the 16th Scientific Meeting, International Society for Magnetic Resonance in Medicine, Toronto, p 2372; 2008

Poser BA, Norris D. *3D single-shot VASO using a Maxwell-gradient compensated GRASE sequence*. In: Proceedings to the second Annual Meeting of the BeNeLux Chapter of ISMRM, Antwerpen; 2008

Poser BA, Koopmans PA, Wald LL, Barth M. *Investigation into the benefits of 3D-EPI for high-resolution fMRI at 7T*. In: Proceedings of the 17th Scientific Meeting, International Society for Magnetic Resonance in Medicine, Honolulu; 2009

Poser BA, Norris D. *3D single-shot VASO using a Maxwell-gradient compensated GRASE sequence*. In: Proceedings of the 17th Scientific Meeting, International Society for Magnetic Resonance in Medicine, Honolulu; 2009

Curriculum Vitae

Andreas Benedikt Poser was born in the German town of Wolfenbüttel on the 4th of October 1978. He grew up with his parents Dorothea Poser, M.D. and architect Wilhelm Poser, Ph.D., and his two younger sisters. Benedikt moved to Kiel at the age of seven where he took up the hobby of sailing which has since been important to him throughout his life. He enjoyed his secondary education at the Heinrich-Heine-Gymnasium Heikendorf and the Alströmer Gymnasiet Alingsås in Sweden, before receiving a two year scholarship to visit the Waterford Kamhlaba United World College of Southern Africa in Swaziland. There he obtained the International Baccalaureate in 1997. In the following year, Benedikt completed his national service in the German forces but later returned several times in his role as reserve officer. In 1998 he started studying Physics with Business and Management at the University of Manchester, UK. During his studies, he spent one year working full-time in the Finance department at the BAE Systems Regional Aircraft Division, and completed multiple internships in aerospace engineering with Airbus in Hamburg and Toulouse. He obtained his First-Class Honours degree (MPhys) in June 2003.

Following his time in the United Kingdom, Benedikt moved to Nijmegen to commence his Ph.D. research under the supervision of David Norris at the then FC Donders Centre for Cognitive Neuroimaging. His research stimulated his interest in the development of new methods for functional magnetic resonance imaging (fMRI), in particular techniques based on echo-planar imaging and the multiple spin-echo experiment. During this period he enjoyed and benefited from working in the stimulating multi-disciplinary environment of the Donders Centre and the close collaborations with neuroscientists from a wide range of fields.

Since late 2006 Benedikt spends much of his time working on the 7 T system at the newly founded Erwin L. Hahn Institute for Magnetic Resonance Imaging in Essen, where his efforts concentrate on the development and optimisation of fMRI methods at high field. He now holds a full position at the Erwin L. Hahn Institute but maintains close ties with the Donders Institute where he still conducts large parts of his research.

Curriculum Vitae

Benedikt Poser, born October 4th, 1978 in Wolfenbüttel, Germany

Professional Experience

08 / 2008 –	Researcher at the Erwin L. Hahn Institute for Magnetic Resonance Imaging, Essen, Germany
11 / 2006 – 08 / 2008	Junior Researcher at the Erwin L. Hahn Institute for Magnetic Resonance Imaging, Essen, Germany
09 / 2003 – 08 / 2008	Junior Researcher at the F.C. Donders Centre for Cognitive Neuroimaging, Nijmegen, The Netherlands; MR-Methods for Cognitive Neuroscience

Education

09 /1998 – 06 / 2003	Physics with Business and Management, University of Manchester, United Kingdom (MPhys, First-Class degree)
02 / 1996 – 12 / 1997	Waterford Kamhlaba United World College of Southern Africa, Swaziland (on scholarship, International Baccalaureate with 42 pts, Abitur 1.0)
08 / 1995 – 12 / 1995	Alströmer Gymnasiet, Alingsås, Sweden
08 / 1986 – 07 / 1995	primary and secondary schools in Heikendorf / Kiel, Germany

Work experience, Internships, Service

09 / 2002 – 09 / 2002	Airbus, Toulouse: definition of flight simulation data packets for the A380
08 / 2002 – 08 / 2002	Airbus, Hamburg: R&D work on a head-mounted visual guidance system
06 / 2001 – 09 / 2001	Airbus, Hamburg: R&D work on A380 vacuum and air-conditioning system
09 / 2000 – 06 / 2001	BAE Systems Regional Aircraft division, Manchester: various positions in Finance
02 / 1998 – 12 / 1998	German national military service; later followed by reserve officer training and several exercises

Appendix Colour Figures

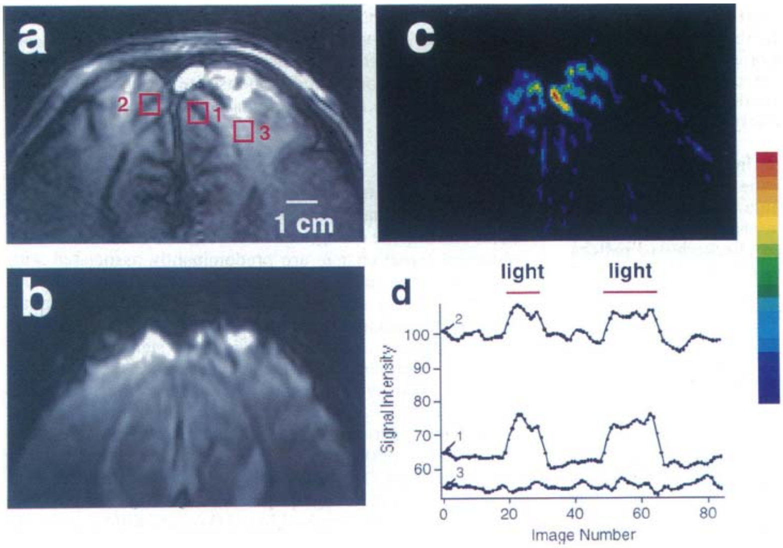

Figure 4.1: *One of the first BOLD activation maps obtained in the human brain by Ogawa and colleagues in 1992. The signal in the ROIs 1 and 2 placed within the visual cortex clearly show a signal increase during in the periods where a visual stimulus was applied (panel d); no change is seen in the ROI outside the visual cortex. Panel c shows a signal change map (Figure adapted from Ogawa et al, PNAS 1992 89:5951-5955 'Intrinsic signal changes accompanying sensory stimulation: functional brain mapping with magnetic resonance imaging').*

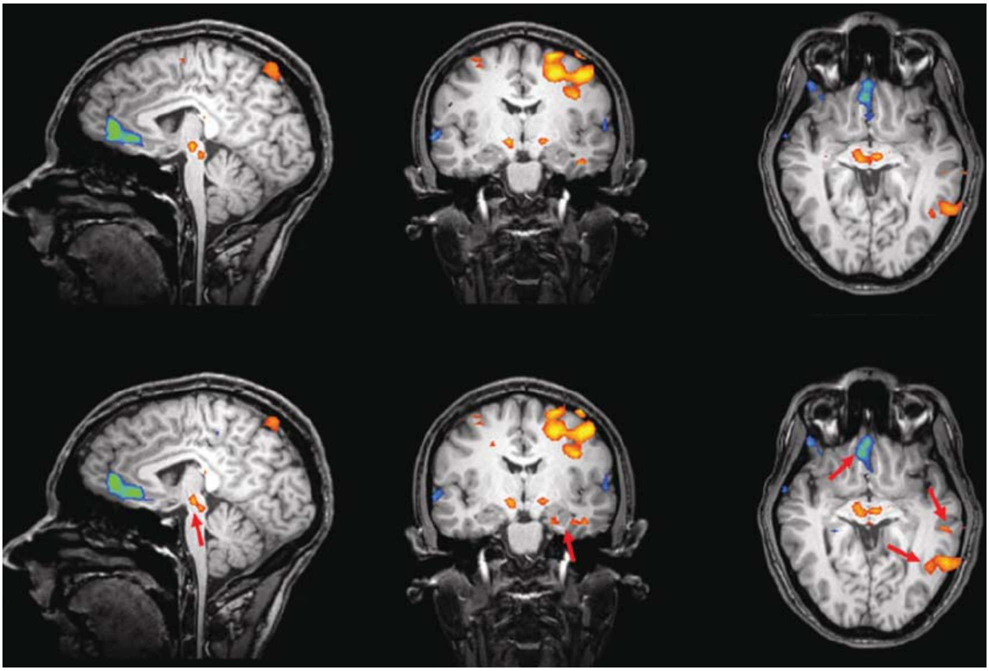

Figure 5.6: *Activation maps for simple (top) and T_2* weighted (bottom) echo combination at acceleration factor 3 (5 echoes). 'Incongruent vs. neutral' task contrast over all subjects is shown at p(corr.) < 0.001 (Talairach coordinates -4, -7, -7). Arrows indicate larger and additional activation sites in the T_2* weighted data.*

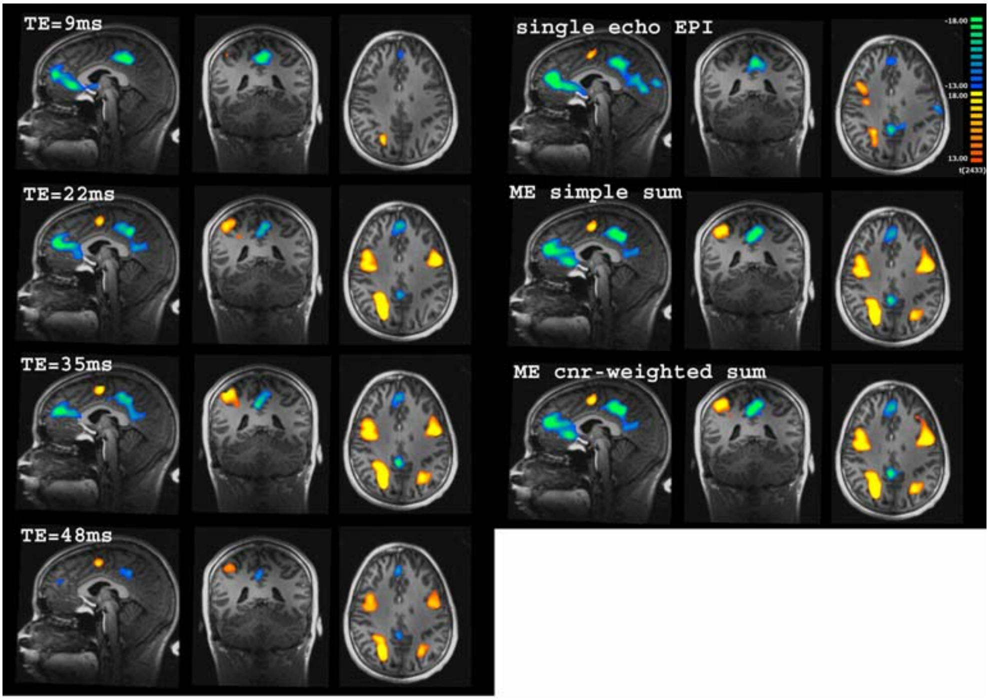

Figure 6.4: *Group activation maps for all task conditions vs. baseline (Talairach coordinate [0 -41 33], t > 13). LEFT: activation maps obtained by separate analysis of the four echo time courses (TE as indicated). Especially the 'deactivation' in anterior and posterior cingulate cortex is well visible at the very short TE of 9 ms. At 22 ms the positive activations become apparent, and a considerable amount is still detected in the latest echo (TE 48 ms). The overall echo time dependence of activation does not appear to be very pronounced. RIGHT: comparison of activation in the single echo EPI data (top), with the multi-echo results for simple (middle) and CNR-weighted summation (bottom). Considerably larger activation clusters are detected with the ME protocol, especially in the more superior brain. Overall, CNR-weighted summation outperforms simple summation, albeit with only a small difference in activation volume and t-score. For detailed results see Table 6.1.*

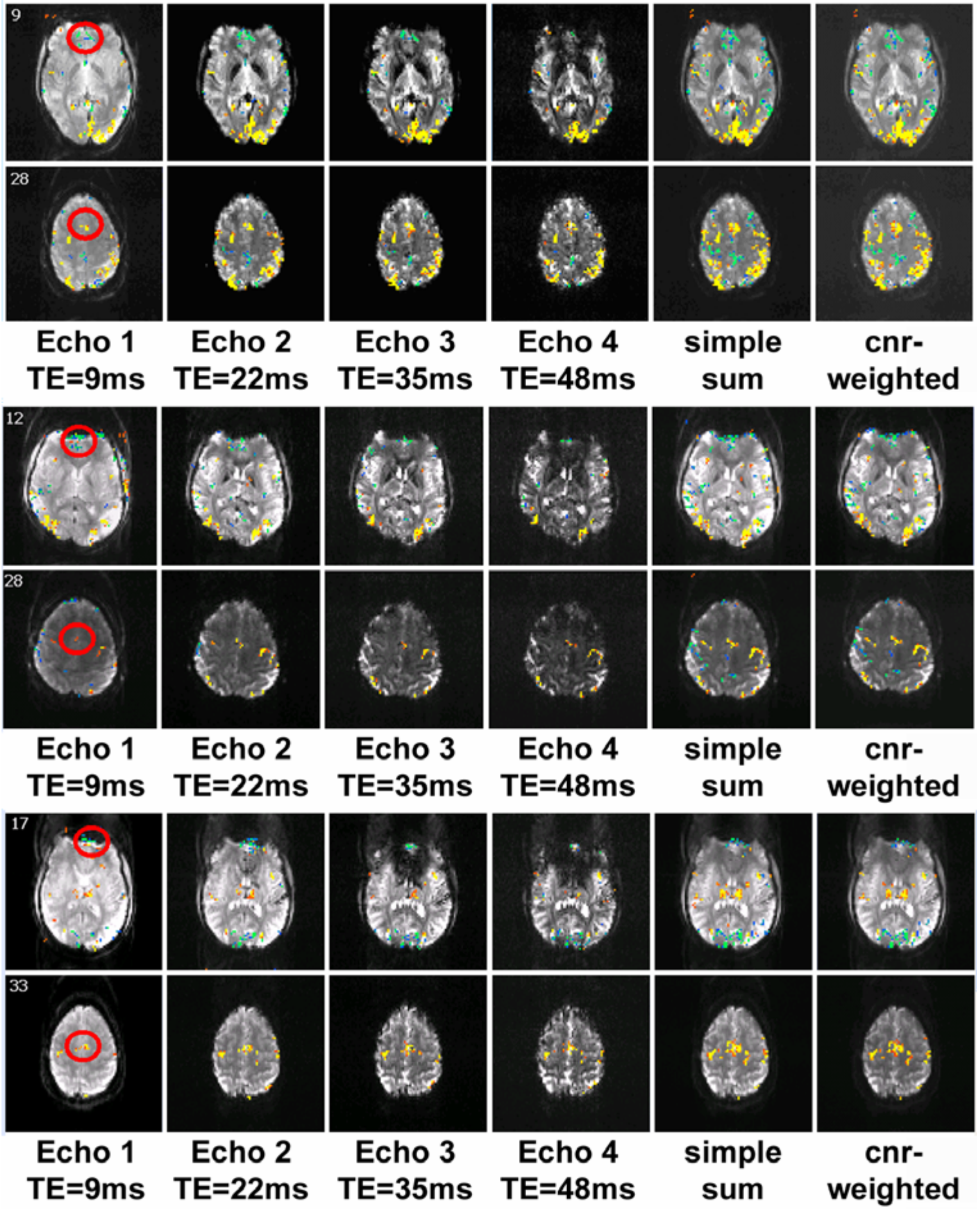

Figure 6.5: *Echo time dependence of activation in the unsmoothed data of three subjects, shown separately for the individual echoes, simply summed and CNR-weighted data (from left to right). A larger than expected amount of activation is detected at the very early (9 ms) and very late (48 ms) echo times. The two ROIs which were investigated in detail are marked by the red circle in the 9 ms echo.which were investigated in detail are marked by the red circle in the 9 ms echo.*

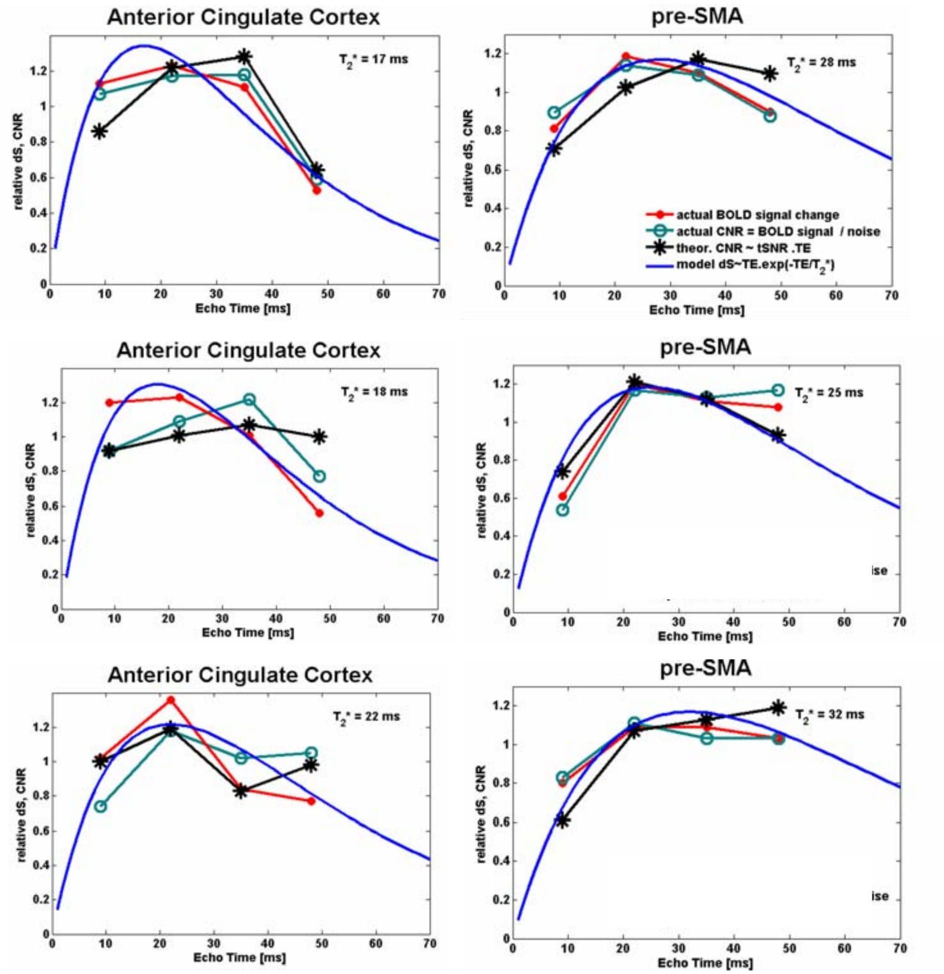

Figure 6.7: *Echo time dependencies of: model BOLD contrast as TE·exp(-TE/T_2*) (solid line), observed absolute BOLD signal change (full circles), actual BOLD CNR as ratio of observed absolute signal change and measured temporal noise (open circles), and theoretical CNR calculated as measured tSNR·TE (asterisk); each curve is normalized to yield a sum of 4 (i.e. an average value of unity) when adding their values at the four echo time points. The 'theoretical CNR' curve (asterisk) is used to obtain the summation weights in CNR-weighted echo summation (albeit in a voxelwise manner, shown here is the ROI average). Its clear departure from the 'actual CNR' for the shorter echo times explains why CNR weighting performs comparable to, or slightly less well than simple echo summation.*

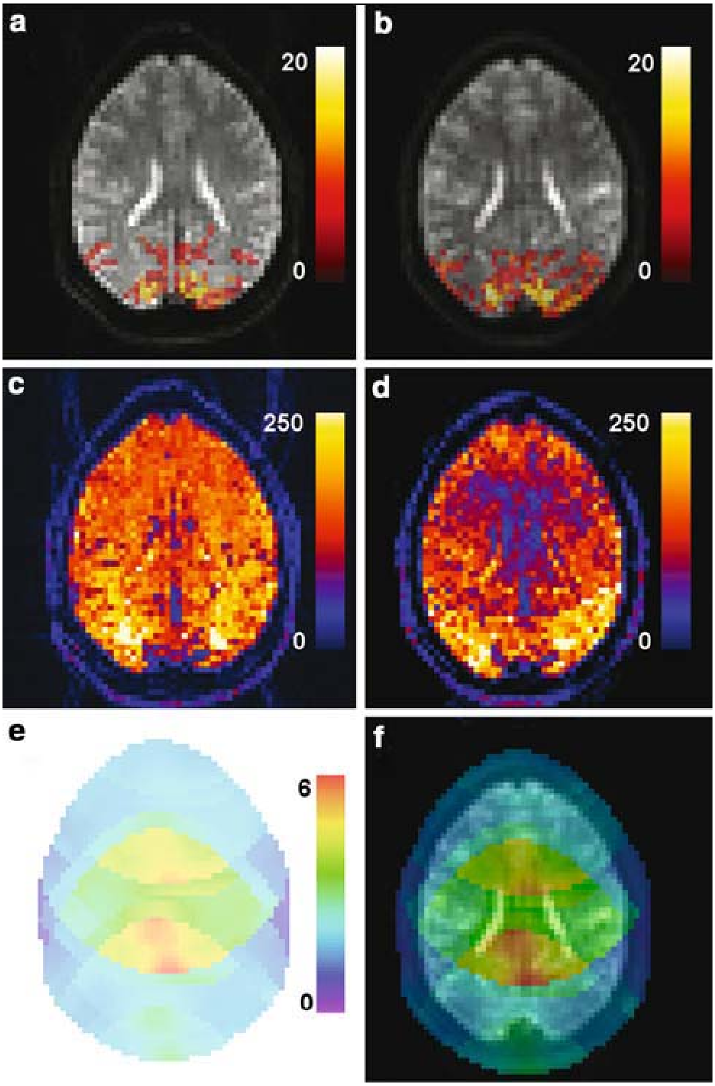

Figure 7.3: *Typical SE-EPI (a) and HASTE (b) images with activation overlays at* $p < 0.0001$ *(colour scale represents t-scores). Subfigures (c) and (d) show tSNR maps of the SE-EPI and HASTE data, respectively. Spatial variation in the latter resembles that of the g-map (e). The overlay of g-map on HASTE image (f) illustrates that visual areas are not strongly affected by g-noise.*

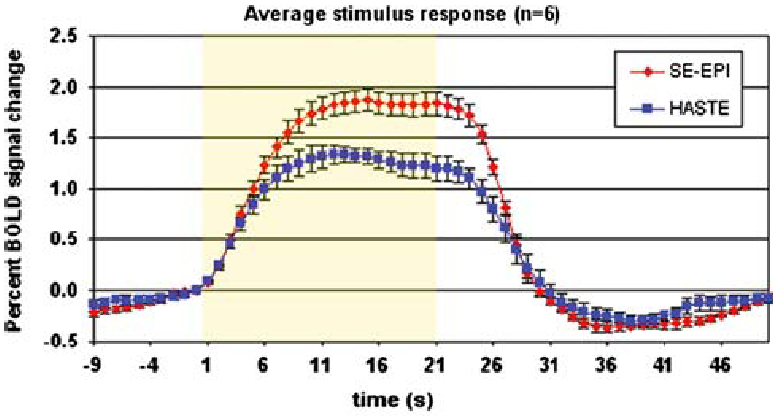

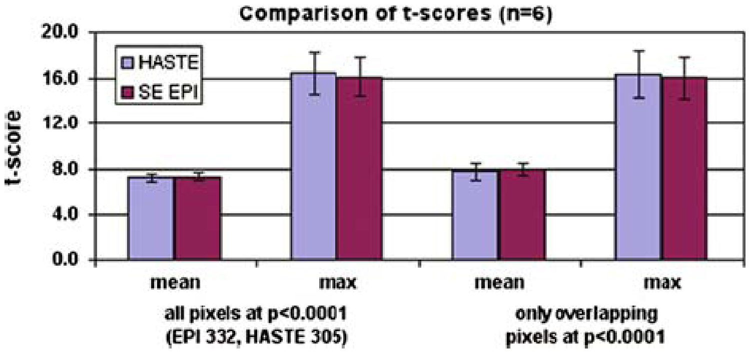

Figure 7.4: *Results of SE-EPI and HASTE BOLD measurements. Top: Stimulus response curve considering all active pixels, averaged over subjects (error bars = SEM over subjects, they reflect variation in signal change across subjects, but not sensitivity). Note that the average response curves of individual subjects were not normalized prior to averaging to allow comparison of the amplitude of the signal change between HASTE and EPI. The shaded region marks the 21 s stimulation period. Bottom: Mean and maximum t-scores at p < 0.0001 (subject average, error bars = SD). For the calculation of overlapping pixels the distortion was assumed to be negligible.*

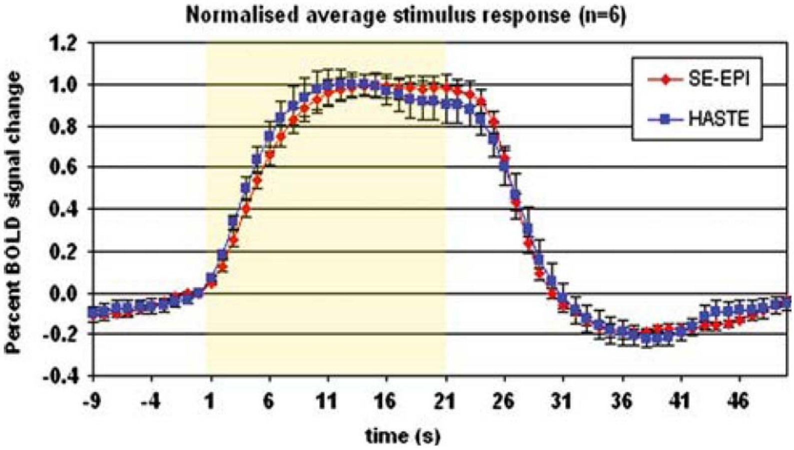

Figure 7.5: *Normalisation of the curves shown in Fig. 7.4 results in both response curves being perfectly aligned, showing that HASTE sensitivity in the main and undershoot response scales by the same factor compared to SE-EPI.*

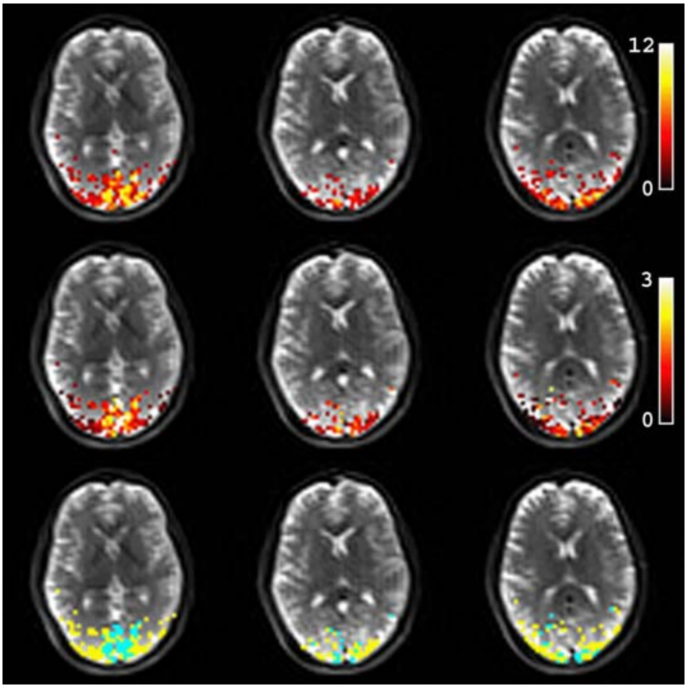

Figure 8.6: *Example of activation maps from one subject at 3 T, overlaid on three slices of the corresponding T_2-weighted HASTE images (top row). Also shown are the percent signal changes (middle row), and the vessel-tissue segmentation map (bottom row). For the latter, active voxels were subdivided into 'tissue' and 'vessel' voxels by sorting them according to positive percent signal change. The top 25% were considered voxels with a large contribution from draining vessels, depicted in green. The remaining 75% were taken as tissue voxels, depicted in yellow.*

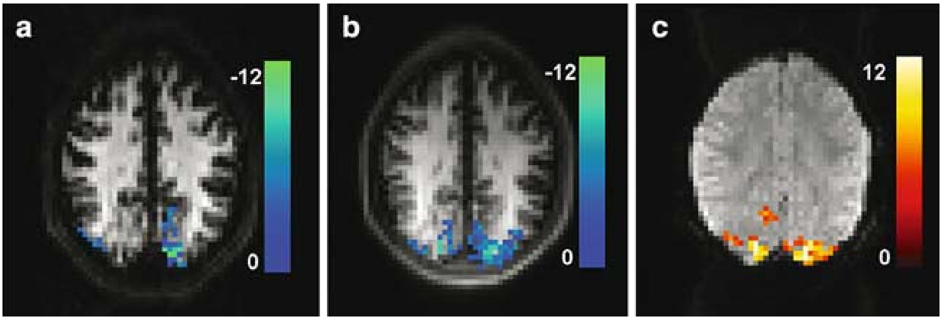

Figure 9.1: *Typical EPI (a) and HASTE (b) VASO images with activation overlays (t-scores, p < 0.0004). Activation regions detected in the HASTE data are considerably larger, suggesting superior functional sensitivity. As a result, the activation pattern of HASTE more closely resembles that of the BOLD measurements (c). The use of pure spin echoes results in nearly factor 1.7 higher grey matter intensity in the HASTE images as compared to the EPI images.*

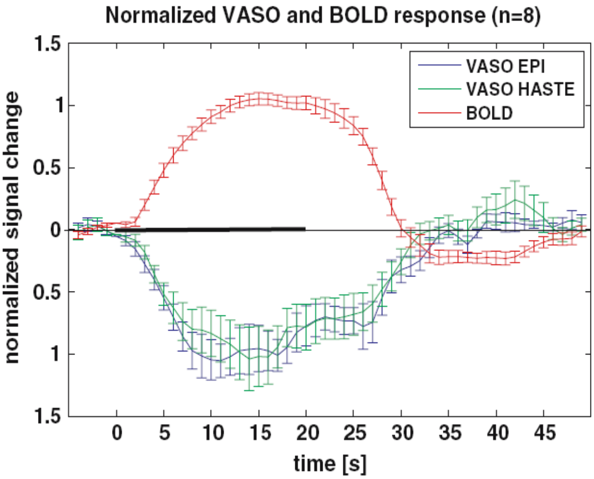

Figure 9.2: *Averaged stimulus response (n = 8) of the EPI and HASTE VASO activation (p < 0.0004). Note the decline of the CBV well before the end of the stimulus; this behaviour is much less pronounced in the BOLD response. The VASO curves show a nearly identical signal time course, with a return to baseline that essentially coincides with that of the BOLD (error bars = SEM). The stimulation period is indicated by the solid line on the time axis. The baseline was taken as the average of the 5 s before stimulus onset.*

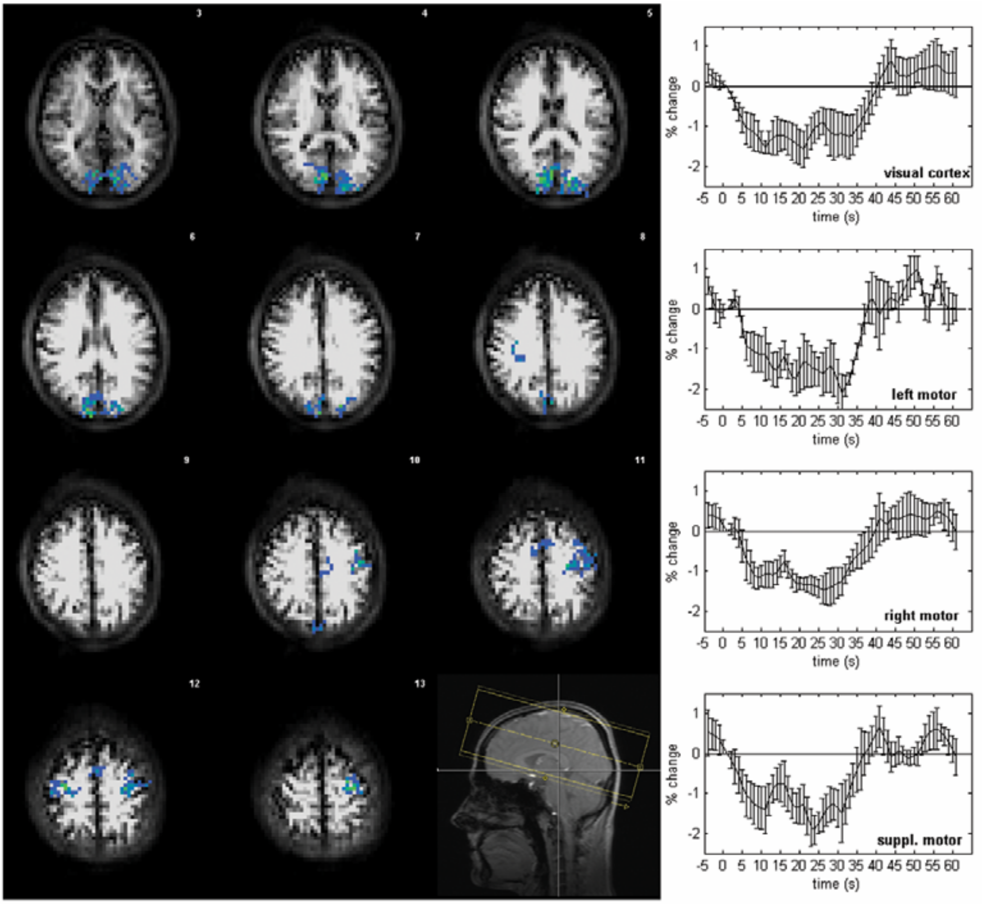

Figure 10.3: ***GRASE VASO activation map (t-test, $p<0.01$) of a single subject (subject two, first run, 150 volumes) overlaid on the native data, showing activation in visual cortex, left and right motor cortex and supplementary motor area. Also shown are the average stimulus responses in the respective ROIs, and the slab positioning.***

Series Donders Institute for Brain, Cognition and Behaviour

1. van Aalderen-Smeets, S.I. (2007). *Neural dynamics of visual selection.* Maastricht University, Maastricht, The Netherlands.
2. Schoffelen, J.M. (2007). *Neuronal communication through coherence in the human motor system.* Radboud University Nijmegen, Nijmegen, The Netherlands.
3. de Lange, F.P. (2008). *Neural mechanisms of motor imagery.* Radboud University Nijmegen, Nijmegen, The Netherlands.
4. Grol, M.J. (2008). *Parieto-frontal circuitry in visuomotor control.* University Utrecht, Utrecht, The Netherlands.
5. Bauer, M. (2008). *Functional roles of rhythmic neuronal activity in the human visual and somatosensory system.* Radboud University Nijmegen, Nijmegen, The Netherlands.
6. Mazaheri, A. (2008). *The Influence of Ongoing Oscillatory Brain Activity on Evoked Responses and Behaviour*. Radboud University Nijmegen, Nijmegen, The Netherlands.
7. Hooijmans, C.R. (2008). *Impact of nutritional lipids and vascular factors in Alzheimer's Disease.* Radboud University Nijmegen, Nijmegen, The Netherlands.
8. Gaszner, B. (2008). *Plastic responses to stress by the rodent urocortinergic Edinger-Westphal nucleus.* Radboud University Nijmegen, Nijmegen, The Netherlands.
9. Willems, R.M. (2009). *Neural reflections of meaning in gesture, language and action.* Radboud University Nijmegen, Nijmegen, The Netherlands.
10. Van Pelt, S. (2009). *Dynamic neural representations of human visuomotor space.* Radboud University Nijmegen, Nijmegen, The Netherlands.
11. Lommertzen, J. (2009). *Visuomotor coupling at different levels of complexity.* Radboud University Nijmegen, Nijmegen, The Netherlands.
12. Poljac, E. (2009). *Dynamics of cognitive control in task switching: Looking beyond the switch cost.* Radboud University Nijmegen, Nijmegen, The Netherlands.
13. Poser, B.A. (2009) *Techniques for BOLD and blood volume weighted fMRI.* Radboud University Nijmegen, Nijmegen, The Netherlands.
14. Baggio, G. (2009). *Semantics and the electrophysiology of meaning. Tense, aspect, event structure*. Radboud University Nijmegen, Nijmegen, The Netherlands.
15. van Wingen, G.A. (2009). *Biological determinants of amygdala functioning*. Radboud University Nijmegen Medical Centre, Nijmegen, The Netherlands.
16. Bakker, M. (2009). *Supraspinal control of walking: lessons from motor imagery.* Radboud University Nijmegen Medical Centre, Nijmegen, The Netherlands.

17. Aarts, E. (2009). *Resisting temptation: the role of the anterior cingulate cortex in adjusting cognitive control.* Radboud University Nijmegen, Nijmegen, The Netherlands.